

# THERMAL STRATIFICATION AND CHEMICAL REACTION EFFECTS ON MHD FLOW THROUGH OSCILLATORY VERTICAL PLATE IN A POROUS MEDIUM WITH TEMPERATURE VARIATION AND EXPONENTIAL MASS DIFFUSION

 Digbash Sahu\*,  Rudra Kanta Deka

*Department of Mathematics, Gauhati University, Guwahati, 781014, Assam, India*

*\*Corresponding Author e-mail: [digbashsahu79@gmail.com](mailto:digbashsahu79@gmail.com)*

Received April 1, 2024; revised April 19, 2024; accepted May 5, 2024

This research paper investigates the thermal stratification and chemical reaction effects on MHD Flow through oscillatory vertical plate in a porous medium with temperature variation and exponential mass diffusion. Through the application of the Laplace transform method, the paper derives analytical solutions that precisely depict the physical dynamics of the flow. The investigation utilizes sophisticated mathematical models to scrutinize the complex dynamics between Magnetohydrodynamics (MHD) and convective movements, considering a range of conditions involving temperature fluctuations and exponential rates of mass diffusion. A pivotal finding from this research is the detailed comparison between the outcomes of thermal stratification and those observed in environments lacking such stratification. It is observed that the implementation of stratification within the flow leads to a more rapid achievement of equilibrium or steady-state conditions.

**Keywords:** *MHD flow; Chemical Reaction; Thermal Stratification; Porous Medium; Oscillatory Vertical Plate; Laplace Transform; Matlab*

**PACS:** 44.05.+e, 44.25.+f, 47.11.-j, 47.55.P-, 47.56.+r, 47.65.-d

## 1. INTRODUCTION

The ubiquitous phenomena of thermal stratification in fluid systems result from fluids innate propensity to arrange themselves into discrete temperature strata according to their thermal characteristics. The temperature distribution that is stratified within a fluid medium is a key factor in determining the thermal properties of different natural and artificial settings. Thermal stratification has a significant impact on heat transport, energy efficiency, and environmental dynamics. It is especially common in water bodies, atmospheric conditions, and industrial operations.

This research represents the first of its kind to examine the combined effects of thermal stratification and chemical reaction on the flow around an oscillating vertical plate, building on a foundation established by previous studies in related areas. Initial efforts by [1] and [2] were crucial in developing an understanding of transient free convection flows along vertical flat plates, which was further expanded upon by [3] who looked into unsteady natural convection adjacent to infinitely long vertical plates. Subsequent research broadened the scope of investigation into various facets of this phenomenon. Investigations into transient buoyant flows within stratified fluids were conducted by [4] and [5, 6], while [7] focused on flow dynamics driven by convection in fluids that were stably stratified. The domain of porous media received significant attention as well, with [8] studying unsteady free convection in a porous medium saturated with fluid, and [9] delving into the dynamics of heat and mass transfer through natural convection in such mediums. The role of radiation and magnetic fields in these processes was not overlooked; [10] assessed MHD boundary layer flow over vertical plates with a gradient in temperature, and [11] evaluated MHD free convective mass transfer effects alongside variable suction and the Soret effect. The interaction between chemical reaction and thermal radiation received particular focus in the works of [12] and [13], who explored the influence of chemical reaction on vertical plates subjected to radiation and thermal stratification. The dynamics of chemically reactive flows were extensively explored by [14], [15], and [16], who concentrated on the consequences of chemical reactions on fluid movement near oscillating plates and stretching surfaces across various scenarios, including heat and mass transfer, and the presence of magnetic fields. This paved the way for more nuanced studies, such as those by [17] and [18, 19], which investigated the unsteady flow near vertical plates with chemical reactions under thermal stratification. [20] extended these observations to porous media with a focus on mass diffusion, and [21] further broadened the scope by examining non-Newtonian fluids in porous media affected by chemical reaction and thermal stratification, highlighting the

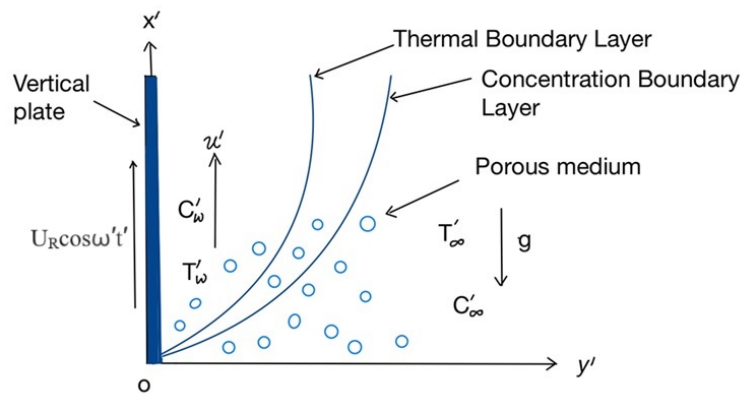


Figure 1. Physical Model and coordinate system

comprehensive exploration of these complex interactions in fluid dynamics.

This research, offering profound implications for industries like chemical manufacturing, polymer production, and crystal separation, encompasses a wide array of studies on MHD unsteady and transient heat transfer in vertical plates. These studies, covering stratification, chemical reaction, magnetic field, porous medium, and radiation, collectively deepen our understanding of natural convection under diverse fluid and environmental conditions.

## 2. MATHEMATICAL ANALYSIS

Consider the problem of an unsteady Magnetohydrodynamic (MHD) flow of a viscous, incompressible, and stratified fluid over a vertically oscillating plate embedded in a porous medium. This setup is described using a rectangular Cartesian coordinate system  $(x', y', t')$ , where the  $y'$  axis is perpendicular to the plate and the  $x'$  axis is aligned vertically along the plate. The fluid velocity at any point  $(x', y', t')$  is denoted by  $q = (u', 0)$ . Initially, at  $t' = 0$ , both the temperature and concentration of the fluid at the plate are  $T'_\infty$  and  $C'_\infty$ , respectively. For times  $t' > 0$ , the plate starts oscillating in its own plane with a velocity of  $U_R \cos \omega t'$  relative to the gravitational field. Concurrently, at  $t' > 0$ , the temperature at the plate rises to  $T'_w + (T'_w - T'_\infty)At'$ , and the concentration increases to  $C'_w + (C'_w - C'_\infty)e^{a't'}$ . These dynamics are analyzed under the assumption of the standard Boussinesq approximation, leading to the formulation of equations for motion, energy, and concentration, alongside the defined boundary conditions.

$$\frac{\partial u'}{\partial t'} = g\beta(T' - T'_\infty) + g\beta^*(C' - C'_\infty) + \nu \frac{\partial^2 u'}{\partial y'^2} - \frac{\sigma B_0^2 u'}{\rho} - \frac{\nu}{k} u' \quad (1)$$

$$\frac{\partial T'}{\partial t'} = \frac{k}{\rho C_p} \frac{\partial^2 T'}{\partial y'^2} - \gamma' u' \quad (2)$$

$$\frac{\partial C'}{\partial t'} = D \frac{\partial^2 C'}{\partial y'^2} - K'_c u' \quad (3)$$

with the following initial and boundary Conditions:

$$\begin{aligned} u' = 0 & & T' = T'_\infty & & C' = C'_\infty & & \forall y', t' \leq 0 \\ u' = U_R \cos \omega t' & & T' = T'_w + (T'_w - T'_\infty)At' & & C' = C'_w + (C'_w - C'_\infty)e^{a't'} & & \text{at } y' = 0, t' > 0 \\ u' \rightarrow 0 & & T' \rightarrow T'_\infty & & C' \rightarrow C'_\infty & & \text{as } y' \rightarrow \infty, t' > 0 \end{aligned}$$

where  $a'$ ,  $\eta$ ,  $\nu$ ,  $D$ , and  $Da$  are respectively constant, similarity parameter, kinematic viscosity, mass diffusion coefficient, darcy number. The "thermal stratification parameter" is termed as  $\gamma = \frac{dT'_\infty}{dx'} + \frac{g}{C_p}$ . The term "thermal stratification" refers to the combination of vertical temperature advection  $\left(\frac{dT'_\infty}{dx'}\right)$ , where the temperature of the surrounding fluid is height-dependent, and work of compression  $\left(\frac{g}{C_p}\right)$ , the rate at which particles in a fluid do reversible work due to compression.

and we provide non-dimensional quantities in the following:

$$U = \frac{u'}{U_R}, \quad t = \frac{t'}{t_R}, \quad y = \frac{y'}{L_R}, \quad \omega = \omega' t_R, \quad \theta = \frac{T' - T'_\infty}{T'_w - T'_\infty}, \quad C = \frac{C' - C'_\infty}{C'_w - C'_\infty}, \quad M = \frac{\sigma B_0^2 \nu}{\rho U_R^2}, \quad A = \frac{1}{t_R}$$

$$Gr = \frac{\nu g \beta (T'_w - T'_\infty)}{U_R^3}, \quad Gc = \frac{\nu g \beta^* (C'_w - C'_\infty)}{U_R^3}, \quad Pr = \frac{\mu C_p}{k}, \quad Sc = \frac{\nu}{D}, \quad a = a' t_R, \quad \Delta T = T'_w - T'_\infty,$$

$$Da = \frac{U_R^2 k'}{\nu^2}, \quad \gamma = \frac{\gamma' L_R}{\Delta T}, \quad K_c = \frac{K'_c L_R^2}{\nu}, \quad U_R = (\nu g \beta \Delta T)^{1/3}, \quad t_R = (g \beta \Delta T)^{-2/3} \nu^{1/3}, \quad L_R = \left( \frac{g \beta \Delta T}{\nu^2} \right)^{-1/3}$$

Where  $Pr$  is Prandtl number,  $Gr$  is thermal Grashof number,  $Gc$  is mass Grashof number,  $M$  is Magnetic parameter,  $Sc$  is Schmidt number,  $t$  is time in dimensionless coordinate,  $L_R$  is reference length,  $t_R$  is reference time,  $U$  is dimensionless velocity,  $U_R$  is reference velocity,  $\mu$  is viscosity of fluid,  $\theta$  is the dimensionless temperature,  $C$  is dimensionless concentration,  $\omega$  is frequency of oscillation. Then non-dimensional forms of the equations (1)-(3) are given by

$$\frac{\partial U}{\partial t} = Gr\theta + GcC + \frac{\partial^2 U}{\partial y^2} - \left( M + \frac{1}{Da} \right) U \tag{4}$$

$$\frac{\partial \theta}{\partial t} = \frac{1}{Pr} \frac{\partial^2 \theta}{\partial y^2} - \gamma U \tag{5}$$

$$\frac{\partial C}{\partial t} = \frac{1}{Sc} \frac{\partial^2 C}{\partial y^2} - K_c C \tag{6}$$

Non-dimensional forms of initial and boundary Conditions are:

$$\begin{array}{llll} U = 0 & \theta = 0 & C = 0 & \forall y, t \leq 0 \\ U = \cos \omega t & \theta = t & C = e^{at} & \text{at } y = 0, t > 0 \\ U \rightarrow 0 & \theta \rightarrow 0 & C \rightarrow 0 & \text{as } y \rightarrow \infty, t > 0 \end{array} \tag{7}$$

### 3. METHOD OF SOLUTION

We discovered that the Laplace transform method produces an equation of non-tractable form for any arbitrary Prandtl or Schmidt number. The non-dimensional governing equations (4)-(6) with boundary conditions (7), are solved for the tractable situation of  $Pr = 1, Sc = 1$ . Hence, the expressions for velocity, temperature, and concentration profiles can be determined with the help of [22] and [23] are as follows

$$\begin{aligned} U = & D_2 \frac{\eta}{t\sqrt{\pi}} e^{-Et-\eta^2} + D_3 f_1(E, -a) - \frac{E}{2(P-E)} [f_1(E, i\omega) + f_1(E, -i\omega)] + \frac{Gr}{P-E} f_2(E) + (D_1 - D_2) \\ & \frac{\eta}{t\sqrt{\pi}} e^{-Pt-\eta^2} + \frac{P}{2(P-E)} [f_1(P, i\omega) + f_1(P, -i\omega)] + (aD_1 + D_1K_c - D_3) f_1(P, -a) - \frac{Gr}{P-E} f_2(P) \\ & D_1(a + K_c) f_1(K_c, -a) \end{aligned} \tag{8}$$

$$\begin{aligned} \theta = & D_4 t \left\{ (1 + 2\eta^2) \operatorname{erfc}(\eta) - \frac{2\eta}{\sqrt{\pi}} e^{-\eta^2} \right\} - \gamma \left[ \left( D_2 + \frac{D_1 - D_2}{P} - \frac{D_1}{K_c} \right) \frac{\eta}{t\sqrt{\pi}} e^{-\eta^2} + \left\{ \frac{D_3}{E} + \frac{aD_1 + D_1K_c - D_3}{P} \right. \right. \\ & \left. \left. - \frac{D_1(a + K_c)}{K_c} \right\} f_3(a) - \frac{D_2}{E} \frac{\eta}{t\sqrt{\pi}} e^{-Et-\eta^2} - \frac{D_1 - D_2}{P} \frac{\eta}{t\sqrt{\pi}} e^{-Pt-\eta^2} + \frac{D_1}{K_c} \frac{\eta}{t\sqrt{\pi}} e^{-K_c t - \eta^2} - \frac{D_3}{E} f_1(E, -a) \right. \\ & \left. - \frac{Gr}{E(P-E)} f_2(E) + \frac{1}{2(P-E)} (f_1(E, i\omega) + f_1(E, -i\omega)) - \frac{1}{2(P-E)} (f_1(P, i\omega) + f_1(P, -i\omega)) \right. \\ & \left. + \frac{aD_1 + D_1K_c - D_3}{P} f_1(P, -a) + \frac{D_1(a + K_c)}{K_c} f_1(K_c, -a) + \frac{Gr}{P(P-E)} f_2(p) \right] \end{aligned} \tag{9}$$

$$C = \frac{1}{2} \left[ e^{-2\eta\sqrt{(a+K_c)t}} \operatorname{erfc} \left( \eta - \sqrt{(a + K_c)t} \right) + e^{2\eta\sqrt{(a+K_c)t}} \operatorname{erfc} \left( \eta + \sqrt{(a + K_c)t} \right) \right] \tag{10}$$

Where,

$$\eta = \frac{y}{2\sqrt{t}}, \quad EP = \gamma Gr, \quad E + P = M + \frac{1}{Da}, \quad E - P = \sqrt{\left(M + \frac{1}{Da}\right)^2 - 4\gamma Gr}$$

$$D_1 = \frac{Gc}{K_c \left(K_c - M - \frac{1}{Da}\right) + \gamma Gr}, \quad D_2 = \frac{4aD_1 - D_1K_c + D_1P}{P - E}$$

$$D_3 = \frac{a^2D_1 + aD_1K_c + aD_1P + D_1K_cP + 3a^2D_1 - 2aD_1K_c - D_1K_c^2 + Gc}{P - E}, \quad D_4 = 1 + \frac{\gamma Gr}{P(P - E)} - \frac{\gamma Gr}{E(P - E)}$$

Also,  $f_i$ 's are inverse Laplace's transforms given by

$$f_1(p, q) = L^{-1} \left\{ \frac{e^{-y\sqrt{s+p}}}{s + q} \right\}, \quad f_2(p) = L^{-1} \left\{ \frac{e^{-y\sqrt{s+p}}}{s^2} \right\}, \quad f_3(q) = L^{-1} \left\{ \frac{e^{-y\sqrt{s}}}{s + q} \right\}$$

We separate the complex arguments of the error function contained in the previous expressions into real and imaginary parts using the formulas provided by [22].

#### 4. CLASSICAL CASE ( $\gamma = 0$ )

We derived solutions for the classical case of no thermal stratification ( $\gamma = 0$ ). We want to compare the results of the fluid with thermal stratification to the case with no stratification. Hence, the solutions for the classical case with boundary conditions (7) by using the Laplace transformation are as follows:

$$\theta_c = (1 + 2\eta^2)erfc(\eta) - \frac{2\eta}{\sqrt{\pi}}e^{-\eta^2} \tag{11}$$

$$U_c = \frac{1}{2} [f_1((E + P), i\omega) + f_1((E + P), -i\omega)] - \frac{Gr}{E + P}f_2(E + P) + \frac{Gc}{K_c - (E + P)}f_1((E + P), -a) + \frac{tGr}{(E + P)} \left\{ (1 + 2\eta^2)erfc(\eta) - \frac{2\eta}{\sqrt{\pi}}e^{-\eta^2} \right\} - \frac{Gc}{K_c - (E + P)}f_1(K_c, -a) \tag{12}$$

##### 4.1. Skin-Friction

The non-dimensional Skin-Friction, which is determined as shear stress on the surface, is obtained by

$$\tau = -\frac{dU}{dy} \Big|_{y=0}$$

The solution for the Skin-Friction is calculated from the solution of Velocity profile  $U$ , represented by (8), as follows:

$$\begin{aligned} \tau = & \frac{D_2e^{-Et}}{2\sqrt{\pi t^3}} + \frac{(D_1 - D_2)e^{-Pt}}{2\sqrt{\pi t^3}} + D_3 \left[ e^{at}\sqrt{a + E} \operatorname{erf}(\sqrt{(a + E)t}) + \frac{e^{-Et}}{\sqrt{\pi t}} \right] - \frac{E}{2(P - E)} \\ & \left[ e^{i\omega t}\sqrt{E + i\omega} \operatorname{erf}(\sqrt{(E + i\omega)t}) + e^{-i\omega t}\sqrt{E - i\omega} \operatorname{erf}(\sqrt{(E - i\omega)t}) + \frac{2e^{-Et}}{\sqrt{\pi t}} \right] + \frac{Gr}{P - E} \\ & \left[ t\sqrt{E} \operatorname{erf}(\sqrt{Et}) - t\sqrt{P} \operatorname{erf}(\sqrt{Pt}) + \sqrt{\frac{t}{\pi}}(e^{-Et} - e^{-Pt}) + \frac{\operatorname{erf}(\sqrt{Et})}{2\sqrt{E}} - \frac{\operatorname{erf}(\sqrt{Pt})}{2\sqrt{P}} \right] \\ & (aD_1 + D_1K_c - D_3) \left[ e^{at}\sqrt{a + P} \operatorname{erf}(\sqrt{(a + P)t}) + \frac{e^{-Pt}}{\sqrt{\pi t}} \right] + \frac{P}{2(P - E)} \\ & \left[ e^{i\omega t}\sqrt{P + i\omega} \operatorname{erf}(\sqrt{(P + i\omega)t}) + e^{-i\omega t}\sqrt{P - i\omega} \operatorname{erf}(\sqrt{(P - i\omega)t}) + \frac{2e^{-Pt}}{\sqrt{\pi t}} \right] \\ & - D_1K_c \left[ e^{at}\sqrt{a + K_c} \operatorname{erf}(\sqrt{(a + K_c)t}) + \frac{e^{-K_c t}}{\sqrt{\pi t}} \right] - (D_1 + aD_1) \frac{e^{K_c t}}{2\sqrt{\pi t^3}} \end{aligned}$$

The solution for the Skin-Friction for the classical case is given from the expression (12), which is represented by



$$\begin{aligned} \tau^* = & \left[ e^{i\omega t} \sqrt{(E+P) + i\omega} \operatorname{erf} \left( \sqrt{(E+P)t + i\omega t} \right) + e^{-i\omega t} \sqrt{(E+P) - i\omega} \operatorname{erf} \left( \sqrt{(E+P)t - i\omega t} \right) \right. \\ & \left. + \frac{2e^{-(E+P)t}}{\sqrt{\pi t}} \right] - \frac{Gr}{(E+P)} \left[ t\sqrt{(E+P)} \operatorname{erf} \left( \sqrt{(E+P)t} \right) + \sqrt{\frac{t}{\pi}} e^{-(E+P)t} + \frac{\operatorname{erf}(\sqrt{(E+P)t})}{2\sqrt{(E+P)}} \right] \\ & + \frac{Gc}{K_c - (E+P)} \left[ e^{at} \sqrt{(E+P) + a} \operatorname{erf} \left( \sqrt{(E+P)t + at} \right) + \frac{e^{-(E+P)t}}{\sqrt{\pi t}} \right] + \sqrt{\frac{t}{\pi}} \frac{2Gr}{(E+P)} \\ & - \frac{Gc}{K_c - (E+P)} \left[ e^{at} \sqrt{K_c + a} \operatorname{erf} \left( \sqrt{(K_c + a)t} \right) + \frac{e^{-K_c t}}{\sqrt{\pi t}} \right] \end{aligned}$$

### 4.2. Nusselt Number

The non-dimensional Nusselt number, which is determined as the rate of heat transfer, is obtained by

$$Nu = - \left. \frac{d\theta}{dy} \right|_{y=0}$$

The solution for the Nusselt number is calculated from the solution of Temperature profile  $\theta$ , represented by (9), as follows:

$$\begin{aligned} Nu = & 2D_4 \sqrt{\frac{t}{\pi}} - \gamma \left[ \frac{D_2}{2E\sqrt{\pi t^3}} + \left\{ \frac{D_3}{E} + \frac{aD_1 - D_1K_c - D_3}{P} - \frac{D_1(a + K_c)}{K_c} \right\} \left\{ e^{at} \sqrt{a} \operatorname{erf}(\sqrt{at}) + \frac{1}{\sqrt{\pi t}} \right\} \right. \\ & + \frac{D_1 - D_2}{2P\sqrt{\pi t^3}} - \frac{D_1}{2K_c\sqrt{\pi t^3}} - \frac{D_2 e^{-Et}}{2\sqrt{\pi t^3}} - \frac{D_3}{E} \left\{ e^{at} \sqrt{a + E} \operatorname{erf} \left( \sqrt{(a + E)t} \right) + \frac{e^{-Et}}{\sqrt{\pi t}} \right\} - \frac{Gr}{E(P - E)} \\ & \left. \left\{ t\sqrt{E} \operatorname{erf}(\sqrt{Et}) + \sqrt{\frac{t}{\pi}} e^{-Et} + \frac{\operatorname{erf}(\sqrt{Et})}{2\sqrt{E}} \right\} - \frac{(D_1 - D_2)e^{-Pt}}{2\sqrt{\pi t^3}} + \frac{1}{2(P - E)} \right. \\ & \left. \left\{ e^{i\omega t} \sqrt{E + i\omega} \operatorname{erf}(\sqrt{(E + i\omega)t}) + e^{-i\omega t} \sqrt{E - i\omega} \operatorname{erf}(\sqrt{(E - i\omega)t}) + \frac{2e^{-Et}}{\sqrt{\pi t}} \right\} - \frac{1}{2(P - E)} \right. \\ & \left. \left\{ e^{i\omega t} \sqrt{P + i\omega} \operatorname{erf}(\sqrt{(P + i\omega)t}) + e^{-i\omega t} \sqrt{P - i\omega} \operatorname{erf}(\sqrt{(P - i\omega)t}) + \frac{2e^{-Pt}}{\sqrt{\pi t}} \right\} - \frac{aD_1 - D_1K_c - D_3}{P} \right. \\ & \left. \left\{ e^{at} \sqrt{a + P} \operatorname{erf}(\sqrt{(a + P)t}) + \frac{e^{-Pt}}{\sqrt{\pi t}} \right\} + \frac{D_1 e^{-K_c t}}{2K_c\sqrt{\pi t^3}} + \frac{D_1(a + K_c)}{K_c} \left\{ e^{at} \sqrt{a + K_c} \operatorname{erf}(\sqrt{(a + K_c)t}) \right. \right. \\ & \left. \left. + \frac{e^{-K_c t}}{\sqrt{\pi t}} \right\} + \frac{Gr}{P(P - E)} \left\{ t\sqrt{P} \operatorname{erf}(\sqrt{Pt}) + \sqrt{\frac{t}{\pi}} e^{-Pt} + \frac{\operatorname{erf}(\sqrt{Pt})}{2\sqrt{P}} \right\} \right] \end{aligned}$$

The solution for the Nusselt number for the classical case is given from the expression (11), which is represented by

$$Nu^* = 2 \sqrt{\frac{t}{\pi}}$$

### 4.3. Sherwood Number

The non-dimensional Sherwood number, which is determined as the rate of mass transfer, is obtained by

$$Sh = - \left. \frac{dC}{dy} \right|_{y=0}$$

The solution for the Sherwood number is calculated from the solution of Concentration profile  $C$ , represented by (10), as follows:

$$Sh = \sqrt{a + K_c} \operatorname{erf}(\sqrt{(a + K_c)t}) + \frac{1}{\sqrt{\pi t}} e^{-(a+K_c)t}$$

### 5. RESULT AND DISCUSSIONS

We calculated the numerical values for velocity, temperature, concentration, skin friction, Nusselt number, and Sherwood number by utilizing the solutions obtained in previous sections, for different values of the physical parameters  $\gamma, Gr, Gc, M, Da, K_c, \omega$ , and  $t$ . This process enhanced our comprehension of the problem's physical importance. Additionally, by employing MATLAB, we visually represented these calculations in Figures 2 through 17.

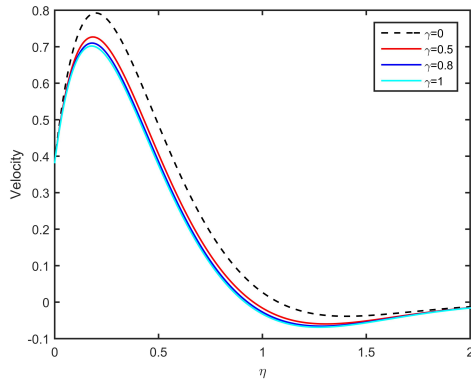


**Figure 2.** Effects of  $\gamma$  on Velocity Profile for  $t = 1.5, a = 0.2, \omega = \pi/4, Gr = 5, Gc = 5, M = 2, Da = 0.5, K_c = 0.2$

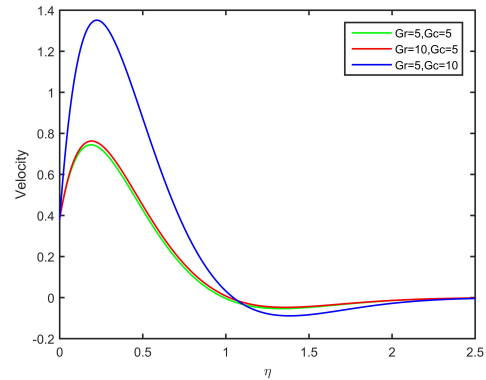


**Figure 3.** Effects of  $\gamma$  on Velocity Profile for  $t = 1.5, a = 0.2, \omega = \pi/4, \gamma = 0.5, M = 2, Da = 0.5, K_c = 0.2$

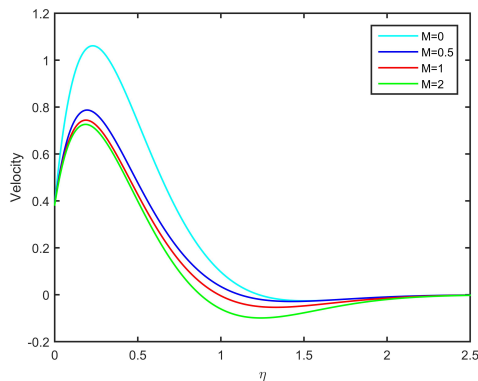


**Figure 4.** Effects of  $M$  on Velocity Profile for  $t = 1.5, a = 0.2, \omega = \pi/4, Gr = 5, Gc = 5, \gamma = 0.5, Da = 0.5, K_c = 0.2$

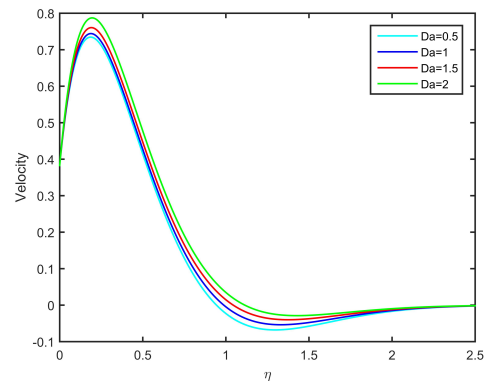


**Figure 5.** Effects of  $Da$  on Velocity Profile for  $t = 1.5, a = 0.2, \omega = \pi/4, Gr = 5, Gc = 5, \gamma = 0.5, M = 2, K_c = 0.2$

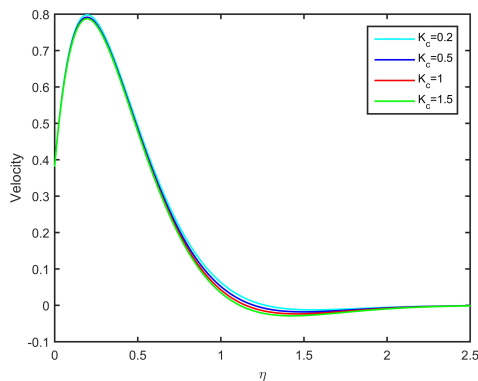


**Figure 6.** Effects of  $K_c$  on Velocity Profile for  $t = 1.5, a = 0.2, \omega = \pi/4, Gr = 5, Gc = 5, \gamma = 0.5, M = 2, Da = 0.5$

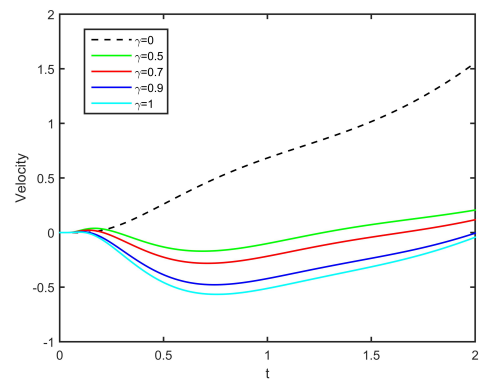


**Figure 7.** Effects of  $\gamma$  on Velocity Profile against time for  $y = 1.2, a = 0.2, \omega = \pi/4, Gr = 5, Gc = 5, \gamma = 0.5, M = 2, Da = 0.5$

The presented Figures 2 through 7 illustrate the influence of various physical parameters on velocity profiles. In Figure 2, as the parameter  $\gamma$  increases, there's a marked reduction in peak velocity, suggesting a damping

effect. In the 3 and 4 Figures, it is evident that increases in Grashof number  $Gr$  for thermal buoyancy and magnetic parameter  $M$  cause velocity profiles to peak at lower values and shift to the left. Figure 5 indicates that with increasing Darcy number  $Da$ , peak velocities increase, suggesting less resistance to flow through porous media. Figure 6 highlights the influence of the chemical reaction parameter  $K_c$ , with higher values leading to lower velocities, indicative of the retarding influence of the chemical reaction on the flow. Lastly, Figure 7 shows that as the thermal stratification parameter ( $\gamma$ ) increases, the fluid's velocity initially decreases and then stabilizes over time, with ( $\gamma = 0$ ) exhibiting the highest velocity.

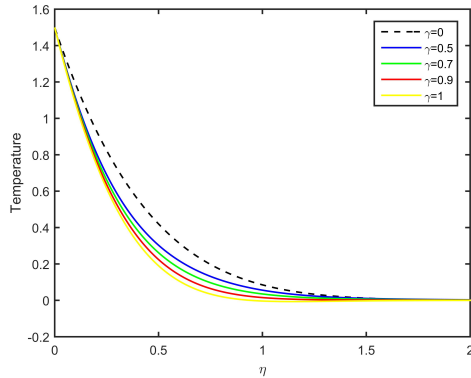


**Figure 8.** Effects of  $\gamma$  on Temperature Profile for  $t = 1.5, a = 0.2, \omega = \pi/4, Gr = 5, Gc = 5, M = 2, Da = 0.5, K_c = 0.2$

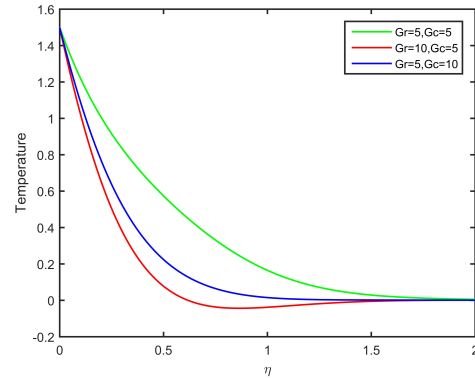


**Figure 9.** Effects of  $\gamma$  on Temperature Profile for  $t = 1.5, a = 0.2, \omega = \pi/4, \gamma = 0.5, M = 2, Da = 0.5, K_c = 0.2$

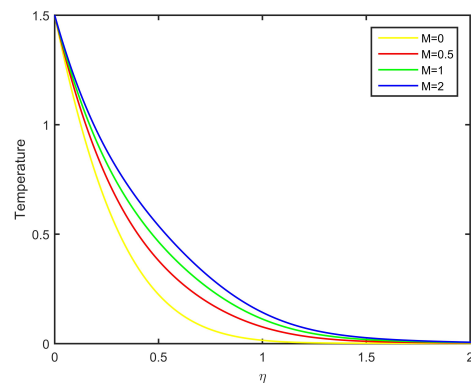


**Figure 10.** Effects of  $M$  on Temperature Profile for  $t = 1.5, a = 0.2, \omega = \pi/4, Gr = 5, Gc = 5, \gamma = 0.5, Da = 0.5, K_c = 0.2$

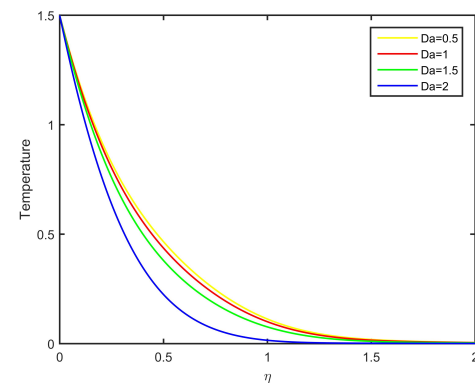


**Figure 11.** Effects of  $Da$  on Temperature Profile for  $t = 1.5, a = 0.2, \omega = \pi/4, Gr = 5, Gc = 5, \gamma = 0.5, M = 2, K_c = 0.2$

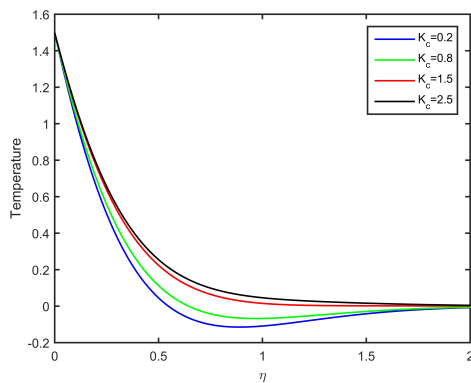


**Figure 12.** Effects of  $K_c$  on Temperature Profile for  $t = 1.5, a = 0.2, \omega = \pi/4, Gr = 5, Gc = 5, \gamma = 0.5, M = 2, Da = 0.5$

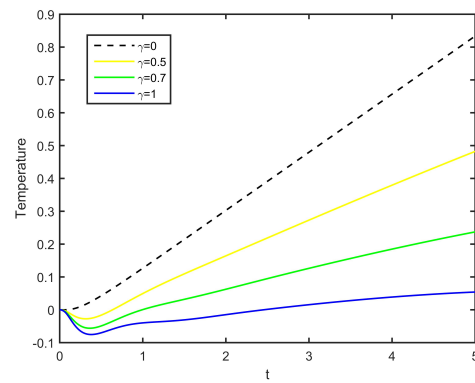


**Figure 13.** Effects of  $\gamma$  on Temperature Profile against time for  $y = 1.2, a = 0.2, \omega = \pi/4, Gr = 5, Gc = 5, \gamma = 0.5, M = 2, Da = 0.5$

Figures 8 through 13 depicts the temperature profiles for various physical parameters. In figure 8 shows that

as the parameter  $\gamma$  increases, the temperature decreases across the profile, with the steepest gradient near  $\gamma = 0$ . Figure 9 indicates that higher Grashof numbers for thermal buoyancy lead to lower temperatures, particularly noticeable for  $Gr = 10, Gc = 5$ . Figure 10 suggests that an increase in the magnetic parameter  $M$  results in a more uniform temperature distribution, highlighting magnetic damping of thermal fluctuations. In Fig 11, higher Darcy numbers result in lower temperatures, indicating reduced resistance to thermal conduction in porous media. Figure 12 shows that reduced chemical reaction parameters  $K_c$  correspond to lower temperatures. Finally, fig 13 demonstrates the time evolution of the temperature profile, with higher  $\gamma$  values leading to a slower increase in temperature over time, likely due to thermal diffusion or delayed thermal response in the system.

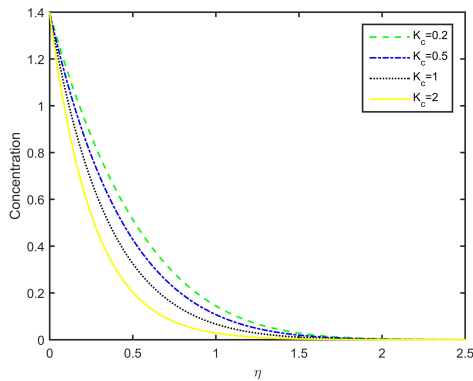


**Figure 14.** Effects of  $K_c$  on Concentration Profile for  $t = 1.6, a = 0.2$

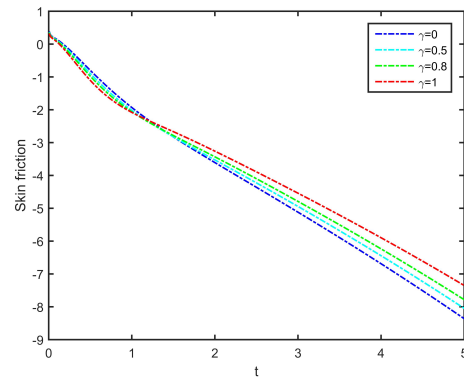


**Figure 15.** Effects of  $\gamma$  on Skin friction for  $a = 0.2, \omega = \pi/4, Gr = 5, Gc = 5, M = 2, Da = 0.5, K_c = 0.2$

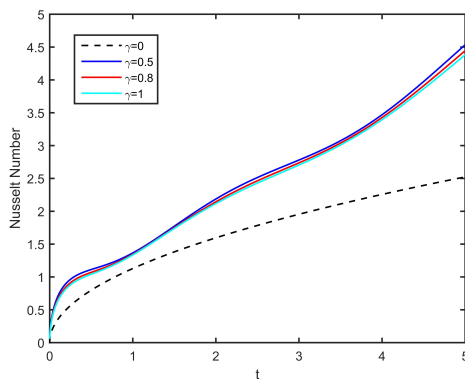


**Figure 16.** Effects of  $\gamma$  on Nusselt Number for  $a = 0.2, \omega = \pi/4, Gr = 5, Gc = 5, M = 2, Da = 0.5, K_c = 0.2$

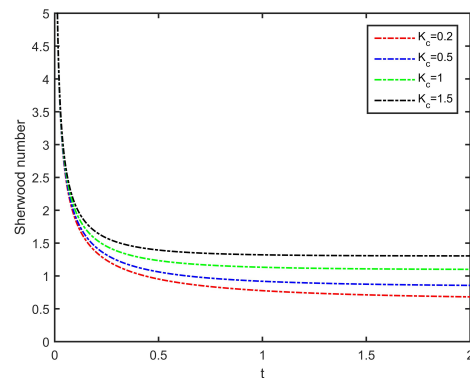


**Figure 17.** Effects of  $K_c$  on Sherwood Number for  $t = 1.6, a = 0.2$

Figure 14 displays concentration profiles for different values of the chemical reaction parameter  $K_c$ . As  $K_c$  increases, concentration within the boundary layer decreases, indicating a stronger chemical reaction diminishes species concentration.

Figure 15 presents skin friction decreasing linearly over time for different values of  $\gamma$ , with the rate of decrease being similar across the values. Nusselt number increases linearly over time for different values of  $\gamma$ , with higher  $\gamma$ , having a steeper slope as shown in figure 16. Figure 17 illustrates the Sherwood number decreasing with time and approaching a constant value for various  $K_c$ , with higher  $K_c$  resulting in a lower asymptote.

## 6. CONCLUSION



Building on the insights garnered from the discussion earlier in this paper, the subsequent sections outline the key conclusions drawn from this research.

- As  $\gamma$  increases, both velocity and temperature decrease due to the stabilizing influence of thermal stratification, leading the fluid towards a steady state. Conversely, in the classical scenario without thermal

stratification, the velocity and temperature remain higher compared to those in the thermally stratified fluid.

- As  $Gr$  and  $Gc$  rise, velocity increases, yet temperature falls with the increase of  $Gr$  and  $Gc$ . Conversely, an increase in  $M$  leads to a decrease in velocity while causing an increase in temperature.
- As the Darcy number  $Da$  increases, there is an increase in velocity, whereas the temperature decreases with the rise of  $Da$ .
- With an increase in the chemical reaction parameter  $K_c$ , both velocity and concentration decrease, while the temperature increases as  $K_c$  rises.
- In the isothermal scenario, there is a reduction in both Skin friction and Nusselt numbers when compared to the stratification scenario.

### ORCID

 **Digbash Sahu**, <https://orcid.org/0009-0005-8925-2048>; 
  **Rudra Kanta Deka**, <https://orcid.org/0009-0007-1573-4890>

### REFERENCES

- [1] R. Siegel, "Transient free convection from a vertical flat plate," Transactions of the American Society of Mechanical Engineers, **80**(2), 347-357 (1958). <https://doi.org/10.1115/1.4012369>.
- [2] E.R. Menold, and K.T. Yang, "Asymptotic solutions for unsteady laminar free convection on a vertical plate," Trans ASME: J. Appl. Mech., **29**, 124-126 (1962). <http://doi.org/10.1115/1.3636443>.
- [3] J.A. Schetz, and R. Eichhorn, "Unsteady natural convection in the vicinity of a doubly infinite vertical plate," Trans ASME C: J. Heat Transfer, **84**(4), 334-338 (1962). <https://doi.org/10.1115/1.3684386>
- [4] U.N. Das, R.K. Deka, and V.M. Soundalgekar, "Transient free convection flow past an infinite vertical plate with periodic temperature variation," J. Heat Transfer, **121**(4), 1091-1094 (1999). <https://doi.org/10.1115/1.2826063>
- [5] J.S. Park, and J.M. Hyun, "Technical Note Transient behavior of vertical buoyancy layer in a stratified fluid," International journal of heat and mass transfer, **41**(24), 4393-4397 (1998). [https://doi.org/10.1016/S0017-9310\(98\)00175-6](https://doi.org/10.1016/S0017-9310(98)00175-6)
- [6] J.S. Park, "Transient buoyant flows of a stratified fluid in a vertical channel," KSME international journal, **15**, 656-664 (2001). <http://doi.org/10.1007/bf03184382>
- [7] A. Shapiro, and E. Fedorovich, "Unsteady convectively driven flow along a vertical plate immersed in a stably stratified fluid," Journal of Fluid Mechanics, **498**, 333-352 (2004). <https://doi.org/10.1017/S0022112003006803>
- [8] E. Magyari, I. Pop, and B. Keller, "Unsteady free convection along an infinite vertical flat plate embedded in a stably stratified fluid-saturated porous medium," Transport in porous media, **62**, 233-249 (2006). <https://doi.org/10.1007/s11242-005-1292-6>
- [9] R.C. Chaudhary, and A. Jain, "MHD heat and mass diffusion flow by natural convection past a surface embedded in a porous medium," Theoretical and Applied Mechanics, **36**(1), 1-27 (2009). <https://doi.org/10.2298/TAM0901001C>
- [10] Y.D. Reddy, B.S. Goud, and M.A. Kumar, "Radiation and heat absorption effects on an unsteady MHD boundary layer flow along an accelerated infinite vertical plate with ramped plate temperature in the existence of slip condition," Partial Differential Equations in Applied Mathematics, **4**, 100166 (2021). <https://doi.org/10.1016/j.padiff.2021.100166>
- [11] G.V.R. Reddy, C.V.R. Murthy, and N.B. Reddy, "Unsteady MHD free convective mass transfer flow past an infinite vertical porous plate with variable suction and Soret effect," Int. J. of Appl. Math. and Mech. **7**(21), 70-84 (2011).
- [12] R. Muthucumaraswamy, and P. Sivakumar, "Hydro magnetic effects on parabolic flow past an infinite isothermal vertical plate with variable mass diffusion in the presence of thermal radiation and chemical reaction," International Journal of Recent Technology and Engineering, **4**(2), 5-10 (2015). <https://doi.org/10.1515/ijame-2016-0006>
- [13] F.M.N. El-Fayez, "Effects of chemical reaction on the unsteady free convection flow past an infinite vertical permeable moving plate with variable temperature," Journal of surface engineered materials and advanced technology, **2**(2), 100- 109 (2012). <http://dx.doi.org/10.4236/jsemat.2012.22016>
- [14] A. Bhattacharya, and R.K. Deka, "Theoretical study of chemical reaction effects on vertical oscillating plate immersed in a stably stratified fluid," Research Journal of Applied Sciences, Engineering and Technology, **3**(9), 887-898 (2011). <https://maxwellsci.com/print/rjaset/v3-887-898.pdf>
- [15] U.N. Das, R. Deka, and V.M. Soundalgekar, "Effects of mass transfer on flow past an impulsively started infinite vertical plate with constant heat flux and chemical reaction," Forschung im Ingenieurwesen, **60**(10), 284-287 (1994). <https://doi.org/10.1007/BF02601318>
- [16] R. Kandasamy, K. Periasamy, and K.K.S. Prabhu, "Chemical reaction, heat and mass transfer on mhd flow over a vertical stretching surface with heat source and thermal stratification effects," International Journal of Heat and Mass Transfer, **48**(21-22), 4557-4561 (2005). <https://doi.org/10.1016/j.ijheatmasstransfer.2005.05.006>

- [17] N. Kalita, R.K. Deka, and R.S. Nath, "Unsteady Flow Past an Accelerated Vertical Plate with Variable Temperature in Presence of Thermal Stratification and Chemical Reaction," East European Journal of Physics, (3), 441-450 (2023). <https://doi.org/10.26565/2312-4334-2023-3-49>
- [18] R. S. Nath, and R.K. Deka, "The Effects of Thermal Stratification on Flow Past an Infinite Vertical Plate in Presence of Chemical Reaction," East European Journal of Physics, (3), 223-232 (2023). <https://doi.org/10.26565/2312-4334-2023-3-19>
- [19] R.S. Nath, R.K. Deka, and H. Kumar, "The Effect of Thermal Stratification on Unsteady Parabolic Flow Past An Infinite Vertical Plate With Chemical Reaction," East European Journal of Physics, (4), 77-86 (2023). <https://doi.org/10.26565/2312-4334-2023-4-08>
- [20] H. Kumar, and R.K. Deka, "Thermal and Mass Stratification Effects on Unsteady Flow Past an Accelerated Infinite Vertical Plate with Variable Temperature and Exponential Mass Diffusion in Porous Medium," East European Journal of Physics, (4), 87-97 (2023). <https://doi.org/10.26565/2312-4334-2023-4-09>
- [21] A.M. Megahed, and W. Abbas, "Non-newtonian cross fluid flow through a porous medium with regard to the effect of chemical reaction and thermal stratification phenomenon," Case Studies in Thermal Engineering, **29**, 101715 (2022). <https://doi.org/10.1016/j.csite.2021.101715>
- [22] Abramowitz, Milton, I.A. Stegun, and R.H. Romer, "Handbook of mathematical functions with formulas, graphs, and mathematical tables," American Journal of Physics, **56**(10), 958 (1988). <https://doi.org/10.1119/1.15378>
- [23] R.B. Hetnarski, "An algorithm for generating some inverse Laplace transforms of exponential form," Zeitschrift für angewandte Mathematik und Physik ZAMP, **26**, 249-253 (1975). <https://doi.org/10.1007/bf01591514>

## ВПЛИВ ТЕРМІЧНОЇ СТРАТИФІКАЦІЇ ТА ХІМІЧНОЇ РЕАКЦІЇ НА МГД-ПОТІК ЧЕРЕЗ КОЛИВАЛЬНУ ВЕРТИКАЛЬНУ ПЛАСТИНУ В ПОРИСТОМУ СЕРЕДОВИЩІ ЗІ ЗМІНОЮ ТЕМПЕРАТУРИ ТА ЕКСПОНЕНЦІАЛЬНОЮ ДИФУЗІЄЮ МАСИ

Дігбаш Саху, Рудра Канта Дека

*Факультет математики, Університет Гаухаті, Гувахаті, 781014, Ассам, Індія*

У цій роботі досліджується термічна стратифікація та вплив хімічної реакції на МГД-потік через коливальну вертикальну пластину в пористому середовищі зі зміною температури та експоненціальною масовою дифузією. Завдяки застосуванню методу перетворення Лапласа в статті отримано аналітичні рішення, які точно відображають фізичну динаміку потоку. Розслідування використовує складні математичні моделі для ретельного вивчення складної динаміки між магнітогідродинамікою (МГД) і конвективними рухами, враховуючи низку умов, що включають температурні коливання та експоненціальну швидкість дифузії маси. Ключовим висновком цього дослідження є детальне порівняння результатів термічної стратифікації та тих, що спостерігаються в середовищах, де така стратифікація відсутня. Помічено, що реалізація стратифікації всередині потоку призводить до більш швидкого досягнення рівноважних або стаціонарних умов.

**Ключові слова:** МГД потік; хімічна реакція; термічна стратифікація; пористе середовище; коливальна вертикальна пластина; перетворення Лапласа; Matlab

## COMPARATIVE ANALYSIS OF THE PLANE COUETTE FLOW OF COUPLE STRESS FLUID UNDER THE INFLUENCE OF MAGNETOHYDRODYNAMICS

 Muhammad Farooq<sup>a</sup>,  Ibrar Khan<sup>a</sup>,  Rashid Nawaz<sup>b</sup>,  Gamal M. Ismail<sup>c,\*</sup>,  Huzaifa Umar<sup>d</sup>,  Hijaz Ahmad<sup>d,c,e</sup>

<sup>a</sup>Department of Mathematics, Abdul Wali Khan University, Mardan 23200, Pakistan

<sup>b</sup>UniSa STEM, University of South Australia

<sup>c</sup>Department of Mathematics, Faculty of Science, Islamic University of Madinah, Madinah, Saudi Arabia

<sup>d</sup>Near East University, Operational Research Center in Healthcare,

Near East Boulevard, PC: 99138 Nicosia/Mersin 10, Turkey

<sup>e</sup>Department of Mathematics and Informatics, Azerbaijan University,

Jeyhun Hajibeyli street, 71, AZ1007, Baku, Azerbaijan

\*Corresponding Author e-mail: [gismail@iu.edu.sa](mailto:gismail@iu.edu.sa)

Received November 12, 2023; revised December 25, 2023; accepted January 5, 2024

The present study aims to perform a comparative analysis of the plane Couette flow of a couple stress fluid under the influence of magnetohydrodynamics (MHD) using two different methods: the Optimal Auxiliary Function Method (OAFM) and the Homotopy Perturbation Method (HPM). The couple stress fluid is known for its non-Newtonian behavior, where the fluid's response to shear is influenced by the presence of internal microstructure. The OAFM and HPM are utilized to solve the governing equations of the couple stress fluid flow under MHD. The OAFM is a numerical technique that involves introducing an auxiliary function to simplify the equations, leading to an easier solution procedure. On the other hand, HPM is an analytical method that employs a series solution. The comparative analysis focuses on examining the accuracy, efficiency, and convergence behavior of the two methods. Various flow parameters such as the couple stress parameter, the magnetic parameter, and the velocity ratio are considered to investigate their influence on the flow behavior. Furthermore the HPM solution was compared with the OAFM solution using different graphs and tables. It reveals that the solution obtained by HPM is better than OAFM solution.

**Keywords:** *Couple stress fluid; Optimal Auxiliary Function Method (OAFM); Homotopy Perturbation Method (HPM); magnetohydrodynamics (MHD)*

**PACS:** specify the PACS code(s) here

### 1. INTRODUCTION

In recent years, the magnetohydrodynamic (MHD) flow and heat transfer have obtained a wide concern, because of its various applications, such as nuclear reactor, physics, ocean dynamics, the generation of MHD energy [1, 2], chemical manufacturing, and the synthesis of magnetic liquids [3, 4, ?, 7, 8, 9, 10, 11]. Ahmed et al. [12] conducted a theoretical study of an electrically conducting couple stress fluid (CSF) in an oscillatory viscous flow with heat transfer influenced by convection and MHD, which has important applications in the production of electro-conductive polymers and liquids. Ajaz [13] investigated the influence of an applied inclined magnetic field on the peristaltic flow that occurs during heat and mass transfer in a CSF. Pei-Ying and colleagues [14] evaluated the velocity and temperature distributions of hafnium nanoparticles subjected to a thermal radiation effect and a magnetic field. They do this by compiling the findings of varying thermal conductivity and viscosity in the hafnium nanoparticles' appearance. Ajala et al. [15] studied how the existence of a variable viscosity and thermal radiation affects the flow of a two-dimensional boundary layer. Falade et al. [16] investigated the minimization of the entropy generation rate as a result of temperature-dependent viscosity and couple stress fluid caused by the heated channel. This is done to lower the entropy production rate to its lowest attainable value. Swarnalathamma et al. [17] and Ramesh [18] studied the influence of heat transfer on the peristaltic flow of a couple stress fluid with MHD and a porous media. They looked at how the new factors affected the peristaltic pumping rate, frictional forces, velocity, temperature, pressure gradient, and concentration fields. Divya et al. [19] reported and analysed the combined impact of temperature-dependent viscosity and thermal conductivity on the MHD peristaltic flow of the Bingham fluid in a porous medium with heat transfer. This is done in order to better understand how these factors affect the flow of the Bingham fluid. The authors analysed

**Cite as:** M. Farooq, I. Khan, G.M. Ismail, H. Umar, H. Ahmad, East Eur. J. Phys. 2, 219 (2023), <https://doi.org/10.26565/2312-4334-2024-2-21>

© M. Farooq, I. Khan, G.M. Ismail, H. Umar, H. Ahmad, 2024; CC BY 4.0 license

the effects of these variables on temperature as well as pumping rate and heat transfer coefficient. In their study of an unsteady three-dimensional flow over a stretched surface accompanied by a chemical reaction, Hayat et al. [20] came to the conclusion that both the velocity field and the associated boundary layer thickness decreased as a function of the couple stress parameter. This is one of the findings of their study.

In this paper, the couette flow of couple stress fluids between two parallel plates under the influence of MHD has been explored utilising the two well known approaches the Homotopy Perturbation Method (HPM)[21],[22] and the Optimal Auxiliary Function Method (OAFM)[23],[24]. Results obtained by the proposed approaches are compared with each other using various graphs and tables. The residual error obtained using the proposed methods reveals the HPM solution is better than the OAFM solution. Graphs have been utilised to demonstrate how the non-dimensional parameters affect the flow pattern.

The rest of the paper is organized as: Section (2) provides general methodology of the HPM and OAFM. Section (3) contains basic equation of couple stress fluid and problem formulation. Solution of the problem is provided in section (4). Section (5) discusses the numerical results and discussion. Section (6) provides final conclusion.

## 2. GENERAL METHODOLOGY OF THE PROPOSED METHODS

### 2.1. Homotopy Perturbation Method

To explain the general idea of the homotopy perturbation method, we consider the nonlinear differential equation illustrated below.

$$N(u(y)) - \eta(r) = 0, \quad r \in \Omega, \tag{1}$$

$$B(u, \frac{\partial u}{\partial y}), \quad r \in \Omega, \tag{2}$$

where  $N$  is the combination of the linear  $\psi(u)$  and nonlinear  $\aleph(u)$ , differential operators and  $B$  represents boundary conditions,  $\eta(r)$  is the known analytical function. Therefore Eq.(1) can be written as:

$$\psi(u) + \aleph(u) - \eta(r) = 0. \tag{3}$$

We construct mapping for homotopy:

$$H(u, \rho) : \Omega \times [0, 1] \rightarrow R, \tag{4}$$

$$H(u, \rho) = (1 - \rho)[\psi(u) - \psi(u_0)] + \rho[\psi(u) + \aleph(u) - \eta(r)] = 0, \tag{5}$$

$$u(y, \rho) : \Omega \times [0, 1] \rightarrow R, \tag{6}$$

where  $\rho$  is the homotopy parameter and when  $\rho = 0$ , then  $u_0$  is the initial approximation that satisfies boundary conditions. When  $\rho = 1$ , the solution can be written in the form

$$u = u_0 + \rho u_1 + \rho^2 u_2 + \rho^3 u_3 + \dots \tag{7}$$

Homotopy perturbation method is the combine process of homotopy and perturbation.

### 2.2. Analysis of Optimal Axillary Functions Method

To explore the general procedure of the optimal axillary functions method, we consider the nonlinear differential equation illustrated below.

$$L(u) + N(u) + h(y) = 0. \tag{8}$$

the associated boundary condition are:

$$B(u(y), \frac{\partial u(y)}{\partial y}) = 0. \tag{9}$$

In Eq.(8)  $L$  is linear ,  $N$  denotes the non-linear differential operator and  $h(y)$  is the known function. The approximate solution of Eq.(8) can be written as

$$u^*(y, C_i) = u_0(y) + u_1(y, C_n), \quad n = 1, 2, 3, 4...s. \tag{10}$$

where  $C_n$  are the auxiliary constant. To fined the initial and first approximate solution of Eq.(8) we use Eq.(10) in Eq.(8), which reveals

$$L(u_0(y) + y_1(y, C_n)) + N(u_0(y) + u_1(y, C_n)) + h(y) = 0. \tag{11}$$



For obtaining the initial approximation  $u_0(y)$ , we use the following linear equation.

$$L(u_0(y)) + h(y) = 0, \quad B(u_0, \frac{du_0}{y}) = 0. \tag{12}$$

The first-order approximation  $u_1(y)$  can be found from the following equation:

$$L(u_1(y, C_n)) + N(u_0(y) + u_1(y, C_n)) = 0, \tag{13}$$

with associated boundary condition:

$$B(u_1(y, C_n), \frac{\partial u_1(y, C_n)}{\partial y}) = 0. \tag{14}$$

The non-linear tern from equation (13) can be expanded in the form

$$N(u_0(y) + u_1(y, C_n)) = N(u_0(y)) + \sum_{k=1}^{\infty} \frac{u_1^{(k)}(y, C_n)}{k!} N^{(k)}(u_0(y)). \tag{15}$$

Equation (15) can be stated in the algorithmic sequence to achieve the limit solution. To control all the challenges that are occur while solving the non-linear differential of Eq.(11) and to accelerate the convergence of the first approximation  $u_1(y, C_n)$ . We use an alternate expression which represent the Eq.(13)

$$L(u_1(y, C_n)) + A_1(u_0(y), C_n)N(u_0(y))) + A_2(u_0(y), C_m) = 0, \tag{16}$$

$$B(u_1(y, C_n), \frac{du_1(y, C_n)}{dy}) = 0, \tag{17}$$

**Remark 1.**  $A_1$  and  $A_2$  are assumed to be two axillary functions which depend on the  $u_0(y)$  and unknown  $C_n$  and  $C_m$  parameters where  $n = 1, 2, 3, \dots, s$  and  $m = s + 1, s + 2, s + 3 \dots q$ .

**Remark 2.**

$A_1$  and  $A_2$  are not fixed. It may be  $u_0(y)$  or  $N(u_0(y))$  and can be the combination of both  $u_0(y)$  and  $N(u_0(y))$ .

**Remark 3.** The auxiliary constants  $C_n$  and  $C_m$  can be determined using different methods either by Collocation method, Least square method or Galerkin’s method.

**3. BASIC EQUATIONS AND PROBLEM FORMULATION**

The basic equations for an incompressible couple stress fluid are as follows [25],[26]:

$$\nabla \cdot \mathbf{V} = 0 \tag{18}$$

$$\rho(\frac{\partial}{\partial t} + \mathbf{V} \cdot \nabla)\mathbf{V} = \nabla \cdot \mathbf{S} - \eta \nabla^4 \mathbf{V} + \rho \mathbf{f} + \mathbf{J} \times \mathbf{B} \tag{19}$$

$$\rho C_p(\frac{\partial}{\partial t} + \mathbf{V} \cdot \nabla)\Theta = \kappa \nabla^2 \Theta + tr(\mathbf{S} \cdot \mathbf{L}) \tag{20}$$

Where the velocity vector is symbolized by  $\mathbf{V}$ , the body force per unit mass is  $\mathbf{f}$ , the constant density is denoted as  $\rho$ ,  $\mathbf{S}$  is the Cauchy stress tensor,  $\Theta$  is the temperature,  $\kappa$  is the thermal conductivity,  $\mathbf{J}$  represents current density,  $\mathbf{B}$  represents magnetic induction,  $C_p$  symbolizes the specific heat, also the gradient of  $\mathbf{V}$  is denoted by  $\mathbf{L}$ , and  $\eta$  is used for couple stress parameter. The material derivative is indicated by  $\frac{D}{Dt}$  and is defined by the following:

$$\frac{D(*)}{Dt} = (\frac{\partial}{\partial t} + \mathbf{V} \cdot \nabla)(*) \tag{21}$$

The Cauchy stress tensor is represented and defined as

$$\mathbf{S} = -p\mathbf{I} + \mu A_1 \tag{22}$$

Where  $\mathbf{I}$  represent the unit tensor,  $p$  indicates the dynamic pressure and  $\mu$  is the viscosity constant. The first Rivilin-Ericksen tensor is defined and represented as

$$A_1 = L + L^t, \tag{23}$$

where  $L^t$  is the transpose of  $L$ .

### 3.1. Problem Formulation

Consider the Couette flow of a couple stress fluid under the influence of MHD between two infinite parallel plates separated by  $2d$ , where the upper plate moves with constant velocity  $U$  and the lower plate remains stationary (Figure 1). The temperature of the lower upper and plates are  $\Theta_0$  and  $\Theta_1$  respectively. Both plates are situated in the plane at  $y = -d$  and  $y = d$  in an orthogonal coordinate system  $(x, y)$ , where the fluid is moving in the  $x$ -axis direction and the  $y$ -axis is perpendicular to the plates. Here, the viscosity is assumed to be a function of temperature  $\Theta(y)$ , the pressure gradient is set to zero, and the velocity and temperature fields are chosen as follows:

$$\mathbf{V} = [u(y), 0, 0], \quad \Theta = \Theta(y) \tag{24}$$

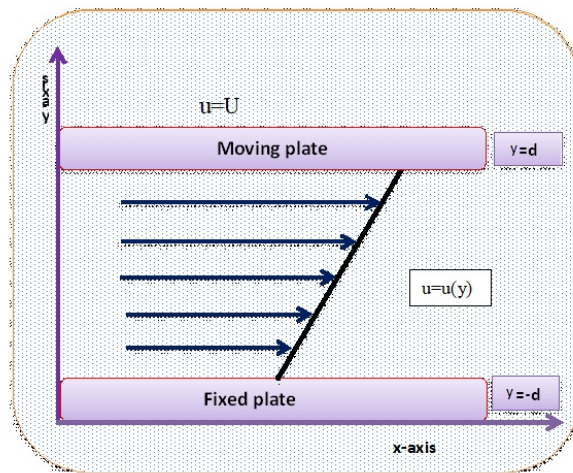


Figure 1. Geometry of the problem

These assumptions lead us to the conclusion that the continuity Eq.(18) is identically satisfied and the momentum Eq.(19) simplifies to

$$0 = -\frac{\partial p}{\partial x} + \frac{\partial \mathbf{S}_{xx}}{\partial x} + \frac{\partial \mathbf{S}_{xy}}{\partial y} + \frac{\partial \mathbf{S}_{xz}}{\partial z} - \eta \frac{d^4 u}{dy^4} - \sigma B_0^2 u, \tag{25}$$

$$0 = -\frac{\partial p}{\partial y} + \frac{\partial \mathbf{S}_{yx}}{\partial x} + \frac{\partial \mathbf{S}_{yy}}{\partial y} + \frac{\partial \mathbf{S}_{yz}}{\partial z}, \tag{26}$$

$$0 = -\frac{\partial p}{\partial z} + \frac{\partial \mathbf{S}_{zx}}{\partial x} + \frac{\partial \mathbf{S}_{zy}}{\partial y} + \frac{\partial \mathbf{S}_{zz}}{\partial z}. \tag{27}$$

Where  $B_0$  represents the applied magnetic field and  $\sigma$  denotes electric conductivity of the fluid. We have

$$\mathbf{S}_{xx} = \mathbf{S}_{yy} = \mathbf{S}_{zz} = \mathbf{S}_{yz} = \mathbf{S}_{zy} = \mathbf{S}_{xz} = \mathbf{S}_{zx} = 0, \quad \mathbf{S}_{xy} = \mathbf{S}_{yx} = \mu \frac{du}{dy}. \tag{28}$$

Obtaining the velocity profile using equation Eq.(25). This equation may also be stated as

$$\eta \frac{d^4 u}{dy^4} - \mu \frac{d^2 u}{dy^2} - \frac{d\mu}{dy} \frac{du}{dy} + \sigma B_0^2 u = 0. \tag{29}$$

After all assumptions are applied, the energy equation (20) simplifies to Eq. (30).

$$\frac{d^2 \Theta}{dy^2} + \frac{\mu}{\kappa} \left(\frac{du}{dy}\right)^2 + \frac{\mu}{\kappa} \left(\frac{d^2 u}{dy^2}\right)^2 = 0. \tag{30}$$

The associated boundary condition are

$$u(-d) = 0, \quad u(d) = U, \tag{31}$$

$$u''(-d) = 0, \quad u''(d) = 0, \quad (32)$$

$$\Theta(-d) = \Theta_0, \quad \Theta(d) = \Theta_1. \quad (33)$$

According to Eq. (32), the couple stresses at the plates are zero. We utilize the non-dimensional parameters mentioned below:

$$y^* = \frac{y}{d}, \quad u^* = \frac{u}{U}, \quad \mu^* = \frac{\mu}{\mu_0}, \quad \Theta^* = \frac{\Theta - \Theta_0}{\Theta_0 - \Theta_1},$$

$$\beta^2 = \frac{d^2 \mu_0}{\eta}, \quad R = \frac{\sigma d^4 B_0^2}{\eta}, \quad \lambda = \frac{\mu_0 U^2}{\kappa(\Theta_0 - \Theta_1)}$$

Where  $\lambda$  is the Brinkman number,  $\mu$  is the reference viscosity, and  $U$  is the reference velocity. Using these dimensionless parameters, Eqs.(29) and (30) along with the boundary conditions becomes.

$$\frac{d^4 u}{dy^4} - \beta^2 \mu \frac{d^2 u}{dy^2} - \beta^2 \frac{d\mu}{dy} \frac{du}{dy} + Ru = 0, \quad u(-1) = 0, \quad u(1) = 1, \quad u''(-1) = 0, \quad u''(1) = 0. \quad (34)$$

$$\frac{d^2 \Theta}{dy^2} + \lambda \mu \left(\frac{du}{dy}\right)^2 + \frac{\lambda}{\beta^2} \left(\frac{d^2 u}{dy^2}\right)^2 = 0, \quad \Theta(-1) = 0, \quad \Theta(1) = 1. \quad (35)$$

The dimensionless form of the Reynolds viscosity is expressed as follows [27, 28, 29].

$$\mu = e^{-M\Theta} \quad (36)$$

Using Taylor series expansion to Eq. (36) we get

$$\mu = 1 - M\Theta, \quad \frac{d\mu}{dy} = -M \frac{d\Theta}{dy} \quad (37)$$

The coupled system illustrated below is created by replacing Eq. (37) in the governing Eqs. (34) and (35), respectively:

$$\frac{d^4 u}{dy^4} - \beta^2(1 - M\Theta) \frac{d^2 u}{dy^2} + \beta^2 M \frac{d\Theta}{dy} \frac{du}{dy} + Ru = 0, \quad (38)$$

$$u(-1) = 0, \quad u(1) = 1, \quad u''(-1) = 0, \quad u''(1) = 0,$$

$$\frac{d^2 \Theta}{dy^2} + \lambda(1 - M\Theta) \left(\frac{du}{dy}\right)^2 + \frac{\lambda}{\beta^2} \left(\frac{d^2 u}{dy^2}\right)^2 = 0, \quad \Theta(-1) = 0, \quad \Theta(1) = 1. \quad (39)$$

## 4. SOLUTION OF THE PROBLEM

### 4.1. HPM Solution

Zeroth order problem.

$$\frac{d^4 u}{dy^4} = 0, \quad (40)$$

$$u(-1) = 0, \quad u(1) = 1, \quad u''(-1) = 0, \quad u''(1) = 0,$$

$$\frac{d^2 \Theta}{dy^2} = 0, \quad (41)$$

$$\Theta(-1) = 0, \quad \Theta(1) = 1.$$

Solution of zeroth order problem

$$u_0(y) = \frac{1+y}{2}, \quad (42)$$

$$\Theta_0(y) = \frac{1+y}{2}. \quad (43)$$

First order problem

$$\frac{d^4 u_1}{dy^4} + (\beta^2 M \Theta_0 - \beta^2) \frac{d^2 u_0}{dy^2} + \beta^2 M \frac{d\Theta_0}{dy} \frac{du_0}{dy} + Ru_0 = 0 \tag{44}$$

$$u_1(-1) = 0, \quad u_1(1) = 0, \quad u_1''(-1) = 0, \quad u_1''(1) = 0,$$

$$\frac{d^2 \Theta_1}{dy^2} + \frac{\lambda}{\beta^2} \left( \frac{d^2 u_0}{dy^2} \right)^2 + (\lambda - M \lambda \Theta_0) \left( \frac{du_0}{dy} \right)^2 = 0, \tag{45}$$

$$\Theta_1(-1) = 0, \quad \Theta_1(1) = 0.$$

Solution of the first order problem.

$$u_1(y) = \frac{1}{1440} \left( -75\beta^2 M + 90\beta^2 M y^2 - 15\beta^2 M y^4 - 150R - 14yR + 180y^2 R + 20y^3 R - 30y^4 R - 6y^5 R \right), \tag{46}$$

$$\Theta_1(y) = \frac{1}{2} (6\lambda - 3M\lambda - My\lambda - 6y^2\lambda + 3My^2\lambda + My^3\lambda). \tag{47}$$

First order HPM solution for velocity profile and temperature distribution are

$$u(y) = u_0(y) + u_1(y) \tag{48}$$

$$\Theta(y) = \Theta_0(y) + \Theta_1(y) \tag{49}$$

$$u(y) = \frac{1+y}{2} + \frac{1}{1440} \left( -75\beta^2 M + 90\beta^2 M y^2 - 15\beta^2 M y^4 - 150\gamma - 14yR + 180y^2 R + 20y^3 R - 30y^4 R - 6y^5 R \right), \tag{50}$$

$$\Theta(y) = \frac{1+y}{2} + \frac{1}{2} (6\lambda - 3M\lambda - My\lambda - 6y^2\lambda + 3My^2\lambda + My^3\lambda). \tag{51}$$

#### 4.2. OAFM Solution

Zeroth component for velocity and temperature distribution.

$$\frac{d^4 u_0}{dy^4} = 0, \tag{52}$$

$$u_0(-1) = 0, \quad u_0(1) = 1, \quad u_0''(-1) = 0, \quad u_0''(1) = 0,$$

$$\frac{d^2 \Theta_0}{dy^2} = 0, \tag{53}$$

$$\Theta_0(-1) = 0, \quad \Theta_0(1) = 0.$$

Their solution are

$$u_0(y) = \frac{1+y}{2}, \tag{54}$$

$$\Theta_0(y) = \frac{1+y}{2} \tag{55}$$

consider non Linear term from Eq. (38) and (39)

$$N(u) = -\beta^2(1 - M\Theta) \frac{d^2 u}{dy^2} + \beta^2 M \frac{du}{dy} \frac{d\Theta}{dy} + Ru, \tag{56}$$

$$N(\Theta) = \lambda(1 - M\Theta) \left( \frac{du}{dy} \right)^2 + \frac{\lambda}{\beta^2} \left( \frac{d^2 u}{dy^2} \right)^2. \tag{57}$$

Replace  $u$  by  $u_0$  and  $\Theta$  by  $\Theta_0$

$$N(u_0) = -\beta^2(1 - M\Theta_0) \frac{d^2 u_0}{dy^2} + \beta^2 M \frac{du_0}{dy} \frac{d\Theta_0}{dy} + Ru_0, \tag{58}$$

$$N(\Theta_0) = \lambda(1 - M\Theta_0)\left(\frac{du_0}{dy}\right)^2 + \frac{\lambda}{\beta^2}\left(\frac{d^2u_0}{dy^2}\right)^2. \tag{59}$$

We are free to choose auxiliary function.

$$\begin{aligned} A_1 &= c1\left(\frac{1+y}{2}\right)^2, & A_2 &= c2\left(\frac{1+y}{2}\right)^3, \\ A_3 &= c3\left(\frac{1+y}{2}\right)^5, & A_4 &= c4\left(\frac{1+y}{2}\right)^7. \end{aligned} \tag{60}$$

Now using Eq.(54), Eq.(55) and Eq.(60) into Eq.(58) and Eq.(59), the nonlinear terms becomes

$$N(u_0) = \frac{\beta^2 M}{4} + \frac{1}{2}R(y+1), \tag{61}$$

$$N(\Theta_0) = \frac{1}{4}\lambda\left(1 - \frac{1}{2}M(y+1)\right). \tag{62}$$

First order approximation can be obtained by

$$\frac{d^4u_1}{dy^4} + A_1N[u_0] + A_2 = 0, \tag{63}$$

$$\frac{d^2\Theta_1}{dy^2} + A_3N[\Theta_0] + A_4 = 0. \tag{64}$$

After applying inverse operator on Eq.(63) and Eq.(64), we get the first order approximation.

$$\begin{aligned} u_1(y) &= \frac{1}{20160} \left( -21\beta^2c_1My^5 - 105B^2c_1My^4 + 70B^2c_1My^3 + 630B^2c_1My^2 \right. \\ &\quad - 49\beta^2c_1My - 525\beta^2c_1M - 1246c_1R - 3c_2y^7 - 14c_1Ry^6 - 21c_2y^6 \\ &\quad - 84c_1Ry^5 - 63c_2y^5 - 210c_1Ry^4 - 105c_2y^4 + 280c_1Ry^3 + 231c_2y^3 \\ &\quad \left. + 1470c_1Ry^2 + 945c_2y^2 - 196c_1Ry - 165c_2y - 819c_2 \right), \end{aligned} \tag{65}$$

$$\begin{aligned} \Theta_1(y) &= \frac{1}{129024} \left( 9c_3My^8\lambda + 72c_3My^7\lambda + 252c_3My^6\lambda + 504c_4My^5\lambda + 630c_3My^4\lambda \right. \\ &\quad + 504c_3My^3\lambda + 252c_3My^2\lambda - 1080c_3My\lambda - 1143c_3M\lambda - 24c_3y^7\lambda - \\ &\quad 168c_3y^6\lambda - 504c_3y^5\lambda - 840c_3y^4\lambda - 840c_3y^3\lambda - 504c_3y^2\lambda + 1368c_3y\lambda + \\ &\quad 1512c_3\lambda - 14c_4y^9 - 126c_4y^8 - 504c_4y^7 - 1176c_4y^6 - 1764c_4y^5 - \\ &\quad \left. 1764c_4y^4 - 1176c_4y^3 - 504c_4y^2 + 3458c_4y + 3570c_4 \right). \end{aligned} \tag{66}$$

According to OAFM Procedure.

$$u(y) = u_0(y) + u_1(y) \tag{67}$$

$$\Theta(y) = \Theta_0(y) + \Theta_1(y) \tag{68}$$

$$\begin{aligned} u(y) &= \frac{1+y}{2} + \frac{1}{20160} \left( -21\beta^2c_1My^5 - 105B^2c_1My^4 + 70B^2c_1My^3 + 630B^2c_1My^2 \right. \\ &\quad - 49\beta^2c_1My - 525\beta^2c_1M - 1246c_1R - 3c_2y^7 - 14c_1Ry^6 - 21c_2y^6 - 84c_1Ry^5 \\ &\quad - 63c_2y^5 - 210c_1Ry^4 - 105c_2y^4 + 280c_1Ry^3 + 231c_2y^3 + 1470c_1Ry^2 + 945c_2y^2 \\ &\quad \left. - 196c_1Ry - 165c_2y - 819c_2 \right), \end{aligned} \tag{69}$$

$$\begin{aligned} \Theta(y) &= \frac{1+y}{2} + \frac{1}{129024} \left( 9c_3My^8\lambda + 72c_3My^7\lambda + 252c_3My^6\lambda + 504c_4My^5\lambda + \right. \\ &\quad 630c_3My^4\lambda + 504c_3My^3\lambda + 252c_3My^2\lambda - 1080c_3My\lambda - 1143c_3M\lambda - 24c_3y^7\lambda \\ &\quad - 168c_3y^6\lambda - 504c_3y^5\lambda - 840c_3y^4\lambda - 840c_3y^3\lambda - 504c_3y^2\lambda + 1368c_3y\lambda + \\ &\quad 1512c_3\lambda - 14c_4y^9 - 126c_4y^8 - 504c_4y^7 - 1176c_4y^6 - 1764c_4y^5 - \\ &\quad \left. 1764c_4y^4 - 1176c_4y^3 - 504c_4y^2 + 3458c_4y + 3570c_4 \right). \end{aligned} \tag{70}$$

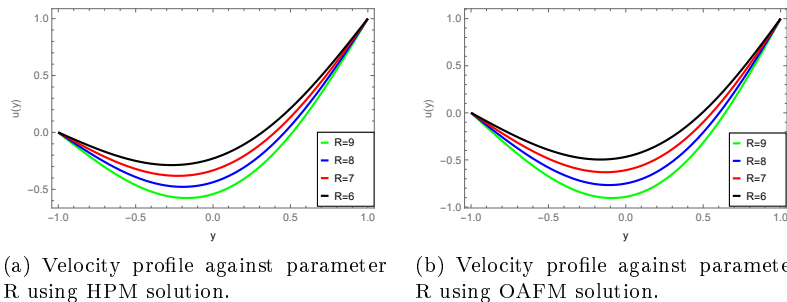


**Figure 2.** Comparison of HPM and OAFM solutions for velocity profile against parameter R when  $\lambda = 4$ ,  $\beta = 1$  and  $M = 2$ .

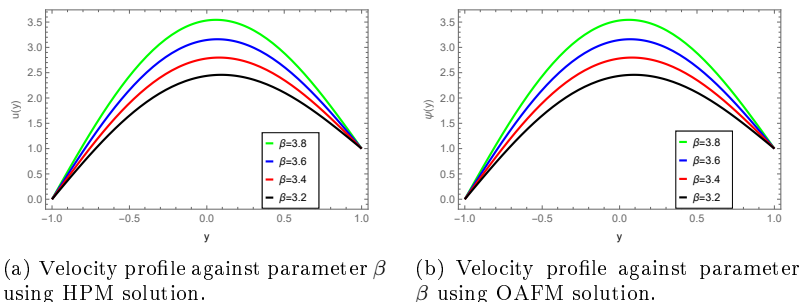


**Figure 3.** Comparison of HPM and OAFM solutions for velocity profile against parameter  $\beta$  when  $\lambda = 4$ ,  $R = 7$  and  $M = -5$ .

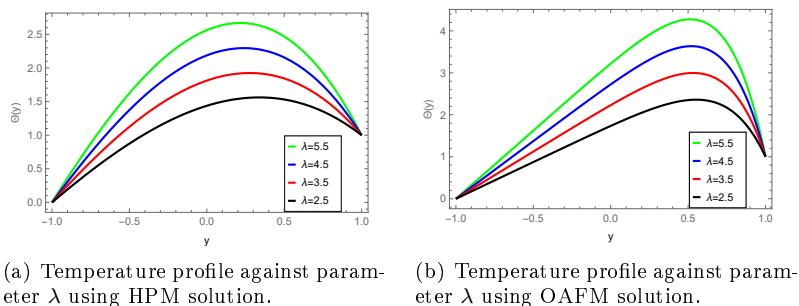


**Figure 6.** Comparison of HPM and OAFM solutions for Temperature profile against parameter  $\lambda$  when  $R=2$ ,  $M = -4$  and  $\beta = 0.4$ .

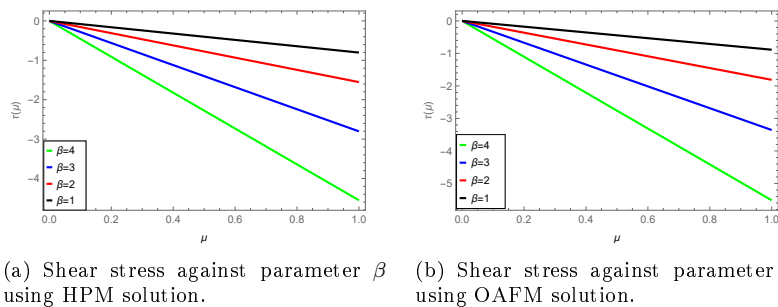


**Figure 7.** Shear stress on upper plate against parameter  $\lambda$  when  $R = 0.3$  and  $M = 3$ .

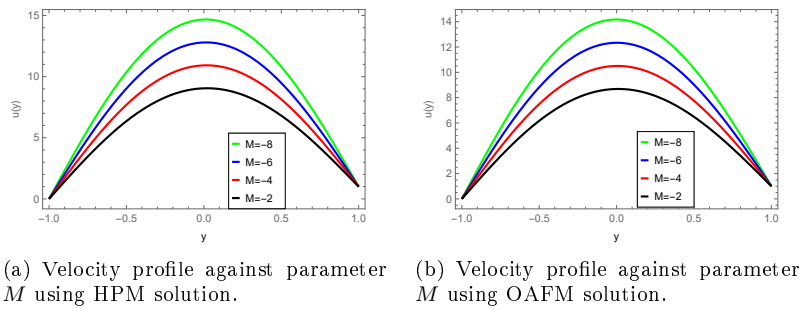


**Figure 4.** Comparison of HPM and OAFM solutions for velocity profile against parameter  $M$  when  $\lambda = 4$ ,  $R = 8$  and  $\beta = 6$ .

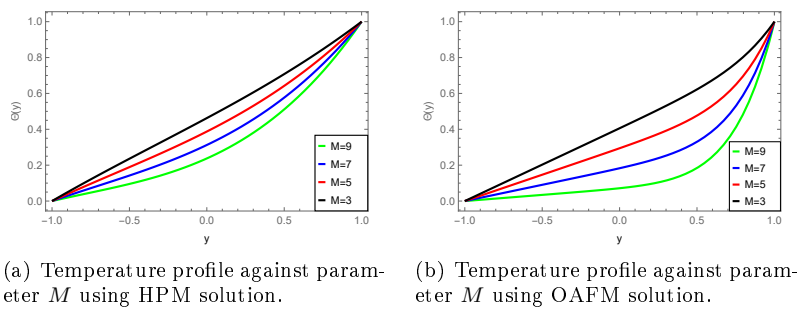


**Figure 5.** Comparison of HPM and OAFM solutions for temperature distribution against parameter  $M$  when  $R=2$ ,  $\lambda = 0.6$  and  $\beta = 0.4$ .

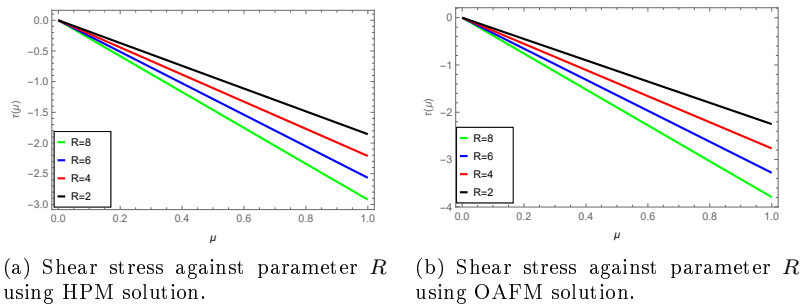


**Figure 8.** Shear stress on upper plate against parameter  $R$  when  $\beta = 2$  and  $M = 3$ .

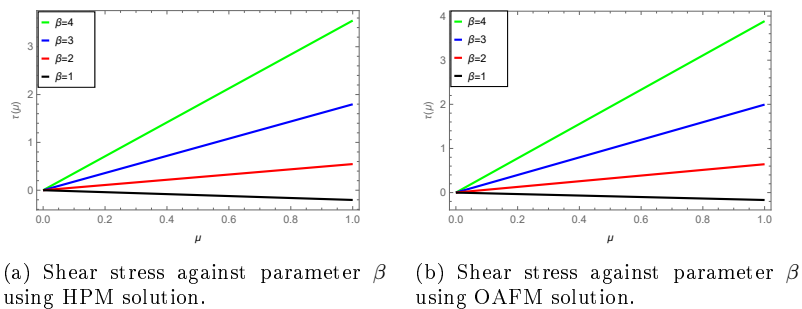


**Figure 9.** Shear stress on lower plate against parameter  $\lambda$  when  $\beta = 2$  and  $R = 0.3$ .

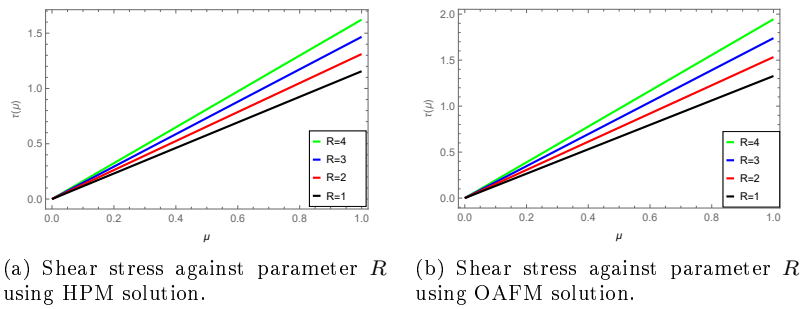


Figure 10. Shear stress on lower plate against parameter  $R$  when  $\beta = 2$  and  $M = 3$ .

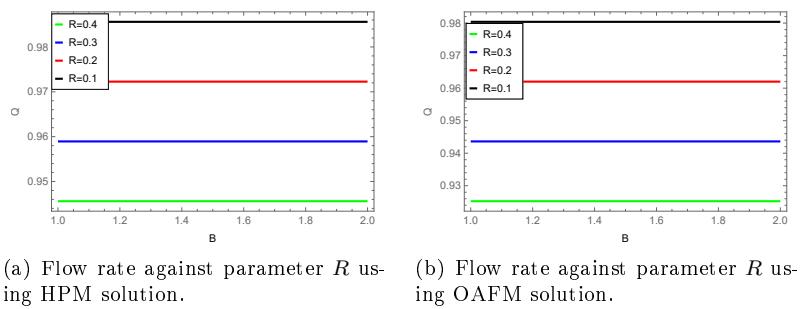


Figure 11. Flow rate against parameter  $R$  at  $\beta = 2$  and  $M = 3$ .

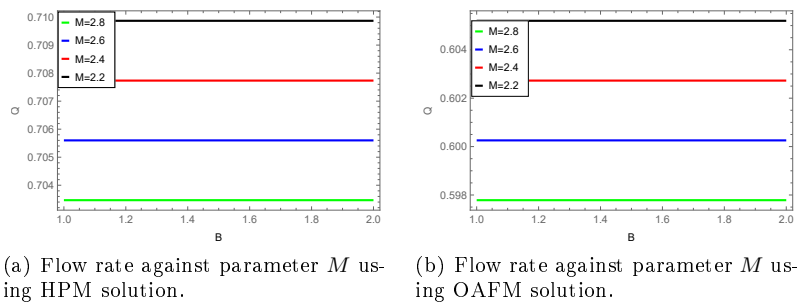


Figure 12. Flow rate against parameter  $M$  at  $\beta = 2$  and  $M = 3$ .

### NUMERICAL RESULTS AND DISCUSSION

In this paper, we utilized the homotopy perturbation method (HPM) and optimal auxiliary function method (OAFM) to investigate the couette flow of couple stress fluid under the influence of MHD. Different graphs are plotted to see the effect of various parameters on the velocity and temperature distribution. The efficiency of the proposed approaches are analyzed using different tables having the comparison of residual error obtained by OAFM and HPM. In Figure (2), the velocity profile of the fluid is plotted using both approaches and found the MHD parameter  $R$  has inverse relation with the velocity profile. Figure (3) show the comparison of HPM and OAFM for the velocity  $u(y)$  against parameter  $\beta$ . It reveals that  $\beta$  has directly relation with the velocity of fluid. Figure (4) show the inverse relation between parameter  $M$  and velocity of the fluid  $u(y)$ . Figure (5) show the impact of parameter  $M$  on the temperature distributions. Figure (6) are plotted to see the effect of parameter  $\lambda$  on temperature distribution  $\Theta(y)$  using OAFM and HPM solutions. The non-dimensional parameter  $\lambda$  denotes Brinkman number, which shows direct relation with the temperature distribution. Figure (7), (8) show the behaviour of shear stress  $S$  on the upper plate against different parameters by using HPM and OAFM solutions. Figure (9), (10) show the behaviour of shear stress  $S$  on the lower plate against different parameters by using HPM and OAFM solutions. Figure (11), (12) demonstrates the effect of Parameters  $R$  and  $M$  on the flow rate



using HPM and OAFM solutions. Table (1) and (2) represent the comparison of OAFM and HPM solutions and their residual error for the Velocity profile and temperature distribution. These tables compare the results obtained by both approaches for the different values of the independent variable  $y$  and parameters  $R$ ,  $\beta$ ,  $M$ , and  $\lambda$ . Table (3)-(6) provides skin friction for different parameter using OAFM and HPM solutions and their absolute differences. The range of residual error obtained by OAFM is -4 to -8 while the range of residual error obtained by HPM is -8 to -16. It is observed that the HPM solution is batter than OAFM solution.

**Table 1. Comparison of OAFM and HPM solutions for the velocity profile keeping  $M=0.00015$ ,  $\lambda = 0.0001$  and  $R = 0.00002$**

$y$	$u_{OAFM}$	$u_{HPM}$	Residual $u_{OAFM}$	Residual $u_{HPM}$
-1.0	$-2.5 \times 10^{-22}$	0	$-1.6968 \times 10^{-6}$	$1.47742 \times 10^{-16}$
-0.8	0.099999	0.099999	$-1.3819 \times 10^{-7}$	$-1.2385 \times 10^{-11}$
-0.6	0.199999	0.199999	$6.2748 \times 10^{-7}$	$-2.3714 \times 10^{-11}$
-0.4	0.299998	0.299998	$7.4888 \times 10^{-7}$	$-3.2990 \times 10^{-11}$
-0.2	0.399998	0.399998	$4.1781 \times 10^{-7}$	$-3.9349 \times 10^{-11}$
0.0	0.499998	0.499998	$-1.0522 \times 10^{-7}$	$-4.2116 \times 10^{-11}$
0.2	0.599998	0.599998	$-4.9810 \times 10^{-7}$	$-4.0874 \times 10^{-11}$
0.4	0.699998	0.699998	$-4.5993 \times 10^{-7}$	$-3.5525 \times 10^{-11}$
0.6	0.799999	0.799999	$7.50698 \times 10^{-8}$	$-2.6355 \times 10^{-11}$
0.8	0.899999	0.899999	$5.25136 \times 10^{-7}$	$-1.4098 \times 10^{-11}$
1.0	1.0000	1.0000	$-1.0300 \times 10^{-6}$	$-1.44731 \times 10^{-16}$

**Table 2. Comparison of OAFM and HPM solutions for temperature distribution keeping  $R=0.00002$ ,  $M=0.00015$ ,  $\beta = 0.0003$  and  $\lambda = 0.0001$**

$y$	$\Theta_{OAFM}$	$\Theta_{HPM}$	Residual $\Theta_{OAFM}$	Residual $\Theta_{HPM}$
-1.0	$-1.7 \times 10^{-20}$	0.0000	$2.5 \times 10^{-5}$	$-3.1111 \times 10^{-10}$
-0.8	0.100011	0.100004	$2.51 \times 10^{-5}$	$1.6381 \times 10^{-9}$
-0.6	0.200023	0.200008	$2.47 \times 10^{-5}$	$7.0229 \times 10^{-9}$
-0.4	0.300034	0.30001	$2.16 \times 10^{-5}$	$1.4525 \times 10^{-8}$
-0.2	0.400045	0.400012	$1.36 \times 10^{-5}$	$2.2185 \times 10^{-8}$
0.0	0.500054	0.500012	$3.37 \times 10^{-6}$	$2.7758 \times 10^{-8}$
0.2	0.600061	0.600012	$-1 \times 10^{-6}$	$2.9209 \times 10^{-8}$
0.4	0.700061	0.70001	$1.351 \times 10^{-6}$	$2.5357 \times 10^{-8}$
0.6	0.800051	0.800008	$-6.2 \times 10^{-5}$	$1.6653 \times 10^{-8}$
0.8	0.900029	0.900004	$6.4 \times 10^{-5}$	$6.1074 \times 10^{-9}$
1.0	1.0000	1.0000	$3.8 \times 10^{-4}$	$3.5550 \times 10^{-10}$

**Table 3. Comparison of  $\Theta_{OAFM}(1)$  and  $\Theta_{HPM}(1)$  and their absolute difference keeping  $\beta = 0.00003$ ,  $M = 0.000015$  and  $R = 0.000002$ .**

$\lambda$	$\Theta_{OAFM}(1)$	$\Theta_{HPM}(1)$	Abs.difference
0	0.500825	0.5	$8.25 \times 10^{-4}$
0.000015	0.500681	0.499996	$6.8 \times 10^{-4}$
0.00003	0.500537	0.499993	$5.45 \times 10^{-4}$
0.000045	0.500394	0.499989	$4.05 \times 10^{-4}$
0.00006	0.50025	0.499985	$2.65 \times 10^{-4}$
0.000075	0.500106	0.499981	$1.25 \times 10^{-4}$
0.00009	0.499962	0.499978	$1.51 \times 10^{-4}$
0.000105	0.499819	0.499974	$1.55 \times 10^{-4}$
0.00012	0.499675	0.49997	$2.95 \times 10^{-4}$
0.000135	0.499531	0.499966	$4.35 \times 10^{-4}$
0.00015	0.499387	0.499963	$5.75 \times 10^{-4}$

**Table 4. Comparison of  $\Theta_{OAFM}(-1)$  and  $\Theta_{HPM}(-1)$  and their absolute difference keeping  $\beta = 0.00003$ ,  $M = 0.000015$  and  $R = 0.000002$ .**

$\lambda$	$\Theta_{OAFM}(-1)$	$\Theta_{HPM}(-1)$	Abs.difference
0.000	0.499897	0.5000	$1.03 \times 10^{-4}$
0.000015	0.499921	0.500004	$8.29 \times 10^{-5}$
0.00003	0.499945	0.500007	$6.27 \times 10^{-5}$
0.000045	0.499969	0.500011	$4.25 \times 10^{-5}$
0.00006	0.499993	0.500015	$2.23 \times 10^{-5}$
0.000075	0.500017	0.500019	$2.07 \times 10^{-6}$
0.00009	0.500041	0.500022	$1.81 \times 10^{-5}$
0.000105	0.500065	0.500026	$3.83 \times 10^{-5}$
0.00012	0.500089	0.50003	$5.85 \times 10^{-5}$
0.000135	0.500112	0.500034	$7.87 \times 10^{-5}$
0.00015	0.500136	0.500037	$9.90 \times 10^{-5}$

**Table 5. Comparison of  $\Theta_{OAFM}(1)$  and  $\Theta_{HPM}(1)$  and their absolute difference keeping  $\beta = 0.00003$ ,  $\lambda = 0.000015$  and  $R = 0.000002$ .**

$M$	$\Theta_{OAFM}(1)$	$\Theta_{HPM}(1)$	Abs.difference
0	0.500681	0.499996	$6.85 \times 10^{-4}$
0.000025	0.500681	0.499996	$6.85 \times 10^{-4}$
0.00005	0.500681	0.499996	$6.85 \times 10^{-4}$
0.000075	0.500681	0.499996	$6.85 \times 10^{-4}$
0.0001	0.500681	0.499996	$6.85 \times 10^{-4}$
0.000125	0.500681	0.499996	$6.85 \times 10^{-4}$
0.00015	0.500681	0.499996	$6.85 \times 10^{-4}$
0.000175	0.500681	0.499996	$6.85 \times 10^{-4}$
0.0002	0.500681	0.499996	$6.85 \times 10^{-4}$
0.000225	0.500681	0.499996	$6.85 \times 10^{-4}$
0.00025	0.500681	0.499996	$6.85 \times 10^{-4}$

**Table 6. Comparison of  $\Theta_{OAFM}(-1)$  and  $\Theta_{HPM}(-1)$  and their absolute difference keeping  $\beta = 0.00003$ ,  $\lambda = 0.000015$  and  $R = 0.000002$ .**

$M$	$\Theta_{OAFM}(-1)$	$\Theta_{HPM}(-1)$	Abs.difference
0	0.499921	0.500004	$8.29 \times 10^{-5}$
0.000015	0.499921	0.500004	$8.29 \times 10^{-5}$
0.00003	0.499921	0.500004	$8.29 \times 10^{-5}$
0.000045	0.499921	0.500004	$8.29 \times 10^{-5}$
0.00006	0.499921	0.500004	$8.29 \times 10^{-5}$
0.000075	0.499921	0.500004	$8.29 \times 10^{-5}$
0.00009	0.499921	0.500004	$8.29 \times 10^{-5}$
0.000105	0.499921	0.500004	$8.29 \times 10^{-5}$
0.00012	0.499921	0.500004	$8.29 \times 10^{-5}$
0.000135	0.499921	0.500004	$8.29 \times 10^{-5}$
0.00015	0.499921	0.500004	$8.29 \times 10^{-5}$

### CONCLUSIONS

In this paper, plane couette flow of a couple stress fluid under the influence of magnetohydrodynamics (MHD) using Reynolds model of viscosity has been explored by employing two reliable techniques. The governing equation of the couple stress fluid under the influence of MHD are solved using Homotopy Perturbation method (HPM) and Optimal Auxiliary Function Method (OAFM). The HPM is an analytical method that employs a

series solution with a parameter to approximate the solution of the problem. On the other hand, the OAFM is a numerical technique that involves introducing an auxiliary function to simplify the equations, leading to an easier solution procedure and gives an efficient solution after two steps. Furthermore the effect of non-dimensional parameters on velocity profile, temperature distribution, shear stresses and flow rate are analysed. The HPM solution and OAFM solution are compared to each other using different graphs and tables involving residual error. It reveals that the HPM solution is more efficient and accurate than OAFM solution. Finally we conclude that both approaches have the capability to solve highly non linear differential equations and physical models.







### Conflicts of Interest

The authors declare that there are no conflicts of interest regarding the publication of this article.

### Acknowledgments

The authors thank the support of the Deanship of Scientific Research at the Islamic University of Madinah, Madinah, Saudi Arabia.

### ORCID

 **Muhammad Farooq**, <https://orcid.org/0000-0003-3392-101X>;  **Ibrar Khan**, <https://orcid.org/0009-0008-2586-9841>;  **Rashid Nawaz**, <https://orcid.org/0000-0002-4773-8446>;  **Gamal M. Ismail**, <https://orcid.org/0000-0002-9060-4371>;  **Huzaifa Umar**, <https://orcid.org/0000-0003-2508-9710>;  **Hijaz Ahmad**, <https://orcid.org/0000-0002-5438-5407>

### REFERENCES

- [1] M.A. Seddeek, "Heat and mass transfer on a stretching sheet with a magnetic field in a visco-elastic fluid flow through a porous medium with heat source or sink," *Computational Materials Science*, **38**(4), 781-787 (2007). <https://doi.org/10.1016/j.commatsci.2006.05.015>
- [2] M.A. Mansour, M.A. El-Hakim, and S.M. El Kabeir, "Heat and mass transfer in magnetohydrodynamic flow of micropolar fluid on a circular cylinder with uniform heat and mass flux," *Journal of Magnetism and Magnetic Materials*, **220**(2-3), 259-270 (2000). [https://doi.org/10.1016/S0304-8853\(00\)00488-1](https://doi.org/10.1016/S0304-8853(00)00488-1)
- [3] O.A. Bég, A.Y. Bakier, V.R. Prasad, J. Zueco, and S.K. Ghosh, "Nonsimilar, laminar, steady, electrically-conducting forced convection liquid metal boundary layer flow with induced magnetic field effects," *International Journal of Thermal Sciences*, **48**(8), 1596-1606 (2009). <https://doi.org/10.1016/j.ijthermalsci.2008.12.007>
- [4] R. Jain, R. Mehta, M.K. Sharma, T. Mehta, H. Ahmad, and F. Tchier, "Numerical analysis of heat and mass transport of hybrid nanofluid over an extending plate with inclined magnetic field in presence of Soret and dufour Effect," *Modern Physics Letters B*, **6**, 2450037 (2023). <https://doi.org/10.1142/S0217984924500374>
- [5] S.F. Megahid, A.E. Abouelregal, H. Ahmad, M.A. Fahmy, and H. Abu-Zinadah, "A generalized More-Gibson-Thomson heat transfer model for the study of thermomagnetic responses in a solid half-space," *Results in Physics*, **51**, 106619 (2023). <https://doi.org/10.1016/j.rinp.2023.106619>
- [6] T. Muhammad, H. Ahmad, U. Farooq, and A. Akgül, "Computational Investigation of Magnetohydrodynamics Boundary of Maxwell Fluid Across Nanoparticle-Filled Sheet," *Al-Salam Journal for Engineering and Technology*, **2**(2), 88-97 (2023). <https://doi.org/10.55145/ajest.2023.02.02.011>
- [7] A.E. Abouelregal, H. Ahmad, M.A. Aldahlan, and X.Z. Zhang, "Nonlocal magneto-thermoelastic infinite half-space due to a periodically varying heat flow under Caputo-Fabrizio fractional derivative heat equation," *Open Physics*, **20**(1), 274-288 (2022). <https://doi.org/10.1515/phys-2022-0019>
- [8] M. Farooq, Z. Ahmad, H. Ahmad, M. Zeb, F. Aouaini, and M. Ayaz, "Homotopy analysis methods with applications to thin-film flow of a magnetohydrodynamic-modified second grade fluid," *Modern Physics Letters B*, **36**(19), 2150617 (2022). <https://doi.org/10.1142/S021798492150617X>
- [9] H. Ahmad, A.E. Abouelregal, M. Benhamed, M.F. Alotaibi, and A. Jendoubi, "Vibration analysis of nanobeams subjected to gradient-type heating due to a static magnetic field under the theory of nonlocal elasticity," *Scientific Reports*, **12**(1), 1894 (2022). <https://doi.org/10.1038/s41598-022-05934-0>
- [10] B. Tashtoush, "Magnetic and buoyancy effects on melting from a vertical plate embedded in saturated porous media," *Energy Conversion and Management*, **46**(15-16), 2566-2577 (2005). <https://doi.org/10.1016/j.enconman.2004.12.004>

- [11] M.F. El-Amin, "Magnetohydrodynamic free convection and mass transfer flow in micropolar fluid with constant suction," *Journal of magnetism and magnetic materials*, **234**(3), 567-574 (2001). [https://doi.org/10.1016/S0304-8853\(01\)00374-2](https://doi.org/10.1016/S0304-8853(01)00374-2)
- [12] S. Ahmed, O.A. Bég, and S.K. Ghosh, "A couple stress fluid modeling on free convection oscillatory hydromagnetic flow in an inclined rotating channel," *Ain Shams Engineering Journal*, **5**(4), 1249-1265 (2014). <https://doi.org/10.1016/j.asej.2014.04.006>
- [13] A.A. Dar, and K. Elangovan, "Influence of an inclined magnetic field on Heat and Mass transfer of the peristaltic flow of a couple stress fluid in an inclined channel," *World Journal of Engineering*, **14**(1), 7-18 (2017). <https://doi.org/10.1108/WJE-11-2016-0124>
- [14] P.Y. Xiong, M. Nazeer, F. Hussain, M.I. Khan, A. Saleem, S. Qayyum, and Y.M. Chu, "Two-phase flow of couple stress fluid thermally effected slip boundary conditions: Numerical analysis with variable liquids properties," *Alexandria Engineering Journal*, **61**(5), 3821-3830 (2022). <https://doi.org/10.1016/j.aej.2021.09.012>
- [15] O.A. Ajala, L.O. Aselebe, S.F. Abimbade, and A.W. Ogunsola, "Effect of magnetic fields on the boundary layer flow of heat transfer with variable viscosity in the presence of thermal radiation," *International Journal of Scientific and Research Publication*, **9**(5), 13-19 (2019). <https://doi.org/10.24297/jam.v12i7.3874>
- [16] J.A. Falade, S.O. Adesanya, J.C. Ukaegbu, and M.O. Osinowo, "Entropy generation analysis for variable viscous couple stress fluid flow through a channel with non-uniform wall temperature," *Alexandria Engineering Journal*, **55**(1), 69-75 (2016). <https://doi.org/10.1016/j.aej.2016.01.011>
- [17] B.V. Swarnalathamma, and M.V. Krishna, "Peristaltic hemodynamic flow of couple stress fluid through a porous medium under the influence of magnetic field with slip effect," In *AIP Conference Proceedings*, **1728**(1), 020603 (2016). <https://doi.org/10.1063/1.4946654>
- [18] K. Ramesh, "Influence of heat and mass transfer on peristaltic flow of a couple stress fluid through porous medium in the presence of inclined magnetic field in an inclined asymmetric channel," *Journal of Molecular Liquids*, **219**, 256-271 (2016). <https://doi.org/10.1016/j.molliq.2016.03.010>
- [19] B.B. Divya, G. Manjunatha, C. Rajashekhar, H. Vaidya, and K.V. Prasad, "Effects of inclined magnetic field and porous medium on peristaltic flow of a Bingham fluid with heat transfer," *Journal of Applied and Computational Mechanics*, **7**(4), 1892-1906 (2021). <https://doi.org/10.22055/JACM.2019.31060.1822>
- [20] T. Hayat, M. Awais, A. Safdar, and A.A. Hendi, "Unsteady three dimensional flow of couple stress fluid over a stretching surface with chemical reaction," *Nonlinear Analysis: Modelling and Control*, **17**(1), 47-59 (2012). <https://doi.org/10.15388/NA.17.1.14077>
- [21] S.T. Mohyud-Din, and M.A. Noor, "Homotopy perturbation method for solving partial differential equations," *Zeitschrift für Naturforschung A*, **64**(3-4), 157-170 (2009). <https://doi.org/10.1515/zna-2009-3-402>
- [22] J. Biazar, and H. Ghazvini, "Convergence of the homotopy perturbation method for partial differential equations," *Nonlinear Analysis: Real World Applications*, **10**(5), 2633-2640 (2009). <https://doi.org/10.1016/j.nonrwa.2008.07.002>
- [23] B. Marinca, and V. Marinca, "Approximate analytical solutions for thin film flow of a fourth grade fluid down a vertical cylinder," *Proceed Romanian Academy, Series A*, **19**(1), 69-76 (2018). <https://acad.ro/sectii2002/proceedings/doc2018-1/10.pdf>
- [24] L. Zada, R. Nawaz, M. Ayaz, H. Ahmad, H. Alrabaiah, and Y.M. Chu, "New algorithm for the approximate solution of generalized seventh order Korteweg-Devries equation arising in shallow water waves," *Results in Physics*, **20**, 103744 (2021). <https://doi.org/10.1016/j.rinp.2020.103744>
- [25] S. Islam, and C.Y. Zhou, "Exact solutions for two dimensional flows of couple stress fluids," *Zeitschrift für angewandte Mathematik und Physik*, **58**(6), 1035-1048 (2007). <https://doi.org/10.1007/s00033-007-5075-5>
- [26] N.T. EL-Dabe, and S.M. El-Mohandis, "Effect of couple stresses on pulsatile hydromagnetic Poiseuille flow," *Fluid Dynamics Research*, **15**(5), 313-324 (1995). [https://doi.org/10.1016/0169-5983\(94\)00049-6](https://doi.org/10.1016/0169-5983(94)00049-6)
- [27] Y. Aksoy, and M. Pakdemirli, "Approximate analytical solutions for flow of a third-grade fluid through a parallel-plate channel filled with a porous medium," *Transport in Porous Media*, **83**, 375-395 (2010). <https://doi.org/10.1007/s11242-009-9447-5>
- [28] M. Massoudi, and I. Christie, "Effects of variable viscosity and viscous dissipation on the flow of a third grade fluid in a pipe," *International Journal of Non-Linear Mechanics*, **30**(5), 687-699 (1995). [https://doi.org/10.1016/0020-7462\(95\)00031-I](https://doi.org/10.1016/0020-7462(95)00031-I)
- [29] T. Chinyoka, and O.D. Makinde, "Analysis of transient Generalized Couette flow of a reactive variable viscosity third-grade liquid with asymmetric convective cooling," *Mathematical and Computer Modelling*, **54**(1-2), 160-174 (2011). <http://dx.doi.org/10.1016/j.mcm.2011.01.047>

ПОРІВНЯЛЬНИЙ АНАЛІЗ ПЛОСКОЇ ТЕЧІЇ КУЕТТА ПАРНО НАПРУЖЕНОЇ  
РІДИНИ ПІД ВПЛИВОМ МАГНІТОГІДРОДИНАМІКИ  
Мухаммад Фарук<sup>a</sup>, Ібрат Хан<sup>a</sup>, Рашид Наваз<sup>b</sup>, Гамаль Мохамед Ісмаїл<sup>c</sup>, Хузайфа Умар<sup>d</sup>,  
Хіджаз Ахмад<sup>c,d,e</sup>

<sup>a</sup> Факультет математики, Університет Абдула Валі Хана, Мардан 23200, Пакистан

<sup>b</sup> UniSa STEM, Університет Південної Австралії

<sup>c</sup> Департамент математики, Факультет природничих наук, Ісламський університет Медіни,  
Медіна, Саудівська Аравія

<sup>d</sup> Близькосхідний університет, Центр оперативних досліджень у сфері охорони здоров'я,  
Близькосхідний бульвар, ПК: 99138 Нікосія/Мерсін 10, Туреччина

<sup>e</sup> Департамент математики, Азербайджанський університет,  
вул. Джейхун Гаджібейлі, 71, AZ1007, Баку, Азербайджан

Це дослідження має на меті виконати порівняльний аналіз плоского потоку Куетта парної напруженої рідини під впливом магнітогідродинаміки (МГД) за допомогою двох різних методів: методу оптимальної допоміжної функції (ОАФМ) і методу гомотопічних збурень (НРМ). Рідина парних напружень відома своєю неньютонівською поведінкою, де реакція рідини на зсув залежить від наявності внутрішньої мікроструктури. ОАФМ і НРМ використовуються для розв'язання керівних рівнянь течії рідини парних напружень під МГД. ОАФМ — це чисельний метод, який передбачає введення допоміжної функції для спрощення рівнянь, що спрощує процедуру розв'язання. З іншого боку, НРМ — це аналітичний метод, який використовує послідовне рішення. Порівняльний аналіз зосереджується на вивченні точності, ефективності та поведінки збіжності двох методів. Для дослідження їх впливу на поведінку потоку розглядаються різні параметри потоку, такі як параметр напруги пари, магнітний параметр і співвідношення швидкостей. Крім того, рішення НРМ порівнювали з рішенням ОАФМ за допомогою різних графіків і таблиць. Це виявило, що рішення, отримане НРМ, є кращим, ніж рішення ОАФМ.

**Ключові слова:** парно напружена рідина; метод оптимальної допоміжної функції (ОАФМ); метод гомотопічних збурень (НРМ); магнітогідродинаміка (МГД)

## HEAT AND MASS TRANSPORT ASPECTS OF NANOFLUID FLOW TOWARDS A VERTICAL FLAT SURFACE INFLUENCED BY ELECTRIFIED NANOPARTICLES AND ELECTRIC REYNOLDS NUMBER

Aditya Kumar Pati, Sujit Mishra, Ashok Misra\*, Saroj Kumar Mishra

Centurion University of Technology and Management, Paralakhemundi, Odisha, India

\*Corresponding author e-mail: [amisra1972@gmail.com](mailto:amisra1972@gmail.com)

Received April 6, 2024; revised May 3, 2024; accepted May 15, 2024

This study examines the heat and mass transfer aspects of the natural convective flow of a nanofluid along a vertical flat surface, incorporating electrified nanoparticles and electric Reynolds number. While conventional nanofluid models like Buongiorno's model overlook the nanoparticle electrification and electric Reynolds number mechanisms, this study addresses the nanoparticle electrification and electric Reynolds number mechanisms by justifying its relevance, particularly when tribo-electrification results from Brownian motion. This incorporation of the electric Reynolds number and nanoparticle electrification mechanism is a unique aspect of this investigation. Using the similarity method and nondimensionalization, the governing partial differential equations of the flow are transformed into a set of locally similar equations. MATLAB's `bvp4c` solver is employed to solve this set of equations, along with the boundary conditions. The obtained results are validated by comparison with those from previously published works. Graphical representations are provided for the numerical outcomes of non-dimensional velocity, concentration and temperature concerning the nanoparticle electrification parameter and electric Reynolds number. The combined effects of the nanoparticle electrification parameter and the electric Reynolds number on non-dimensional heat and mass transfer coefficients are examined in tabular form. Furthermore, the impact of the nanoparticle electrification parameter on both heat and mass transfer for varying values of the Brownian motion parameter is explored graphically. The primary finding of this investigation indicates that the electrification mechanism of nanoparticles quickens the transfer of heat and mass from a flat surface to nanofluid, suggesting promising prospects for utilization in cooling systems and biomedical applications.

**Keywords:** *Electrified Nanoparticles; Nanofluid; Buongiorno's model; Electric Reynolds number; Natural convection*

**PACS:** 44.20.+b, 44.25.+f, 47.10.ad, 47.55.pb, 47.15.Cb

### 1. INTRODUCTION

The incorporation of heat and mass transfer in the natural convective boundary layer flow around a vertical flat surface has garnered significant interest due to its myriad practical implications. These include applications in industries such as crude oil extraction, nuclear waste storage, packed bed reactors, aviation insulation, heat exchangers, geothermal ventures, and the cooling of electronic equipment. These examples underscore the utilization of the earth's natural heat across various technological domains. Recent technological advancements in the manipulation of standard fluids now involve the integration of nanometer-sized particle fibers into primary fluids, leading to the creation of nanofluids. These nanofluids are primarily utilized to augment the heat transfer capabilities of the base fluid. Over time, the progression and refinement of technology, particularly in the realm of nanotechnology, are expected to significantly impact future markets. Nanotechnology, which involves the study and application of structures at the nanoscale level, has facilitated the development of various effective products. Its applications span across multiple domains, including medicine, therapy, diagnostics, sequencing, electronics, and material manufacturing. Choi et al. [1] illustrated that adding nanoparticles to a base fluid can significantly enhance thermal conductivity, effectively doubling it.

Several researchers have proposed numerous physical factors that enhance heat transmission in nanofluid flow. Buongiorno [2] emphasized that thermophoresis and Brownian motion are pivotal slip mechanisms for modelling nanofluid flow. However, the impact of nanoparticle electrification and electric Reynolds number mechanisms has been overlooked in this context. Several studies (Kuznetsov and Nield [3], Khan and Aziz [4], Aziz and Khan [5], Das and Jana [6], Goyal and Bhargabha [7], Jeevandar et al. [8], Reddy and Goud [9], Dey et al. [10]) have explored the simulation of free convective nanofluid flow along a vertical flat plate using Buongiorno's model [2]. Notably, the mechanism of nanoparticle electrification remains unaddressed in all these studies ([2] to [10]). Nonetheless, due to Brownian motion leading to nanoparticle collisions, the significance of the electrification mechanism is justified (Soo [11]; Kang and Wang [12]).

This study delves into the combined effects of electric Reynolds number and electrified nanoparticles on the flow of nanofluid near a vertical flat surface. Integrating the electric Reynolds number and electrified nanoparticles into Buongiorno's model allows for an exploration of the heat and mass transport dynamics of the nanofluid, which is a uniqueness of the current work not considered in earlier literature on nanofluid flow past a vertical flat surface.

## 2. MATHEMATICAL FORMULATION

A  $Cu$ -water steady laminar nanofluid flow with electrified nanoparticles is examined. The vertical flat surface is chosen along the  $x$  axis. The wall surface maintains constant values for concentration ( $C_w$ ) and temperature ( $T_w$ ). The values for temperature and concentration outside the boundary layer are taken as  $T_\infty$  and  $C_\infty$ , respectively. The schematic view is displayed in Fig 1.

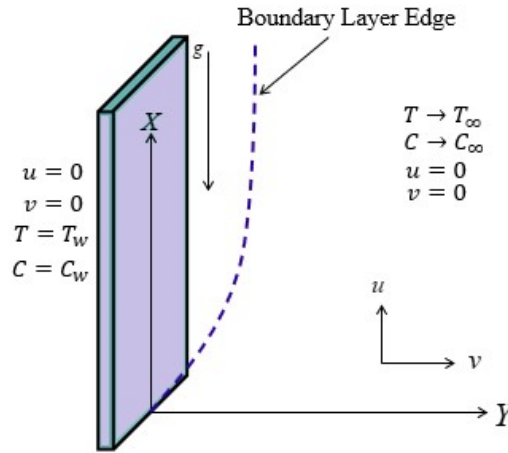


Figure 1. Coordinate system and schematic view

The governing equations with electrified nanoparticles (Pati et al. [13]) and using the Oberbeck-Boussinesq approach can be formulated as follows:

$$\frac{\partial u}{\partial x} + \frac{\partial v}{\partial y} = 0, \quad (1)$$

$$\rho_{nf} \left( u \frac{\partial u}{\partial x} + v \frac{\partial u}{\partial y} \right) = \rho_s \frac{q}{m} (C - C_\infty) E_x + \mu_{nf} \left( \frac{\partial^2 u}{\partial y^2} \right) + (T - T_\infty) \beta_{f\infty} \rho_{f\infty} g (1 - C_\infty) - (\rho_s - \rho_{f\infty}) (C - C_\infty) g, \quad (2)$$

$$u \frac{\partial T}{\partial x} + v \frac{\partial T}{\partial y} = \frac{(\rho c)_s}{(\rho c)_{nf}} \frac{q}{m} \frac{C}{F} \left( E_x \frac{\partial T}{\partial x} + E_y \frac{\partial T}{\partial y} \right) + \frac{k_{nf}}{(\rho c)_{nf}} \left( \frac{\partial^2 T}{\partial y^2} \right) + \frac{(\rho c)_s}{(\rho c)_{nf}} \frac{D_T}{T_\infty} \left( \frac{\partial T}{\partial y} \right)^2 + \frac{(\rho c)_s}{(\rho c)_{nf}} D_B \frac{\partial C}{\partial y} \frac{\partial T}{\partial y} \quad (3)$$

$$u \frac{\partial C}{\partial x} + v \frac{\partial C}{\partial y} = \frac{D_T}{T_\infty} \frac{\partial^2 T}{\partial y^2} + \left( \frac{q}{m} \right) \frac{1}{F} \left[ \frac{\partial(C E_x)}{\partial x} + \frac{\partial(C E_y)}{\partial y} \right] + D_B \frac{\partial^2 C}{\partial y^2}, \quad (4)$$

$$\frac{\partial E_y}{\partial y} = \frac{\rho_s q}{\epsilon_0 m}, \quad (5)$$

and the boundary conditions:

$$\left. \begin{aligned} y = 0, v = 0, u = 0, C = C_w, T = T_w \\ y \rightarrow \infty, v = 0, u = 0, C \rightarrow C_\infty, T \rightarrow T_\infty \end{aligned} \right\} \quad (6)$$

where  $C$  and  $T$  signify the local concentration and local temperature, respectively. The velocity and electric intensity components in the  $(x, y)$  direction is represented by  $(u, v)$  and  $(E_x, E_y)$ , respectively. The subscripts  $f$ ,  $s$  and  $nf$  represent the base fluid, nanoparticle, and nanofluid thermophysical properties, respectively. The symbols  $(\rho c)$ ,  $k$ ,  $\mu$ , and  $\rho$  signify heat capacity, thermal conductivity, viscosity, and density, respectively.  $F$  represents the momentum transfer time constant between the fluid and the nanoparticles.  $g$  denotes the gravitational acceleration.  $D_T$ ,  $\beta_f$  and  $D_B$  stands the thermophoretic diffusion coefficient, volumetric thermal expansion coefficient and Brownian diffusion coefficient, respectively.  $m$  and  $q$  denotes the mass and charge of the nanoparticles, respectively.  $\epsilon_0$  denotes the permittivity. The free stream values are represented by the subscript  $\infty$ .

By considering the stream function  $\psi$  with  $\frac{\partial \psi}{\partial x} = -v$  and  $\frac{\partial \psi}{\partial y} = u$ , equation (1) is clearly satisfied. The variables mentioned below are employed in transforming equations (2), (3), and (4) into equations (8), (9), and (10) and the equations (1) and (5) are identically satisfied.

$$\eta = \frac{y}{x} (Ra_x)^{\frac{1}{4}}, \psi = \alpha_f (Ra_x)^{\frac{1}{4}} f(\eta), s(\eta) = \frac{C - C_\infty}{C_w - C_\infty}, \theta(\eta) = \frac{T - T_\infty}{T_w - T_\infty}, \quad (7)$$

where  $\eta$  denotes similarity variable and  $Ra_x = \frac{x^3 (T_w - T_\infty) \beta_f g (1 - C_\infty)}{\alpha_f \nu_f}$ , is the local Rayleigh number.

The non-dimensional equations are as follows:

$$f'''' + \frac{\phi_1}{4Pr} [3ff'' - 2(f')^2] + \frac{\phi_1\phi_2M}{PrN_F} s + \frac{1}{\phi_5} (\theta - Nr s) = 0, \tag{8}$$

$$\theta'' + \frac{1}{\phi_4} Pr Nt(\theta')^2 + \frac{1}{\phi_4} Sc Nb \left[ \frac{N_F}{N_{Re}} - \frac{1}{4} M \right] (s + Nc)\eta\theta' + \frac{1}{\phi_4} Pr Nbs'\theta' + \frac{3}{4} \frac{1}{\phi_3\phi_4} f\theta' = 0, \tag{9}$$

$$s'' + \frac{Nt}{Nb} \theta'' - \frac{1}{4} \frac{M Sc}{Pr} \eta s' + \frac{N_F Sc}{Pr N_{Re}} (\eta s' + s + Nc) + \frac{3}{4} \frac{Sc}{Pr} f s' = 0, \tag{10}$$

where prime (') indicates derivative with respect to  $\eta$ .  
 The equations (6) are simplified to

$$\left. \begin{aligned} \eta = 0, f(0) = f'(0) = 0, s(0) = \theta(0) = 1 \\ \eta \rightarrow \infty, f'(\infty) \rightarrow 0, s(\infty) \rightarrow 0, \theta(\infty) \rightarrow 0 \end{aligned} \right\}. \tag{11}$$

The nondimensional parameters are represented as

$$\begin{aligned} Nr &= \frac{(\rho_s - \rho_f)(C_w - C_\infty)}{(1 - C_\infty)\rho_f\beta_f(T_w - T_\infty)}, Nt = \frac{(\rho c)_s D_T (T_w - T_\infty)}{(\rho c)_f \nu_f T_\infty}, Pr = \frac{\nu_f}{\alpha_f}, \\ Nc &= \frac{C_\infty}{(C_w - C_\infty)}, Nb = \frac{(\rho c)_s D_B (C_w - C_\infty)}{(\rho c)_f \nu_f}, Sc = \frac{\nu_f}{D_B}, \\ \frac{1}{N_{Re}} &= \left(\frac{q}{m}\right)^2 \frac{\rho_s}{\epsilon_0} \frac{x^2}{\left(\frac{\alpha_f (Ra_x)^{\frac{1}{2}}}{x}\right)^2}, N_F = \frac{\left(\frac{\alpha_f (Ra_x)^{\frac{1}{2}}}{x}\right)}{F_x}, M = \left(\frac{q}{m}\right) \frac{1}{F \left(\frac{\alpha_f (Ra_x)^{\frac{1}{2}}}{x}\right)} E_x. \end{aligned}$$

Here  $Nr$ ,  $Nt$ ,  $Pr$ ,  $Nc$ ,  $Nb$ ,  $Sc$ ,  $N_{Re}$ ,  $N_F$ , and  $M$  denote the buoyancy ratio, thermophoresis parameter, Prandtl number, concentration ratio, Brownian motion parameter, Schmidt number, electric Reynolds number, momentum transfer number, and electrification parameter, respectively.

The thermophysical constants (Maharukh et al., [14]) are represented as

$$\begin{aligned} \phi_1 &= \frac{\nu_f}{\nu_{nf}} = \left[ C_\infty \frac{\rho_s}{\rho_f} + (1 - C_\infty) \right] (1 - C_\infty)^{2.5}, \\ \phi_2 &= \frac{c_f}{c_s} \frac{1}{\left[ \frac{\rho_s C_\infty + (1 - C_\infty)}{\rho_f} \right]}, \tau = \frac{(\rho c)_s}{(\rho c)_f}, \\ \phi_3 &= \frac{(\rho c)_f}{(\rho c)_{nf}} = \frac{1}{C_\infty \tau + (1 - C_\infty)}, \\ \phi_4 &= \frac{k_{nf}}{k_f} = \frac{(k_s + 2k_f) - 2C_\infty(k_f - k_s)}{(k_s + 2k_f) - C_\infty(k_s - k_f)}, \\ \phi_5 &= \frac{\mu_{nf}}{\mu_f} = (1 - C_\infty)^{-2.5}. \end{aligned}$$

The investigation utilizes a nanofluid with a 1% concentration of copper nanoparticles. The thermophysical characteristics of both pure water and the nanoparticles are evaluated based on the criteria established by Oztop and Abu-Nada [15].

The local Nusselt number  $Nu_x$  and Sherwood number  $Sh_x$  are provided for applications involving heat and mass transfer as

$$\begin{aligned} Nu_x &= \frac{xq_w}{k_f(T_w - T_\infty)}, \text{ where } q_w = -k_f \left( \frac{\partial T}{\partial y} \right)_{y=0}, \\ Sh_x &= \frac{xq_m}{D_B(C_w - C_\infty)}, \text{ where } q_m = -D_B \left( \frac{\partial C}{\partial y} \right)_{y=0}. \end{aligned}$$

The reduced Nusselt number  $(-\theta'(0))$  and the reduced Sherwood number  $(-s'(0))$  can be expressed in dimensionless form as

$$\begin{aligned} Nu_x / (Ra_x)^{1/4} &= -\theta'(0), \\ Sh_x / (Ra_x)^{1/4} &= -s'(0). \end{aligned}$$



### 3. METHOD OF SOLUTION

The MATLAB bvp4c solver is employed for solving equations (8) to (10) along with the equation (11) and it is noted that these equations are specifically local similarity equations, as the parameters  $M$ ,  $N_F$  and  $N_{Re}$  continue to rely on  $x$ . Numerical results are deemed appropriate, as long as they yield a locally similarity solution, as emphasized by Habibi and Jahangiri [16]. Additionally,  $M$ ,  $N_F$  and  $N_{Re}$  treated as constants in this context following [16].

### 4. RESULTS AND DISCUSSION

The computed numerical values of  $-\theta'(0)$  in the standard fluid scenario are cross-referenced with Kuznetsov and Nield's findings [3] to validate the accuracy of the calculations. Table 1 illustrates a significant alignment between the two sets of data.

**Table 1.** Comparison of  $-\theta'(0)$

$Pr$	1.0	10.0	100.0	1000.0
$-\theta'(0)$ (Kuznetsov and Nield [3])	0.401	0.463	0.481	0.484
$-\theta'(0)$ (present results)	0.401	0.463	0.480	0.482

Fig. 2 illustrates the distributions of dimensionless longitudinal velocity  $\frac{df(\eta)}{d\eta}$ , concentration  $s(\eta)$  and temperature  $\theta(\eta)$  of the flow.

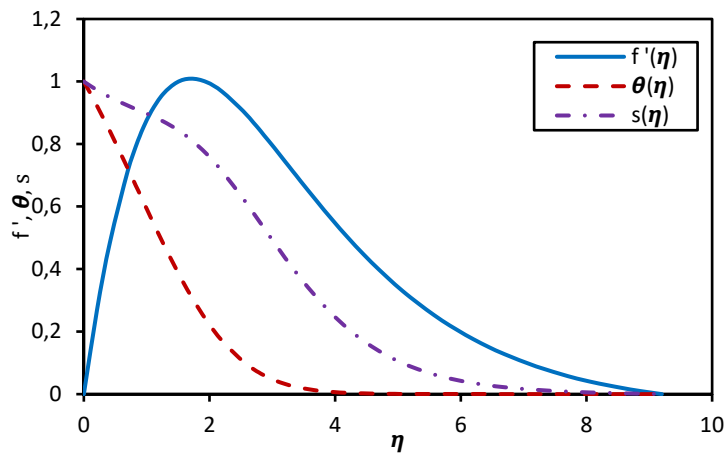


**Figure 2.** Plots of  $\frac{df(\eta)}{d\eta}$ ,  $\theta(\eta)$  and  $s(\eta)$  for the case  $Pr = 6.2$ ,  $N_{Re} = Sc = 2.0$ ,  $Nc = N_F = M = Nr = Nb = Nt = 0.1$ .

#### 4.1. Impact of Electrification Parameter on Velocity, Temperature and Concentration Profiles

Numerical analysis is conducted to investigate the impact of  $M$  on  $f'(\eta)$ ,  $\theta(\eta)$ , and  $s(\eta)$  distributions with respect to  $\eta$ , represented graphically. Figure 3 illustrates the effect of  $M$  on  $f'(\eta)$ , revealing an enhancement in  $f'(\eta)$  with increasing  $M$ .

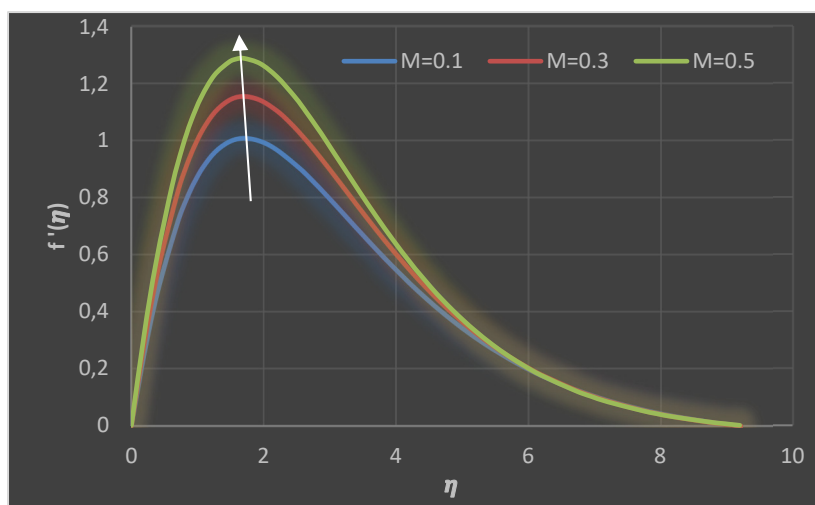


**Figure 3.** Effects of  $M$  on velocity profiles

This phenomenon occurs due to the escalation of the electrification parameter, which subsequently augments the drag force on ions, inducing an opposite and equal reaction force on neutral fluid molecules within the boundary layer,

thereby causing an increase in  $f'(\eta)$ . By increasing  $M$ ,  $\theta(\eta)$  decrease, as shown in Fig. 4. The rise in  $M$  leads to an increase in fluid velocity, causing the hotter fluid particles to move away. Consequently, the fluid cools, resulting in a decrease in  $\theta(\eta)$ . Fig. 5 shows that  $s(\eta)$  reduces with increasing  $M$ . This occurs due to a rise in  $M$ , causing nanoparticles to move from the fluid region towards the flat surface, resulting in a decrease in  $s(\eta)$ . The values  $Pr = 6.2, Nc = N_F = Nr = Nb = Nt = 0.1$  and  $N_{Re} = Sc = 2.0$  remain constant across all the findings depicted in figures 3 to 5.

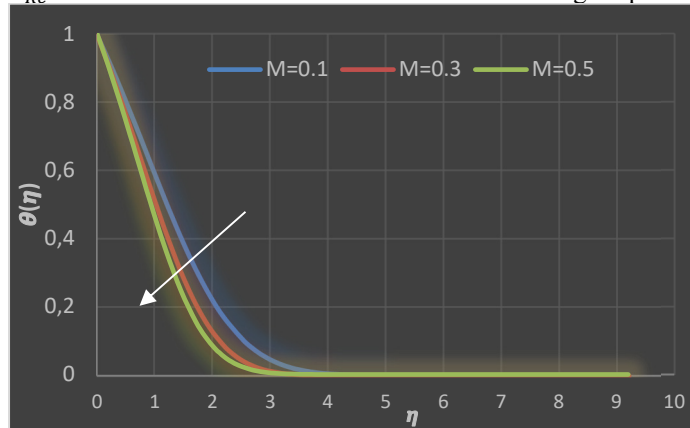


Figure 4. Effects of  $M$  on temperature profiles.

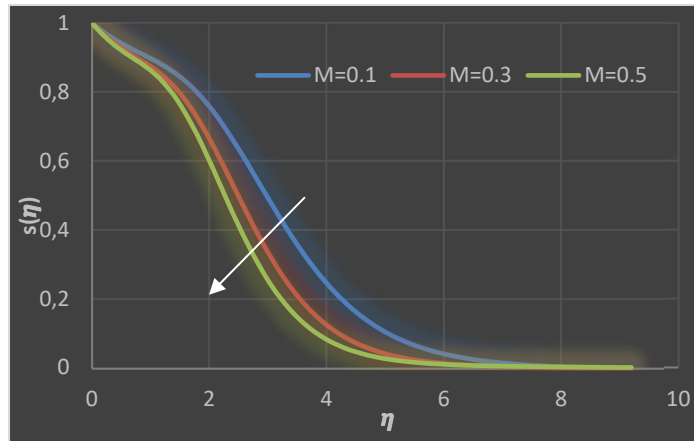


Figure 5. Effects of  $M$  on concentration profiles

#### 4.2. Impact of Electric Reynolds Number on Velocity, Temperature and Concentration Profiles

Numerical investigation is conducted to examine the impact of  $N_{Re}$  on  $f'(\eta)$ ,  $\theta(\eta)$ , and  $s(\eta)$  distributions with respect to  $\eta$ , represented graphically. Figure 6 and 7 shows the effect of  $N_{Re}$  on  $f'(\eta)$  and  $\theta(\eta)$  respectively, revealing an improvement in  $f'(\eta)$  and  $\theta(\eta)$  as  $N_{Re}$  increases. Fig. 8 indicates that  $s(\eta)$  reduces near the flat surface while the opposite trend is noticed far away from the flat surface with increasing  $N_{Re}$ . The values  $Pr = 6.2, Nc = M = N_F = Nr = Nb = Nt = 0.1$  and  $Sc = 2.0$  remain constant across all the findings depicted in figures 6 to 8.

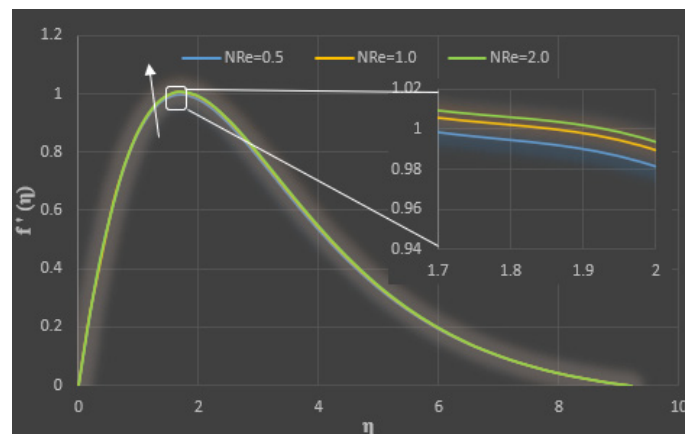


Figure 6. Effects of  $N_{Re}$  on velocity profiles.

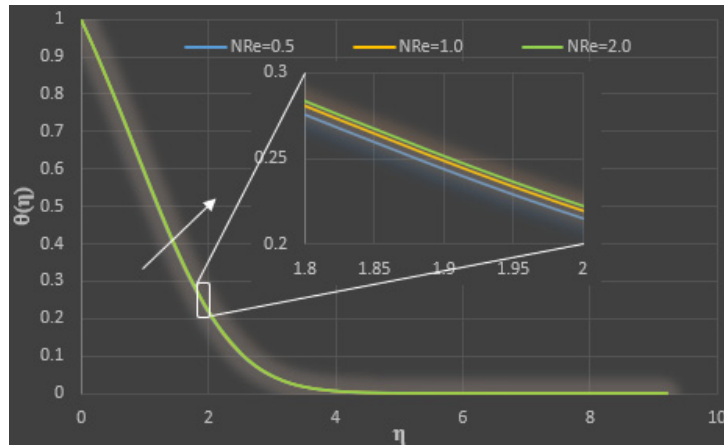


Figure 7. Effects of  $N_{Re}$  on temperature profiles.

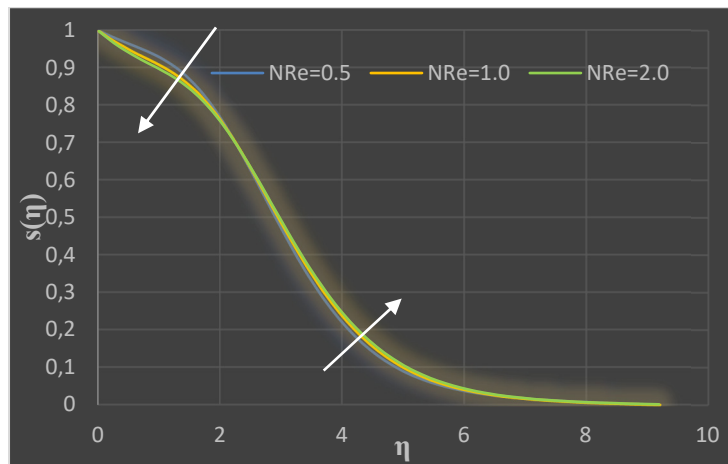


Figure 8. Effects of  $N_{Re}$  on concentration profiles.

**4.3. Combined effects of Electric Reynolds Number and Electrification parameter on Non-dimensional Heat and Mass Transfer Coefficients**

The combined effects of  $N_{Re}$  and  $M$  on  $-\theta'(0)$  and  $-s'(0)$  is depicted in Table 2. It is observed that for various values of the electric Reynolds number, both  $-\theta'(0)$  and  $-s'(0)$  enhances as  $M$  increases. It has been noted that as the electric Reynolds number ( $N_{Re}$ ) increases,  $-\theta'(0)$  reduces whereas  $-s'(0)$  improves across different values of electrification parameter.

Furthermore, the effect of  $M$  on  $-\theta'(0)$  and  $-s'(0)$  for varied values of  $Nb$  is depicted in Figs. 9 and 10, respectively. It is found that for various values of the Brownian motion parameter, both  $-\theta'(0)$  and  $-s'(0)$  improve as  $M$  grows. This is because as  $M$  grows, the values of  $\theta(\eta)$  and  $s(\eta)$  near the flat surface both drops.

Table 2. Combined effects of  $N_{Re}$  and  $M$  on  $-\theta'(0)$  and  $-s'(0)$  when  $Sc = 2.0, Pr = 6.2, Nr = Nc = Nb = Nt = N_F = 0.1$ .

$M$	$N_{Re}$	$-\theta'(0)$	$-s'(0)$
0.1	0.5	0.37543	0.07865
	1.0	0.36667	0.11995
	1.5	0.36378	0.13370
	2.0	0.36235	0.14057
	2.5	0.36148	0.14469
0.2	0.5	0.41083	0.10685
	1.0	0.40229	0.14506
	1.5	0.39948	0.15774
	2.0	0.39808	0.16407
	2.5	0.39725	0.16786
0.3	0.5	0.43878	0.12520
	1.0	0.43040	0.16132
	1.5	0.42764	0.17330
	2.0	0.42627	0.17926
	2.5	0.42545	0.18284

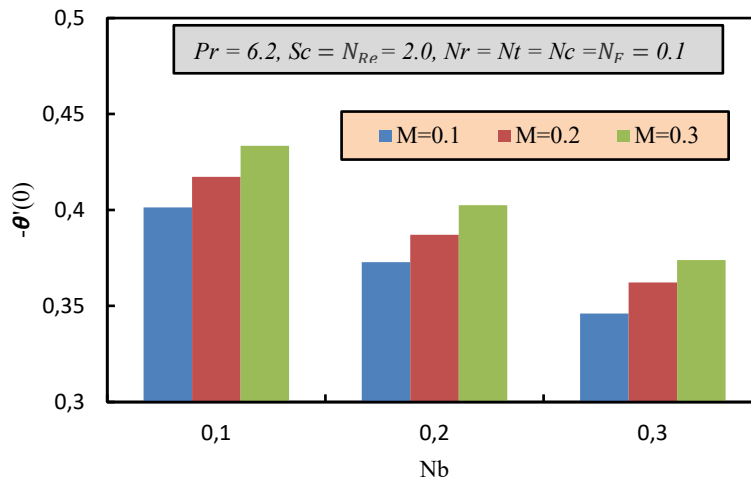


Figure 9. Effects of  $M$  on  $-\theta'(0)$  for varied values of  $Nb$ .

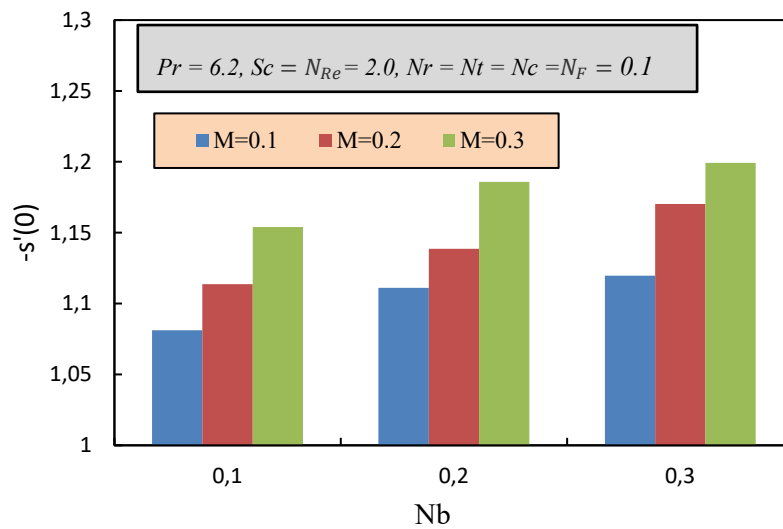


Figure 10. Effects of  $M$  on  $-s'(0)$  for varied values of  $Nb$ .

### 5. CONCLUSIONS

The heat and mass transfer aspects of natural convective nanofluid flow involves examining the impact of  $M$  and  $N_{Re}$  on  $f'(\eta)$ ,  $\theta(\eta)$ ,  $s(\eta)$ ,  $-\theta'(0)$  and  $-s'(0)$ . The numerical investigation focuses on studying the variations of  $-\theta'(0)$  and  $-s'(0)$  concerning the values of  $M$  and  $N_{Re}$ , with the results presented in graphical and tabular forms. The analysis of these findings yields the following conclusions:

- As the electrification parameter  $M$  increases, there is an increase in the non-dimensional velocity, accompanied by a reduction in the dimensionless concentration and temperature within the boundary layer region.
- As the electric Reynolds number  $N_{Re}$  rises, the non-dimensional velocity and temperature experiences a growth, while the dimensionless concentration experiences dual nature within the boundary layer region.
- As the dimensionless heat transfer rate rises from a flat wall to a nanofluid, there's a consequent increase in  $M$ , prompting heat conduction into the cooler fluid and subsequently cooling the flat surface.
- An increase in the values of  $M$  results in a boost in the dimensionless mass transfer rate from a flat surface to a nanofluid, consequently bolstering drug delivery efficacy in biomedical uses.
- The dimensionless heat transfer coefficient decreases as the electric Reynolds number increases.
- The dimensionless mass transfer coefficient enhances as the values of  $N_{Re}$  increase.

Furthermore, alongside thermophoresis and Brownian motion, as proposed by Buongiorno, the inclusion of electrified nanoparticles emerges as a pivotal element in the modelling of nanofluid flow. This aspect notably enhances both heat and mass transfer mechanisms.

### ORCID

## REFERENCES

- [1] S.U.S. Choi, Z.G. Zhang, W. Yu, F.E. Lockwood, and E.A. Grulke, "Anomalous thermal conductivity enhancement in nanotube suspensions," *Applied Physics Letters*, **79**, 2252-2254 (2001). <https://doi.org/10.1063/1.1408272>
- [2] J. Buongiorno, "Convective transport in nanofluids," *ASME J. Heat Transf.* **128**, 240-250 (2006). <https://doi.org/10.1115/1.2150834>
- [3] A.V. Kuznetsov, and D.A. Nield, "Natural convective boundary-layer flow of a nanofluid past a vertical plate," *Int. J. Thermal Sci.* **49**, 243-247 (2010). <https://doi.org/10.1016/j.ijthermalsci.2009.07.015>
- [4] W.A. Khan, and A. Aziz, "Natural convection flow of a nanofluid over a vertical plate with uniform surface heat flux," *Int. J. Therm. Sci.* **50**, 1207-1214 (2011). <https://doi.org/10.1016/j.ijthermalsci.2011.02.015>
- [5] A. Aziz, and W.A. Khan, "Natural convective boundary layer flow of a nanofluid past a convectively heated vertical plate," *International Journal of Thermal Sciences*, **52**, 83-90 (2012). <https://doi.org/10.1016/j.ijthermalsci.2011.10.001>
- [6] S. Das, and R.N. Jana, "Natural convective magneto-nanofluid flow and radiative heat transfer past a moving vertical plate," *Alexandria Engineering Journal*, **54**, 55-64 (2015). <https://doi.org/10.1016/j.aej.2015.01.001>
- [7] M. Goyal, and R. Bhargava, "Simulation of natural convective boundary layer flow of a nanofluid past a convectively heated inclined plate in the presence of magnetic field," *Int. J. Appl. Comput. Math.* **4**, 63 (2018). <https://doi.org/10.1007/s40819-018-0483-0>
- [8] S.P. Jeevandar, V. Kedla, N. Gullapalli, and S.K. Thavada, "Natural Convective Effects on MHD Boundary Layer Nanofluid Flow over an Exponentially Accelerating Vertical Plate," *Biointerface Research in Applied Chemistry*, **11**(6), 13790-13805 (2021). <https://doi.org/10.33263/BRIAC116.1379013805>
- [9] Y.D. Reddy, and B.S. Goud, "Comprehensive analysis of thermal radiation impact on an unsteady MHD nanofluid flow across an infinite vertical flat plate with ramped temperature with heat consumption," *Results in Engineering*, **17**, 100796 (2023). <https://doi.org/10.1016/j.rineng.2022.100796>
- [10] S. Dey, S. Mukhopadhyay, and K. Vajravelu, "Nonlinear natural convective nanofluid flow past a vertical plate," *Numerical Heat Transfer, Part A: Applications*, 1-23 (2024). <https://doi.org/10.1080/10407782.2024.2302966>
- [11] S.L. Soo, "Effect of electrification on the dynamics of a particulate system," *Industrial and Engineering Chemistry Fundamentals* **3**, 75-80 (1964). <https://doi.org/10.1021/i160009a013>
- [12] Z. Kang, and L. Wang, "Effect of thermal-electric cross coupling on heat transport in nanofluids," *Energies*, **10**(1), 1-13 (2017). <https://doi.org/10.3390/en10010123>
- [13] A.K. Pati, A. Misra, and S.K. Mishra, "Effect of electrification of nanoparticles on heat and mass transfer in boundary layer flow of a copper water nanofluid over a stretching cylinder with viscous dissipation," *JP journal of heat and mass transfer*, **17**(1), 97-117 (2019). <http://dx.doi.org/10.17654/HM017010097>
- [14] M. Mahrukh, A. Kumar, S. Gu, S. Kamnis, and E. Gozali, "Modeling the Effects of Concentration of Solid Nanoparticles in Liquid Feedstock Injection on High-Velocity Suspension Flame Spray Process," *Ind. Eng. Chem. Res.* **55**, 2556-2573 (2016). <https://doi.org/10.1021/acs.iecr.5b03956>
- [15] H.F. Oztop, and E. Abu-Nada, "Numerical study of natural convection in partially heated rectangular enclosures filled with nanofluids," *International Journal of Heat Fluid Flow*, **29**, 1326-1336 (2008). <https://doi.org/10.1016/j.ijheatfluidflow.2008.04.009>
- [16] M.H. Habibi, and P. Jahangiri, "Forced convection boundary layer magnetohydrodynamic flow of nanofluid over a permeable stretching plate with viscous dissipation," *Thermal Science*, **18**(Suppl. 2), 587-598 (2014). <https://doi.org/10.2298/TSCI120403049H>

**АСПЕКТИ ПЕРЕНЕСЕННЯ ТЕПЛА ТА МАСИ ПОТОКОМ НАНОФЛЮІДІВ ДО ВЕРТИКАЛЬНОЇ ПЛОСКОЇ ПОВЕРХНІ ПІД ВПЛИВОМ ЕЛЕКТРИФІКОВАНИХ НАНОЧАСТИНОК ТА ЕЛЕКТРИЧНОГО ЧИСЛА РЕЙНОЛЬДСА**

**Адітя Кумар Паті, Суджит Мішра, Ашок Місра, Сародж Кумар Мішра**

*Університет технології та менеджменту Центуріон, Паралахемунді, Одіша, Індія*

У цьому дослідженні розглядаються аспекти тепло- та масообміну природного конвективного потоку нанофлюїду вздовж вертикальної плоскої поверхні, що включає електрифіковані наночастинки та електричне число Рейнольдса. У той час як звичайні моделі нанофлюїдів, такі як модель Буонджорно, не помічають механізми електризації наночастинок і електричних чисел Рейнольдса, це дослідження розглядає механізми електризації наночастинок і електричних чисел Рейнольдса, обґрунтовуючи їх актуальність, особливо коли трибоелектризація є результатом броунівського руху. Таке включення електричного числа Рейнольдса та механізму електризації наночастинок є унікальним аспектом цього дослідження. Використовуючи метод подібності та безрозмірність, керівні диференціальні рівняння в частинних похідних потоку перетворюються на набір локально подібних рівнянь. Розв'язувач `bvp4c` MATLAB використовується для вирішення цього набору рівнянь разом із граничними умовами. Отримані результати підтверджуються порівнянням з результатами раніше опублікованих робіт. Наведено графічні представлення числових результатів безвимірної швидкості, концентрації та температури щодо параметра електризації наночастинок та електричного числа Рейнольдса. У табличній формі розглянуто сукупний вплив параметра електризації наночастинок та електричного числа Рейнольдса на безрозмірні коефіцієнти тепло- та масовіддачі. Крім того, графічно досліджено вплив параметра електризації наночастинок як на тепло-, так і на масообмін для різних значень параметра броунівського руху. Основний висновок цього дослідження вказує на те, що механізм електризації наночастинок прискорює передачу тепла та маси від плоскої поверхні до нанорідини, що передбачає багатообіцяючі перспективи використання в системах охолодження та біомедичних додатках.

**Ключові слова:** *наелектризовані наночастинки; нанофлюїд; модель Буонджорно; електричне число Рейнольдса; природна конвекція*

## MHD FLOW PAST A STRETCHING POROUS SURFACE UNDER THE ACTION OF INTERNAL HEAT SOURCE, MASS TRANSFER, VISCOUS AND JOULES DISSIPATION

Sourave Jyoti Borborah<sup>a\*</sup>, Shyamanta Chakraborty<sup>bS</sup>

<sup>a</sup>Department of Mathematics, Gauhati University, Guwahati, Assam, India

<sup>b</sup>UGC-HRDC, Gauhati University, Guwahati, Assam, India

\*Corresponding Author e-mail: [souravborborah725@gmail.com](mailto:souravborborah725@gmail.com)

Received April 10, 2024; revised May 13, 2024; accepted May 16, 2024

The paper investigates two-dimensional, steady, nonlinear laminar boundary layer heat and mass transfer MHD flow past a stretching porous surface embedded in a porous medium under the action of internal heat generation with the consideration of viscous and joules heat dissipation in the presence of a transverse magnetic field. The two-dimensional governing equations are solved by using MATLAB built in bvp4c solver technique for different values of physical parameters. The numerical values of various flow parameters such as velocity, temperature, concentration are calculated numerically and analysed graphically for various values of the non-dimensional physical parameters of the problem followed by conclusions. The study concludes opposite behaviour of transverse and longitudinal velocity under the action of suction velocity in addition to the effects of heat source on fluid velocities, temperature and concentration.

**Keywords:** MHD-flow; Porous-surface; Internal heat-source; Mass-transfer; Viscous and Joules Dissipation

**PACS:** 47.85. -g, 47.56. +r

### INTRODUCTION

Since last few years the two-dimensional boundary layer flow, heat and mass transfer over a porous stretching surface under various geometrical situations with heat generation has been a great attention because of its practical applications in the fields of science-technology and industry; for instance, in petroleum industry, polymer technology, power generation, crude oil processing, aerodynamic heating and many others. In the field of nuclear technology MHD convection flow is employed to study the magnetic behaviour of plasmas in fusion reactors, liquid metal cooling of nuclear reactors, electro-magnetic casting etc. It may be pointed out that many metallurgical processes involve the colling of continuous strips by drawing them through a quiescent fluid where in the process of drawing these strips are many times strips are stretched. On the other hand, by playing a role like an energy source the viscous dissipation changes the temperature distributions that in turn lead to affect heat transfer rates as well. The merit of the effect of viscous dissipation depends on whether the plate is being cooled or heated. Moreover, in MHD flows, the joules dissipation acts as a volumetric heat source. Due to abundant applications the heat transfer over a porous surface is a much practical interest of research today. The heat generated from the combustion process is used to convert fluid into high-pressure steam that can drive turbines connected to a generator converting thermal energy into electrical energy. To be more specific instances, heat treated materials travelling between a feed roll and wind-up roll or materials manufactured by extrusion, glass-fiber and paper production, colling of metallic sheets or electronic chips, crystal growing are few to be added. In these cases, the final product of desired characteristics depends on the rate of colling in the process of stretching. MHD flow of variable physical parameters has been investigated to a large extent by many researchers because of its numerous applications in the field of science, technology, industry, in case of extraction of geo-thermal energy, and in many such situations.

In 1977, T.C. Chaim [1] have discussed about magnetohydrodynamic heat transfer over a non-isothermal stretching sheet. In 1979, A. Chakrabarti et al. [2] studied about the hydromagnetic flow and heat transfer over a stretching sheet. About heat transfer in a viscous fluid over a stretching sheet with viscous dissipation and internal heat generation is discussed by K. Vajravelu et al. [3]. The problem of viscous dissipation, joule heating and heat source/sink on non-Darcy MHD natural convection flow over an isoflux permeable sphere in a porous medium is numerically analyzed by K.A. Yih [4]. B. Ganga et al. [5] investigated about the non-linear hydrodynamic flow and heat transfer due to a stretching porous surface with prescribed heat flux and viscous dissipation effects. Viscous dissipation effects on MHD natural convection flow over a sphere in the presence of heat generation are discussed by Md. M. Alam et al. [6]. Saxena and Dubey [7] studied about unsteady MHD heat and mass transfer free convection flow of polar fluids past a vertical moving porous plate in a porous medium with heat generation and thermal diffusion. Chen [8] discussed about Combined heat and mass transfer in MHD free convection from a vertical surface with ohmic heating and viscous dissipation. Effects of viscous and joules dissipation on MHD flow, heat and mass transfer past a stretching porous surface embedded in a porous medium is analyzed by Devi et al. [9]. Abel et al. [10] discussed about viscoelastic MHD flow and heat transfer over a stretching sheet with viscous and ohmic dissipations. Sajid et al. [11] studied about non-similar analytic solution for MHD flow and heat transfer in a third-order fluid over a stretching sheet. Study of MHD boundary layer flow over a heated stretching sheet with variable viscosity: a numerical reinvestigation was investigated by Pantokratoras [12]. Sonth et al. [13]



discussed about heat and mass transfer in a visco-elastic fluid over an accelerating surface with heat source/sink and viscous dissipation. Eldahab et al. [14] discussed about viscous dissipation and joule heating effects on MHD free convection from a vertical plate with power-law variation in surface temperature in the presence of Hall and ion-slip currents. Flow and heat transfer due to a stretching porous surface in presence of transverse magnetic field was discussed by Tak et al. [15].

In recent times, Goswami et al. [16] discussed about the Unsteady MHD free convection flow between two heated vertical parallel plates in the presence of a uniform magnetic field. Khan et al. [17] studied on magnetohydrodynamics Prandtl fluid flow in the presence of stratification and heat generation. Induced magnetic field effect on MHD free convection flow in nonconducting and conducting vertical microchannel was discussed by Goud et al. [18]. Waqas et al. [19] studied about thermo-solutal robin conditions significance in thermally radiative nanofluid under stratification and magneto hydrodynamics. Effect of chemical reaction and joule heating on MHD generalized Couette flow between two parallel vertical porous plates with induced magnetic field and Newtonian heating/cooling was discussed by J. Ming' ang' a [20]. Influence of MHD mixed convection flow for Maxwell nanofluid through a vertical cone with porous material in the existence of variable heat conductivity and diffusion was studied by Kodi et al. [21]. Kodi et al. [22] studied about radiation absorption on MHD free conduction flow through porous medium over an unbounded vertical plate with heat source.

Motivating with the above works, we have tried to investigate the effect of viscous and joules dissipation on a fully developed MHD flow where heat and mass transfer past a stretching porous surface embedded in a porous medium under the influence of heat generation due to an internal heat source in presence of transverse magnetic field. The two-dimensional governing equations are solved by using MATLAB built in bvp4c solver technique for different values of physical quantities influencing the physics. The numerical values of various flow parameters such as velocity, temperature, concentration are calculated numerically and analysed graphically for various values of the non-dimensional physical parameters of the problem. The study concludes opposite behaviour of transverse and longitudinal velocity under the action of suction velocity in addition to the effects of heat source on fluid velocities, temperature and concentration.

### MATHEMATICAL ANALYSIS

We have considered two-dimensional, steady, nonlinear MHD laminar boundary layer flow with heat and mass transfer of a incompressible, viscous and electrically conducting fluid over a porous surface embedded in a porous medium under the action of internal heat source in the presence of a transverse magnetic field applied parallel to y-axis of strength  $B_0$ . The situation is similar to the case of a polymer sheet emerging out of a slit and subsequently being stretched at  $x = 0, y = 0$  that often happens in the process of extrusion of polymer, rayon etc. The speed of the flow at a point on the sheet is assumed to be proportional to some positive power of its distance ( $x$ ) from the slit while the boundary layer approximations are applicable. It is considered that the flow has viscous and Joule heat dissipation whereas the induced magnetic field, the electrical field due to polarization of charges and the external electrical field are negligible. Considering these conditions, the governing boundary layer equations of equation of continuity, momentum, energy, diffusion with viscous and joules dissipation are

$$u \frac{\partial u}{\partial x} + v \frac{\partial v}{\partial y} = 0 \quad (1)$$

$$u \frac{\partial u}{\partial x} + v \frac{\partial u}{\partial y} = \nu \frac{\partial^2 u}{\partial y^2} - \frac{\sigma B_0^2 u}{\rho} - \frac{\nu}{K_p} u \quad (2)$$

$$u \frac{\partial T}{\partial x} + v \frac{\partial T}{\partial y} = \frac{K}{\rho C_p} \frac{\partial^2 T}{\partial y^2} + \frac{\nu}{C_p} \left( \frac{\partial u}{\partial y} \right)^2 + \left( \frac{\sigma B_0^2}{\rho C_p} \right) u^2 + \frac{S^*(T-T_\infty)}{\rho C_p} \quad (3)$$

$$u \frac{\partial C}{\partial x} + v \frac{\partial C}{\partial y} = D \frac{\partial^2 C}{\partial y^2} \quad (4)$$

The boundary conditions are

$$\left. \begin{aligned} u &= ax^m, \quad v = v_w(x), \quad T = T_w(x) = T_\infty + T_0 x^n \\ C &= C_w(x) = C_\infty + C_0 x^n \quad \text{at } y = 0 \\ u &= 0, \quad T = T_\infty, \quad C = C_\infty \quad \text{at } y \rightarrow \infty \end{aligned} \right\} \quad (5)$$

Here,  $u$  and  $v$  are the velocity components along  $x$  and  $y$  respectively.  $K_p$  is the permeability of the medium,  $\sigma$  is the electrical conductivity of the fluid,  $\rho$  is the density of the fluid,  $B_0$  is the applied magnetic field,  $T$  is the temperature of the fluid,  $S^*$  is the coefficient of heat source,  $K$  is thermal conductivity,  $T_w$  is wall temperature,  $T_\infty$  is the temperature far away from the surface,  $C_p$  is specific heat at constant pressure,  $C$  is the species concentration of the fluid,  $C_w$  is species concentration of the fluid near the wall,  $C_\infty$  is species concentration of the fluid away from the wall,  $D$  is the diffusivity coefficient;  $a, T_0, C_0$  are dimensional constants,  $m$  is index of power-law velocity and  $n$  is index of power-law variation of wall temperature which is constant.

Following [15], we introduce the stream function

$$\left. \begin{aligned} \Psi(x, y) &= \left[ \frac{2vxU(x)}{1+m} \right]^{\frac{1}{2}} F(\eta), \\ \text{where, } \eta &= \left[ \frac{(1+m)U(x)}{2vx} \right]^{\frac{1}{2}} y, \\ v_w(x) &= -\lambda \sqrt{\frac{va(m+1)}{2}} x^{\frac{(m-1)}{2}}, \text{ where } \lambda > 0 \text{ for suction at the stretching plate.} \\ n &= 2m, \end{aligned} \right\} \quad (6)$$

the velocity components are

$$u = \frac{\partial \Psi}{\partial y}, \quad v = -\frac{\partial \Psi}{\partial x}. \quad (7)$$

The equation of continuity is satisfied by the above conditions and introduce the non-dimensional form of temperature and the concentration is given bellow as

$$\theta = \frac{T-T_\infty}{T_w-T_\infty}, \quad h = \frac{c-c_\infty}{c_w-c_\infty}. \quad (8)$$

For the feasibility of the analytic solutions of the problem, we take the value  $\beta = 1$ , i.e.  $m=1$  that makes velocity of the stretching plate as  $ax$ ,  $a$  being a positive constant; this means the plate stretches with a velocity varying linearly with distance. Using equations 6,7 & 8, equations 2, 3 & 4 are reducing to a nonlinear system of equations given as

$$F''' + FF'' - F'^2 - (M^2 + R_1^{-1})F' = 0 \quad (9)$$

$$\theta'' + PrF\theta' - 2PrF'\theta = -EcPr[F''^2 + M^2F'^2] + SPrReB \quad (10)$$

$$h'' + ScFh' - 2SchF' = 0 \quad (11)$$

The corresponding Boundary conditions are now

$$\left. \begin{aligned} F(0) &= \lambda, \quad F'(0) = 1, \quad F'(\infty) = 0, \\ \theta(0) &= 1, \quad \theta(\infty) = 0, \\ h(0) &= 1, \quad h(\infty) = 0. \end{aligned} \right\} \quad (12)$$

where,  $V_0$  is a scale of suction velocity,  $B$  is a dimensionless velocity ratio.

### METHOD OF SOLUTION

The couple of non-linear differential equations (9), (10) & (11) with respect to the boundary conditions (12) are solved by using MATLAB inbuilt function 'bvp4c' for different values of physical parameters. In this method we convert the non-linear differential equations into a set of first order differential equations for which we have considered the followings.

$$F = y(1), F' = y(1)' = y(2), F'' = y(2)' = y(3),$$

$$\theta = y(4), \theta' = y(5),$$

$$h = y(6), h' = y(7).$$

The transformed first order differential equations are

$$y(3)' = -Y(1) * y(3) + y(2) * y(2) + (M^2 + R_1^{-1}) * y(2)$$

$$y(5)' = -Pr * y(1) * y(5) * +2 * Pr * y(2) * y(4) - Ec * Pr * [y(3)^2 + M^2 * (y(2))^2] + S * Pr * Re * B,$$

$$y(7)' = -Sc * y(1) * y(7) + 2 * Sc * y(6) * y(2),$$

The boundary conditions are reduced to

$$y0(1) - \lambda; y0(2) - 1; y0(4) - 1; y0(6) - 1; y1(2) - 0; y1(4) - 0; y1(6) - 0.$$

### RESULTS AND DISCUSSIONS

The numerical calculations have been carried out for different values of heat source parameter ( $S$ ), magnetic parameter ( $M^2$ ), suction velocity parameter ( $\lambda$ ), Eckert number ( $Ec$ ), Prandtl number ( $Pr$ ) and Schmidth number ( $Sc$ ). We assume  $B = 1$ ; so that the problem has a physical point of view.

In Fig. 1&2, the dimensionless transverse and longitudinal velocity profiles for different values of magnetic parameter with constant values of heat source parameter, suction parameter, Eckert number, Prandtl number, Schmidth number and permeability parameter are shown. It is clear from Fig.1 that the transverse velocity rises sharply near the plate for a smaller



distance from the plate ( $\eta \cong 1.5$ ) thereafter, becomes uniform away from the plate for all values of magnetic field. The trend is quite opposite in case of longitudinal velocity Fig.2 where it decreases sharply initially then becomes almost uniform or unchanged away from the plate. However, both transverse and longitudinal velocity decreases for increases of magnetic field parameter  $M^2$ , this is because of the fact that the magnetic field exerts a restraining force on the fluid flow.

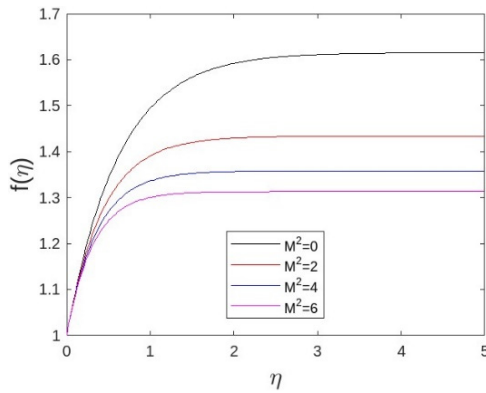


**Figure 1.** Non-dimensional transverse velocity Profiles for different values of  $M^2$ , at  $\lambda = 2, R_1 = 100, Pr = 0.71, Ec = 0.2, S = 2.0$

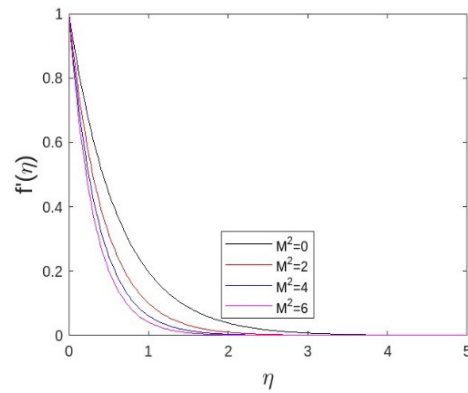


**Figure 2.** Non-dimensional longitudinal velocity Profiles for different values of  $M^2$ , at  $\lambda = 2, R_1 = 100, Pr = 0.71, Ec = 0.2, S = 2.0$

The effect of suction parameter over the non-dimensional transverse and longitudinal velocity profiles are shown in the Figs. 3&4 for different values of suction velocity parameter ( $\lambda$ ). It is seen that near the plate ( $\eta \cong 0.0$  to  $1.0$ ) the transverse velocity rises sharply, thereafter, almost uniform away from the plate ( $\eta \geq 1.0$ ). Longitudinal velocity has exponential decrease near the plate ( $\eta \cong 0.0$  to  $2.0$ ) and thereafter gradually becomes ineffective. These nature of variation of both transverse and longitudinal velocity are same for all the values of suction velocity parameter ( $\lambda$ ). For higher value of  $\lambda$ . Magnitude of transverse velocity is higher while opposite for longitudinal velocity.

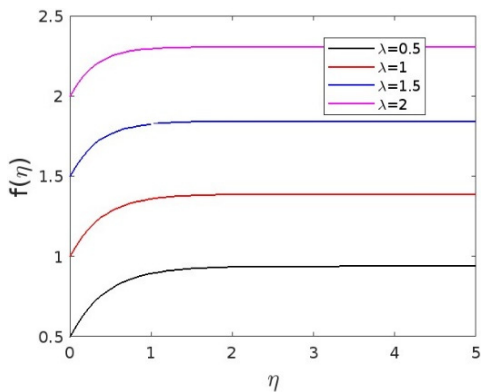


**Figure 3.** Non-dimensional transverse velocity profile for different values of  $\lambda$ , at  $M^2 = 3, R_1 = 100, Pr = 0.71, Ec = 0.2, S = 2.0$ .

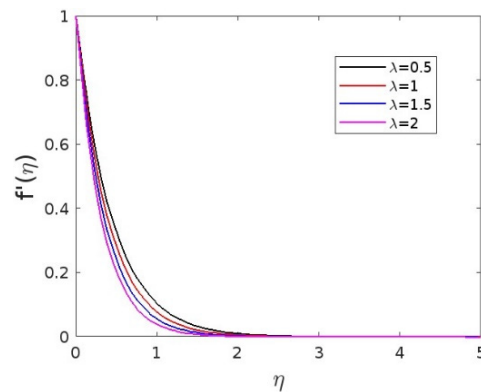


**Figure 4.** Non-dimensional longitudinal velocity profile for different values of  $\lambda$ , for  $M^2 = 3.0, R_1 = 100, Pr = 0.71, Ec = 0.2, S = 2.0$

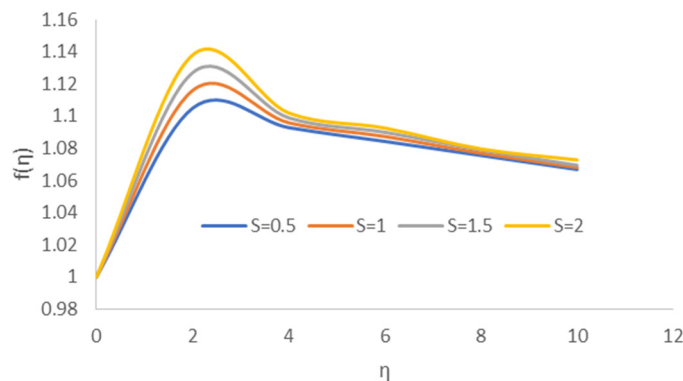


**Figure 5.** Non-dimensional transverse velocity profile for different values of  $S$ , for  $M^2 = 3, R_1 = 100, Pr = 0.71, Ec = 0.2, \lambda = 1, Re = 4$ .

In Fig.5, transverse velocity profile is shown for various values of heat source parameter  $S \cong 0.5$  to  $2.0$ . Transverse velocity increases sharply within the range ( $\eta \cong 0.0$  to  $2.0$ ), thereafter, decreases gradually for  $\eta \geq 2.3$ . The magnitude of transverse velocity is higher for higher values of heat source parameter ( $S$ ).

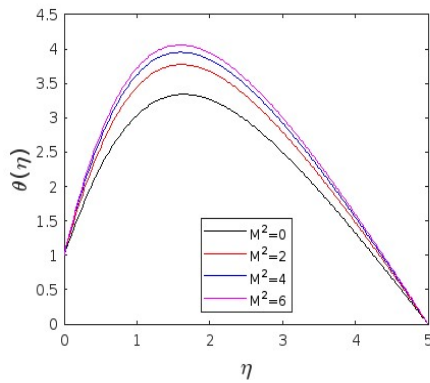


**Figure 6.** Temperature profile for different values of  $M^2$ , at  $\lambda = 1, R_1 = 100, Pr = 0.71, Ec = 0.2, S = 2, Re = 4.0$

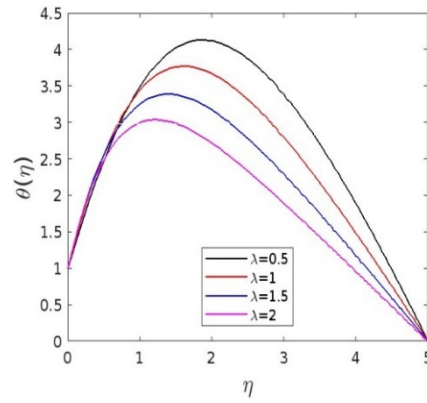


**Figure 7.** Temperature profile for different  $\lambda$ , for  $M^2 = 2, R_1 = 100, Ec = 0.2, \lambda = 1, Re = 4.0$

The effects of magnetic field parameter and suction velocity parameter over the temperature are shown in the Fig. 6 & 7 respectively. In fig.6, temperature sharply to a certain point ( $\eta \cong 1.5$ ), thereafter, decreases gradually away from the plate. This nature of variation is same for all the values of magnetic field parameter  $M$ . temperature has the peak value at ( $\eta \cong 1.5$ ). In fig.7, the rise of suction velocity ( $\lambda$ ) has very less impact on temperature near the plate ( $\eta \cong 1.0$ ) within which it increases sharply, thereafter, decreases gradually away from the plate  $\eta \geq 1.0$ . An increase in suction velocity parameter  $\lambda$  causes decrease in temperature distribution.

In Fig. 8, the effect of  $Pr$  on temperature profile is shown; temperature experienced some increases subject to rise of  $Pr$ . An increase in  $Ec$  small enhancement in the profile of temperature as observed in Fig. 9, this may be due to the frictional heating the heat energy is stored in the liquid. The effect of  $Ec$  is distinct near the plate  $\eta \leq 2.0$ .

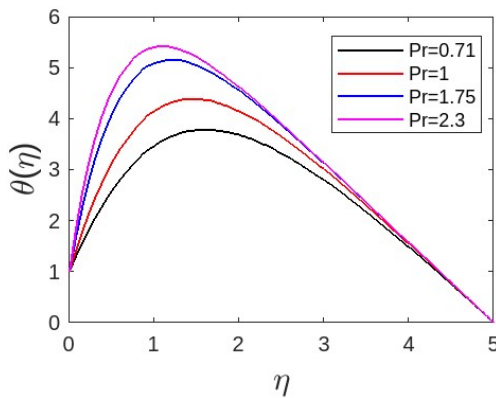


**Figure 8.** Temperature profile for different values of  $Pr$ , at  $M^2 = 2, R_1 = 100, Ec = 0.2, \lambda = 1, Re = 4.0$

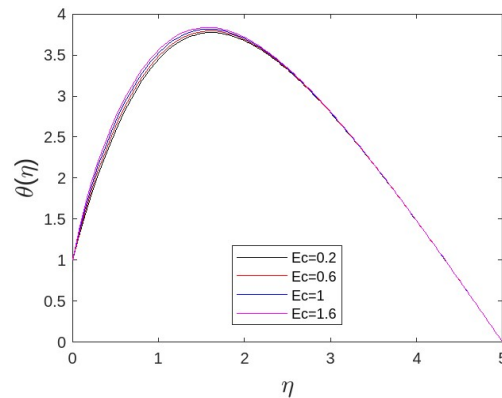


**Figure 9.** Temperature profile for different  $Ec$ , at  $M^2 = 2, R_1 = 100, \lambda = 1, Re = 4, Pr = 0.71$ .

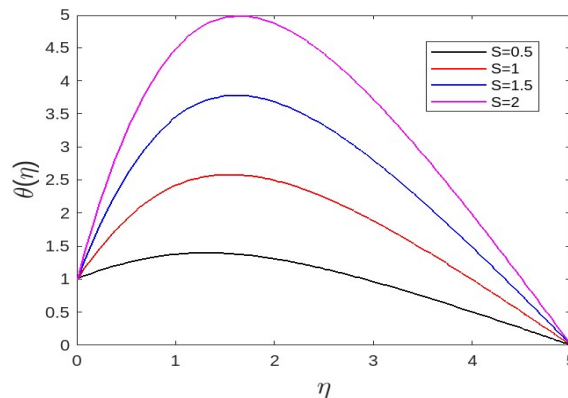


**Figure 10.** Temperature profile for different values of  $S$ , for  $M^2 = 2, R_1 = 100, Pr = 0.71, Ec = 0.2, \lambda = 1, Re = 4$ .

In Fig. 10, The temperature profile is shown for various values of heat source parameter  $S$ , it is seen that the temperature has clear increase as heat source parameter enhances. In Fig. 11-14, Fluid concentration  $h(\eta)$  is shown for values of physical parameters  $M, \lambda, Sc$  &  $S$ . Fluid concentration  $h(\eta)$  decreases exponentially from the plate away from

it. Higher the magnetic field,  $h(\eta)$  is higher. This is in contrary to the variation of  $h(\eta)$  with suction velocity  $\lambda$ . Fluid concentration decreases with the increases of  $\lambda$ , Fig. 12. When the Schmidt number  $Sc$  is increased,  $h(\eta)$  decreases, Fig. 13. Distribution of fluid concentration for different values of heat source parameter  $S$  is shown in fig.14; although in the plot  $h(\eta)$  is seen to be unchanged with the variation of  $S$ , but when we observe their numerical values, then it may be concluded the  $h(\eta)$  is higher for higher values of  $S$ , e.g. at  $\eta=4$ ; for  $S=1.0$ ,  $h(\eta=4) \cong 0.91693$  while at  $S=2$ ,  $h(\eta=4) \cong 0.91776$ ; thus fluid concentration increases with the rise of heat source parameter.

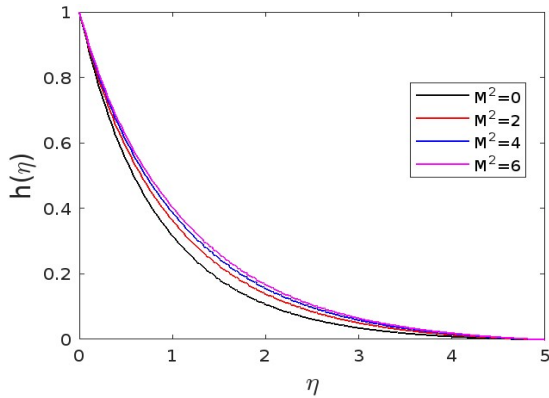


Figure 11, Dimensionless concentration distribution for different  $M^2$  at  $R_1 = 100, Sc = 0.62, \lambda = 1$ .

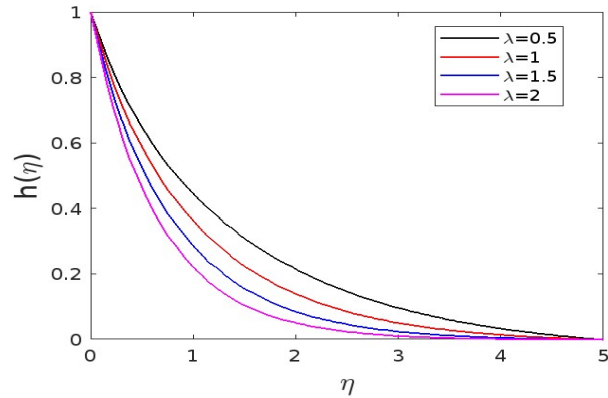


Figure 12, Dimensionless concentration distribution for different  $\lambda$  at for  $M^2 = 2, R_1 = 100, Sc = 0.62$

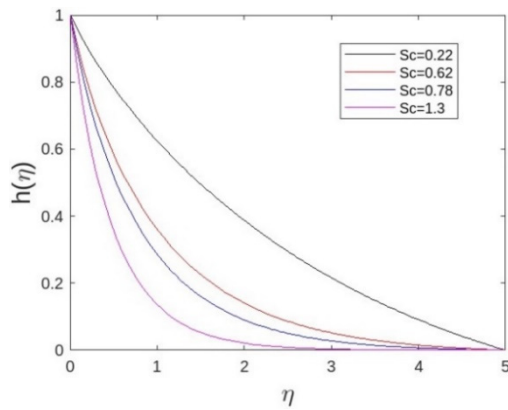


Figure 13, Dimensionless concentration distribution for different values of  $Sc$ , at  $M^2 = 2, R_1 = 100, \lambda = 1.0$

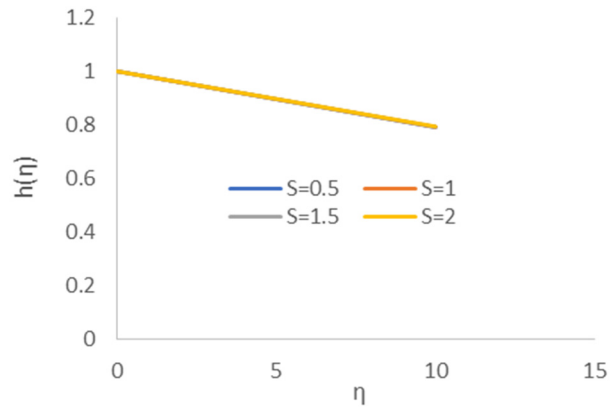


Figure 14, Dimensionless concentration distribution for different values of  $S$ , at  $M^2 = 2, R_1 = 100, \lambda = 1, Sc = 0.62$ .

CONCLUSIONS

From the above results and discussions following conclusions can be made in brief.

- With the rise of suction velocity, transverse velocity increases whereas longitudinal velocity, temperature and concentration decreases.
- With the rise of magnetic field both transverse and longitudinal velocity decreases, whereas fluid temperature and fluid concentration decreases.
- The effect of heat source is that it increases that the fluid velocity transverse and longitudinal, temperature and concentration.
- Temperature distribution has increase with the rise of Prandtl number and also Eckert number
- Rise of Schmidt number reduces the fluid concentration

Appendices

$Pr = \frac{\mu C_p}{K}$  is Prandtl number  
 $R_1 = \frac{K_p a}{v}$  is permeability parameter  
 $M^2 = v \frac{2\sigma B_0^2}{\rho a(1+m)}$  is magnetic parameter  
 $\beta = \frac{2m}{m+1}$ , is stretching parameter  
 $Re = \frac{V_0 L}{v}$ , is Reynold number

$Sc = \frac{\nu}{D}$  is Schmidt number  
 $E_c = \frac{a^2}{C_p T_0}$  is Eckert number  
 $\nu = \frac{\mu}{\rho}$  is kinematic viscosity  
 $S = \frac{S^* v}{\rho C_p V_0^2}$ , is the heat source parameter

ORCID

## REFERENCES

- [1] T.C. Chaim, "Magnetohydrodynamic heat transfer over a non-isothermal stretching sheet," *Acta Mech.* **122**, 169-179 (1977). <https://doi.org/10.1007/BF01181997>
- [2] A. Chakrabarty, and A.S. Gupta, "Hydromagnetic flow and heat transfer over a stretching sheet," *Q. Appl. Math.* **37**, 73-78 (1979).
- [3] K. Vajravelu, and A. Hadjinicolaou, "Heat Transfer in a viscous fluid over a stretching sheet with viscous dissipation and internal heat generation," *Int. Commun. Heat Mass*, **20**, 417-430 (1993). [https://doi.org/10.1016/0735-1933\(93\)90026-R](https://doi.org/10.1016/0735-1933(93)90026-R)
- [4] K.A. Yih, "Viscous and Joule heating effects on non-Darcy MHD natural convection flow over a permeable sphere in porous media with internal heat generation," *Int. Commun. Heat Mass*, **27**(4), 591-600 (2000). [https://doi.org/10.1016/S0735-1933\(00\)00141-X](https://doi.org/10.1016/S0735-1933(00)00141-X)
- [5] B. Ganga, S.P. Anjali Devi, and M. Kayalvizhi, "Nonlinear hydromagnetic flow and heat transfer due to a stretching porous surface with prescribed heat flux and viscous dissipation effects", *Proceedings of the National Conference on applications of Partial Differential Equations*, 107-117 (2007).
- [6] Md.M. Alam, M.A. Alim, and Md.M. K. Chowdhury, "Viscous dissipation effects on MHD natural convection flow over a sphere in the presence of heat generation," *Nonlinear Anal. Model. Control*, **12**(4), 447-459 (2007).
- [7] S.S. Saxena, and G.K. Dubey, "Unsteady MHD heat and mass transfer free convection flow of polar fluids past a vertical moving porous plate in a porous medium with heat generation and thermal diffusion," *Advances in Applied Science Research*, **2**(4), 259-278 (2011).
- [8] C.H. Chen, "Combined heat and mass transfer in MHD free convection from a vertical surface with ohmic heating and viscous dissipation," *Int. J. Eng. Sci.*, **42**, 699-713 (2004). <https://doi.org/10.1016/j.ijengsci.2003.09.002>
- [9] S.P. Anjali Devi, and B. Ganga, "Effects of Viscous and Joules Dissipation on MHD Flow, Heat and Mass Transfer Past a Stretching Porous Surface Embedded in a Porous Medium," *Nonlinear Analysis: Modelling and control*, **14**(3), 303-314 (2009). <https://doi.org/10.15388/NA.2009.14.3.14497>
- [10] M.S. Abel, E. Sanjayan, and M. Nadeppanvar, "Viscoelastic MHD flow and heat transfer over a stretching sheet with viscous and ohmic dissipations," *Communication in Nonlinear Science and Numerical simulation*, **13**, 1808-1821 (2008). <https://doi.org/10.1016/j.cnsns.2007.04.007>
- [11] M. Sajid, T. Hayat, and S. Asghar, "Non-similar analytic solution for MHD flow and heat transfer in a third-order fluid over a stretching sheet," *Int. J. Heat Mass Tran.*, **50**, 1723-1736 (2007). <http://dx.doi.org/10.1016/j.ijheatmasstransfer.2006.10.011>
- [12] A. Pantokratoras, "Study of MHD boundary layer flow over a heated stretching sheet with variable viscosity: A numerical reinvestigation," *Int. J. Heat Mass Tran.*, **51**, 104-110 (2008). <https://doi.org/10.1016/j.ijheatmasstransfer.2007.04.007>
- [13] R.M. Sonth, S.K. Khan, M.S. Abel, and K.V. Prasad, "Heat and Mass transfer in a visco-elastic fluid over an accelerating surface with heat source/sink and viscous dissipation," *Heat Mass Transfer*, **38**, 213-220 (2002). <https://doi.org/10.1007/s002310100271>
- [14] E.M. Abo-Eldahab, and M.A. El Aziz, "Viscous dissipation and joule heating effects on MHD-free convection from a vertical plate with power-law variation in surface temperature in the presence of Hall and ion-slip currents," *Appl. Math. Model.*, **29**, 579-595 (2005). <https://doi.org/10.1016/j.apm.2004.10.005>
- [15] S.S. Tak, and A. Lodha, "Flow and heat transfer due to a stretching porous surface in presence of transverse magnetic field," *Acta Ciencia Indica*, **XXXIM**(3), 657-663 (2005).
- [16] A. Goswami, M. Goswami and K. G. Singha, "Unsteady MHD free convection flow between two heated vertical parallel plates in the presence of a uniform magnetic field," *International Journal of Scientific Research in Mathematical and Statistical Sciences*, **7**, 86-94 (2020). [https://www.isroset.org/pdf\\_paper\\_view.php?paper\\_id=1837&12-IJSRMSS-03181.pdf](https://www.isroset.org/pdf_paper_view.php?paper_id=1837&12-IJSRMSS-03181.pdf)
- [17] I. Khan, A. Hussain, M. Y. Malik, and S. Mukhtar, "On magnetohydrodynamics Prandtl fluid flow in the presence of stratification and heat generation," *Physica A: Statistical Mechanics and its Applications*, **540**, 123008 (2020). <https://doi.org/10.1016/j.physa.2019.123008>
- [18] B.K. Goud, P.P. Kumer, and B.S. Malga, "Induced magnetic field effect on MHD free convection flow in nonconducting and conducting vertical microchannel," *Heat transfer*, **57**, 2201-2218 (2021). <https://doi.org/10.1002/htj.22396>
- [19] M. Waqas, Z. Asghar, and W.A. Khan, "Thermo-solutal Robin conditions significance in thermally radiative nanofluid under stratification and magneto hydrodynamics," *The European Physical Journal Special Topics*, **230**(5), 1307-1316 (2021). <https://doi.org/10.1140/epjs/s11734-021-00044-w>
- [20] J. Ming'ang'a, "Effect of chemical reaction and joule heating on MHD generalized Couette flow between two parallel vertical porous plates with induced magnetic field and Newtonian heating/cooling," **2023**, 9134811 (2023). <https://doi.org/10.1155/2023/9134811>
- [21] R. Kodi, C. Ganteda, A. Dasore, M.L. Kumar, G. Laxmaiah, M.A. Hasan, S. Islam, and A. Razak, "Influence of MHD mixed convection flow for Maxwell nanofluid through a vertical cone with porous material in the existence of variable heat conductivity and diffusion," *Case Studies in Thermal Engineering*, **44**, 102875 (2023). <https://doi.org/10.1016/j.csite.2023.102875>
- [22] R. Kodi, M. Obulesa, and K.V. Raju, "Radiation absorption on MHD free conduction flow through porous medium over an unbounded vertical plate with heat source," *International Journal of Ambient Energy*, **44**(1), 1712-1720 (2023). <https://doi.org/10.1080/01430750.2023.2181869>

### МГД ПОТІК ПОВЗ ПОРИСТОЇ ПОВЕРХНІ, ЩО РОЗТЯГУЄТЬСЯ, ПІД ДІЄЮ ВНУТРІШНЬОГО ДЖЕРЕЛА ТЕПЛА, МАСОПЕРЕНОСУ, В'ЯЗКОЇ ТА ДЖОУЛЕВОЇ ДИСИПАЦІЇ

Сурав Джіоті Борборрах<sup>а</sup>, Шьяманта Чакраборгі<sup>б</sup>

<sup>а</sup>Факультет математики, Університет Гаухаті, Гувахаті, Ассам, Індія

<sup>б</sup>UGC-HRDC, Університет Гаухаті, Гувахаті, Ассам, Індія

У статті досліджено двовимірний, стаціонарний, нелінійний ламінарний МГД-теплообмін прикордонного шару, повз розтягнуту пористу поверхню, вбудовану в пористе середовище, під дією внутрішнього теплоутворення з урахуванням в'язкої та джоулевої тепловиділення за наявності поперечне магнітне поле. Двовимірні керівні рівняння розв'язуються за допомогою MATLAB, вбудованого в розв'язувач bvp4c, для різних значень фізичних параметрів. Числові значення різних параметрів потоку, таких як швидкість, температура, концентрація, обчислюються чисельно та аналізуються графічно для різних значень безрозмірних фізичних параметрів задачі з подальшими висновками. Дослідження робить висновок про протилежну поведінку поперечної та поздовжньої швидкості під дією швидкості всмоктування на додаток до впливу джерела тепла на швидкість рідини, температуру та концентрацію.

**Ключові слова:** МГД-потік; пориста поверхня; внутрішнє джерело тепла; масообмін; в'язка і джоулева дисипація

## NEW TREND OF AUTOMOBILE ASPECTS ON MHD OF HYBRID NANOFLUID FLOW OVER A POROUS STRETCHING CYLINDER: A NUMERICAL STUDY

 **Gunisetty Ramasekhara<sup>a\*</sup>, Y. Rameswara Reddy<sup>b#</sup>, Sura Sreenivasulu<sup>c</sup>,  Shaik Jakeer<sup>d</sup>,  Seethi Reddy Reddisekhara Reddy<sup>e</sup>,  Sangapatnam Suneetha<sup>f</sup>, T. Aditya Sai Srinivas<sup>g</sup>, Ashok Sarabu<sup>h</sup>**

<sup>a</sup>Department of Mathematics, Rajeev Gandhi Memorial College of Engineering and Technology (Autonomous), Nandyal – 518501, Andhra Pradesh, India

<sup>b</sup>Department of Mechanical Engineering, JNTUACE, Pulivendula – 516390, Andhra Pradesh, India

<sup>c</sup>Department of Chemistry, SVR Engineering College, Ayyaluru Meta, Nandyal – 518501, Andhra Pradesh, India

<sup>d</sup>School of Technology, The Apollo University, Chittoor, Andhra Pradesh 517127, India

<sup>e</sup>Department of Mathematics, Koneru Lakshmaiah Education Foundation, Bowrampet, Hyderabad, Telangana – 500043, India

<sup>f</sup>Department of Applied Mathematics Yogi Vemana University Kadapa – 516003, Andhra Pradesh, India

<sup>g</sup>Department of Computer Science & Engineering, Jaya Prakash Narayan College of Engineering, Mahabubnagar, Telangana, India

<sup>h</sup>Department of Computer Science and Engineering, BVRIT Hyderabad College of Engineering for Women, Hyderabad – 500090, India

\*Corresponding authors email [yrameswarareddy.mech@jntua.ac.in](mailto:yrameswarareddy.mech@jntua.ac.in), [gunisettyrama@gmail.com](mailto:gunisettyrama@gmail.com)

Received February 2, 2024; revised March 20, 2024, accepted March 23, 2024

Heat transfer innovation is essential in modern society because thermal management systems need effective heating and cooling processes. It is also an essential component in the vehicle industry and other types of transportation, in addition to automobile industry, aviation technology, the computer industry, and the manufacturing industry. By the inspiration of importance of magnetohydrodynamic hybrid nanofluid over a stretching cylinder with the influence of Williamson fluid and porous medium is examined in this current study. To convert the PDEs into ODEs, suitable self-similarity transformation is used. After applying transformations, for graphical purpose we have used the bvp5c technique. The impact of active parameters affecting the fluid's capacity to transfer significance is demonstrated in graphs and tables. In the result section we noticed on the velocity outlines decreased for increasing M parameter. The Cf and Nu increased for larger values of the M and curvature parameters. Additional properties of M and Rd parameter inputs result in improved temperature profiles.

**Keywords:** Williamson fluid; MHD; Porous medium; Heat source; Hybrid nanofluids

**PACS:** 44.05.+e, 44.30.+v, 44.40.+a, 47.10.ad.

### 1. INTRODUCTION

Researchers have shown a great deal of interest in tiny fluids due to the fact that they are able to generate a significant amount of heat in a variety of contemporary and industrial applications. Water, gasoline, and automotive oils are examples of basic functioning liquids that have limited warm displays, which limit their employment in innovative chilling appeals. Other examples include heating oil and motor oil. As a case study, tiny fluids are composed of tiny particles such as aluminium oxide, the metal copper, iron oxides, nanotubes made of carbon carbides, and nitric oxide. These small particles enhance the thermal resistance of base fluids. Such tiny fluids possess a wide range of applications in modern systems, including, but not limited to, heating and cooling, hybrid-powered motors, sunlight-based tissues, chemotherapy for cancer, and the development of novel fuels, delivery of medications, and drugs. Choi [1] was the one who made the most significant contribution to the field of nanofluid design, which resulted in changed behaviours. Many studies into the development of tiny fluids have been carried out as a result of the various applications made of nanofluids. Researchers in the fields of applied mathematics and engineering have recently shown a large amount of interest in non-Newtonian fluid mechanics as a result of contemporary advances in technology [2][3][4]. A number of disciplines, including biological sciences, drugs, and chemistry, place a significant amount of significance on the motion and heat transfer characteristics associated with these fluids. Standard approaches cannot correctly explain non-Newtonian liquids' shearing dimension, typical stress variation, and viscoelastic properties due to underlying nonlinear stress-strain rate connections. The complicated dynamics of fluids that are not Newtonian, which includes elastomeric fluids, necessitates the development of accurate forecasting frameworks. These kinds of fluids play an important role in a wide variety of settings [5][6][7].

A mixed nanofluid is an improved version of regular tiny fluids that has enhanced heat transfer, thermophysical properties, and elasticity. In order to achieve the production of a mixed nanofluid, several tiny particles are combined with a base fluid in order to achieve a beneficial interaction that results in increased thermal characteristics. In order to ensure that the heat exchanger's heating and cooling operation was carried out effectively, the performance of a nanofluid hybrid was used. In addition, the application of nanofluid mixtures may be associated with the production of thermal conversion, cooling, technological coolants, and cars. When compared to other nanofluids, hybrid nanofluids are often more difficult to



generate and required for more sophisticated character development procedures in order to comprehend the characteristics of the various nanoparticles as well as how they communicate with one another [8][9][10][11].

Magnetohydrodynamics, often known as MHD, is a branch of study that examines the interaction among magnetic fields and speed forces in liquids that conduct electricity, such as plasma-based solutions, minerals, and metals that are liquid. Hartmann [12] was the first person to suggest the idea of producing regular magnetic forces inside a fluid with electrolytes, which is considered to be the foundation for magnetically induced dissipation (MHD) investigation. In its most basic form, MHD is used to examine the behavior of substances that conduct electricity. For technical and medicinal purposes, MHD liquids have a wide range of uses. MHD barrier layer fluctuations exert a pulling force on liquids that transmit electricity thanks to their magnetic properties. The enforced MHD results in the generation of a drag force, which is known as the Lorentz force, which acts towards the perimeter of the motion. A wide variety of fluid circulation simulations have been seen to include MHD, which has uses in pharmaceutical manufacturing, producing electricity, and other areas. Radiation has a considerable influence on thermal boundaries, particularly in highly heated processes that are used in engineering fields. Because the result is dependent on the pace of the cooling process, the function that heat conduction plays in achieving the intended output is important [13][14].

According to the current literature, the simultaneous effects of MHD, porous medium, Williamson hybrid nanofluid flow over a stretching cylinder has been illustrated and which all are taken into the model, as per the author knowledge this kind of model have not been examined before. Equations in the form of PDEs are generated as a result of this process. In order to change PDEs into ODEs, the appropriate self-similarity conversion must be performed. After applying transformations, for graphical purpose we have used the numerical method that is bvp5c scheme. In the results and discussion section, graphs for different physical significance are given. Hybrid nanofluid with Ag-Go and kerosine oil enhances solar thermal efficiency. Applications include concentrated automobile, thermal collectors, and lubrication in solar tracking. Therefore, the use of a combination of tiny fluids as traditional cooling agents may serve to enhance the entire heat transfer performance of an automotive system.

## 2. MATHEMATICAL MODELING

- A steady, incompressible hybrid nanofluid with the presence of magnetic field along a permeable stretched cylinder of radius  $a$  is scrutinized.
- The hybrid nanofluid is assumed to flow in the axial  $x$ -direction while normal to  $x$  is the  $r$ -coordinate as illustrated in Fig. 1.
- The deformable (stretching or shrinking) cylinder has a linear velocity  $U_w(x)$  with constant characteristic velocity  $u_0$  such that  $U_w(x) = u_0 x/L$ .
- $v_w(r)$  is the constant mass flux velocity where  $v_w(r) > 0$  represents injection or fluid removal and  $v_w(r) < 0$  stands for suction.

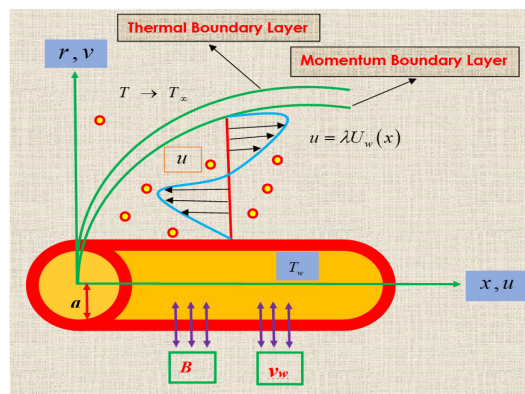


Figure 1. Flow justification of the model.

The mathematical flow equations are constructed as [15][16][17][18].

$$u \frac{\partial u}{\partial x} + v \frac{\partial u}{\partial r} = 0, \tag{1}$$

$$u \frac{\partial u}{\partial x} + v \frac{\partial u}{\partial r} = \frac{\mu_{hnf}}{\rho_{hnf}} \left( \frac{\partial^2 u}{\partial r^2} + \frac{1}{r} \frac{\partial u}{\partial r} + \sqrt{2} \Gamma \frac{\partial u}{\partial r} \frac{\partial^2 u}{\partial r^2} + \frac{\Gamma}{r\sqrt{2}} \left( \frac{\partial u}{\partial r} \right)^2 \right) - \frac{\mu_{hnf}}{\rho_{hnf}} \frac{u}{K^*} - \frac{\sigma_{hnf}}{\rho_{hnf}} (B^2 u), \tag{2}$$

$$u \frac{\partial T}{\partial x} + v \frac{\partial T}{\partial r} = \frac{k_{hnf}}{(\rho c_p)_{hnf}} \left( \frac{\partial^2 T}{\partial r^2} \right) + \frac{\mu_{hnf}}{(\rho c_p)_{hnf}} \left( 1 + \frac{\Gamma}{\sqrt{2}} \left( \frac{\partial u}{\partial r} \right) \right) \left( \frac{\partial u}{\partial r} \right)^2 + \frac{Q_0}{(\rho c_p)_{hnf}} (T - T_\infty) + \frac{\sigma_{hnf}}{(\rho c_p)_{hnf}} B^2 u^2. \tag{3}$$

Along with the boundary conditions are [15]

$$\begin{aligned} v &= v_w(r), \quad u = \lambda U_w(x), \quad T = T_w(x), \quad \text{at } r = a \\ u &\rightarrow 0, \quad T \rightarrow T_\infty, \quad \text{as } r \rightarrow \infty \end{aligned} \tag{4}$$

where the velocities along  $x$  and  $r$  - axes are denoted by  $u$  and  $v$ , accordingly and  $T$  is the Hnf temperature. The ambient temperature  $T_\infty$  is constant and the variable wall temperature is considered as  $T_w = T_\infty + T_0 \left(\frac{x}{L}\right)^2$ , where  $T_0$  is the characteristic temperature.  $\lambda$  means the constant parameter of shrinking ( $\lambda < 0$ ) or stretching ( $\lambda > 0$ ) parameters while ( $\lambda = 0$ ) symbolizes the static cylinder.

The following suitable self-similarity transformations are defined as:

$$u = \frac{u_0 x}{L} F'(\eta), \quad v = -\frac{a}{r} \sqrt{\frac{u_0 v_f}{L}} F(\eta), \quad \theta(\eta) = \frac{T - T_\infty}{T_w - T_\infty}, \quad \eta = \sqrt{\frac{u_0}{v_f L}} \frac{r^2 - a^2}{2a}, \tag{5}$$

So that

$$v_w(r) = -\frac{a}{r} \sqrt{\frac{u_0 v_f}{L}} S. \tag{6}$$

The following is a list of the thermophysical characteristics of Hnf:

$$Q_1 = \frac{\mu_{hnf}}{\mu_f}, \quad Q_2 = \frac{\rho_{hnf}}{\rho_f}, \quad Q_3 = \frac{(\rho c_p)_{hnf}}{(\rho c_p)_f}, \quad Q_4 = \frac{k_{hnf}}{k_f}, \quad Q_5 = \frac{\sigma_{hnf}}{\sigma_f}.$$

In order to create the following dimensionless ODEs, Eqs. (2) to (4) are transformed using the ideal technique indicated in Eqs. (5 and 6).

$$\begin{aligned} &\frac{Q_1}{Q_2} \left( (1+2\gamma\eta) F''' + 2\gamma F'' \right) + \frac{Q_1}{Q_2} \left[ \frac{3}{2} \gamma (1+2\gamma\eta)^{1/2} We F''^2 + We (1+2\gamma\eta)^{3/2} F'' F''' \right] \\ &+ FF'' - (F')^2 - \frac{Q_1}{Q_2} KF' - \frac{Q_5}{Q_2} MF' = 0, \end{aligned} \tag{7}$$

$$\begin{aligned} &\frac{1}{Pr} \frac{Q_5}{Q_2} \left( (1+2\gamma\eta) \theta'' + 2\gamma\theta' \right) + \frac{Q_1}{Q_3} Ec \left[ \left( 1 + We F'' (1+2\gamma\eta)^{1/2} \right) F''^2 (1+2\gamma\eta) + F\theta' - 2F'\theta \right] \\ &+ \frac{Q\theta}{Q_3} + \frac{Q_5}{Q_3} EcM (F')^2 = 0. \end{aligned} \tag{8}$$

The boundaries of the change are described as:

$$\begin{aligned} f(0) &= S, \quad f'(0) = \lambda, \quad \theta(0) = 1 \\ f'(\infty) &= 0, \quad \theta'(\infty) = 0. \end{aligned} \tag{9}$$

Note that  $M = \frac{\sigma_f B^2 L}{\rho_f u_0}$  Magnetic field parameter,  $Pr = \frac{\mu_f (c_p)_f}{k_f}$  Prandtl number,  $\gamma = \sqrt{\frac{v_f L}{u_0 a^2}}$  is the Curvature parameter,  $Ec = \frac{u_w^2}{c_p (T_w - T_\infty)}$  is the Eckert number,  $K = \frac{v_f L}{aK^*}$  is the porosity parameter, and  $Q = \frac{Q_0 L}{v_f (\rho C_p)_f}$

dimensional heat generation/absorption,  $We = \sqrt{\frac{2u_0}{v_f L}} \frac{u_0 x}{L} \Gamma$  is Weissenberg number.

The dimensional form of  $C_f$  and  $Nu_r$  are given by

$$C_f = \frac{\mu_{hnf}}{\rho_f U_w^2} \left( \frac{\partial u}{\partial r} \right)_{r=0}, \quad Nu_x = \frac{x k_{hnf}}{k_f (T_w - T_\infty)} \left( -\frac{\partial T}{\partial r} \right)_{r=a}, \tag{10}$$

The non-dimensional form of Eq. (11) converted is

$$Re_x^{1/2} C_f = Cf = Q_1 f''(0), \quad Re_x^{-1/2} Nu_x = Nu = -Q_4 \theta'(0). \tag{11}$$

Where  $Re_x$  is the local Reynolds number.

### 3. SOLUTION METHODOLOGY

The nature of the ODE system (7–8) with BCs (9) is extremely nonlinear in its characteristics. For the purpose of dealing with these equations, we adopt a computational approach known as the bvp5c method. Using MATLAB solver, we are able to solve the control problem. The midway method's standard operating procedure is laid out in detail below (Fig. 2).

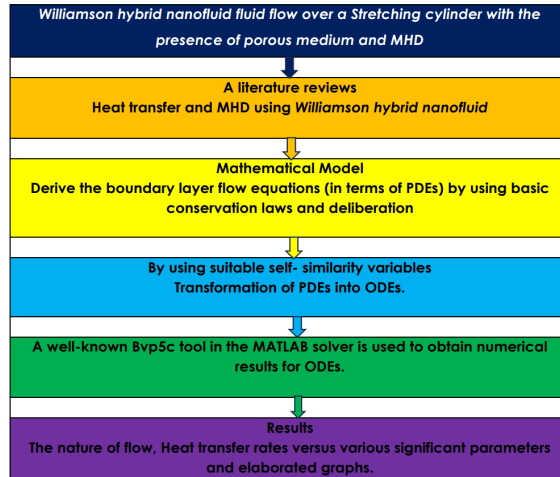


Figure 2. Flow chart of the present investigation problem.

### 4. RESULTS AND DISCUSSION

In order to describe the behavior of the Williamson hybrid nanofluid flow over a Stretching Cylinder, along with the bvp5c process in MATLAB solver were used in this investigation phase. The properties of hybrid nanofluid are presented in Table 1, as well as validation of comparison results are demonstrated in Table 2.

Table 1. Thermophysical properties of base fluid and hybrid nanofluids[19].

Property	Kerosene Oil	Ag	Go
Density $\rho$ ( $kgm^{-3}$ )	783	10,500	1800
Specific heat $C_p$ ( $Jkg^{-1}K^{-1}$ )	2090	235	717
Heat conductivity $k_f$ ( $Wm^{-1}K^{-1}$ )	0.145	429	5000
Electrical conductivity $\sigma$ ( $\Omega m$ ) <sup>-1</sup>	$21 \times 10^{-6}$	$63 \times 10^{-6}$	$6.30 \times 10^7$

Table 2. The quantitative results of the skin friction coefficient of different of values for  $\phi_2$  by fixing parameter values  $S = \gamma = M = Ec = 0$ , and  $Pr = 21$ ,  $\phi_1 = 0.01$ ,  $\lambda = 1$ .

$\phi_2$	Najiyah et al. [15]	Present results
0.005	-1.327098	-1.3270827
0.02	-1.409490	-1.4094721
0.04	-1.520721	-1.5207003
0.06	-1.634119	-1.6341005

Velocity and temperature profiles shows several flow properties, including the Magnetic field (M), Weissenberg number (We), Porous medium (K), and  $Q$ . The velocity profile decreases with increasing M Parameter, as seen in Fig. 3. Magnetic field lead to more confined Lorentz power, which in turn leads to a reduced velocity profile, which is a practical consequence. Understanding that the nanofluid’s movement decreases as a consequence of the fact that the fluid’s movement in the material is inversely related to viscosity. While the opposite nature we noticed on energy profile which is presented in Fig. 6. The effect of the Weissenberg number  $We$  on the velocity profile  $f'(\eta)$  it is shown in Fig. 4. The force boundary layer of the Williamson nanofluid shrinks for higher values of the  $We$ . From a physical standpoint, we are aware that  $We$  represents the proportion of time spent relaxing to time spent calculating. A decrease in velocity is the result of a longer processing period, which is caused by an increase in the number of  $We$ . While the reverse trend we observed on energy profile, which is demonstrated in Fig. 7. The effect of the  $K$  on the  $f'(\eta)$  is apparent in Fig. 5. It is shown that the velocity outline declines with increasing  $K$  parameter, which is in tune with



reality. Furthermore, when we the trip away from the border, as far the liquid movement is concerned, the porous nature of the border is insignificant. Fig. 8 represents the impact of  $Q$  on energy outline. For the larger values of the  $Q$  in energy profile increased. Physically, when heat generation rises, so does the inherent energy of liquid particles, resulting in a rise in the temperature outline.

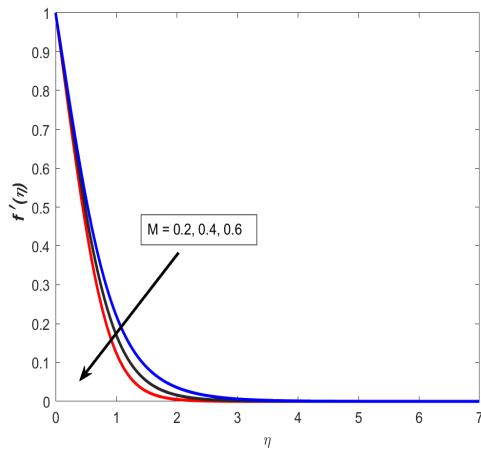


Figure 3. Influence of  $M$  on  $f'(\eta)$

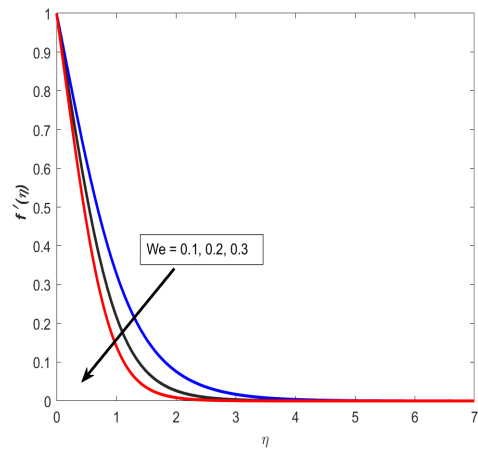


Figure 4. Impact of  $We$  on  $f'(\eta)$

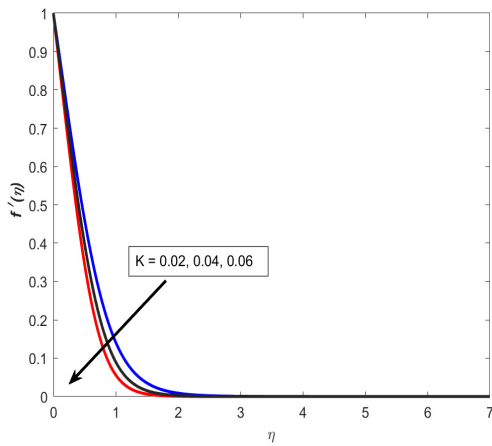


Figure 5. Impact of  $K$  on  $f'(\eta)$

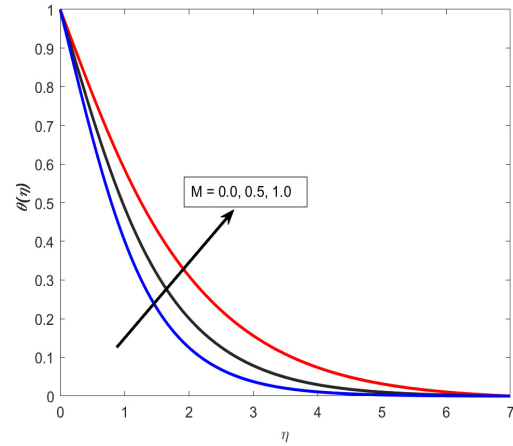


Figure 6. Impact of  $M$  on  $\theta(\eta)$

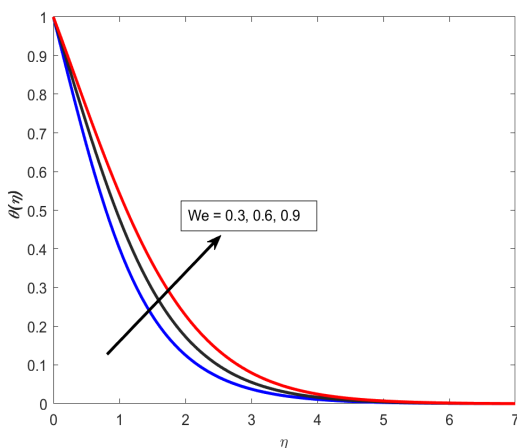


Figure 7. Impact of  $We$  on  $\theta(\eta)$

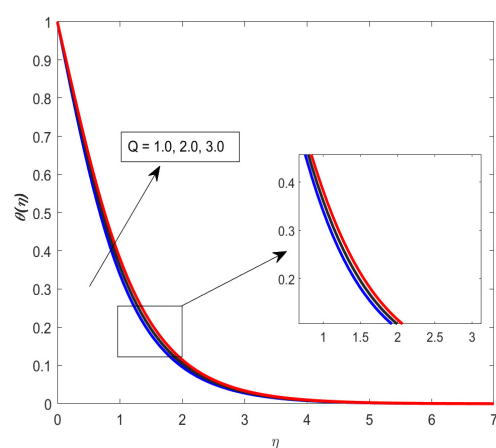


Figure 8. Impact of  $Q$  on  $\theta(\eta)$

The effect of  $M$  and  $K$  on  $Cf$  outline is demonstrated in Fig. 9. For the higher values of the  $M$  on the  $Cf$  profile decreased, due to the physical phenomenon of lot of Lorentz force is applied on the fluid movement so that's why the profile decreased. The impact of  $M$  and  $Rd$  parameters on  $Nu$  outline is presented in Fig. 10. For the larger values of the magnetic field the  $Nu$  profile increased. From a physical point of view, here the Lorentz force is act as an electric nature and this force is mixed with the fluid movement so that's why the profile enhanced.

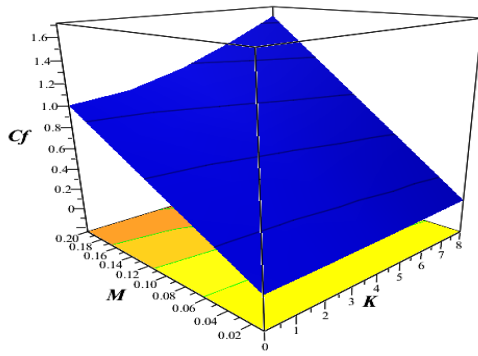


Figure 9. Impact of  $M$  and  $K$  on  $C_f$

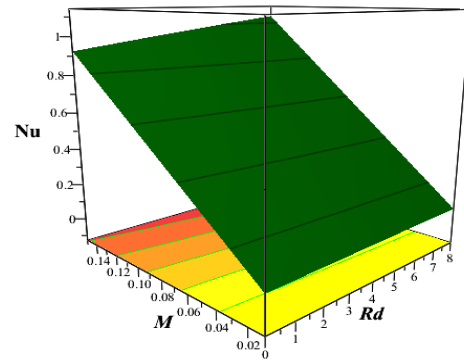


Figure 10. Impact of  $M$  and  $Rd$  on  $Nu$

### Streamlines profiles

Streamlines, the investigation of fluid behavior and the portrayal of flow, in particular, provide a range of qualities that, when taken into account together, allow them to be excellent tools for analyzing and conducting research on the movements of fluids. This is particularly true when used to the investigation of fluid movement. Figs. 11 and 12 exhibit magnetic parameter for various values of  $M=0.3, 0.5$  influences on streamlines plots. Magnetic parameter strength draws electrical conductivity molecules more towards the main stream.

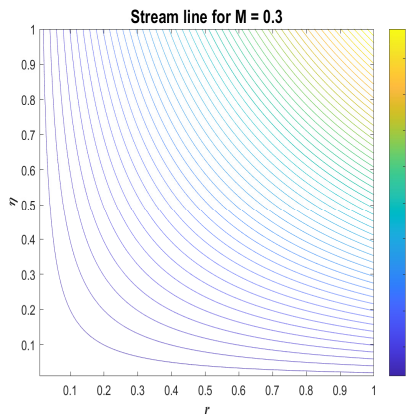


Figure 11. Stream lines for  $M=0.3$

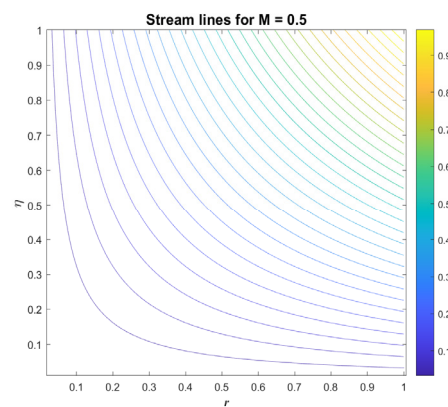


Figure 12. Stream lines for  $M=0.5$

### 5. CONCLUSIONS

The current examination work explored the numerical solution for MHD of *Ag-Go* hybrid nanofluid over a Stretching Cylinder. The *bvp5c* technique was used to solve the issue of velocity, temperature and the outcome was truly the solution to the problem. And also, in order to demonstrate the impact of important parameters graphs are generated. The results are presented in a variety of graphical formats, including a 2D plots, 3D plots, and streamlines. The following list includes the study's noteworthy results:

- Velocity profile declines for the higher values of the  $M$  parameter on the other hand we noticed the opposite tendency in energy profile.
- Velocity outline decreased for the larger values of the  $We$  parameter.
- Increasing the radiation parameter enhanced the temperature profile.
- The skin friction factor decreases for the higher values of the porous and magnetic parameter.
- The Nusselt number profile enhanced, for the higher values of the  $M$  and  $Rd$ .
- Streamlines have an oscillating character, which is necessary for magnifying the various values of nanoparticles volume fractions.

### ORCID

©Gunisetty Ramasekhar, <https://orcid.org/0000-0002-3256-3145>; ©Sangapatnam Suneetha, <https://orcid.org/0000-0001-6627-6446>  
 ©Shaik Jakeer, <https://orcid.org/0000-0002-6350-1457>; ©Seethi Reddy Reddissekhar Reddy, <https://orcid.org/0000-0001-5501-570X>

### REFERENCES

- [1] S. Choi, and J. Eastman, Enhancing thermal conductivity of fluids with nanoparticles, in: *ASME International Mechanical Engineering Congress & Exposition*, (San Francisco, CA, 1995). [https://ecotert.com/pdf/196525\\_From\\_unt-edu.pdf](https://ecotert.com/pdf/196525_From_unt-edu.pdf)
- [2] S.R. Reddissekhar Reddy, S. Jakeer, V.E. Sathishkumar, H.T. Basha, and J. Cho, "Numerical study of TC4-NiCr/EG+Water hybrid nanofluid over a porous cylinder with Thompson and Troian slip boundary condition: Artificial neural network model," *Case Stud. Therm. Eng.* **53**, 103794 (2024). <https://doi.org/10.1016/J.CSITE.2023.103794>

- [3] G. Ramasekhar, and P.B.A. Reddy, "Entropy generation on EMHD Darcy-Forchheimer flow of Carreau hybrid nano fluid over a permeable rotating disk with radiation and heat generation : Homotopy perturbation solution," Proc. Inst. Mech. Eng. Part E, J. Process Mech. Eng. 2022, <https://doi.org/10.1177/09544089221116575>
- [4] G. Ramasekhar, and P.B.A. Reddy, "Entropy generation on Darcy–Forchheimer flow of Copper–Aluminium oxide/Water hybrid nanofluid over a rotating disk: Semi-analytical and numerical approaches," Sci. Iran. **30**(6), 2245–2259 (2023). <https://doi.org/10.24200/sci.2023.60134.6617>
- [5] S. Jakeer, and S.R.R. Reddy, "Electrokinetic membrane pumping flow of hybrid nanofluid in a vertical microtube with heat source/sink effect," Eur. Phys. J. Plus, **138**(6), 489 (2023). <https://doi.org/10.1140/EPJP/S13360-023-04118-7>
- [6] S. Jakeer, and P.B.A. Reddy, "Entropy generation on the variable magnetic field and magnetohydrodynamic stagnation point flow of Eyring – Powell hybrid dusty nano fluid : Solar thermal application," Proc. Inst. Mech. Eng. Part C: Journal of Mechanical Engineering Science, **236**(13), 7442-7455 (2022). <https://doi.org/10.1177/09544062211072457>
- [7] I. Haider, U. Nazir, M. Nawaz, S.O. Alharbi, and I. Khan, "Numerical thermal study on performance of hybrid nano-Williamson fluid with memory effects using novel heat flux model," Case Stud. Therm. Eng. **26**, 101070 (2021). <https://doi.org/10.1016/j.csite.2021.101070>
- [8] P.T. Kapen, C.G.N. Ketchate, D. Fokwa, and G. Tchuen, "Linear stability analysis of (Cu-Al<sub>2</sub>O<sub>3</sub>)/water hybrid nanofluid flow in porous media in presence of hydromagnetic, small suction and injection effects," Alexandria Eng. J. **60**(1), 1525–1536 (2021). <https://doi.org/10.1016/J.AEJ.2020.11.007>
- [9] A. Almanea, "Numerical study on heat and mass transport enhancement in MHD Williamson fluid via hybrid nanoparticles," Alexandria Eng. J. **61**(10), 8343-8354 (2022). <https://doi.org/10.1016/j.aej.2022.01.041>
- [10] R. Gunisetty, P.B.A. Reddy, and A. Divya, "Entropy generation analysis on EMHD non-Newtonian hybrid nanofluid flow over a permeable rotating disk through semi analytical and numerical approaches," Proc. Inst. Mech. Eng. Part E, J. Process Mech. Eng. (2023). <https://doi.org/10.1177/09544089231199640>
- [11] M.K. Nayak et al., "Thermo-fluidic significance of non Newtonian fluid with hybrid nanostructures," Case Stud. Therm. Eng. **26**, 101092 (2021). <https://doi.org/10.1016/J.CSITE.2021.101092>
- [12] J. Hartmann, and F. Lazarus, *Hg-dynamics*, 1937. [https://gymarkiv.sdu.dk/MFM/kdvs/mfm\\_10-19/mfm-15-6.pdf](https://gymarkiv.sdu.dk/MFM/kdvs/mfm_10-19/mfm-15-6.pdf)
- [13] A. Tulu, and W. Ibrahim, "MHD Slip Flow of CNT-Ethylene Glycol Nanofluid due to a Stretchable Rotating Disk with Cattaneo-Christov Heat Flux Model," Math. Probl. Eng. **2020**, 1374658 (2020). <https://doi.org/10.1155/2020/1374658>
- [14] S.R.R. Reddy, and P.B.A. Reddy, "Thermal radiation effect on unsteady three-dimensional MHD flow of micropolar fluid over a horizontal surface of a parabola of revolution," Propuls. Power Res. **11**(1), 129–142 (2022). <https://doi.org/10.1016/j.jprr.2022.01.001>
- [15] N.S. Khashi'ie, N.M. Arifin, I. Pop, and N.S. Wahid, "Flow and heat transfer of hybrid nanofluid over a permeable shrinking cylinder with Joule heating: A comparative analysis," Alexandria Eng. J. **59**(3), 1787–1798 (2020). <https://doi.org/10.1016/j.aej.2020.04.048>
- [16] A.U. Awan, B. Ali, S.A.A. Shah, M. Orejiah, K. Guedri, and S.M. Eldin, "Numerical analysis of heat transfer in Ellis hybrid nanofluid flow subject to a stretching cylinder," Case Stud. Therm. Eng. **49**, 103222 (2023). <https://doi.org/10.1016/j.csite.2023.103222>
- [17] M. Umeshaiyah, et al., "Dusty Nanofluid Flow through a Stretching Cylinder in a Porous Medium with the Influence of the Melting Effect," Processes, **10**(6), (2022). <https://doi.org/10.3390/pr10061065>
- [18] H.A. Ogunseye, S.O. Salawu, and E.O. Fatunmbi, "A numerical study of MHD heat and mass transfer of a reactive Casson–Williamson nanofluid past a vertical moving cylinder," Partial Differ. Equations Appl. Math. **4**, 100148 (2021). <https://doi.org/10.1016/j.padiff.2021.100148>
- [19] F. Ahmad, S. Abdal, H. Ayed, S. Hussain, S. Salim, and A.O. Almatroud, "The improved thermal efficiency of Maxwell hybrid nanofluid comprising of graphene oxide plus silver/kerosene oil over stretching sheet," Case Stud. Therm. Eng. **27**, 101257 (2021). <https://doi.org/10.1016/J.CSITE.2021.101257>

**НОВА ТЕНДЕНЦІЯ АВТОМОБІЛЬНИХ АСПЕКТІВ МГД ПОТОКУ ГІБРИДНОЇ НАНОРІДИНИ ЧЕРЕЗ ПОРИСТИЙ ЦИЛІНДР ЩО РОЗТЯГУЄТЬСЯ: ЧИСЛІВЕ ДОСЛІДЖЕННЯ**  
**Гунісетті Рамасекхар<sup>a</sup>, Ю. Рамешвара Редді<sup>b</sup>, Сура Шрінівасулу<sup>c</sup>, Шайк Джакір<sup>d</sup>, Сітхі Редді Реддісекхар Редді<sup>e</sup>, Сангапатнам Сунітха<sup>f</sup>, Т. Адітья Саї Шрінівас<sup>g</sup>, Ашок Сарабу<sup>h</sup>**

<sup>a</sup>Факультет математики Меморіального інженерно-технологічного коледжу Раджива Ганді (автономний), Нандьял 518501, Андхра-Прадеш, Індія

<sup>b</sup>Факультет машинобудування, JNTUACE, Пулівендула 516390, Андхра-Прадеш, Індія

<sup>c</sup>Факультет хімії, Інженерний коледж SVR, Аялур Мета, Нандьял 518501, Андхра-Прадеш, Індія

<sup>d</sup>Школа технологій, Університет Аполло, Чіттур, Андхра-Прадеш 517127, Індія

<sup>e</sup>Департамент математики, Освітній фонд Конера Лакимайї, Борампет, Хайдарабад, Телангана 500043, Індія

<sup>f</sup>Факультет прикладної математики Університету Йоги Вемана Кадана 516003, Андхра-Прадеш, Індія


<sup>g</sup>Факультет комп'ютерних наук та інженерії, Інженерний коледж Джая Пракаш Нараян, Махабубнагар, Телангана, Індія

<sup>h</sup>Факультет комп'ютерних наук та інженерії, Хайдарабадський інженерний жіночий коледж BVRIT, Хайдарабад, Індія

Інновації в галузі теплопередачі мають важливе значення в сучасному суспільстві, оскільки системи управління температурним режимом потребують ефективних процесів нагрівання та охолодження. Вони також є важливим компонентом в автомобільній промисловості та інших видах транспорту, а окрім автомобільної промисловості, в авіаційній техніці, комп'ютерній індустрії та обробній промисловості. У цьому дослідженні розглядається важливість магнітогідродинамічної гібридної нанорідини Вільямсона в циліндрі, що розтягується, і пористого середовища. Для перетворення PDEs в PDEs використовується відповідне перетворення самоподібності. Після застосування перетворень для графічних цілей ми використали техніку bvp5c. Вплив активних параметрів, що впливають на здатність рідини передавати параметри, показано на графіках і таблицях. У розділі результатів ми помітили, що контури швидкості зменшуються зі збільшенням параметра  $M$ .  $C_f$  і  $Nu$  збільшувалися за великих значеннях параметрів  $M$  і кривизни. Додаткові властивості вхідних параметрів  $M$  та  $Rd$  призводять до покращення температурних профілів.

**Ключові слова:** рідина Вільямсона; МГД; пористе середовище; джерело тепла; гібридні нанорідини

## COMPUTER SIMULATION OF ADSORPTION OF C<sub>60</sub> FULLERENE MOLECULE ON RECONSTRUCTED Si(100) SURFACE

**Ikrom Z. Urolov<sup>a,c</sup>, Farid F. Umarov<sup>b</sup>,  Ishmumin D. Yadgarov<sup>a\*</sup>, Ganiboy T. Rakhmanov<sup>c</sup>,  
Khayitmurad I. Jabbarov<sup>d</sup>**

<sup>a</sup>*Institute of Ion-Plasma and Laser Technologies named after U.A. Arifov, Uzbekistan Academy Sciences,  
Tashkent, 100125 Uzbekistan*

<sup>b</sup>*Kazakh-British Technical University, Almaty, 050000, Kazakhstan*

<sup>c</sup>*National University of Uzbekistan named after Mirzo Ulugbek, Tashkent, 100174, Uzbekistan*

<sup>d</sup>*Tashkent University of Information Technologies named after Muhammad al-Khwarizmi, Tashkent, 100084 Uzbekistan*

\*Corresponding Author e-mail: [ishmuminyadgarov@gmail.com](mailto:ishmuminyadgarov@gmail.com)

Received February 28, 2024; revised March 20, 2024; accepted, March 30, 2024

The adsorption of the C<sub>60</sub> fullerene molecule has been studied in various configurations on a reconstructed Si(100) silicon surface. Among fullerenes, fullerene C<sub>60</sub> is of particular importance, since it has the most stable form and consists of 60 carbon atoms. Monocrystalline silicon has the diamond structure, the size of its crystal lattice is 5.43 Å. The MD-simulation calculations have been performed using the open source LAMMPS MD-simulator software package and the Nanotube Modeler computer program. The Tersoff interatomic potential has been used to determine the interactions between the Si-Si, C-C and Si-C atoms. The adsorption energy of the C<sub>60</sub> molecule on the reconstructed Si(100) surface, the bond lengths and the number of bonds formed depend on the adsorption geometry, i.e. at what point on the substrate the molecule is adsorbed and in what configuration.

**Key words:** Surface; Fullerene molecule; Adsorption; Silicon; Simulation; Brenner potential; Bond length; Atom; potential energy; Interaction

**PACS:** 61.48.-c, 02.70.Ns

### INTRODUCTION

Fullerenes are of growing interest following the discovery of C<sub>60</sub> by Kroto H. W. et al. [1] and the success of Kratschmer W. et al. in obtaining pure C<sub>60</sub> and other members of the fullerene family [2]. Fullerenes are a promising material for creating electro-active elements in solar cells and active layers in thin-film organic transistors [3]. One of the current topics related to fullerenes is their adsorption on various substrates. Fullerenes adsorbed on substrates have great potential for practical application and the studies of fullerene and its compounds is of great fundamental importance [4,5]. The molecule adsorption of a number of substances, such as water, ammonia, ethylene and vinyl bromide, on the Si(100) surface has been studied experimentally [6-8]. The high density of  $\pi$  electrons of the C<sub>60</sub> molecules gives them the energy potential of a small organic molecule. The C<sub>60</sub> nanofullerene molecule is expected to provide high-performance electronics and optical functions, as well as exhibit interesting fabrication, high spherical symmetry, and ease of connectivity. Obviously, the use of C<sub>60</sub> adsorbed on an ideal Si(100) surface is very topical and actual in modern semiconductor technology [9, 10]. One of these promising applications is the use of endohedrally embedded fullerenes in quantum computers, for which the fullerene molecules are to be adsorbed on the surface silicon [11-13]. The appearance of superconducting properties in some alkali metals when they are coated with C<sub>60</sub> and C<sub>70</sub> fullerenes [14] and the treatment of the silicon surface with ions has intensified research in the field of HTSC materials science [15].

A number of theoretical and experimental studies of the interaction of C<sub>60</sub> and other representatives of the fullerene family with the Si(111) surface have been carried out. When designing and developing devices based on fullerenes in molecular electronics, information technology, and biomedical developments [16-18], C<sub>60</sub>/Si(100) is of great importance [19-22]. In recent years, the adsorption of C<sub>60</sub> molecules on the Si(111) surface has been studied by density functional theory (DFT) [17,23,24]. The interaction between C<sub>60</sub> and the Si(111) surface was experimentally studied by scanning tunneling microscopy and spectroscopy (STM/STS) [22-26], as well as by other methods [18,27]. The experimental results on the temperature dependence of the adsorption of C<sub>60</sub> molecules on the Si(111) surface were published in [28].

To clarify the nature of the adsorption of C<sub>60</sub> molecules on the Si(100) surface, a great number of contradictory studies have been carried out. In some of these works, the researchers showed that the adsorption of C<sub>60</sub> is physisorption [29-31], while in some other studies this was denied and it was stated that the adsorption is chemisorption in its nature [32-37]. Among the theoretical calculations performed in this direction, ab initio theoretical calculations stand out [38-40], but the studies in this direction was carried out by predicting the structures formed when fullerene molecules are placed on the substrate surface, without taking into account any structural changes caused by the bonds between atoms on the silicon surface and C<sub>60</sub> atoms [21]. In the works of C. Hobbs et al. [41,42], the average Si-C bond length and adsorption energy for the adsorption of the C<sub>60</sub> molecule on the Si(100) surface were determined by ab initio DFT using Spanish Initiative for Electronic Simulations with Thousands of Atoms codes (SESTA). From the results of these works it is clear



that the bond length and the adsorption energy depend on configuration and number of bonds of the C<sub>60</sub> molecules adsorbed on the base surface. The work of K. Beardmore et al., using classical many-body potentials of the Brenner/Tersoff form [44-46], suggests that the bonds between the fullerene and the silicon surface are closer to Van der Waals bonds than to covalent ones. In this formalism, the silicon-carbon interactions are adapted to SiC bulk structures and C<sub>60</sub> molecules can be transferred incorrectly to the silicon surface.

The aim of this work is to determine adsorption energies and bond lengths for various adsorption configurations of C<sub>60</sub> fullerene molecules on the reconstructed Si(100) silicon surface, as well as to determine the dependence of these parameters on all possible adsorption configurations that can be realized on the Si(100) surface.

In connection with the above, in this work, the results of studying the interaction of the C<sub>60</sub> molecule with the reconstructed Si(100) surface have been highlighted, and the interaction process has been considered by molecular dynamics (MD) simulation.

### DESCRIPTION OF THE OBJECT AND RESEARCH METHODS

Fullerenes are large carbon-framework molecules that are considered to be three-dimensional analogues of benzene. Among fullerenes, Buckminster fullerene (C<sub>60</sub>) is of particular importance, since it has the most stable form and consists of 60 carbon atoms. The molecule shape resembles a truncated icosahedron, that is, a soccer ball consisting of 12 pentagons and 20 hexagons [2]. One of the important properties of C<sub>60</sub> is its high symmetry having 120 symmetry operations in which the molecule can return to itself, like rotation around an axis and reflection in a plane. This makes C<sub>60</sub> the most symmetrical molecule [47]. C<sub>60</sub> has two types of bonds: a C<sub>5</sub>-C<sub>5</sub> single bond in a pentagon (the bond length 1.45±0.015 Å) and a C<sub>5</sub>-C<sub>6</sub> double bond in a hexagon (the bond length 1.40±0.015 Å). Each carbon atom in the molecule forms a bond with three side atoms through sp<sup>2</sup>-hybridization [48,49]. The diameter of the C<sub>60</sub> molecule is about 7 Å. Chemically, the fullerene molecule is quite stable; it decomposes at a temperature of 1000°C, and when heated to a temperature of 1500°C in the absence of air, it takes the form of graphite [50].

Silicon is a chemical element with atomic number 14, chemical symbol Si, and atomic weight 28.085. Monocrystalline silicon has the structure of diamond, the size of its crystal lattice is 5.43 Å. The closest distance between atoms in the lattice is 2.35 Å [51].

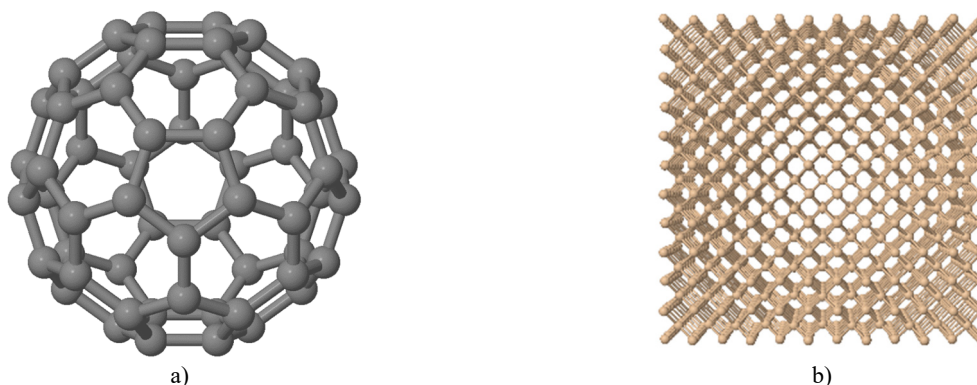


**Figure 1.** Geometric structures of fullerene C<sub>60</sub> (a) and silicon (b) used in this work

All MD-simulation calculations in our work were performed using the open source LAMMPS MD-simulator software package [52] and the Nanotube Modeler computer program [53]. The Tersoff interatomic potential was used to determine the interactions between Si-Si, C-C and Si-C atoms. In all cases, a reconstructed silicon single crystal measuring 34 × 34 × 15.2 Å with 1083 atoms (Fig. 1b) and a fullerene molecule with 60 atoms (Fig. 1a) with periodic boundary conditions were used. The generated C<sub>60</sub> molecule, the reconstructed silicon single crystal and the interaction processes between them were visualized in the JMOL computer program [54]. When comparing the results obtained for reconstructed single crystals with the number of atoms 1963 and 17670, no size effects were found. To maintain a constant selected temperature of the NVT ensemble, a Nose-Hoover thermostat was used [55]. The Wehrl speed synchronization circuit was integrated with a time step of 1.0 fs. The system's center of mass was fixed to avoid any forward motion during the simulation. Each simulation lasted from 10 to 40 ns until equilibrium was reached.

### CALCULATION OF ADSORPTION ENERGY

The adsorption energy  $E_{ads}$  for a molecule or atom adsorbed on the substrate surface is the total potential energy of the substrate and the adsorbed molecule  $E_{ads/sub}^{tot}$ , the potential energy of the substrate in the state when they do not interact  $E_{sub/tot}$  and the potential energy of the adsorbed molecule  $E_{ads/tot}$  is equal to the subtraction of the sum [56,57]:

$$E_{ads} = E_{ads/sub}^{tot} - (E_{sub}^{tot} + E_{ads}^{tot}). \quad (1)$$

Initially, the potential energy  $E_{sub/tot}$  of interaction of the atoms composing a silicon single crystal at a temperature of 0 K was determined, and in the same test the potential energy  $E_{sub/tot}$  of interaction of the C<sub>60</sub> molecule atoms was

obtained. At the next stage, the potential energy of the entire system  $E_{ads/sub}^{tot}$  was determined for the case when a  $C_{60}$  molecule is adsorbed on a silicon substrate. All the calculations were performed in the LAMMPS package program.

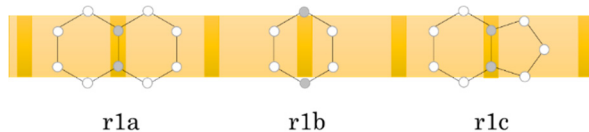


**Fig. 2.** Bonds of the  $C_{60}$  molecule in a dimer series with one dimer

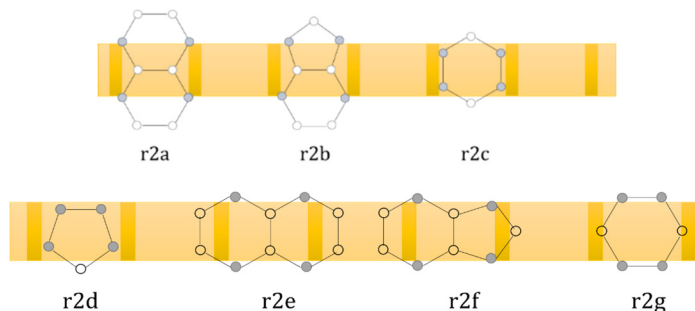


**Fig. 3.** Bonds of the  $C_{60}$  molecule with two dimers on rows of dimers

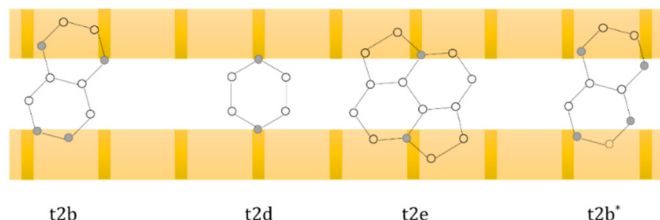


**Fig. 4.** Bonds of the  $C_{60}$  molecule on a trench with two dimers

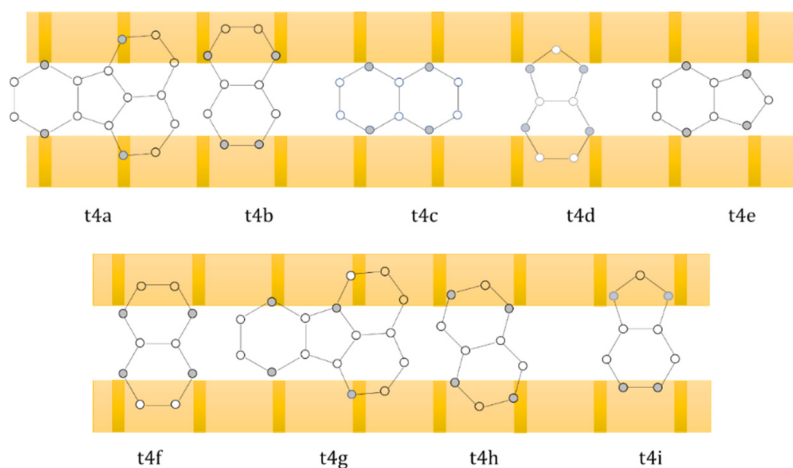


**Fig. 5.** Bonds of the  $C_{60}$  molecule on the trench with four dimers

### DESCRIPTION AND ANALYSIS OF RESULTS

The results obtained are very convenient to analyze, classifying them into different configurations. A similar classification was made in [21,41-43]. A recent work by C. Hobbs et al. [42] studied the adsorption of  $C_{60}$  in 26 different configurations on a Si(100) surface; in this work, most of the above configurations and two new adsorption configuration states were classified as follows: trench is the space between two rows of dimers; adsorption on trench between four dimers (t4); adsorption on trench between two dimers (t2); adsorption with two dimers in a series of dimers (r2); adsorption with one dimer in a series of dimers (r1).

The adsorption of fullerenes on all the configuration classifications is schematically presented in Figures 2-5. New configurations are marked with an asterisk (\*). In the Figures, the rows of dimers are shown in golden color, and individual dimers are shown in dark golden color. The colorless space between the dimers represents trenches; the carbon atoms that formed the Si-C bond upon adsorption are shown as black circles, and those that did not participate in the bond are shown as white circles. These atoms belong to hexagons and pentagons that participate in adsorption.

The adsorption energy values calculated in this work are given in Table. 1 in comparison with the results obtained in GGA (generalized gradient approximation) and LDA (local-density approximation) [41,42] and [21]. All the energy values are in eV. The Si-C bond lengths are calculated for all configurations in Table 2 and given in Å, as compared to adsorption energies.

**Table 1.** Adsorption energies calculated in the LAMMPS program, as compared to the GGA, LDA methods and values calculated in [21].

№	Configuration	LAMMPS	GGA (SIESTA)	LDA (SIESTA)	[21]
1	r1a	-1.984	-1.72	-2.72	-3.53
2	r1b	-1.434	-1.50	-2.53	-3.28
3	r1c	-2.061	-0.93	-1.87	-2.90
4	r2a	-3.538	-2.58	-3.93	-4.83
5	r2b	-3.860	-2.49	-3.74	-4.33
6	r2c	-3.594	-2.00	-3.27	-4.15
7	r2d	-2.602	-0.87	-2.08	-2.69
8	r2e	-2.493	-1.69	-3.01	-3.94
9	r2f	-2.990	-2.19	-3.40	-4.10
10	r2g	-1.988	-1.1	-2.38	-3.13
11	t2a	-	-	-	-4.78
12	t2b	-4.744	-	-	-4.40
13	t2b*	-4.953	-	-	-
14	t2c	-	-0.07	-1.56	-3.08
15	t2d	-	-1.61	-2.83	-
16	t2d*	-5.752	-	-	-
17	t2e	-3.168	-1.57	-2.72	-
18	t4a	-3.438	-2.16	-3.94	-5.71
19	t4b	-4.743	-2.53	-4.00	-5.31
20	t4c	-5.755	-2.63	-4.1	-4.96
21	t4d	-5.167	-1.96	-3.42	-4.85
22	t4e	-5.433	-1.90	-3.38	-
23	t4f	-4.799	-2.17	-3.59	-
24	t4g	-5.058	-2.53	-4.02	-
25	t4h	-4.882	-1.94	-3.59	-
26	t4i	-4.571	-1.83	-3.41	-
27	t4j	-	-1.98	-3.55	-

**Table 2.** Si-C bond lengths (in Å) for all configurations

№	Configuration	LAMMPS	GGA (SIESTA)	LDA (SIESTA)	[21]
1	r1a	1.99-2.00	2.02-2.03	1.98-1.99	1.99-1.99
2	r1b	2.02-2.02	2.01-2.02	1.97-1.97	1.98-1.98
3	r1c	1.99-2.02	2.02-2.03	1.97-2.01	1.99-2.00
4	r2a	1.99-2.00	1.98-1.99	1.94-1.97	1.96-1.98
5	r2b	1.96-1.98	1.99-2.07	1.93-2.05	1.97-2.02
6	r2c	1.99-2.00	2.05-2.09	2.02-2.05	2.01-2.07
7	r2d	2.00-2.06	2.03-2.06	2.00-2.02	2.00-2.02
8	r2e	2.02-2.02	2.01-2.05	1.98-2.01	1.99-1.99
9	r2f	1.99-2.01	2.01-2.07	1.96-2.04	1.97-2.04
10	r2g	2.02-2.07	2.05-2.10	2.02-2.05	2.03-2.07
11	t2a	-	-	-	2.02-2.11
12	t2b	1.95-1.99	-	-	1.92-2.47
13	t2b*	1.93-2.00	-	-	-
14	t2c	-	2.08-2.10	2.04-2.06	2.03-2.03
15	t2d	-	1.99-2.03	1.95-1.99	-
16	t2d*	1.96-1.97	-	-	-
17	t2e	1.93-1.94	2.00-2.04	1.95-1.99	-
18	t4a	1.96-2.01	2.00-2.03	1.96-1.98	1.93-1.98
19	t4b	1.95-1.99	1.97-2.03	1.95-2.01	1.95-1.98
20	t4c	1.97-1.97	2.02-2.20	1.98-1.99	1.96-1.98
21	t4d	1.98-1.99	2.02-2.19	1.98-2.12	1.97-2.19
22	t4e	1.96-1.99	2.03-2.09	1.98-2.06	-
23	t4f	1.98	2.01-2.03	1.97-1.98	-
24	t4g	1.93-1.99	2.00-2.04	1.97-1.99	-
25	t4h	1.93-1.99	2.02-2.06	1.98-2.03	-
26	t4i	1.95-2.01	2.04-2.10	2.00-2.05	-
27	t4j	-	1.95-2.07	1.93-2.02	-

Table 1 shows that by comparing the adsorption energies of the C<sub>60</sub> molecule obtained in LAMMPS calculations, one can see that the bond energies of the t4 type have significantly higher values than the bond energies of other types (r2 or t2). The bond lengths shown in Table. 2 have slightly larger values in the bond configurations r1 and r2 than in the bond configurations t2 and t4. It can be seen that the adsorption energies of the C<sub>60</sub> molecule are closer to the results given in [21], and the obtained bond lengths do not differ sharply from the results of GGA, LDA and [21] given in Table 2.

### CONCLUSION

As a result of the study, the following conclusions can be made: a) the adsorption energies of the C<sub>60</sub> molecule on the reconstructed Si(100) surface, the bond lengths and the number of formed bonds depend on adsorption geometry, i.e. at what point on the substrate the molecule is adsorbed and in what configuration; b) comparison of the obtained adsorption energies shows that the adsorption states on the rows of dimers (on the trench) become stable; c) adsorption energy depends on the number of bonds, and an increase in the number of bonds leads to an increase in adsorption energy; d) bonds with high adsorption energy have a shorter length.

### Acknowledgements

The authors are grateful for fruitful collaborations with Dr. Farid Umarov. This work was assisted by the fundamental research program of the Academy Sciences of Uzbekistan.

### ORCID

©Ishmumin D. Yadgarov, <https://orcid.org/0000-0002-4808-2258>

### REFERENCE

- [1] H.W. Kroto, J.R. Heath, S.C. O'Brein, R.F. Curl, and R.E. Smalley, "C<sub>60</sub>: Buckminsterfullerene," *Nature*, **318**, 162–163 (1985). <https://doi.org/10.1038/318162a0>
- [2] W. Kratschmer, L.D. Lamb, and D.R. Hoffman, "Solid C<sub>60</sub>: a new form of carbon," *Nature*, **347**, 354–358 (1990). <https://doi.org/10.1038/347354a0>
- [3] M. Paukov, Ch. Kramberger, I. Begichev, M. Kharlamova, and M. Burdanova, "Functionalized Fullerenes and Their Applications in Electrochemistry," *Solar Cells, and Nanoelectronics, Materials*, **16**(3), 1276 (2023). <https://doi.org/10.3390/ma16031276>
- [4] S.A. Bakhramov, U.K. Makhmanov, and A.M. Kokhkharov, "Synthesis of Nanoscale Fullerene C<sub>60</sub> Filaments in the Volume of an Evaporating Drop of a Molecular Solution and Preparation of Thin Nanostructured Coatings on Their Basis," *Applied Solar Energy*, **55**(5), 309–314 (2019). <https://doi.org/10.3103/S0003701X19050049>
- [5] A. Ulukmuradov, I. Yadgarov, V. Stelmakh, and F. Umarov, "Computer Simulation of Adsorption of Fullerene on Graphene," *Journal of Nano- and Electronic Physics*, **13**(2), 02025-1–02025-5 (2021). [https://doi.org/10.21272/jnep.13\(2\).02025](https://doi.org/10.21272/jnep.13(2).02025)
- [6] J.N. Luy, and R. Tonner, "Organic Functionalization at the Si(001) Dimer Vacancy Defect-Structure, Bonding, and Reactivity," *J. Phys. Chem. C*, **125**, 5635–5646 (2021). <https://doi.org/10.1021/acs.jpcc.1c00262>
- [7] X. Meng, "An overview of molecular layer deposition for organic and organic–inorganic hybrid materials: mechanisms, growth characteristics, and promising applications," *Mater. Chem. A*, **5**, 18326–18378 (2017). <https://doi.org/10.1039/C7TA04449F>
- [8] P. Sundberg, M. Karppinen, and Beilstein, "Organic and inorganic–organic thin film structures by molecular layer deposition: A review," *J. Nanotechnol.* **5**, 1104–1136 (2014). <https://doi.org/10.3762/bjnano.5.123>
- [9] J. Lee, and M. Kang, "Structure and bonding nature of C<sub>60</sub>/Si(100)-c(4×4): density-functional theory calculations," *Phys. Rev. B*, **7**, 25305.1–25305.5 (2007). <https://doi.org/10.1103/PhysRevB.75.125305>
- [10] V.N. Arustamov, I.Kh. Khudaykulov, M.V. Kremkov, Kh.B. Ashurov, I.O. Kosimov, V.P. Kharyakov, and U.F. Berdiyev, "Creation of lowohmic copper contacts on the silicon crystals surface for application in photocells," *Applied Solar Energy*, **59**(1), 7–16 (2023). <https://doi.org/10.3103/S0003701X22601612>
- [11] P. Seongjun, S. Deepak, and Ch. Kyeongjae, "Endo-fullerenes and Doped Bucky Onions as Seed Materials for Solid State Quantum Bits, *Mat. Res. Soc. Symp. Proc.* **675**, 181 (2001). <https://doi.org/10.1557/PROC-675-W1.8.1>
- [12] W. Harnett, "Fullerene-based electron-spin quantum computer," *Phys. Rev. A*, **65**, 032322 (2002). <https://doi.org/10.1103/PhysRevA.65.032322>
- [13] C. Meyer, W. Harnett, B. Naydenov, K. Lips, and A. Weidinger, "N@C and P@C as quantum bits," *Appl. Magn. Reson.* **27**, 123–132 (2004). <https://doi.org/10.1007/BF03166307>
- [14] R.C. Haddon, A.F. Hebard, M.J. Rosseinsky, D.W. Murphy, S.J. Duclos, K.B. Lyons, B. Miller, et al., "Conducting films of C<sub>60</sub> and C<sub>70</sub> by alkali-metal doping," *Nature*, **350**, 320–322 (1991). <https://doi.org/10.1038/350320a0>
- [15] S.K. Kuchkanov, et al., "Thermalvoltaic Effect in Si-Ge/Si and Si-Ge/Si Film Structures Subjected to Ion Treatment," *Applied Solar Energy*, **58**(3), 355–359 (2022). <https://doi.org/10.3103/S0003701X22030100>
- [16] R. Rurali, R. Cuadrado, and J. I. Cerdá, "C<sub>60</sub> adsorption on the Si(111)-p(7×7) surface: A theoretical study," *Physical Review B*, **81**, 075419 (2010). <https://doi.org/10.1103/PhysRevB.81.075419>
- [17] L.J. Yo., and H.K. Myung, "Adsorption structure of a single C<sub>60</sub> molecule on Si(111)-(7×7): density-functional calculations," *Surface Science*, **602**, 1408–1412 (2008). <https://doi.org/10.1016/j.susc.2008.02.014>
- [18] F. Yasunori, S. Koichiro, and K. Atsushi, "Transition of an adsorption state of C<sub>60</sub> on a Si(111)7×7 surface revealed by high-resolution electron-energy-loss spectroscopy," *Physical Review B*, **56**, 12124 (1997). <https://doi.org/10.1103/PhysRevB.56.12124>
- [19] M. Huijing, F. Xuyang, K. Shuangyu, and C. Yingxiang, "Adsorption geometries and interface electronic structure of C<sub>60</sub> on Si(100)2 × 1 reconstruction surface," *Surface Science*, **690**, 121484 (2019). <https://doi.org/10.1016/j.susc.2019.121484>
- [20] P.D. Godwin, S.D. Kenny, R. Smith, and J. Belbruno, "The structure of C<sub>60</sub> and endohedral C<sub>60</sub> on the Si(100) surface," *Surface Science*, **490**, 409–414 (2001). [https://doi.org/10.1016/S0039-6028\(01\)01365-6](https://doi.org/10.1016/S0039-6028(01)01365-6)



- [21] P.D. Godwin, S.D. Kenny, and R. Smith, "The bonding sites and structure of C<sub>60</sub> on the Si(100) surface," *Surf. Sci.* **529**, 237-246 (2003). [https://doi.org/10.1016/S0039-6028\(03\)00074-8](https://doi.org/10.1016/S0039-6028(03)00074-8)
- [22] D.A. Olyanicha, V.V. Mararova, T.V. Utas, A.V. Zotova, and A.A. Saranin, "Adsorption and self-assembly of fullerenes on Si(111) $\sqrt{3} \times \sqrt{3}$ -Ag: C<sub>60</sub> and C<sub>70</sub>," *Surface Science*, **653**, 138-142 (2016). <https://doi.org/10.1016/j.susc.2016.06.016>
- [23] B. Khaoula, D. Eric, S. Regis, H. Marie-Christine, and S. Philippe, "C<sub>60</sub> molecules grown on a Si-supported Nanoporous Supramolecular Network: a DFT study," *Physical Chemistry Chemical Physics*, **16**(28), 14722-14729 (2014). <https://doi.org/10.1039/C4CP01677G>
- [24] L.J. Yo, and H.K. Myung, "Structure and bonding nature of C<sub>60</sub>/Si(100)-c(4 $\times$ 4): Density-functional theory calculations," *Physical Review B*, **75**, 125305 (2007). <https://doi.org/10.1103/PhysRevB.75.125305>
- [25] S. Suto, K. Sakamoto, D. Kondo, T. Wakita, A. Kimura, A. Kakizaki, C.-W. Hu, and A. Kasuya, "Interaction of C<sub>60</sub> with Si(111)7 $\times$ 7 and Si(100)2 $\times$ 1 surfaces studied by STM, PES and HREELS: annealing effect," *Surface Science*, **438**, 242-247 (1999). [https://doi.org/10.1016/S0039-6028\(99\)00576-2](https://doi.org/10.1016/S0039-6028(99)00576-2)
- [26] W. Haiqian, Z. Changgan, L. Qunxiang, W. Bing, Ya. Jinlong, J.G. Hou, and Q. Zhu, "Scanning tunneling spectroscopy of individual C<sub>60</sub> molecules adsorbed on Si(111)-7 $\times$ 7 surface," *Surface Science*, **442**, 1024-1028 (1999). [https://doi.org/10.1016/S0039-6028\(99\)00977-2](https://doi.org/10.1016/S0039-6028(99)00977-2)
- [27] O. Kazuhiro, N. Masashi, U. Hirobumi, K. Tetsuo, Ya. Yoshiyuki, M. Kozo, J. Yoshinobu, et al., "Regioselective cycloaddition reaction of alkene molecules to the asymmetric dimer on Si(100)c(4 $\times$ 2)," *J. Am. Chem. Soc.* **129**, 1242-1245 (2007). <https://doi.org/10.1021/ja066285i>
- [28] Ch. Dong, and S. Dror, "Temperature effects of adsorption of C<sub>60</sub> molecules on Si(111)-(7 $\times$ 7) surfaces," *Physical Review B*, **49**, 7612 (1994). <https://doi.org/10.1103/PhysRevB.49.7612>
- [29] S. Suto, K. Sakamoto, T. Wakita, C.-W. Hu, and A. Kasuya, "Vibrational properties and charge transfer of C<sub>60</sub> adsorbed on Si(111)-(7 $\times$ 7) and Si(100)-(2 $\times$ 1) surfaces," *Phys. Rev. B*, **56**, 7439 (1997). <https://doi.org/10.1103/PhysRevB.56.7439>
- [30] D. Chen, and D. Sarid, "An STM study of C<sub>60</sub> adsorption on Si(100)-(2 $\times$ 1) surfaces: from physisorption to chemisorption," *Surf. Sci.* **329**, 206-218 (1995). [https://doi.org/10.1016/0039-6028\(95\)00051-8](https://doi.org/10.1016/0039-6028(95)00051-8)
- [31] D. Klyachko, and D.M. Chen, "Ordering of C<sub>60</sub> on Anisotropic Surfaces," *Phys. Rev. Lett.* **75**, 3693 (1995). <https://doi.org/10.1103/PhysRevLett.75.3693>
- [32] T. Hashizume, X.D. Wang, Y. Nishina, H. Shinohara, Y. Saito, Y. Kuk, and T. Sakurai, "Field Ion-Scanning Tunneling Microscopy Study of C<sub>60</sub> on the Si(100) Surface," *Jpn. J. Appl. Phys.* **31**, L880 (1992). <https://doi.org/10.1143/JJAP.31.L880>
- [33] S. Suto, K. Sakamoto, D. Kondo, T. Wakita, A. Kimura, and A. Kakizaki, "Bonding nature of C<sub>60</sub> adsorbed on Si(111)7 $\times$ 7 and Si(100)2 $\times$ 1 surfaces studied by HREELS and PES," *Surf. Sci.* **85**, 427-428 (1999). [https://doi.org/10.1016/S0039-6028\(99\)00238-1](https://doi.org/10.1016/S0039-6028(99)00238-1)
- [34] P. Moriarty, M.D. Upward, A.W. Dunn, Y.-R. Ma, P.H. Beton, and D. Teehan, "C<sub>60</sub>-terminated Si surfaces: Charge transfer, bonding, and chemical passivation," *Phys. Rev. B*, **57**, 362 (1998). <https://doi.org/10.1103/PhysRevB.57.362>
- [35] X.D. Wang, T. Hashizume, H. Shinohara, Y. Saito, Y. Nishina, and T. Sakurai, "Adsorption of C<sub>60</sub> and C<sub>84</sub> on the Si(100)2 $\times$ 1 surface studied by using the scanning tunneling microscope," *Phys. Rev. B*, **47**, 15923 (1993). <https://doi.org/10.1103/PhysRevB.47.15923>
- [36] M. De Seta, D. Sanvitto, and F. Evangelisti, "Direct evidence of C<sub>60</sub> chemical bonding on Si(100)," *Phys. Rev. B*, **59**, 9878 (1999). <https://doi.org/10.1103/PhysRevB.59.9878>
- [37] K. Sakamoto, D. Kondo, M. Harada, A. Kimura, A. Kakizaki, and S. Suto, "Electronic structures of C<sub>60</sub> adsorbed on Si(111)-(7 $\times$ 7) and Si(001)-(2 $\times$ 1) surfaces," *Surf. Sci.* **642**, 433-435 (1999). [https://doi.org/10.1016/S0039-6028\(99\)00094-1](https://doi.org/10.1016/S0039-6028(99)00094-1)
- [38] Y. Kawazoe, H. Kamiyama, Y. Maruyama, and K. Ohno, "Electronic Structures of Layered C<sub>60</sub> and C<sub>70</sub> on Si(100) Surface," *Jpn. J. Appl. Phys. Part 1*, **32**, 1433 (1993). <https://doi.org/10.1143/JJAP.32.1433>
- [39] T. Yamaguchi, "Electronic states of C<sub>60</sub> molecules on Si(001)2 $\times$ 1 and Si(111)7 $\times$ 7 surfaces," *J. Vac. Sci. Technol. B*, **12**, 1932 (1994). <https://doi.org/10.1116/1.587674>
- [40] A. Yajima, and M. Tsukada, "Electronic structure of monolayer C<sub>60</sub> on Si(100)2 $\times$ 1 surface," *Surf. Sci.* **355**, 357-358 (1996). [https://doi.org/10.1016/0039-6028\(96\)00181-1](https://doi.org/10.1016/0039-6028(96)00181-1)
- [41] Ch. Hobbs, and L. Kantorovich, "Adsorption of C<sub>60</sub> on the Si(001) surface calculated within the generalized gradient approximation," *Nanotechnology*, **15**, S1-S4 (2004). <https://doi.org/10.1088/0957-4484/15/2/001>
- [42] Ch. Hobbs, L. Kantorovich, and J.D. Gale, "An ab initio study of C<sub>60</sub> adsorption on the Si(001) surface," *Surf. Sci.* **591**, 45-55 (2005). <https://doi.org/10.1016/j.susc.2005.06.038>
- [43] Ch. Weiguang, L. Chong, P. Lijun, W. Fei, S. Qiang, and J. Yu, "First-principles investigation of C<sub>60</sub> molecule adsorption on a diamond (100)-2 $\times$ 1 surface," *Modelling Simul. Mater. Sci. Eng.* **19**, 045001 (2011). <https://doi.org/10.1088/0965-0393/19/4/045001>
- [44] R. Smith, and K. Beardmore, "Molecular dynamics studies of particle impacts with carbon-based materials," *Thin Solid Films*, **272**, 255 (1996). [https://doi.org/10.1016/0040-6090\(95\)06052-9](https://doi.org/10.1016/0040-6090(95)06052-9)
- [45] K. Beardmore, and R. Smith, "C<sub>60</sub> film growth and the interaction of fullerenes with bare and H terminated Si surfaces, studied by molecular dynamics," *Nucl. Instrum. Meth. B*, **106**, 74 (1995). [https://doi.org/10.1016/0168-583X\(95\)00682-6](https://doi.org/10.1016/0168-583X(95)00682-6)
- [46] K. Beardmore, R. Smith, A. Richter, and B. Winzer, *Mol. Mater.* **7**, 155 (1996).
- [47] R. Taylor, J.P. Hare, A.K. Abdul-Sada, and H.W. Kroto, "Isolation, separation and characterisation of the fullerenes C<sub>60</sub> and C<sub>70</sub>: the third form of carbon," *J. Chem. Soc. Chem. Commun.* **20**, 1423-1425, (1990). <https://doi.org/10.1039/C39900001423>
- [48] J.M. Hawkins, A. Meyer, L.A. Lewis, S. Loren, and Hollander, "Crystal Structure of Osmylated C<sub>60</sub>: Confirmation of the Soccer Ball Framework," *Science*, **252**, 312-313 (1991). <https://doi.org/10.1126/science.252.5003.312>
- [49] R.C. Haddon, L.E. Brus, and K. Raghavachari, "Rehybridization and  $\pi$ -orbital alignment: the key to the existence of spheroidal carbon clusters," *Chem. Phys. Lett.* **131**, 165-169 (1986). [https://doi.org/10.1016/0009-2614\(86\)80538-3](https://doi.org/10.1016/0009-2614(86)80538-3)
- [50] A.L. Balch, V.J. Catalano, J.W. Leen, M.M. Olmstead, and S.R. Parkin, "(eta-2-C<sub>70</sub>)Ir(CO)Cl(PPh<sub>3</sub>)<sub>2</sub>: the synthesis and structure of an iridium organometallic derivative of a higher fullerene," *J. Amer. Chem. Soc.* **113**, 8953-8955 (1991). <https://doi.org/10.1021/ja00023a057>
- [51] A. Augustyn, *Silicon*, (Encyclopædia Britannica, Inc). <https://www.britannica.com/science/silicon/Uses>

- [52] M. Yoshida, *Nanotube Modeler* (Nanocoones, Bucky-Ball, Fullerenes, Simulation Software) (JCrystalSoft, 2005-2018). <http://www.jcrystal.com/products/wincnt/index.htm>
- [53] Sandia National Laboratories, Large-scale Atomic/Molecular Massively Parallel Simulator (LAMMPS), 2023, <https://www.lammps.org/>
- [54] Java, Jmol, 2023, <http://www.jmol.org/>
- [55] W.G. Hoover, "Canonical dynamics: Equilibrium phase-space distributions", *Physical Review A*, **31**, 1695, (1985). <https://doi.org/10.1103/PhysRevA.31.1695>
- [56] Y. S. Al-Hamdani, D. Alfe, O. A. von Lilienfeld, and A. Michaelides, "Tuning dissociation using isoelectronically doped graphene and hexagonal boron nitride: Water and other small molecules," *J. Chem. Phys.* **144**, 154706 (2016). <https://doi.org/10.1063/1.4945783>
- [57] D.C. Sorescu, D.L. Thompson, M.M. Hurley, and C.F. Chabalowski, "First-principles calculations of the adsorption, diffusion, and dissociation of a CO molecule on the Fe(100) surface," *Phys. Rev. B*, **66**, 035416 (2002). <https://doi.org/10.1103/PhysRevB.66.035416>

**КОМП'ЮТЕРНЕ МОДЕЛЮВАННЯ АДСОРБЦІЇ МОЛЕКУЛИ ФУЛЕРЕНУ C60  
НА РЕКОНСТРУКЦІЙНІЙ ПОВЕРХНІ Si(100).**

**Ікром З. Уролов<sup>a,c</sup>, Фарід Ф. Умаров<sup>b</sup>, Ішмумін Д. Ядгаров<sup>a</sup>, Ганібой Т. Рахманов<sup>c</sup>, Хайтмурод І. Джабборов<sup>d</sup>**

<sup>a</sup>Інститут іонно-плазмових і лазерних технологій імені У.А. Аріфов, Академія наук Узбекистану,  
Ташкент, 100125 Узбекистан

<sup>b</sup>Казахсько-Британський технічний університет, Алмати, 050000, Казахстан

<sup>c</sup>Національний університет Узбекистану імені Мірзо Улугбека, Ташкент, 100174, Узбекистан

<sup>d</sup>Ташкентський університет інформаційних технологій імені Мухаммеда аль-Хорезмі, Ташкент, 100084 Узбекистан

Досліджено адсорбцію молекули фулерену C60 у різних конфігураціях на реконструйованій поверхні Si(100) кремнію. Серед фулеренів особливе значення має фулерен C60, який має найбільш стабільну форму і складається з 60 атомів вуглецю. Монокристалічний кремній має структуру алмазу, розмір його кристалічної решітки 5,43 Å. Розрахунки MD-симуляції були виконані з використанням пакета програмного забезпечення LAMMPS MD-simulator з відкритим кодом та комп'ютерної програми Nanotube Modeler. Міжатомний потенціал Терсоффа використовувався для визначення взаємодії між атомами Si-Si, C-C і Si-C. Енергія адсорбції молекули C60 на реконструйованій поверхні Si(100), довжини зв'язків і кількість утворених зв'язків залежать від геометрії адсорбції, тобто в якій точці на підкладці молекула адсорбується та в якій конфігурації.

**Ключові слова:** *поверхня; молекула фулерену; адсорбція; кремній; моделювання; потенціал Бреннера; довжина зв'язку; атом; потенційна енергія; взаємодія*

## STRENGTH PROPERTIES OF 25CrMoV STEEL MODIFIED BY COMPLEX ION PLASMA TREATMENT WITH DEPOSITION OF INTERLAYER METAL COATINGS

Yuriy A. Zadneprovskiy\*, Vitaliy A. Belous, Yuliya A. Besedina, Galyna N. Tolmachova

National Science Center "Kharkiv Institute of Physics and Technology", Kharkiv, Ukraine

\*Corresponding Author e-mail: [yaz@kipt.kharkov.ua](mailto:yaz@kipt.kharkov.ua)

Received March 24, 2024; revised April 19, 2024; accepted April 30, 2024

To improve erosion resistance, strength, and other protective properties, a comprehensive modification of the surface layers of 25CrMoV steel, which is widely used in turbine construction, was performed. For comparative studies, modifications with different interlayer materials (Mo and Ti) and modifications without interlayer were used. The Mo and Ti layers were deposited on a nitrided ion plasma surface. The outer protective layer for all modifications was unchanged and consisted of a Mo<sub>2</sub>N coating. To determine the role of the deposition of interlayer metal coatings on the strength properties of the complex modified coatings, the distributions of hardness (H, GPa), Young's modulus (E, GPa), and other strength parameters (H/E and H<sup>3</sup>/E<sup>2</sup>) measured by cross sections (h, μm) were investigated. The hardness of the Mo<sub>2</sub>N coating was ~30 GPa, and the hardness of the nitrided layer was ~12 GPa. The modulus of elasticity for the Mo<sub>2</sub>N coating was ~415 GPa, and for the nitrided steel - ~270 GPa. It was found that the main factor influencing the strength properties of a multilayer structure is related to the different materials of the metal layers. For the Mo and Ti layers, the values of E differ significantly (~340 GPa and ~180 GPa, respectively), with almost identical values of H (~6.5 GPa). The distributions of elastic modulus  $E = f(h)$  measured in the modified layers correlate well with the distributions of nitrogen concentration  $C_N = f(h)$ . The distributions of  $H/E = f(h)$  and  $H^3/E^2 = f(h)$  for the modifications with Mo and Ti layers show a decrease in mechanical properties in the areas of the intermediate layers (Mo and Ti). For the modification without interlayer, the distributions of these indicators do not show such a drawback. The cavitation resistance of the comprehensively modified 25CrMoV steel is up to 2 times higher than that of the steel in the original condition. NSC KIPT performed extensive ion plasma modification on a pilot batch of turbine parts. These products, which are part of the steam distribution mechanisms, were manufactured by Ukrainian Power Machines JSC (Kharkiv) for the thermal power industry.

**Keywords:** Complex surface modification; Steel; Ion-plasma nitriding; Vacuum-arc coatings; Hardness; Elastic modulus; Wear resistance; Strength

**PACS:** 52.77.Dq, 66.30.-h

### INTRODUCTION

An effective way to protect against various types of erosive wear is ion-plasma modification of the surface of structural materials, which can be realized both by ion-plasma nitriding [1, 2] and by deposition of vacuum-arc PVD coatings [3]. One of the disadvantages of nitriding, which limits the prospects of its application, is considered to be the low hardness of the nitrided surface compared to nitride coatings, which causes its increased erosive wear. Methods of ion-plasma treatment of working surfaces, including the combined effect associated with nitriding and deposition of hardening coatings, provide protection against a complex of various destructive factors [4, 5]. Thus, in order to increase the service life of parts of power engineering, where it is necessary to ensure both the strength of working surfaces against the effects of high mechanical loads and their various anti-erosion resistance, a complex ion-plasma modification of 25CrMoV steel was used [6, 7]. It consisted of surface hardening by ion nitriding followed by deposition of protective anti-erosion coatings. The advantages of such a complex treatment are the creation of a strong structure of modified surface layers with high interlayer adhesion properties. The structure of this layered structure with a hardness gradient in depth from the surface can be represented by modified layers: nitride coating with high hardness  $H \geq 25$  GPa and nitrided steel  $H \geq 8$  GPa. The initial value of hardness of the non-nitrided surface of 25CrMoV steel is ~4 GPa.

At the same time, metal layers are used to improve the adhesion of nitride layers to various substrate materials during vacuum arc deposition. Such layers are usually conveniently deposited from the same cathode material as the nitride layers. When metal films are used in a multilayer structure, the strength and performance of the structure may depend on the material and its mechanical properties.

The distributions of hardness (H, GPa), elastic modulus (E, GPa), and other strength indices (H/E and H<sup>3</sup>/E<sup>2</sup>) measured from cross-slits have been investigated to determine the role of interlayer metal coating deposition on the strength characteristics of complex-modified layers. The dependence of the distributions of these mechanical properties and nitrogen distributions on the distance across the interlayer boundaries (h, μm) was considered. For comparative studies intermediate layers of Mo and Ti metals were used. The metal layers were deposited on the surface of 25CrMoV steel nitrided by ion-plasma method. The outer protective layer for all variants of modifications was unchanged and consisted of Mo<sub>2</sub>N coating. The erosion resistance of complexly modified steel samples with different composition of intermediate layers was investigated during cavitation tests.

### EXPERIMENTAL DETAILS

The ion-plasma treatment of samples and working surfaces of parts was carried out on the "Bulat" equipment, specially modernized for complex modification (Fig. 1).

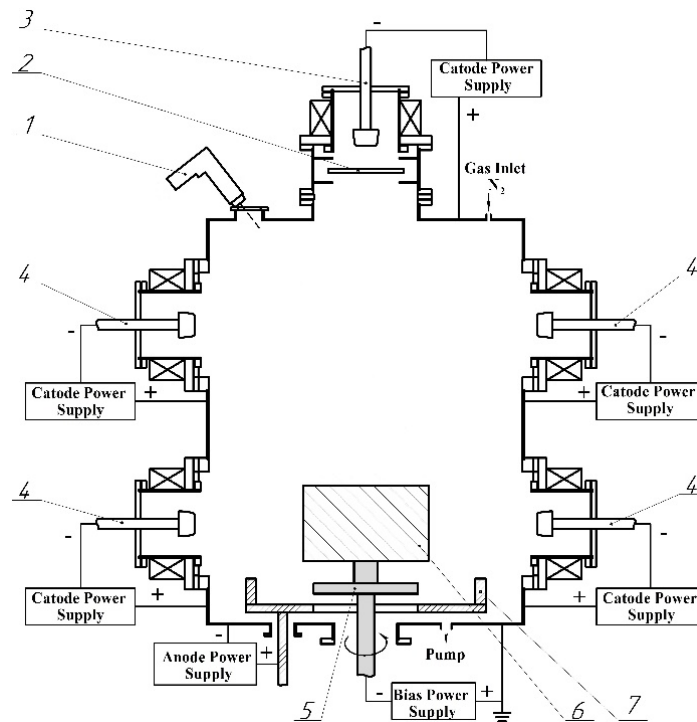


**Figure 1.** Scheme of the experiment: 1 - pyrometer, 2 - shield, 3 - plasma source of the first stage of two-stage discharge, 4 - plasma sources with Mo or Ti cathodes, 5 - rotation device, 6 - model of the part, 7 - electrode of the second stage of discharge

The dimensions of the vacuum chamber (600 mm × 650 mm × 850 mm) and the equipment of the unit (Fig. 1) allow both small and large parts weighing up to 15 kg to be subjected to complex processing. A detailed scheme of the experiment with placement of the part model and research samples inside the vacuum chamber is presented in [8]. 25CrMoV steel was subjected to surface modification. At the initial stage of the complex modification in the working chamber of the equipment ion nitriding of products in a two-stage vacuum arc discharge took place [9]. In this case, the pressure of the working gas, nitrogen, automatically supplied to the vacuum chamber was  $2.7 \times 10^{-1}$  Pa. The current density of gas ions accelerated by the potential - 500 V applied to the substrate was  $\sim 10$  mA/cm<sup>2</sup>. The temperature of the substrate was kept between 550 °C and 600 °C and monitored by a pyrometer. The nitriding time was 40 minutes. The next step in the complex process was the vacuum arc deposition of an interlayer coating of Mo or Ti metals. The deposition of this layer was performed under high vacuum conditions  $\sim 2.7 \times 10^{-3}$  Pa. The thicknesses of the layers were 3 μm and 6 μm. Part of the experiments was carried out without deposition of the intermediate layer. In the final stage of the complex modification, a Mo<sub>2</sub>N protective coating with a thickness of  $\sim 10$  μm was deposited at a nitrogen pressure of  $3 \times 10^{-1}$  Pa.

The following mechanical properties were used to study the strength properties of the modified layers:

H - hardness, GPa; E - Young's modulus, GPa;

H/E - coefficient characterizing the resistance of the material to mechanical action (elastic fracture deformation) [10] or its resistance to wear;

$H^3/E^2$  - coefficient characterizing the material's resistance to plastic deformation [11] (it is used to assess the strength of coatings).

The study was conducted using the Nanoindenter G200 with a Berkovich diamond indenter. The G200 instrument meets the requirements of the international standard ISO 14577 [12]. Hardness and Young's modulus measurements of the modified coatings were performed on cross sections of the samples with the indenter passes at an acute angle ( $\sim 10^\circ$ ) to the interlayer boundaries. A step-by-step indentation mode with 2 μm spacing and 200 nm nanoindenter penetration depth was used.

The distributions of nitrogen concentrations along the cross sections of the modified layers were studied using a scanning electron microscope (SEM) JSM 700-1F (Jeol, Japan) equipped with an X-ray energy dispersive microanalysis system.

Cavitation tests of samples with complex modified surface were performed on the apparatus [13]. The setup was an ultrasonic generator providing oscillations of the emitter at a frequency of 20 kHz. Erosion of the surface of the modified sample occurs when the device is operated in water, where a cavitation region is created under the end of the emitter. The total time of cavitation action on each sample was 6 hours. The degree of coating destruction was determined by weight loss ( $\Delta p$ , mg) as a function of cavitation exposure time (t, hours).

## RESULTS AND DISCUSSION

Fig. 2 shows hardness distributions ( $H$ , GPa) obtained by indenting the surface of cross sections of complexly modified 25CrMoV steel specimens with different thicknesses of Mo and Ti interlayer coatings. The vertical lines in the figure indicate the boundaries between the modified layers.

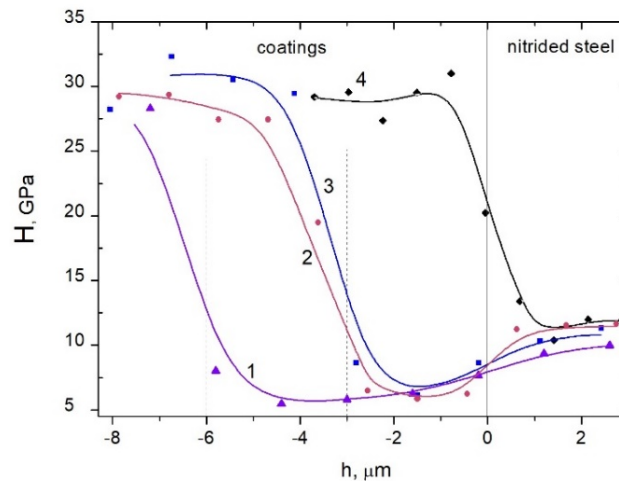


**Figure 2.** Hardness distributions along cross sections of modified coatings with Mo (1, 3), Ti (2) interlayers and no metal layer (4). The layer thicknesses are: 3  $\mu\text{m}$  (2, 3) and 6  $\mu\text{m}$  (1).

Figure 2. illustrates that all hardness distributions (1, 2, 3, and 4) exhibit similar characteristics. Curve 4, which represents the distribution for the sample without a metal layer, shows a sharp transition from the hardness values of the Mo<sub>2</sub>N coating (approximately 30 GPa) to the hardness of nitrided steel (approximately 12 GPa). Curves 2 and 3, which represent modifications with metal layers of the same thickness (3  $\mu\text{m}$ ) but different materials (Ti and Mo), are nearly identical. During these curves, we observe the same transition in Mo<sub>2</sub>N hardness values. However, the transition occurs up to approximately 6.5 GPa in the metal layers section. To the right of the coating-nitrided steel interface, there is a further increase in hardness to the level of nitrided steel, which is approximately 12 GPa. The distributions for the same layer material (Mo) but with different thicknesses (3  $\mu\text{m}$  or 6  $\mu\text{m}$ ) differ in the width of the section with a hardness of 6.5 GPa by a factor of almost 2. The differences in the distributions are due to the difference in the thicknesses of the metal layers.

Figure 3 displays the distributions of Young's modulus ( $E$ , GPa) in the modified layers and nitrogen concentrations ( $C_N$ , at. %) for steel specimens with different coatings as a function of distance  $h$  across the specimen slit.

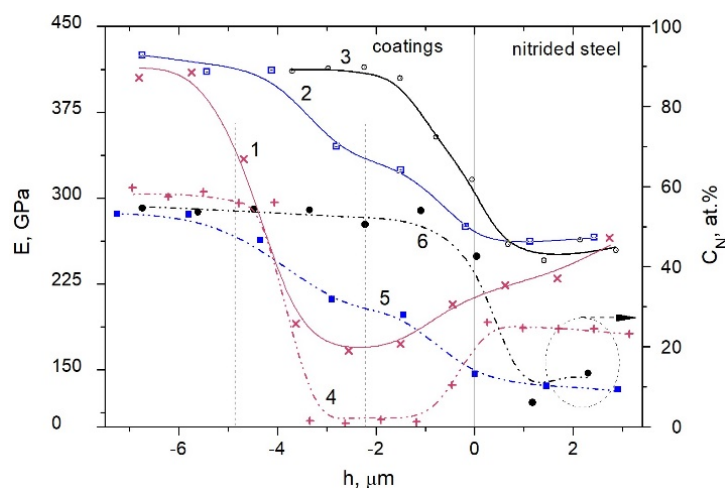


**Figure 3.** Distributions of Young's modulus (1, 2, 3) and nitrogen concentrations (4, 5, 6) along the cross sections of modified layers with Ti (1, 4), Mo (2, 5) and without metal layer (3, 6) coatings. The thicknesses of the layers (1, 2, 4 and 5) are 3  $\mu\text{m}$ .

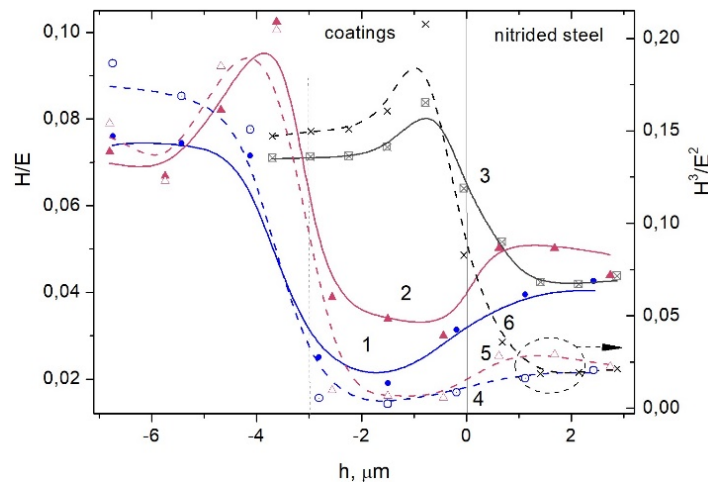
Fig. 3 shows that the Young's modulus distributions (1, 2, and 3) are nearly identical for both the Mo<sub>2</sub>N coating (approximately 415 GPa) and nitrided steel (approximately 270 GPa). The difference in the curves is due to the intermediate layer materials. Specifically, the  $E$  values for the Mo and Ti layers are significantly different, at approximately 340 GPa and 180 GPa, respectively. It can be observed from Figure 2 that the hardness of these layer materials is practically the same. Additionally, Figure 3 shows a strong correlation between the distributions of elastic



modulus  $E = f(h)$  and nitrogen concentration  $C_N = f(h)$ , indicating a direct relationship between the elasticity characteristics of the modified layers and their nitrogen content.

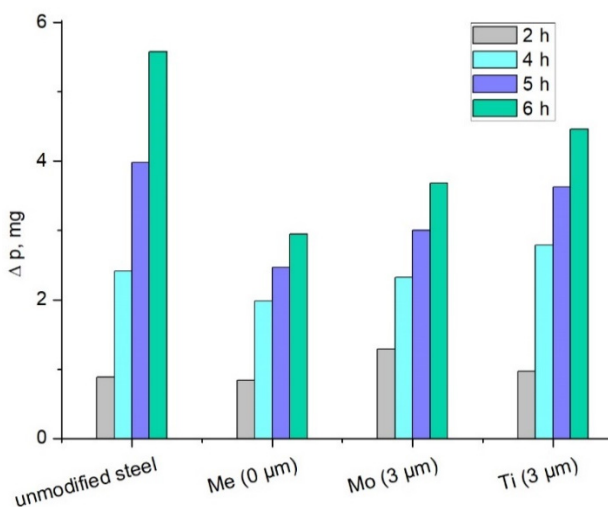
The nitrogen content in the Ti layer is low, at approximately 2 at.%. In contrast, the Mo layer has a significantly higher nitrogen content, at approximately 30 at.%. This difference can be attributed to the formation of  $Ti_xN$  compounds at the boundaries of the Ti layer, which reduces the mobility of  $N_2$  and prevents its penetration into the layer. The Mo layer has a lower affinity for nitrogen than titanium. As a result, the hardness values of the Mo layer (Fig. 2 (3)) are lower compared to the high values typically found in molybdenum nitride compounds.

Figure 4 displays the distribution curves of wear resistance  $H/E$  and strength  $H^3/E^2$  at the boundaries of the modified layers for steel specimens with various interlayer coatings.



**Figure 4.** Distributions of  $H/E$  and  $H^3/E^2$  ratios across the interlayer boundaries of modified layers using Mo (1, 4) and Ti (2, 5) coatings as well as without metal layer (3, 6). The thicknesses of the layers are: 3  $\mu\text{m}$ .

Figure 4 shows the correlation between the wear resistance characteristics  $H/E = f(h)$  (1, 2, 3) and strength characteristics  $H^3/E^2 = f(h)$  (4, 5, 6) for the modified specimens with the same intermediate layers. The curves behave differently for the Mo, Ti, or no layer. For instance, the  $H/E$  ratio average for Mo layer material (1) is approximately 0.02, while for Ti layer (2) it is higher at around 0.035. The figure shows that the  $H/E$  values of the surface layer of nitrided steel for samples with Mo layer and without an intermediate layer (1, 3) are about 0.04, whereas for samples with Ti layer (2) it is significantly higher at around 0.05. The wear resistance characteristics of  $Mo_2N$  coating are high, with an index value of approximately 0.072 for all modifications (1, 2, 3). Curves 2 and 3 show maxima in the transition to  $Mo_2N$  sites, unlike curve 1. These maxima can be attributed to the formation of structural zones during the formation of transition layers. The thickness of these zones, as shown in the figure, is approximately 2  $\mu\text{m}$  or more.



**Figure 5.** Weight loss during cavitation tests of unmodified steel samples and complex-modified samples with interlayers of different compositions

As can be seen from Figure 5, the lowest wear up to the cavitation impact at each time stage of the test is characterized by the specimen that has undergone complex treatment without the deposition of a metal layer. Furthermore, the wear increases almost linearly from the sample with Mo layer to the sample with Ti layer. Therefore, the cavitation wear of the

The wear resistance and strength of the modified steel layers depend on the material of the deposited metal layer. The analysis shows that modifications with Mo and Ti layers exhibit a decrease in mechanical properties in the areas of metal layers (Mo and Ti), which can affect the strength properties of the entire multilayer structure. It is important to note that  $H/E = f(h)$  and  $H^3/E^2 = f(h)$  distributions are also affected. Modifications without an intermediate layer at the transition section of the nitrided steel coating do not exhibit a decrease in characteristics.

The results indicate that when using a metal layer material in a multilayer structure, reducing the thickness of interlayer coatings by at least half can prevent a decrease in mechanical properties.

Figure 5 displays the weight loss diagram ( $\Delta p = f(t)$ ) for the complex modified samples resulting from cavitation tests. Tests were conducted on modified samples of 25CrMoV steel with different coating materials (Mo, Ti or no coating) for 6 hours ( $t$ , hours). The Mo and Ti layers had a thickness of 3  $\mu\text{m}$ .

Mo<sub>2</sub>N layer for the complex modification with Ti interlayer is higher than that for the modification with Mo layer. The maximum wear is that of the untreated steel sample. As can be seen from the diagram, complex modification improves the surface resistance of 25CrMoV steel to cavitation-erosion wear up to 2 times. The highest erosion resistance is shown by the modification without interlayer coating.

Figure 6 shows images of the surface microstructure of the original steel and modified samples after 6 hours of cavitation testing.

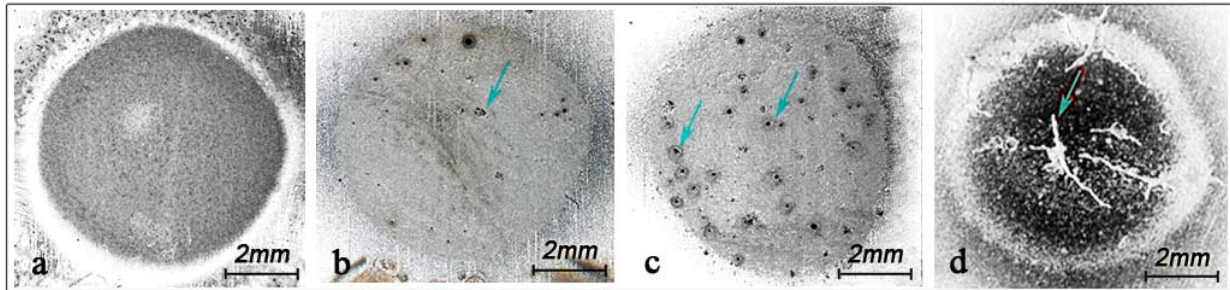


**Figure 6.** Surface microstructure of specimens after 6 h of cavitation tests: untreated steel (a), Mo<sub>2</sub>N coating without interlayer (b), Mo<sub>2</sub>N with 3 μm Mo layer (c) and Mo<sub>2</sub>N with 3 μm Ti layer (d).

Figure 6 illustrates that the wear characteristics of the surfaces differ qualitatively. The untreated steel surface (a) exhibits uniform erosive wear across the area, while the Mo<sub>2</sub>N coating surface deposited without an interlayer (b) and with a Mo layer (c) is characterized by pitting wear, which occurs in the places where macroparticles of the cathode material are deposited [15]. The figure shows that the number of pitting failures is higher for the sample with Mo interlayer. The defects on the surface of the Mo<sub>2</sub>N coating with Ti layer (d) after cavitation impact are different from those on the samples with Mo layer. In this modification, larger defects in the form of 'crack stars' are observed on the surface of Mo<sub>2</sub>N.

Fractures are caused by the microshock action of cavitation bubbles, which apply pressure on the surface areas of the specimen, leading to their vibration and deformation [16, 17]. It is important to note that in multilayer structures, there is a softer metal layer beneath the hard coating of molybdenum nitride. As a result, the outer Mo<sub>2</sub>N layer of such specimens' experiences more intense vibration and deformation. Furthermore, molybdenum nitride is known for its increased internal stress, which makes it quite brittle [7, 18]. These factors contribute to the formation of microcracks, which can lead to increased erosion into the material over time. Samples that are strengthened in a complex manner without metal coating do not have a soft layer and the process of microcrack formation is slower.

The nature of Mo<sub>2</sub>N coating surface failures varies depending on the material of the intermediate layers (Mo or Ti). This can be attributed to the different physical and mechanical properties generated during the deposition process. The dependencies presented in Fig. 3 show that the intermediate layers have different values of Young's modulus: for Mo ~ 340 GPa and for Ti ~ 180 GPa. When the multilayer structure contains a more ductile titanium coating, the surface Mo<sub>2</sub>N layer experiences greater deformations in the vibrating areas, resulting in larger-scale failures in the form of 'star-cracks' in the pitting areas.

The NSC KIPT utilized the complex ion-plasma modification method to strengthen a research batch of turbine parts. JSC Ukrainian Energy Machines, Kharkiv, manufactures these products for nuclear and thermal power engineering. The hardened parts are utilized in hinge joints and other friction pairs of steam distribution mechanisms.

Figure 7 displays images of steel parts that have been modified with Mo<sub>2</sub>N coating deposition on the nitrided surface. The 'Pull rod' part (a) was hardened with Mo layer deposition, while the 'Axle' parts (b) were hardened with both modifications: with and without layer deposition.

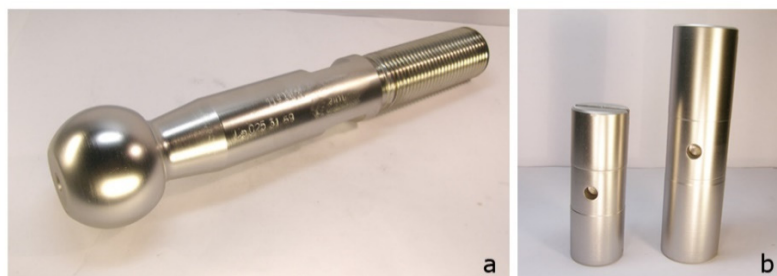


**Figure 7.** Image of parts "Pull rod" (a) and "Axle" (c), strengthened by complex method with Mo<sub>2</sub>N deposition and different thicknesses of interlayer coatings.

Figure 8 displays the friction pair used in the steam distribution mechanisms of the K-325 turbine, consisting of the 'Axle' (located in the center) and the 'Insert' parts. The 'Axle' part is coated with Mo<sub>2</sub>N, with an intermediate layer of Mo (0.7 μm) after ion nitriding. The 'Insert' part is coated with titanium nitride TiN, without an intermediate layer.



**Figure 8.** Images of parts ("Axis" - in the center and "Insert" - on the edges) of the friction pair included in the steam distribution unit of the K-325 turbine.

Table 1 shows the dimensional characteristics and types of protective coatings of parts strengthened by complex ion-plasma treatment.

**Table 1.** Specifications of parts strengthened by complex ion-plasma treatment.

Name of the parts	Overall dimensions (mm)	Material of parts	Weight (kg)	Protective coating
Pull rod	Ø 60×285	35CrMo	2.8	Mo <sub>2</sub> N
Axle	Ø 40×150	25CrMoV	1.5	Mo <sub>2</sub> N
Axle	Ø 35×98	25CrMoV	0.7	Mo <sub>2</sub> N
Insert	Ø 35×25	25CrMoV	0.2	TiN

The strengthened parts were handed over to the manufacturer for installation in mechanisms working in operational conditions of steam turbines.

### CONCLUSIONS

- To enhance the protective characteristics of 25CrMoV steel, a complex ion-plasma modification was performed. This involved depositing external Mo<sub>2</sub>N and interlayer coatings of either Mo or Ti on the surface.
- The Mo<sub>2</sub>N coating in the multilayer structure has a hardness of approximately 30 GPa, while the nitrided steel layer has a hardness of approximately 12 GPa. The Young's modulus E of these coatings is ~ 415 GPa and ~ 270 GPa, respectively.
- The elastic properties of the interlayer coatings are the main factor influencing the wear resistance and strength properties of the modified layers. For Mo and Ti layers, the average E values are significantly different (around 340 GPa and 180 GPa, respectively), while the H values are practically the same (around 6.5 GPa).
- The resistance of 25CrMoV steel surface to cavitation-erosion wear can be improved up to two times by making complex modifications. The modification without an interlayer has the highest resistance. The inclusion of a more ductile Ti layer in the multilayer structure leads to large-scale surface failures.
- NSC KIPT performed ion-plasma strengthening of a research batch of parts for steam distribution mechanisms of turbines produced by JSC "Ukrainian Energy Machines". The strengthened parts will be installed in the mechanisms working under the operating conditions of steam turbines.

### Acknowledgment

The work was financially supported by the National Academy of Science of Ukraine (program "Support of the development of main lines of scientific investigations" (KPKVK 6541230)).

### ORCID

- Yuriy A. Zadneprovskiy, <https://orcid.org/0000-0003-2754-4051>;
Vitaliy A. Belous, <https://orcid.org/0000-0002-9371-4138>  
Yuliya A. Besedina, <https://orcid.org/0009-0004-3323-1478>;
Galyna N. Tolmachova, <https://orcid.org/0000-0002-0786-2979>

### REFERENCES

- J. Vetter, W. Burgmer, and A.J. Perry, *Surface and Coatings Technology*, **59**(1-3), 152 (1993), [https://doi.org/10.1016/0257-8972\(93\)90074-X](https://doi.org/10.1016/0257-8972(93)90074-X)
- N.A. Dolgov and A.V. Rutkovskiy, *Strength of Materials*, **54**(5), 819 (2022), <https://doi.org/10.1007/s11223-022-00458-4>
- I.I. Akseonov, V.A. Belous, V.E. Strel'nitskij, and D.S. Aksyonov, *Problems of Atomic Science and Technology*, **104**(4), 58 (2016), [https://vant.kipt.kharkov.ua/ARTICLE/VANT\\_2016\\_4/article\\_2016\\_4\\_58.pdf](https://vant.kipt.kharkov.ua/ARTICLE/VANT_2016_4/article_2016_4_58.pdf)
- Y. Sun, and T. Bell, *Transactions of the Institute of Metal Finishing*, **70**(1), 38 (1992), <https://doi.org/10.1080/00202967.1992.11870939>
- L. Escalada, J. Lutz, S.P. Brühl, M. Fazio, A. Márquez, S. Mändl, D. Manova, and S.N. Simison, *Surface and Coatings Technology*, **223**, 41 (2013), <https://doi.org/10.1016/j.surfcoat.2013.02.025>
- V.A. Belous, I.G. Ermolenko, Y.A. Zadneprovskiy, and N.S. Lomino, "HighMatTech-2015", Kyiv, Ukraine, (2015), [https://compnano.kpi.ua/pdf\\_files/conf-mems/hi-m-t-progr-15-eng.pdf](https://compnano.kpi.ua/pdf_files/conf-mems/hi-m-t-progr-15-eng.pdf)
- V.A. Belous, I.G. Yermolenko, Yu.A. Zadneprovskiy, and N.S. Lomino, *Problems of Atomic Science and Technology*, **104**(4), 93 (2016), [https://vant.kipt.kharkov.ua/ARTICLE/VANT\\_2016\\_4/article\\_2016\\_4\\_93.pdf](https://vant.kipt.kharkov.ua/ARTICLE/VANT_2016_4/article_2016_4_93.pdf)



- [8] V.A. Belous, Yu.A. Zadneprovsky, and I.S. Domnich, Problems of Atomic Science and Technology, **135**(5), 115 (2021), <https://doi.org/10.46813/2021-135-115>
- [9] A.A. Andreev, V.V. Kunchenko, L.P. Sablev, and V.M. Shulaev, "Duplex processing of tool steels in vacuum," in: *Equipment and technologies for heat treatment of metals and alloys in mechanical engineering*, part 2, (NSC KIPT, Kharkiv, 2001), p. 48-56. (in Russian)
- [10] V.I. Kushch, S.N. Dub, R.S. Shmegeera, Y.V. Sirota, and G.N. Tolmacheva, Journal of Superhard Materials, **37**(3), 173 (2015), <https://doi.org/10.3103/S1063457615030041>
- [11] V.I. Kushch, and S.N. Dub, Journal of Superhard Materials, **34**(3), 149 (2012), <https://doi.org/10.3103/S106345761203001X>
- [12] ISO/CD 14577-1 Metallic materials. Instrumented indentation test for hardness and materials parameters. Part 1: Test method. <https://www.iso.org/standard/85223.html>
- [13] I.O. Klimenko, V.G. Marinin, V.A. Belous, N.A. Azarenkov, M.G. Ishchenko, V.S. Goltvyanytsya, and A.S. Kuprin, Problems of Atomic Science and Technology, **147**(5), 126 (2023), <https://doi.org/10.46813/2023-147-126>
- [14] M. Drouet, and E. Le Bourhis, Materials, **16**(13), 4704 (2023), <https://doi.org/10.3390/ma16134704>
- [15] A. Krella, Coatings, **10** (10), 921 (2020), <https://doi.org/10.3390/coatings10100921>
- [16] V. Safonov, A. Zykova, J. Steller, G. Tolmachova, and N. Donkov, Journal of Physics: Conference Series, **2487**(1), 012034 (2023), <https://doi.org/10.1088/1742-6596/2487/1/012034>
- [17] A.K. Krella, Materials, **16** (5), 2058 (2023), <https://doi.org/10.3390/ma16052058>
- [18] A. Gilewicz, B. Warcholinski, and D. Murzynski, Surface and Coatings Technology, **236**, 149 (2013), <https://doi.org/10.1016/j.surfcoat.2013.09.005>

### ХАРАКТЕРИСТИКИ МІЦНОСТІ МОДИФІКОВАНОЇ КОМПЛЕКСНОЮ ІОННО-ПЛАЗМОВОЮ ОБРОБКОЮ СТАЛІ 25ХМ1Ф З ОСАДЖЕННЯМ МІЖШАРОВИХ МЕТАЛЕВИХ ПОКРИТТІВ

Юрій О. Задніпровський, Віталій А. Білоус, Юлія А. Беседіна, Галина М. Толмачова

*Національний науковий центр «Харківський фізико-технічний інститут», Харків, Україна*

З метою підвищення ерозійної стійкості, міцності та інших захисних характеристик проведено комплексне модифікування поверхневих шарів сталі 25CrMoV, яка широко застосовується в турбобудуванні. Для проведення порівняльних досліджень використано модифікації з різними матеріалами проміжних шарів (Mo і Ti) і модифікації без проміжного шару. Шари з Mo і Ti осаджували на азотовану іонно-плазмовим способом поверхню. Зовнішній захисний шар для всіх модифікацій був незмінним і складався з покриття Mo<sub>2</sub>N. Для визначення ролі осадження міжшарових металевих покриттів на характеристики міцності модифікованих комплексно шарів досліджено розподіли твердості (H, GPa), Модуля пружності (E, GPa) та інших показників міцності (H/E та H<sup>3</sup>/E<sup>2</sup>), виміряні за поперечними шліфами (h, μm). Твердість покриття Mo<sub>2</sub>N склала ~ 30 GPa, а твердість азотованого шару ~ 12 GPa. Модуль пружності для покриття Mo<sub>2</sub>N склав ~ 415 GPa, для азотованої сталі - ~ 270 GPa. Встановлено, що основний фактор, який впливає на характеристики міцності багатошарової конструкції, пов'язаний із різним матеріалом металевих шарів. Для Mo і Ti шару значення E істотно відрізняються (~ 340 GPa і ~ 180 GPa, відповідно), при практично однакових значеннях H (~ 6,5 GPa). Розподіли модуля пружності  $E = f(h)$ , виміряні в модифікованих шарах, добре корелюють із розподілами концентрації азоту  $C_N = f(h)$ . Розподіли  $H/E = f(h)$  і  $H^3/E^2 = f(h)$  для модифікацій з Mo і Ti шарами демонструють зниження механічних характеристик на ділянках проміжних шарів (Mo і Ti). Для модифікації без проміжного шару розподіли цих показників такого недоліку не мають. Кавітаційна стійкість комплексно модифікованої сталі 25CrMoV до 2 разів вища, ніж сталі у вихідному стані. В ННЦ ХФТІ було проведено комплексну іонно-плазмову модифікацію дослідної партії деталей турбін. Ці вироби, що входять до механізмів паророзподілу, виготовлені АТ "Українські енергетичні машини" (м. Харків) для теплової енергетики.

**Ключові слова:** комплексна модифікація поверхні; сталь; іонно-плазмове азотування; вакуумно-дугові покриття; твердість; модуль пружності; зносостійкість; міцність

## ANALYSIS OF KINETIC PROPERTIES AND TUNNEL-COUPLED STATES IN ASYMMETRICAL MULTILAYER SEMICONDUCTOR STRUCTURES

 Rustam Y. Rasulov<sup>a</sup>,  Voxob R. Rasulov<sup>a\*</sup>, Kamolakhon K. Urinova<sup>b</sup>,

 Islombek A. Muminov<sup>a</sup>,  Bakhodir B. Akhmedov<sup>a</sup>

<sup>a</sup> Fergana State University, Fergana, Uzbekistan

<sup>b</sup> Kokand State pedagogical Institute, Kokand, Uzbekistan

\*Corresponding Author e-mail: [vrrasulov83@gmail.com](mailto:vrrasulov83@gmail.com)

Received February 26, 2024; revised March 30, 2024; accepted April 2, 2024

This study investigates the kinetic properties of both symmetrical and asymmetrical multilayer and nano-sized semiconductor structures. We develop a theoretical framework using various models and mathematical methods to solve the Schrödinger matrix equation for a system of electrons, taking into account the Bastard condition, which considers the difference in the effective masses of current carriers in adjacent layers. We analyze tunnel-coupled electronic states in quantum wells separated by a narrow tunnel-transparent potential barrier. Our findings provide insights into the electronic properties of semiconductor structures, which are crucial for applications in micro- or nanoelectronics and other areas of solid-state physics.

**Keywords:** Multilayer and nano-sized semiconductor structures; Schrödinger matrix equation; Hamiltonian; Electrons; Quantum wells; Effective mass; Tunneling effect; Electronic transport; Bastard condition

**PACS:** 71.20. – b, 71.28. + d

### INTRODUCTION

The exploration of electronic properties in semiconductor structures, whether symmetrical or asymmetrical, holds significant relevance for their application in micro- and nanoelectronics, as well as broader fields of solid-state physics. While prior research has delved into the kinetic properties of these multilayer and nanoscale structures, employing a variety of models and mathematical methodologies to tackle the full Schrödinger equation for electron systems, a gap remains. Notably, these investigations have overlooked the Bastard condition, which accounts for the variance in effective masses of charge carriers across adjacent layers. Furthermore, there has been a lack of focus on the study of tunnel-coupled electronic states within quantum wells, especially those delineated by narrow, tunnel-permeable potential barriers. Our research is designed to bridge these gaps, offering new insights into the physics of semiconductor structures by incorporating these critical factors.

### METHODS

In structures featuring two or more closely spaced potential wells, the wave functions from adjacent wells significantly overlap within the barrier region. This overlap leads to a substantial probability of detecting an electron within this barrier region, thereby enabling charge carriers to transition from one well to another, even without their energies surpassing the barrier height. This quantum mechanical phenomenon, known as the tunneling effect [9-10], is particularly notable in quantum wells where the tunneling probability is considerable, rendering these wells tunnel-coupled.

The phenomenon of tunnel coupling, which becomes more pronounced as the wells draw nearer to each other, significantly affects both the positioning of energy levels and the characteristics of the wave functions within the wells. To accurately determine the levels of size quantization and their corresponding wave functions, it's essential to solve the Schrödinger equation under a specific potential while adhering to Bastard boundary conditions. These conditions necessitate the continuity of the wave function  $\psi(x)$  and its derivative with respect to mass  $\frac{1}{m} \frac{d\psi}{dx}$  at the interface between the potential well (denoted as Layer A) and the barrier (Layer B). In mathematical terms, this continuity is expressed as:

$$\psi|_A = \psi|_B, \left. \frac{1}{m} \frac{d\psi(x)}{dx} \right|_A = \left. \frac{1}{m} \frac{d\psi(x)}{dx} \right|_B \quad (1)$$

Following the establishment of the Bastard boundary conditions, as denoted by equation (1), it's imperative to incorporate these conditions into our calculations at each interface between different materials within the nanostructure. This approach is critical for accurately modeling the behavior of charge carriers, especially when considering the real wave vector scenarios that result in the wave functions decaying to zero at the limits of  $x \rightarrow \pm\infty$ . Given a nanostructure composed of two quantum wells, we encounter two distinct interfaces that necessitate the resolution of a system comprising equations for eight variables, reflecting the complexity of electron behavior in these confined spaces.

To facilitate our analysis, we define  $U_1(x)$  and  $U_2(x)$  as the potentials for the left and right wells, respectively. These are treated as independent entities within their own spatial domains. For simplicity, and without loss of generality, we position our energy reference at the barrier level, allowing us to consider  $U_1(x)$  and  $U_2(x)$  as being effective only within their respective wells. Consequently, the potential ( $U(z)$ ) describing the dual-well structure emerges as the summation of  $U_1(x)$  and  $U_2(x)$ .

$$H\psi = E\psi, \quad (2)$$

where  $H = H_1 + H_2 + U_1 + U_2$ , with  $H_1(U_1)$  and  $H_2(U_2)$  being the Hamiltonian (potential) operators for the left and right potential wells, respectively. Thus, the general Schrödinger equation takes the form:

$$\left( -\frac{\hbar^2}{2m_1} \vec{\nabla}^2 - \frac{\hbar^2}{2m_2} \vec{\nabla}^2 + U_1 + U_2 \right) \psi = E\psi$$

Transitioning to a one-dimensional analysis simplifies our approach to:

$$\left( -\frac{\hbar^2}{2\mu_{12}^+} \frac{\partial^2}{\partial z^2} + U_1 + U_2 \right) \psi(x) = \left( E - \frac{\hbar^2 k_{\perp}^2}{2\mu_{12}^+} \right) \psi(x) \quad (3)$$

Here,  $\mu_{12}^+$  represents the effective mass term, accounting for the combined mass effects from both wells, and  $k_{\perp}^2 = k_x^2 + k_y^2$  reflects the transverse component of the wave vector. This nuanced formulation provides a direct pathway to solving the individual Schrödinger equations for each well:

$$\left( -\frac{\hbar^2}{2m_1} \frac{\partial^2}{\partial z^2} + U_1 \right) \psi_1 = \left( E_1 - \frac{\hbar^2 k_{\perp}^2}{2m_1} \right) \psi_1, \quad \left( -\frac{\hbar^2}{2m_2} \frac{\partial^2}{\partial z^2} + U_2 \right) \psi_2 = \left( E_2 - \frac{\hbar^2 k_{\perp}^2}{2m_2} \right) \psi_2. \quad (4)$$

Leveraging the principle of superposition, we express the system's wave function as a linear combination of the well-specific wave functions:

$$\psi(x) = C_1 \psi_1(x) + C_2 \psi_2(x) \quad (5)$$

Substituting equation (5) into equation (3) and reconciling this with equation (4), we arrive at a composite equation that encapsulates the interaction between the two wells through the coefficients  $C_1$  and  $C_2$ , manifesting in:

$$\begin{aligned} & C_1 \left( \frac{m_1}{\mu_{12}^+} \left[ -\frac{\hbar^2}{2m_1} \frac{\partial^2 \psi_1(x)}{\partial z^2} + U_1 \psi_1(x) \right] + \left( 1 - \frac{m_1}{\mu_{12}^+} \right) U_1 \psi_1(x) + U_2 \psi_1(x) \right) + \\ & + C_2 \left( \frac{m_2}{\mu_{12}^+} \left[ -\frac{\hbar^2}{2m_2} \frac{\partial^2 \psi_2(x)}{\partial z^2} + U_2 \psi_2(x) \right] + U_1 \psi_2(x) + \left( 1 - \frac{m_2}{\mu_{12}^+} \right) U_2 \psi_2(x) \right) = \\ & = C_1 \left( E - \frac{\hbar^2 k_{\perp}^2}{2\mu_{12}^+} \right) \psi_1(x) + C_2 \left( E - \frac{\hbar^2 k_{\perp}^2}{2\mu_{12}^+} \right) \psi_2(x) \end{aligned} \quad (6)$$

To delve deeper into the system's quantum mechanics, we apply integration by multiplying equation (6) from the left with  $\psi_2^*(x)$ , and similarly with  $\psi_1^*(x)$ , to integrate over the spatial domain. This operation is crucial for isolating the coefficients  $C_1$  and  $C_2$ , facilitating the extraction of meaningful physical parameters:

$$\int \psi_2^*(x) [Equation (6)] dx \text{ and similarly for } \psi_1^*(x)$$

Through this process, we obtain a system of homogeneous equations that encapsulate the interaction dynamics between the quantum wells, structured as follows:

$$\begin{cases} C_1 \left[ \tilde{E}_1 \sigma + \left( 1 - \frac{m_1}{\mu_{12}^+} \right) U_1^{(21)} + U_2^{(21)} - \tilde{E} \sigma \right] + C_2 \left[ \tilde{E}_2 + U_1^{(22)} + \left( 1 - \frac{m_2}{\mu_{12}^+} \right) U_2^{(22)} - \tilde{E} \right] = 0, \\ C_1 \left[ \tilde{E}_1 + \left( 1 - \frac{m_1}{\mu_{12}^+} \right) U_1^{(11)} + U_2^{(11)} - \tilde{E} \right] + C_2 \left[ \tilde{E}_2 \sigma + U_1^{(12)} + \left( 1 - \frac{m_2}{\mu_{12}^+} \right) U_2^{(12)} - \tilde{E} \sigma \right] = 0. \end{cases} \quad (7)$$

The overlaps  $U_1^{(ij)}$  and  $U_2^{(ij)}$  are integrals representing the interaction terms between the wells, and  $\sigma$  symbolizes the overlap integral between  $\psi_2^*$  and  $\psi_1$ . This configuration allows us to calculate the adjusted energies  $\tilde{E}_1$  and  $\tilde{E}_2$ , reflecting the modified energy levels due to the coupling between the wells.

$$\begin{aligned}
 U_1^{(21)} &= \int \psi_2^*(x)U_1\psi_1(x) \cdot dx, U_2^{(21)} = \int \psi_2^*(x)U_2\psi_1(x) \cdot dx, & U_1^{(22)} &= \int \psi_2^*(x)U_1\psi_2(x) \cdot dx, \\
 U_2^{(22)} &= \int \psi_2^*(x)U_2\psi_2(x) \cdot dx, U_1^{(11)} = \int \psi_1^*(x)U_1\psi_1(x)dx, U_2^{(11)} = \int \psi_1^*(x)U_2\psi_1(x) dx, \\
 U_1^{(12)} &= \int \psi_1^*(x)U_1\psi_2(x) dx, U_2^{(12)} = \int \psi_1^*(x)U_2\psi_2(x) dx, \sigma = \int \psi_2^*(x)\psi_1(x) \cdot dx, \tilde{E}_a = E_a - \frac{\hbar^2 k_a^2}{2\mu_{12}^+}, \\
 \tilde{E} &= E - \frac{\hbar^2 k_a^2}{2m_a}, \tilde{E}_1 = \frac{m_1}{\mu_{12}^+} \left( E_1 - \frac{\hbar^2 k_1^2}{2m_1} \right), \tilde{E}_2 = \frac{m_2}{\mu_{12}^+} \left( E_2 - \frac{\hbar^2 k_2^2}{2m_2} \right).
 \end{aligned}$$

For a non-trivial solution of equation (7), the determinant of the system must be set to zero, leading us to:

$$\begin{bmatrix} \tilde{E}_1\sigma + \left(1 - \frac{m_1}{\mu_{12}^+}\right)U_1^{(21)} + U_2^{(21)} - \tilde{E}\sigma & \tilde{E}_2 + U_1^{(22)} + \left(1 - \frac{m_2}{\mu_{12}^+}\right)U_2^{(22)} - \tilde{E} \\ \tilde{E}_1 + \left(1 - \frac{m_1}{\mu_{12}^+}\right)U_1^{(11)} + U_2^{(11)} - \tilde{E} & \tilde{E}_2\sigma + U_1^{(12)} + \left(1 - \frac{m_2}{\mu_{12}^+}\right)U_2^{(12)} - \tilde{E}\sigma \end{bmatrix} = 0. \tag{8}$$

From this, we derive a second-degree algebraic equation for the variable  $\tilde{E}$ , which can be represented in the general form:

$$a\tilde{E}^2 - b \cdot \tilde{E} + c = 0, \tag{9}$$

which has two roots,  $\tilde{E}_{\pm}$ , representing the sought-after energy levels of the electron in the double-well potential  $U(x)$

$$\tilde{E}_+ = \frac{b}{2a} \left( -1 + \sqrt{1 - 4\frac{ac}{b^2}} \right), \tilde{E}_- = \frac{b}{2a} \left( -1 - \sqrt{1 - 4\frac{ac}{b^2}} \right) \tag{10}$$

where

$$\begin{aligned}
 a &= (1 + \sigma^2), b = (1 + \mathcal{E}_6 + \mathcal{E}_2 + \mathcal{E}_3), c = \mathcal{E}_4 - \mathcal{E}_1, \\
 \mathcal{E}_1 &= \left( \tilde{E}_1\sigma + \left(1 - \frac{m_1}{\mu_{12}^+}\right)U_1^{(21)} + U_2^{(21)} \right) \left( \tilde{E}_2\sigma + U_1^{(12)} + \left(1 - \frac{m_2}{\mu_{12}^+}\right)U_2^{(12)} \right), \\
 \mathcal{E}_2 &= \left( \tilde{E}_2\sigma + U_1^{(12)} + \left(1 - \frac{m_2}{\mu_{12}^+}\right)U_2^{(12)} \right) \sigma, \mathcal{E}_3 = \left( \tilde{E}_1\sigma + \left(1 - \frac{m_1}{\mu_{12}^+}\right)U_1^{(21)} + U_2^{(21)} \right) \sigma, \\
 \mathcal{E}_4 &= \left( \tilde{E}_1 + \left(1 - \frac{m_1}{\mu_{12}^+}\right)U_1^{(11)} + U_2^{(11)} \right) \cdot \left( \tilde{E}_2 + U_1^{(22)} + \left(1 - \frac{m_2}{\mu_{12}^+}\right)U_2^{(22)} \right), \\
 \mathcal{E}_5 &= \left( \tilde{E}_2 + U_1^{(22)} + \left(1 - \frac{m_2}{\mu_{12}^+}\right)U_2^{(22)} \right), \mathcal{E}_6 = \left( \tilde{E}_1 + \left(1 - \frac{m_1}{\mu_{12}^+}\right)U_1^{(11)} + U_2^{(11)} \right)
 \end{aligned}$$

By substituting these roots,  $\tilde{E}_+$  and  $\tilde{E}_-$ , back into equation (7) in turn, one can find two solutions of the system,  $\left(\frac{C_1}{C_2}\right)_+$  for  $\tilde{E}_+$  and another  $\left(\frac{C_1}{C_2}\right)_-$  for  $\tilde{E}_-$ , which according to equation (7) determine the wave functions  $\tilde{\psi}_1(z), \tilde{\psi}_2(z)$ , corresponding to the energy levels  $\tilde{E}_+$  and  $\tilde{E}_-$ , respectively.

### CONCLUSIONS

Thus, in tunnel-coupled wells, the energy levels are shifted relative to the levels of isolated wells, and the wave functions emerge from the wave functions of isolated wells as a result of their interaction. The system of equations (7) can be simplified, preserving the main features of its solutions, if we neglect the contributions with terms  $U_{1,2}^{(nn)}$ , where  $n = 1,2$  exceeds the considered range. Consequently, equation (7) takes the form:

$$\begin{cases} \mathfrak{R}_1 C_1 + C_2(\tilde{E}_2 - \tilde{E}') = 0, \\ C_1(\tilde{E}_1 - \tilde{E}') + \mathfrak{R}_2 C_2 = 0, \end{cases} \tag{11}$$

where  $\mathfrak{R}_1 = \left(1 - \frac{m_1}{\mu_{12}^+}\right)U_1^{(21)} + U_2^{(21)}$ ,  $\mathfrak{R}_2 = U_1^{(12)} + \left(1 - \frac{m_2}{\mu_{12}^+}\right)U_2^{(12)}$ . Then, by setting the determinant of the system of equations (11) to zero, we obtain a less cumbersome equation instead of (8):

$$\tilde{E}'^2 - (\tilde{E}_1 + \tilde{E}_2)\tilde{E}' + \tilde{E}_1\tilde{E}_2 + \mathfrak{R}_1\mathfrak{R}_2 = 0, \tag{12}$$

whose roots are equal

$$\tilde{E}'_{\pm} = \frac{1}{2} \left[ \tilde{E}_1 + \tilde{E}_2 \pm \sqrt{(\tilde{E}_1 - \tilde{E}_2)^2 + 4\mathfrak{R}_1\mathfrak{R}_2} \right]. \tag{13}$$

Analyzing the expression for the energy level gap  $\Delta E = |\tilde{E}'_+ - \tilde{E}'_-|$  from equation (13), the quantity  $\Delta E_{asym} = |\tilde{E}'_1 - \tilde{E}'_2|$  serves as a measure of the asymmetry between the two quantum wells and equals zero for symmetric wells. If its square dominates under the square root in equation (4), then  $\Delta E \approx \Delta E_{asym}$ . In this scenario, the solutions of the system (11) correspond to wave functions  $\tilde{\psi}_1(z), \tilde{\psi}_2(z)$  that are close to the original functions  $\psi_1, \psi_2$ , indicating that mixing of the wave functions is almost nonexistent. Conversely, when the asymmetry of the wells is negligibly small, the gap between levels (13) in tunnel-coupled wells is given by  $\Delta E \approx \sqrt{4\mathfrak{R}_1\mathfrak{R}_2}$ , where this quantity characterizes the tunnel splitting of energy levels. In this case, the solutions of the system (11) correspond to a strong mixing of the original wave functions, where the coefficients  $C_1$  and  $C_2$  are comparable in magnitude.

#### ORCID

✉ Rustam Y. Rasulov, <https://orcid.org/0000-0002-5512-0654>; ✉ Voxob R. Rasulov, <https://orcid.org/0000-0001-5255-5612>

✉ Bakhodir B. Akhmedov, <https://orcid.org/0000-0003-4894-3588>; ✉ Islom A. Muminov, <https://orcid.org/0000-0002-2622-6097>

#### REFERENCES

- [1] M. Baldo, *Introduction to Nanoelectronics*, (MIT Open Course Ware, 2011).
- [2] V.V. Mitin, A. Kochelap, and M.A. Strosio, *Introduction to Nanoelectronics: Science, Nanotechnology, Engineering, and Applications*, (Cambridge University Press, 2007). <https://doi.org/10.1017/CBO9780511809095>
- [3] E.P. O'Reilly, and M. Seifkar, "Theory of Electronic Transport in Nanostructures," in *Semiconductor Modeling Techniques*, edited by N. Balkan, and M. Xavier, Springer Series in Materials Science, Vol. 159 (Springer, Berlin, Heidelberg, 2012), pp. 41-69. [https://doi.org/10.1007/978-3-642-27512-8\\_3](https://doi.org/10.1007/978-3-642-27512-8_3)
- [4] D. Szczęśniak, Ph.D. Thesis, "Theoretical and Numerical Modelling of Electronic Transport in Nanostructures," Université du Maine, 2013. <https://www.researchgate.net/publication/278643031>
- [5] E.L. Ivchenko, and G.E. Pikus, *Superlattices and Other Heterostructures: Symmetry and Optical Phenomena*, 2nd ed. Springer Series in Solid-State Sciences (Springer-Verlag, Berlin, Heidelberg, 1997).
- [6] R. Ya. Rasulov, V.R. Rasulov, N.Z. Mamadalieva et al., "Subbarrier and Overbarrier Electron Transfer through Multilayer Semiconductor Structures," *Russ. Phys. J.* **63**, 537–546 (2020). <https://doi.org/10.1007/s11182-020-02067-7>
- [7] V.R. Rasulov, R.Ya. Rasulov, M.A. Mamatova, and F. Qosimov, "Semiclassical Theory of Electronic States in Multilayer Semiconductors" Part 1, in "IV International Conference on Applied Physics, Information Technologies and Engineering (APITECH-IV 2022)", *Journal of Physics: Conference Series*, **2388**, Bukhara, Uzbekistan, (IOP Publishing Ltd, 2022).
- [8] V.R. Rasulov, R.Ya. Rasulov, M.A. Mamatova, and F. Qosimov, "Semiclassical Theory of Electronic States in Multilayer Semiconductors." Part 2, in: *IV International Conference on Applied Physics, Information Technologies and Engineering (APITECH-IV 2022)*, *Journal of Physics: Conference Series*, Vol. 2388, Bukhara, Uzbekistan, (IOP Publishing Ltd, 2022).
- [9] G.H. Shin, C. Park, K.J. Lee, H.J. Jin, and S.-Y. Choi, "Ultrasensitive Phototransistor Based on WSe<sub>2</sub>-MoS<sub>2</sub> van der Waals Heterojunction," *Nano Lett.* **20**, 5741–5746 (2020). <https://doi.org/10.1021/acs.nanolett.0c01460>
- [10] T. Wang, F. Zheng, G. Tang, J. Cao, P. You, J. Zhao, and F. Yan, "Two Dimensional WSe<sub>2</sub> Flakes for Synergistic Modulation of Grain Growth and Charge Transfer in Tin-Based Perovskite Solar Cells," *Adv. Sci.* **8**(11), 2004315 (2021). <https://doi.org/10.1002/advs.202004315>
- [11] E.L. Ivchenko, *Optical Spectroscopy of Semiconductor Nanostructures*, (Alpha Science International Ltd., Harrow, UK, 2005).
- [12] M.M. Glazov, *Electron and Nuclear Spin Dynamics in Semiconductor Nanostructures, Series on Semiconductor Science and Technology*, (OUP Oxford, 2018), <https://doi.org/10.13140/RG.2.2.18718.56640>

#### АНАЛІЗ КІНЕТИЧНИХ ВЛАСТИВОСТЕЙ ТА ТУНЕЛЬНО-ЗВ'ЯЗАНИХ СТАНІВ В АСИМЕТРИЧНИХ БАГАТОШАРОВИХ НАПІВПРОВІДНИКОВИХ СТРУКТУРАХ

Рустам Я. Расулов<sup>а</sup>, Вокхоб Р. Расулов<sup>а</sup>, Камолахон К. Урінова<sup>б</sup>, Ісламбек А. Мумінов<sup>а</sup>, Баходір Б. Ахмедов<sup>а</sup>

<sup>а</sup> Ферганський державний університет, Фергана, Узбекистан

<sup>б</sup> Кокандський державний педагогічний інститут, Коканд, Узбекистан

Це дослідження досліджує кінетичні властивості як симетричних, так і асиметричних багатошарових і нанорозмірних напівпровідникових структур. Ми розробляємо теоретичну базу з використанням різних моделей і математичних методів для вирішення рівняння матриці Шредінгера для системи електронів, враховуючи умову Бастарда, яка враховує різницю в ефективних масах носіїв струму в суміжних шарах. Ми аналізуємо тунельно-зв'язані електронні стани в квантових ямах, розділених вузьким тунельно-прозорим потенційним бар'єром. Наші висновки дають змогу зрозуміти електронні властивості напівпровідникових структур, які мають вирішальне значення для застосування в мікро- чи наноелектроніці та інших областях фізики твердого тіла.

**Ключові слова:** багатошарові та нанорозмірні напівпровідникові структури; матричне рівняння Шредінгера; Гамільтоніан; електрони; умова Бастарда

## RESEARCH OF THE IMPACT OF SILICON DOPING WITH HOLMIUM ON ITS STRUCTURE AND PROPERTIES USING RAMAN SCATTERING SPECTROSCOPY METHODS

Sharifa B. Utamuradova<sup>a</sup>, Shakhrukh Kh. Daliev<sup>a</sup>, Alisher Kh. Khaitbaev<sup>a</sup>, Jonibek J. Khamdamov<sup>a</sup>, Khusniddin J. Matchonov<sup>a\*</sup>, Xushnida Y. Utemuratova<sup>b</sup>

<sup>a</sup>*Institute of Semiconductor Physics and Microelectronics at the National University of Uzbekistan, 20 Yangi Almazar st., Tashkent, Uzbekistan*

<sup>b</sup>*Karakalpak State University, Nukus, Karakalpakstan*

\*Corresponding Author e-mail: [husniddin94\\_04@bk.ru](mailto:husniddin94_04@bk.ru)

Received January 27, 2024; revised April 8, 2024; accepted April 12, 2024

Each crystal structure has its own phonon modes, which appear in the Raman spectrum of Raman scattering. In the case of silicon, phonon modes associated with the diamond structure of silicon can be detected. In a Raman spectrum, the position of the lines, their intensity, and the width of the lines are usually measured. Raman spectroscopy is a powerful tool for studying crystalline materials at the molecular level, and its application in the study of semiconductors and nanomaterials provides important information about their structure and properties. In this study, the spectra of two types of silicon were analyzed: n-Si and p-Si, as well as their doped analogues n-Si<Ho> and p-Si<Ho>. The obtained Raman imaging results demonstrated spatially varying nanocrystallinity and microcrystallinity of the samples. The n-Si<Ho> and p-Si<Ho> spectra indicate the appearance of a Raman band at 525 cm<sup>-1</sup> with a shift of -5 cm<sup>-1</sup> and +5 cm<sup>-1</sup>, respectively, relative to the position of the silicon substrate peak, indicating the presence of tensile strain in the materials. The absence of other impurity peaks indicates the high purity of the n-Si<Ho> and p-Si<Ho> samples. The holmium doped Si material exhibits additional peaks in the Raman spectra, which is attributed to the presence of vacancies and defects in the newly formed Si-Ho compositions. The results of the analysis of the spectra indicate the influence of doping silicon with holmium on its structure and properties, forming new bonds and defects.

**Key words:** *Silicon; Holmium; Rare Earth Elements; Raman Spectra; Diffusion; Heat Treatment; Defects*

**PACS:** 33.20.Ea, 33.20.Fb

### INTRODUCTION

When characterizing crystalline silicon, which is widely used in the production of semiconductor electronic devices, Raman spectroscopy methods are actively used [1-6]. Raman spectroscopy measures the change in frequency of light scattered by the molecules of a sample. These frequency changes are associated with molecular vibrations and can provide information about the chemical composition, structure and physical properties of the materials being studied. Raman spectroscopy technique is used in various fields such as chemistry, biology, physics, materials science and surface science [14]. Widely used for the analysis of chemical compounds, biological research, as well as quality control and materials research. To study the composition and structure of nanocrystalline silicon, a combination of transmission electron microscopy, Raman spectroscopy, and the effect of extremely small silicon grain sizes is used [7-10]. It is critical to recognize the consequences of nanocrystallinity in the Raman spectrum to avoid erroneously attributing spectral features of nanocrystals to deformation of microcrystalline or larger grains [15-17].

### MATERIALS AND METHODS

n-Si and p-Si samples with an initial resistivity from 0.3 to 40 Ω×cm were selected for the study. Before alloying, the samples were subjected to thorough acid-peroxide washing, and the oxide layers were removed from the surface of the samples using a HF solution. After thoroughly cleaning the surface of the samples, films of holmium impurities of special purity (99.999%) were deposited onto the clean Si surfaces using vacuum deposition. Vacuum conditions in the volume of the working chamber of the order of 10<sup>-7</sup>-10<sup>-8</sup> torr were provided by an oil-free vacuum pumping system.

Before diffusion annealing, the samples were placed in evacuated quartz ampoules. Doping of samples with Ho impurities was carried out by the diffusion method at a temperature of 1200 °C for 5 hours, followed by rapid cooling.

Raman spectra were studied using a SENTERRA II Bruker Raman spectrometer. This fully automated instrument combines excellent sensitivity and high resolution of 4.0 cm<sup>-1</sup>. Senterra calibration was automatic and referenced to NIST acetaminophen and silica standards, resulting in wavelength accuracy of 0.2 cm<sup>-1</sup>. The experiments were carried out using a laser with a wavelength λ<sub>0</sub>=532 nm, maximum power P<sub>max</sub>=25 mW, acquisition time 100 s and addition of two spectra. This device allows you to obtain spectra in the range from 50 to 4265 cm<sup>-1</sup>. The Raman spectra were specially processed to be able to compare intensity ratios between samples. Before normalizing the spectra to the peak at 510 cm<sup>-1</sup>, which corresponded to the most intense peak in the spectral region 4265-50 cm<sup>-1</sup>, we subtracted the baseline for each spectrum.



## RESULTS AND DISCUSSION

Heterostructures (Ho-Si) and solid solutions ( $n\text{-Si}\langle\text{Ho}\rangle$ ) crystal lattice constants of Ho and Si materials are always different, therefore, if another (Ho) is grown on top of a substrate of one material (Si), built-in elastic stresses appear in the Ho layers, Si, Ho-Si multilayer structures. In this case, elastic stresses turn out to be so significant that they significantly affect the band structure of charge carriers and phonon spectra. The magnitude of the mismatch of crystal lattices largely determines the quality of structures, since stresses give rise to the formation of structural defects and in some cases greatly limit the possibility of creating perfect heterocompositions. Changes in composition and deformation of the material change the crystal structure, and thereby manifest themselves in changes in vibrational and phonon spectra. One of the methods of structural analysis that allows one to study phonon spectra and their changes is Raman spectroscopy. In this work, the Raman spectrum of an  $n\text{-Si}\langle\text{Ho}\rangle$  sample ( $x = 0.25$ ) grown on a Si substrate with (100) orientation was studied. The thickness of the solid solution layer is 5 microns. The solid solution contains Si-Si, Ho-Ho and Ho-Si bonds. Therefore, light scattering involving these vibrational modes should be expected.

Below are the Raman spectra of both the initial  $n\text{-Si}$  silicon material (Fig. 1.) and the resulting  $n\text{-Si}\langle\text{Ho}\rangle$  sample (Fig. 2.). In this case, the Raman image was visualized using color coding.

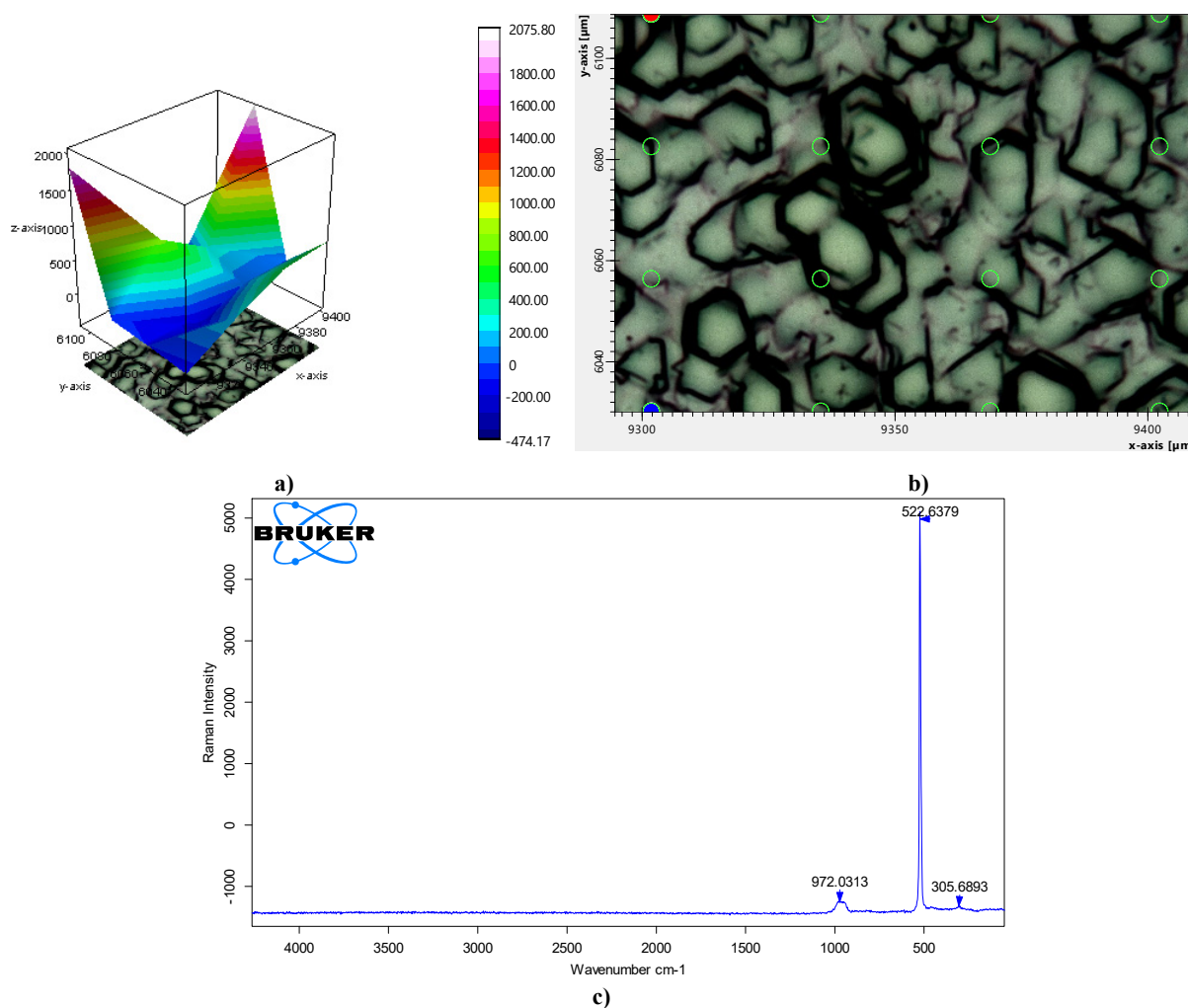
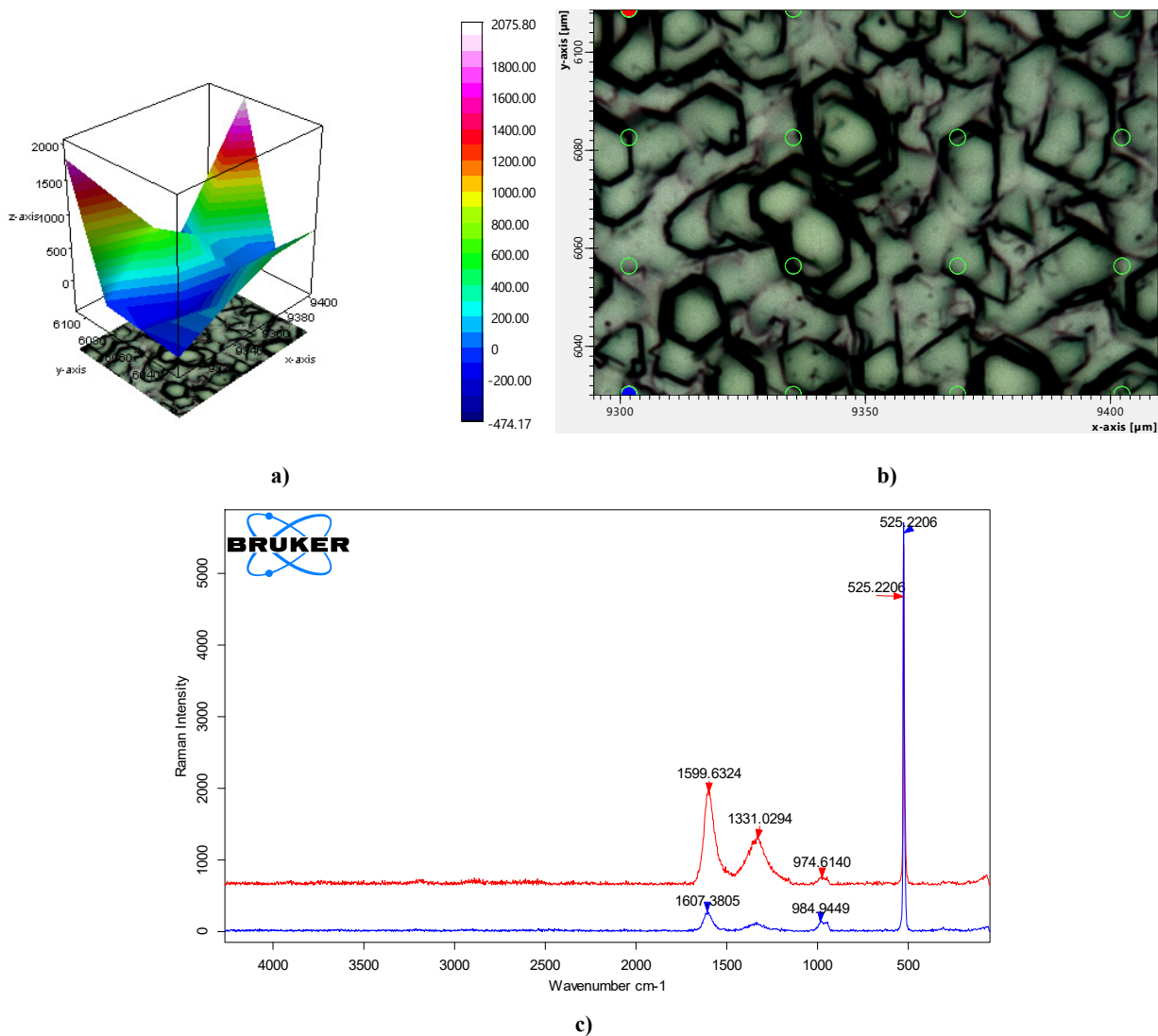


Figure 1. Raman spectrum  $n\text{-Si}_{\text{initial}}$

As can be seen from the data in Figure 1, when studying the  $n\text{-Si}_{\text{initial}}$ , a strong signal appears in the region of  $522\text{ cm}^{-1}$ , resulting from a first-order optical phonon in the Brillouin center region. An increase in band width indicates that there is a distribution of strains and the band shift is not the result of a single uniaxial stress. The shoulder at  $522\text{ cm}^{-1}$  can be attributed to crystalline silicon.

When studying the Raman spectra of the resulting material, it was revealed that the studied material consists of a silicon substrate (or grown single-crystalline silicon) with different oxide thicknesses. The spatial variation of the material's Raman signal power closely matches the physical optical effect of the oxide thickness, and even small impurities or defects are visible in the reflected light image (Figures 1b and 2b). Moreover, due to the thinness of the silicon structure (Fig. 1a and 2a), it is possible to see through the picture the components of the resulting material. Note that the bright green dots in the Raman image correspond precisely to the black specks in the reflection of the light image. A careful examination of the central strip reveals the same speckles in the silicon deposited on top of it.



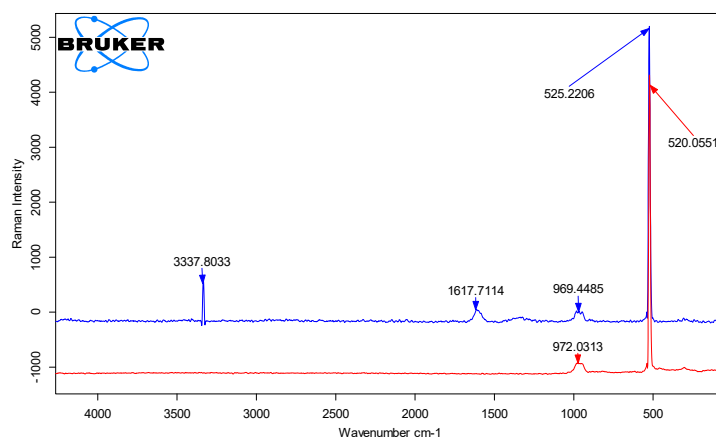
**Figure 2.** Raman spectra of n-Si<Ho>

As can be seen from the given spectrum (Fig. 3.) silicon consists of Raman scattering of light at  $525\text{ cm}^{-1}$  for n-Si and  $530\text{ cm}^{-1}$  for p-Si, respectively, resulting from the first order of optical phonon in the Brillouin center region, Raman the band in the spectra of the resulting n-Si<Ho> appears at  $525\text{ cm}^{-1}$  (shift  $-5\text{ cm}^{-1}$ ), and in the case of p-Si<Ho> appears at  $525\text{ cm}^{-1}$  (shift  $+5\text{ cm}^{-1}$ ) relative to the position peak of the silicon substrate, thereby indicating the presence of tensile strain. The absence of other impurity peaks of the samples indicates a higher purity of the samples. Both types of Si and Si<Ho> samples obtained on their basis have a strong, broad absorption at  $\sim 960\text{ cm}^{-1}$ , which corresponds to the Si-O-Si stretching vibration. Apparently, the above results demonstrate the successful production of the Si<Ho> composite on the surface of the material. When studying Raman spectroscopy of materials, two Si peaks located at  $\sim 522$  and  $\sim 950\text{ cm}^{-1}$  correspond well to the Si peak symbol, which can also be observed in the resulting Si<Ho> materials. The increased Raman bandwidth of silicon indicates that there is a distribution of strains and the band shift is not the result of a single uniaxial stress. The shoulder at  $\sim 522\text{ cm}^{-1}$  may be attributed to crystalline silicon.

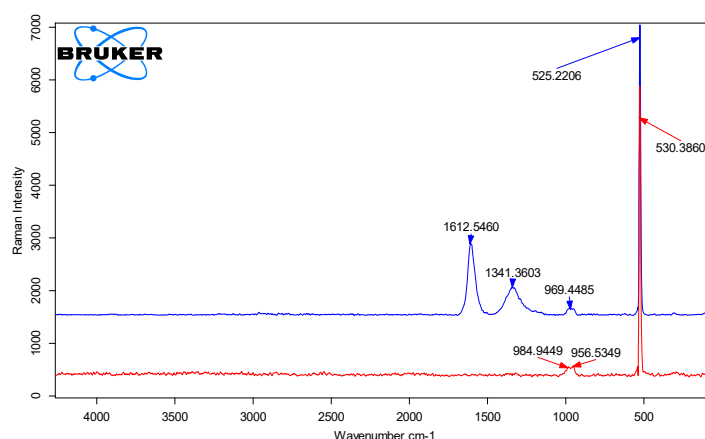
Ho-doped Si material also has additional peaks in its Raman spectra, which is expected due to the presence of vacancies, defects in the newly formed Si<Ho> compositions. Ho-doped silicon surfaces exhibit higher absorption rates after grinding to  $50\text{ }\mu\text{m}$ . An additional peak at  $805\text{ cm}^{-1}$  is assigned to the hydrogen wagging mode. The frequency range ( $2000\text{-}2150\text{ cm}^{-1}$ ) is deconvoluted to study possible local vibrational modes arising from defects and new bonds formed in which Ho is involved. Peaks between  $2021\text{ cm}^{-1}$  and  $2150\text{ cm}^{-1}$  usually result from Ho-Ho stretches. The peak at  $2060\text{ cm}^{-1}$  is due to adsorbed hydrogen at defect sites. The peaks at  $2058\text{ cm}^{-1}$  and  $2098\text{ cm}^{-1}$  are attributed to Ho-Si and Si-Ho<sub>2</sub>, respectively. The peak at  $2074\text{ cm}^{-1}$  corresponds to db-Si-Si-H, where db means dangling bond. The small peak at  $2190\text{ cm}^{-1}$  may be due to Ho-induced microcrystallites.

Raman spectra of two types of silicon n-Si and p-Si, and n-Si<Ho> and p-Si<Ho> obtained on their basis, deposited on crystalline Si substrates and annealed at  $1373\text{ K}$  for 5 hours, are presented in Fig. 1-3. a tail that does not develop into a clearly visible peak in any sample. We hypothesize that the tail is primarily scattering from annealed-grown silicon nanocrystals, and this is supported by a similar low-energy tail observed in other Raman scattering studies of silicon nanocrystals [11-13,19]. In these studies, the peak of the Raman band is slightly shifted relative to the Si single crystal band, but its low-energy tail is highly asymmetric and extends to  $480\text{ cm}^{-1}$ , similar to the tail of our Raman spectra. However, some small portion of the scattering in the low-frequency tail of our spectra may be due to n-Si, whose Raman peak [12,13,18] at  $480\text{ cm}^{-1}$  extends asymmetrically to  $242\text{-}341\text{ cm}^{-1}$ . We do not observe any scattering below  $400\text{ cm}^{-1}$ , which means that most of the scattering in the low-energy tail of our spectra is due to Si nanocrystals.





a) n-Si (-); n-Si&lt;Ho&gt; (-).



b) p-Si (-); composite p-Si&lt;Ho&gt; (-)

**Figure-3.** Comparative analysis of Raman spectra

### CONCLUSION

The spectra of two types of silicon, n-Si and p-Si, and samples obtained on their basis, n-Si<Ho> and p-Si<Ho>, were studied. Raman imaging studies revealed spatially varying nanocrystallinity and microcrystallinity of the resulting samples.

To summarize, the intensity variations of monocrystalline silicon correspond to the physical optical effects of varying oxide film thicknesses and surface contaminants. In addition, Raman imaging shows the spatial variation of nanocrystallinity and microcrystallinity in silicon. From the studies conducted, we can conclude that these structural differences arise either as a result of processing conditions, or from interaction with neighboring or host materials in which silicon is in contact with other components.

Spectral analysis of silicon shows characteristic Raman peaks at 520 cm<sup>-1</sup> for n-Si and 530 cm<sup>-1</sup> for p-Si, caused by the first order of the optical phonon in the Brillouin center region. The n-Si<Ho> and p-Si<Ho> spectra show the appearance of a Raman band at 525 cm<sup>-1</sup> with a shift of -5 cm<sup>-1</sup> and +5 cm<sup>-1</sup>, respectively, relative to the position of the silicon substrate peak. This indicates the presence of tensile strain in the materials. The absence of other impurity peaks indicates the high purity of the n-Si<Ho> and p-Si<Ho> samples. Both types of Si and Si<Ho> samples have a strong broad absorption at ~960 cm<sup>-1</sup>, which corresponds to the Si-O-Si stretching vibration. An increase in the Raman bandwidth of silicon indicates the distribution of strains and the absence of uniaxial stress. The Si material doped with Ho exhibits additional peaks in the Raman spectra, which is explained by the presence of vacancies and defects in the newly formed Si-Ho compositions. Peaks at 805 cm<sup>-1</sup> and in the frequency range 2000-2150 cm<sup>-1</sup> indicate hydrogen vibrations arising from defects and the formation of new bonds in which Ho is involved. Peaks between 2021 cm<sup>-1</sup> and 2150 cm<sup>-1</sup>, including peaks at 2058 cm<sup>-1</sup> and 2098 cm<sup>-1</sup>, indicate the interaction of Ho with Si and the formation of Ho-Si and Si-Ho<sub>2</sub> type bonds. The peak at 2190 cm<sup>-1</sup> may be due to Ho-induced microcrystallites.

In general, the results of the analysis of the spectra indicate that doping silicon with holmium affects its structure and properties, forming new bonds and defects.

### ORCID

©Sharifa B. Utamuradova, <https://orcid.org/0000-0002-1718-1122>; ©Jonibek J. Khamdamov, <https://orcid.org/0000-0003-2728-3832>  
©Khusniddin J. Matchonov, <https://orcid.org/0000-0002-8697-5591>

### REFERENCES

- [1] Sh.B. Utamuradova, Kh.J. Matchonov, J.J. Khamdamov, and Kh.Y. Utemuratova, "X-ray diffraction study of the phase state of silicon single crystals doped with manganese," *New Materials, Compounds and Applications*, 7(2), 93-99 (2023). [http://jomardpublishing.com/UploadFiles/Files/journals/NMCA/v7n2/Utamuradova\\_et\\_al.pdf](http://jomardpublishing.com/UploadFiles/Files/journals/NMCA/v7n2/Utamuradova_et_al.pdf)

- [2] Y. Inoue, S. Nakashima, A. Mitsuishi, T. Nishimura, and Y. Akasaka, "The Depth Profiling of the Crystal Quality in Laser-Annealed Polycrystalline Si Films by Raman Microprobe," *Jpn. J. Appl. Phys.* **25**, 798–801 (1986). <https://doi.org/10.1143/JJAP.25.798>
- [3] Sh.B. Utamuradova, Sh.Kh. Daliev, D.A. Rakhmanov, S.F. Samadov, and A.S. Doroshkevich, "Investigation of radiation defect formation of irradiated n-Si<Pt>," *Advanced Physical Research*, **5**(3), 183-191 (2023). <http://jomardpublishing.com/UploadFiles/Files/journals/APR/V5N3/7.Utamuradova.pdf>
- [4] Sh.B. Utamuradova, Sh.Kh. Daliev, A.V. Stanchik, D.A. Rakhmanov, "Raman spectroscopy of silicon, doped with platinum and irradiated by protons", *E3S Web of Conferences*, **402**, 14014(2023). <https://doi.org/10.1051/e3sconf/202340214014>
- [5] Z.T. Azamatov, Sh.B. Utamuradova, M.A. Yuldoshev, N.N. Bazarbayev, "Some properties of semiconductor-ferroelectric structures", *East European Journal of Physics*, **2**, 187–190 (2023). <https://doi.org/10.26565/2312-4334-2023-2-19>
- [6] Kh.S. Daliev, Sh.B. Utamuradova, J.J. Khamdamov, and Z.E. Bahronkulov, "Electrophysical properties of silicon doped with lutetium," *Advanced Physical Research*, **6**(1), 42-49 (2024). <https://doi.org/10.62476/apr61.49>
- [7] V. A. Volodin, M. D. Efremov, and V. A. Gritsenko, "Raman Spectroscopy Investigation of Silicon Nanocrystals Formation in Silicon Nitride Films," *Solid State Phenom.* **57-58**, 501–506 (1997). <https://doi.org/10.4028/www.scientific.net/SSP.57-58.501>
- [8] Sh.B. Utamuradova, Z.T. Azamatov, and M.A. Yuldoshev, "Optical Properties of ZnO–LiNbO<sub>3</sub> and ZnO–LiNbO<sub>3</sub>:Fe Structures", *Russian Microelectronics*, **52**, 99–103(2023). <https://doi.org/10.1134/S106373972360022X>
- [9] H. Xia, Y.L. He, L.C. Wang, W. Zhang, X.N. Liu, X.K. Zhang, D. Feng, and H.E. Jackson, "Phonon mode study of Si nanocrystals using micro-Raman spectroscopy," *J. Appl. Phys.* **78**, 6705–6708 (1995). <https://doi.org/10.1063/1.360494>
- [10] Z. Iqbal, and S. Veprek, "Raman scattering from hydrogenated microcrystalline and amorphous silicon," *J. Phys. C*, **15**, 377 (1982). <https://doi.org/10.1088/0022-3719/15/2/019>
- [11] J. Gonzales-Hernandez, G.H. Azarbajani, R. Tsu, and F.H. Pollak, "Raman, transmission electron microscopy, and conductivity measurements in molecular beam deposited microcrystalline Si and Ge: A comparative study," *Appl. Phys. Lett.* **47**, 1350 (1985). <https://doi.org/10.1063/1.96277>
- [12] I.H. Campbell, and P.M. Fauchet, "The effects of microcrystal size and shape on the one phonon Raman spectra of crystalline semiconductors," *Solid State Commun.* **52**, 739 (1986). [https://doi.org/10.1016/0038-1098\(86\)90513-2](https://doi.org/10.1016/0038-1098(86)90513-2)
- [13] J.E. Smith, Jr., M.H. Brodsky, B.L. Crowder, M.I. Nathan, and A. Pinczuk, "Raman Spectra of Amorphous Si and Related Tetrahedrally Bonded Semiconductors," *Phys. Rev. Lett.* **26**, 642 (1971). <https://doi.org/10.1103/PhysRevLett.26.642>
- [14] Kh.S. Daliev, Sh.B. Utamuradova, Z.E. Bahronkulov, A.Kh. Khaitbaev, and J.J. Hamdamov, "Structure Determination and Defect Analysis n-Si<Lu>, p-Si<Lu> Raman Spectrometer Methods," *East Eur. J. Phys.* (4), 193 (2023). <https://doi.org/10.26565/2312-4334-2023-4-23>
- [15] P.A. Temple, and C.E. Hathaway, "Multiphonon Raman spectrum of silicon," *Physical Review B*, **7**(8), 3685–3697 (1973). <https://doi.org/10.1103/PhysRevB.7.3685>
- [16] Sh.B. Utamuradova, Sh.Kh. Daliev, E.M. Naurzalieva, X.Yu. Utemuratova, "Investigation of defect formation in silicon doped with silver and gadolinium impurities by raman scattering spectroscopy", *East European Journal of Physics*, (3), 430–433(2023). <https://doi.org/10.26565/2312-4334-2023-3-47>
- [17] K.J. Kingma, and R.J. Hemley, "Raman spectroscopic study of microcrystalline silica," *American Mineralogist*, **79**(3-4), 269-273 (1994). [https://pubs.geoscienceworld.org/msa/ammin/article-pdf/79/3-4/269/4209223/am79\\_269.pdf](https://pubs.geoscienceworld.org/msa/ammin/article-pdf/79/3-4/269/4209223/am79_269.pdf)
- [18] G.E. Walrafen, Y.C. Chu, and M.S. Hokmabadi, "Raman spectroscopic investigation of irreversibly compacted vitreous silica," *The Journal of Chemical Physics*, **92**(12), 6987–7002 (1990). <https://doi.org/10.1063/1.458239>
- [19] B. Champagnon, C. Martinet, M. Boudeulle, D. Vouagner, C. Coussa, T. Deschamps, and L. Grosvalet, "High pressure elastic and plastic deformations of silica: in situ diamond anvil cell Raman experiments," *Journal of Non-Crystalline Solids*, **354**(2-9), 569–573 (2008). <https://doi.org/10.1016/j.jnoncrsol.2007.07.079>

## ДОСЛІДЖЕННЯ ВПЛИВУ ЛЕГУВАННЯ КРЕМНІЮ ГОЛЬМІЄМ НА ЙОГО СТРУКТУРУ ТА ВЛАСТИВОСТІ МЕТОДАМИ СПЕКТРОСКОПІЇ КРЕМНІЮ

Шаріфа Б. Утамурадова<sup>а</sup>, Шахрух Х. Далієв<sup>а</sup>, Алішер Х. Хаитбасв<sup>а</sup>, Джонібек Дж. Хамдамов<sup>а</sup>, Хуснідін Дж. Магчонов<sup>а</sup>, Хусніда Й. Утемурадова<sup>б</sup>

<sup>а</sup>Інститут фізики напівпровідників і мікроелектроніки Національного університету Узбекистану, вул. Янги Алмазара, 20, Ташкент, Узбекистан

<sup>б</sup>Каракалпакський державний університет, Нукус, Каракалпакстан

Кожна кристалічна структура має власні фононні моди, які з'являються в спектрі комбінаційного розсіювання. У випадку кремнію можна виявити фононні моди, пов'язані з алмазною структурою кремнію. У раманівському спектрі зазвичай вимірюють положення ліній, їх інтенсивність і ширину ліній. Раманівська спектроскопія є потужним інструментом для вивчення кристалічних матеріалів на молекулярному рівні, і її застосування у вивченні напівпровідників і наноматеріалів дає важливу інформацію про їх структуру та властивості. У даній роботі проаналізовано спектри двох типів кремнію: n-Si та p-Si, а також їх легуваних аналогів n-Si<Ho> та p-Si<Ho>. Отримані результати комбінаційного зображення продемонстрували просторово змінну нанокристалічність і мікрокристалічність зразків. Спектри n-Si<Ho> та p-Si<Ho> вказують на появу раманівської смуги при 525 см<sup>-1</sup> зі зсувом на -5 см<sup>-1</sup> та +5 см<sup>-1</sup> відповідно відносно положення пік кремнієвої підкладки, що вказує на наявність деформації розтягу в матеріалах. Відсутність інших домішкових піків свідчить про високу чистоту зразків n-Si<Ho> та p-Si<Ho>. Si-матеріал, легований гольмієм, демонструє додаткові піки в спектрах комбінаційного розсіювання, що пояснюється наявністю вакансій і дефектів у новоутворених композиціях Si-Ho. Результати аналізу спектрів свідчать про вплив легування кремнію гольмієм на його структуру та властивості, утворення нових зв'язків і дефектів.

**Ключові слова:** кремній; гольмій; рідкоземельні елементи; Раманівські спектри; дифузія; теплоносії; дефекти

## MECHANISM OF CHANGE IN THE EMISSION AND OPTICAL PROPERTIES OF W AND Mo AFTER BOMBARDMENT WITH LOW-ENERGY IONS

**D.A. Tashmukhamedova<sup>a\*</sup>, B.E. Umirzakov<sup>a</sup>, Y.S. Ergashov<sup>b</sup>, F.Y. Khudaykulov<sup>c</sup>, X.E. Abdiev<sup>a</sup>**

<sup>a</sup>Tashkent State Technical University named after Islam Karimov, Tashkent, 100095 Republic of Uzbekistan

<sup>b</sup>National University of Uzbekistan named after Mirzo-Ulugbek, Tashkent, 100173 Republic of Uzbekistan

<sup>c</sup>Belarusian-Uzbek Intersectoral Institute of Applied Technical Qualifications in Tashkent, 100071 Republic of Uzbekistan

\*Corresponding Author e-mail: [abdiev.xasan.92@bk.ru](mailto:abdiev.xasan.92@bk.ru)

Received February 21, 2024; revised March 28, 2024; accepted April 2, 2024

The paper reports the results of study of composition, emission, and optical properties of polycrystalline W and Mo samples implanted with Ba<sup>+</sup> ions and coated with submonolayer Ba atoms by applying Auger electron spectroscopy, secondary electron emission coefficient  $\sigma$  technique, as well as the photoelectron quantum yield  $Y$ . The experimental part was carried out by using the instrumentation and under vacuum  $P \approx 10^{-6}$  Pa. It is shown that during the implantation of Ba ions in the surface layers of refractory metals, a mechanical mixture of the W + Ba and Mo-Ba types is formed. It has been established that the values of the coefficient of secondary electron emission  $\sigma$  and the quantum yield of photoelectrons  $Y$  at the same value of the work function  $\varphi_0$  in the case of implantation of Ba<sup>+</sup> ions are much larger than in the case of deposition of atoms. The obtained experimental results are substantiated by theoretical calculations.

**Keywords:** Mechanical bonds; Ion implantation; Emission efficiency; Auger spectrum; Quantum yield; Plasma oscillations; Fermi level

**PACS:** 61.72.uj, 68.55.Ln

### INTRODUCTION

Over recently, refractory metals, in particular Mo, W and their alloys, have been widely used and could also be used in the aviation and rocket building industries, i.e., in the development of new generation high-performance gas-tube engines [1-4], thus improving the resistance to plasma beams of the first wall of thermonuclear reactors [5-6], as well as in vacuum technologies and microwave devices [7,8].

Under the influence of ions and plasma on the material, the material is sputtered and evaporated, the structure and phase state change, new chemical compounds are formed on the surface, etc. [9]. At the same time, it is very important to minimize the erosion of materials both during normal functioning and transient events alike, as well as the appropriate choice of these materials is essential [10]. On this purposes, W and Mo can be used, which are characterized by a set of unique physical properties: low physical sputtering ratio, high melting point, high thermal conductivity, low accumulation of tritium. After exposure to plasma irradiation, the creation of an etching relief on the surfaces of metals and alloys is determined by tracing ionic component. Also, the nature of erosion of materials significantly depends on the operating temperature range. The results of [1] show that when tungsten and molybdenum are irradiated with hydrogen plasma, the main relief-forming mechanism happens to be surface sputtering, which is characterized by thermal etching of the surface. In this case, the development of the relief on the tungsten surface due to different erosion rates of adjacent areas during plasma irradiation is due to the fact that differently oriented surface crystals are characterized by different sputtering coefficients [11]. It was found that after irradiation, a fragmented substructure is observed in the surface layer of molybdenum.

At present, the physical and chemical properties of such structures obtained by sputtering, thermal diffusion, and mixing of fine particles with subsequent pressing are well studied. One of the promising methods for engineering a nanofilm structure in the surface layer of materials of various nature is the method of low-energy ion implantation in combination with annealing [12-14]. The use of materials with surface nanosized structures in a particular area of electronic technology is mainly determined by the composition and structure of the surface [15-18].

The present research is devoted to studying the effect of ion implantation on the composition, emission, and optical properties of polycrystalline samples of W and Mo.

### EXPERIMENTAL TECHNIQUE

Mo(111) and W(111) single-crystal wafers with a diameter of 8 – 10 mm and a thickness of 0.8 mm were used for experiments. Ion implantation, annealing and all studies using Auger electron spectroscopy (AES), measurements of the total secondary electron emission (SEE) coefficient  $\sigma$  and photoelectron quantum yield  $Y$  were carried out by using the same experimental instrumentation under ultrahigh vacuum conditions ( $P = 10^{-6}$  Pa). Ba<sup>+</sup> ions were obtained by surface ionization of Ba atoms. The diameter of the ion beam on the sample surface was  $\sim 1.5 \dots 2$  mm. Implantation with Ba<sup>+</sup>

ions was carried out mainly with energy  $E_0 = 1$  keV and dose  $D = 6 \cdot 10^{16}$  cm<sup>-2</sup> (saturation dose). The current of Ba<sup>+</sup> ions could be increased up to  $\sim 0.3$   $\mu$ A. The experimental technique is described in more detail in [18].

**EXPERIMENTAL RESULTS AND DISCUSSION**

On Fig. 1 shows the dependences  $\sigma(E_p)$  for pure W and W implanted with Ba<sup>+</sup> ions with energy  $E_0=0.5$  keV at a dose of  $D = 6 \cdot 10^{16}$  cm<sup>-2</sup> and coated with Ba atoms  $\sim 1$  monolayer thick. On Fig. 2 for the same samples shows the dependences of the photoelectron quantum yield  $Y$  on the photon energy in the range  $h\nu = 2 - 6$  eV.

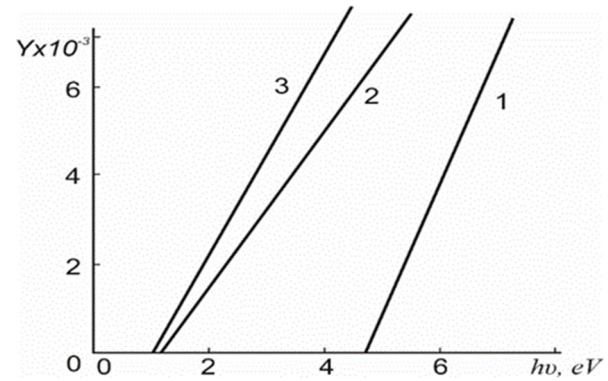
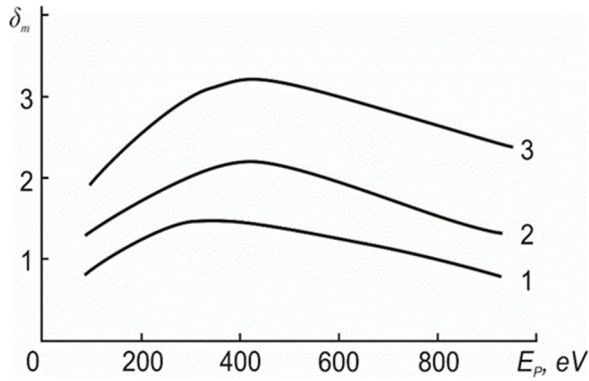


**Figure 1.** Dependences  $\sigma_m(E_p)$  for: 1 – W(111), 2 – W(111) with surface film Ba with  $\theta \approx 1$  monolayer, 3 – W implanted with Ba<sup>+</sup> ions with  $E = 0.5$  keV at  $D = 6 \cdot 10^{16}$  cm<sup>-2</sup>

**Figure 2.** Dependences of  $Y_{1/2}$  on  $h\nu$  for: 1 – pure W(111), 2 - W(111) with a Ba film with a thickness of 1 monolayer, 3 - W(111) implanted with Ba<sup>+</sup> ions with  $E = 0.5$  keV at  $D = 6 \cdot 10^{16}$  cm<sup>-2</sup>

To determine the concentration and mobility of charge carriers at the base region of the structure, the authors have applied the Hall factor technique at various temperatures. Also the authors have studied the photovolt-ampere characteristic at various values of monochromatic illumination at ( $h\nu \geq E_g$ ).

It can be seen from these figures that the increase in  $\sigma$  and  $Y$  of tungsten in the case of implantation of Ba<sup>+</sup> ions is significantly greater than in the case of deposition of Ba with a thickness of  $\theta \approx 1$  monolayer.

It is known that the increase in the SEE coefficient  $\sigma$  and the quantum yield of photoelectrons in the case of deposition (at  $\theta \approx 1$ ) is mainly determined by a decrease in the work function, and in the case of ion doping, both by a decrease in  $e\phi$  and by a change in the bulk physical properties of the emitting layer [19, 20].

The true secondary electrons (TSE) coefficient  $\delta$  can be determined by the following formula:

$$\delta = \int_0^\infty n(E_p, x) \cdot f(x) \cdot dx, \tag{1}$$

where  $n(E_p, x)$  is the density of internal secondary electrons formed primary electrons with energy  $E_p$  at depth  $x$ ;  $f(x)$  – probabilities exit of secondary electrons from this depth  $x$ .  $f(x)$  is defined as

$$f(x) = \psi(x) \cdot p(e\phi), \tag{2}$$

where  $\psi(x)$  is the probability that electrons from depth  $x$  will approach the surface, and  $p(e\phi)$  is the probability of exit of secondary electrons approaching the metal-vacuum boundary. Thus,  $\delta$  depends both on the work function and on the density of internal secondary electrons  $n(E_p, x)$  formed by primary electrons in the IVE exit zone –  $\lambda$ .

In order to evaluate the role of the surface and volume in increasing the coefficients  $\sigma_m$  and  $Y$  of ion-doped samples, we compared the results of measurements of  $Y$  and  $\sigma_m$  for W coated with a barium layer of different thicknesses and doped with Ba<sup>+</sup> ions with different energies at  $D=D_{sat}=6 \cdot 10^{16}$  cm<sup>-2</sup> ( $D_{sat}$  - saturation dose). For comparison, such values of the ion energy  $E_0$  and layer thickness  $\theta$  were chosen at which the work function for both samples was approximately the same (Table 1).

**Table 1.** Values of  $\sigma_m$ ,  $Y$  and  $e\phi$  for W(111) implanted with barium ions with different energies and coated with a barium layer of different thicknesses

Ba <sup>+</sup> → W, D = 6·10 <sup>16</sup> cm <sup>-2</sup>				Ba/W				$\sigma_i/\sigma_d$	$Y_i/Y_d$
$E_0$ , keV	$\sigma_m$	$Y \cdot 10^6$	$e\phi$	$\theta$	$\sigma_m$	$Y \cdot 10^6$	$e\phi$		
0.5	3.4	56	2.3	0.7	2.0	30	2.35	1.7	1.8
3.0	2.6	30	3.2	0.4	1.75	19	3.15	1.45	1.6
5.0	2.1	11	3.9	0.2	1.55	9	3.85	1.3	1.2

The values  $\sigma = \sigma_m$  corresponded to the energy  $E_{pm} \approx 450 - 500$  eV.

It can be seen from the table that, with the same changes in  $\epsilon\phi$ , the values  $\sigma_m$  of  $\sigma m$  and  $Y$  for doped samples are greater than for deposited ones. A significant difference in  $\sigma$  and  $Y$  between implanted and deposited samples is observed at  $E_0 = 1$  keV, and in this case  $\sigma_i/\sigma_d$  and  $Y_i/Y_d$  are  $\sim 1.7$ . The calculated value of the depth of the EVE and photoelectron exit zone for pure W was  $20 - 25$  Å.

In this case, the main part of the intercalated atoms is located at a depth of  $0 - 20$  Å, which is close to the ISE exit zone. This, as well as a strong decrease in  $\epsilon\phi$ , explains the largest increase in  $\sigma$  and  $Y$  at  $E_0 = 0.5 - 1$  keV. As the ion energy increases, the concentration of interstitial atoms in the emitting layer decreases, which leads to a decrease in the ratio  $\sigma_i/\sigma_n$  and  $Y_i/Y_n$ .

According to formula (1), the growth of  $\sigma$  and  $Y$  in the case of doping is associated with an increase in the density of internal secondary electrons  $n(Ep, x)$ , which is proportional to the energy loss per unit path of the primary or inelastically reflected electron:

$$dE/dx = n_e \int_0^\infty \epsilon \cdot d\delta(E, \epsilon). \quad (3)$$

Here  $(E, \epsilon)$  is the differential scattering cross section with energy loss  $\epsilon$ . The value of  $n_e$  increases significantly with increasing impurity concentration in the emitting layer.

At low energies of primary electrons, a certain contribution to the number of TSEs and photoelectrons comes from those electrons of the introduced impurity that are located at the upper energy levels. Table 2 lists the energies of the levels of Mo, W, and Ba atoms.

**Table 2.** Energy levels of Mo, W, and Ba atoms

Mo	N <sub>45</sub>	N <sub>23</sub>	N <sub>1</sub>	M <sub>5</sub>	M <sub>4</sub>	M <sub>3</sub>	M <sub>2</sub>
	2	35	62	227	230	392	410
W	P <sub>1</sub>	N <sub>7</sub>	N <sub>6</sub>	N <sub>5</sub>	N <sub>4</sub>	N <sub>3</sub>	N <sub>2</sub>
	4	34	37	46	259	426	492
Ba	V	O <sub>3</sub>	O <sub>2</sub>	O <sub>1</sub>	N <sub>5</sub>	N <sub>4</sub>	N <sub>3</sub>
	3	15	17	39	90	92	180

It can be seen that many of the barium levels are located in the band gap region of Mo, W. For example, the Ba levels with energies of 3, 15, 17 eV are located between the conduction band and the first filled Mo band. The probabilities of excitation of electrons from these levels Ba are greater than the probabilities of excitation of electrons from the filled Mo band (in addition, the ionization of O<sub>3</sub> and O<sub>2</sub> levels can lead to the appearance of the O<sub>2</sub>VV and O<sub>3</sub>VV Auger process). Therefore, in the region of small  $E_p$  at high impurity concentrations, these levels will make a significant contribution to the number of TSEs, the presence of such levels also increases the inelastic reflected electrons (IRE) efficiency.

In the case of metals W and Mo, the formula [21] can also be used for calculation

$$\delta = \frac{B}{\epsilon} \int_0^\infty F(x) e^{-\frac{\lambda}{x}} dx. \quad (4)$$

Here  $F(x)$  is the energy loss distribution function of absorbed and inelastically reflected electrons.  $B$  is the probability of exit of SEs approaching the surface, and  $\epsilon$  is the average energy required for the formation of one secondary or photoelectrons,  $\lambda$  is the depth of exit of the EVE. The values of  $\lambda$  range from 10 to 30 Å for most metals, and the value  $\frac{\epsilon}{B}$ , according to Dekker, does not depend on the energy of primary electrons and has a value of  $\sim 100 \div 200$ . We performed calculations for  $\lambda = 10, 15, 20$  and  $30$  Å. The best agreement with experiment is obtained in the case of  $\lambda = 10$  Å:  $\epsilon/B = 140$  for Mo and 170 for W.

Table 3 shows the calculated  $\delta_C$  and experimental  $\delta_E$  values of the TSE coefficients for Mo and W. It can be seen from the table that agreement with experiment is good for  $E_p > 800$  eV, and for lower  $E_p$ , the calculated values turn out to be lower than the experimental ones.

The reason is that at such energies the parameter  $\epsilon/B$  begins to depend on the energy of the primary electron.

**Table 3.** Calculated and experimental values of true-secondary electron coefficient  $\delta_m$

	$E_0, \text{эВ}$	600	800	1000	3000	4000
Mo	$\delta_C$	0.87	0.95	0.94	0.54	0.45
	$\delta_E$	0.98	0.95	0.92	0.55	0.46
W	$\delta_C$	0.7	0.78	0.84	0.56	0.46
	$\delta_E$	0.91	0.88	0.81	0.6	0.48

Indeed, at low energies, the role of excitation and decay of plasmons in the formation of SE increases and the mechanism of excitation of electrons from deep levels is "switched off", which should lead to a decrease in  $\xi$  - the average energy spent on the formation of one SE. At the same time, the conditions for the release of secondary electrons also change. The results obtained are consistent with the conclusions that, at large  $E_0$ , the SEE coefficients are determined mainly by the energy losses of primary electrons, but not by the secondary electron release mechanism.



## CONCLUSIONS

It is shown that the increase in the coefficient of secondary electron emission and the quantum yield of W and Mo photoelectrons after implantation of Ba<sup>+</sup> ions is mainly due to a decrease in the work function of the surface and an increase in energy losses for the absorption of electrons in the ion-implanted layer.

It has been found that at low electron energies ( $E \leq 0.8$  keV), the calculated values of the TSE coefficient are significantly lower than the experimental ones. For  $E_0 \geq 1$  keV, they are in good agreement with each other.

The results obtained are employed in various branches of electronic and chemical industry, in particular, production of pure Mo and its alloys and catalysts for processing of oil and oil products and are promising in the development of OLED displays, optical resonators and filters, sensors, and solar cells.

## ORCID

- © D.A. Tashmukhamedova, <https://orcid.org/0000-0001-5813-7518>; © B.E. Umirzakov, <https://orcid.org/0000-0002-9815-2111>  
© Y.S. Ergashov, <https://orcid.org/0000-0002-1884-9462>; © F.Y. Khudaykulov, <https://orcid.org/0009-0000-7250-3836>  
© X.E. Abdiev, <https://orcid.org/0000-0003-3843-1503>

## REFERENCES

- [1] B.K. Rakhadilov, A.Zh. Miniyazov, M.K. Skakov, Zh.B. Sagdoldina, T.R. Tulenbergenov, and E.E. Sapataev, *Technical Physics*, **65**, 382 (2020). <https://doi.org/10.1134/S1063784220030202>
- [2] V. KurnaeV, I. Vizgalov, K. Gutorov, T. Tulenbergenov, I. Sokolov, A. Kolodeshnikov, and V. Ignashev, *J. Nucl. Mater.* **463**, 228 (2015). <https://doi.org/10.1016/j.jnucmat.2014.12.076>
- [3] J. Roth, E. Tsirone, A. Loarte, Th. Loarer, G. Counsell, R. Neu, V. Philipps, et al., *J. Nucl. Mater.* **390–391**, 1 (2009). <https://doi.org/10.1016/j.jnucmat.2009.01.037>
- [4] T. Teusch, and T. Kluener, *Journal of Physical Chemistry C*, **123** (46), 28233 (2019). <https://doi.org/10.1021/acs.jpcc.9b08268>
- [5] O.G. Ospennikova, V.N. Pod'yachev, and Yu.V. Stolyankov, *Trudy VIAM*, **10**(46), 55 (2016). <https://doi.org/10.18577/2307-6046-2016-0-10-5-5> (in Russian)
- [6] E.N. Kablov, *Aviation materials and technologies*, **1**(34), 3 (2015). <https://doi.org/10.18577/20719140-2015-0-1-3-33> (in Russian)
- [7] Y. Yao, D. Sang, L. Zou, Q. Wang, and C. Liu, *Nano-materials*, **11**(8), 2136 (2021). <https://doi.org/10.3390/nano11082136>
- [8] E.P. Surovoi, V.E. Surovaia, and L.N. Bugerko, *J. Phys. Chem. A*, **87** (5), 826 (2013). <https://doi.org/10.1134/S0036024413050257>
- [9] ITER Joint Central Team, Report No. G AO FDR 4 01-07-21 R0.4 (Garching, 2001).
- [10] V. Philipps, J. Roth, and A. Loarte, *Plasma Phys. Control. Fusion*, **45**, A17 (2003). <https://doi.org/10.1088/0741-3335/45/12A/002>
- [11] B.K. Rakhadilov, M.K. Skakov, and T.R. Tulenbergenov, *Key Engineer. Mater.* **736**, 46 (2017). <https://doi.org/10.4028/www.scientific.net/KEM.736.46>
- [12] E.S. Ergashov, D.A. Tashmukhamedova, and B.E. Umirzakov, *Journal of Surface Investigation: X-ray, Synchrotron and Neutron Techniques*, **11**, 480 (2017). <https://doi.org/10.1134/S1027451017020252>
- [13] D.A. Tashmukhamedova, and M.B. Yusupjanova, *Journal of Surface Investigation: X-ray, Synchrotron and Neutron Tech.* **10**(6), 1273 (2016). <https://doi.org/10.1134/S1027451016050438>
- [14] B.E. Umirzakov, D.A. Tashmukhamedova, and F.Ya. Khudaykulov, *Journal of Surface Investigation: X-ray, Synchrotron and Neutron Techniques*, **16**(6), 992 (2022). <https://doi.org/10.1134/S1027451022050202>
- [15] B.E. Umirzakov, A.K. Tashatov, D.A. Tashmukhamedova, and M.T. Normuradov, *Poverkhnost. Rentgenovskie, Sinkhronnye i Neitronnye Issledovaniya*, **12**, 90 (2004). <https://www.elibrary.ru/item.asp?id=17669389>. (in Russian)
- [16] D.A. Tashmukhamedova, B.E. Umirzakov, and M.A. Mirzhaliyeva, *Izvestiya Akademii Nauk. Ser. Fizicheskaya*, **68**(3), 424 (2004). <https://www.elibrary.ru/item.asp?id=17641066>. (in Russian)
- [17] D.A. Tashmukhamedova, *Izvestiya Akademii Nauk. Ser. Fizicheskaya*, **70**(8), 1230 (2006). <https://elibrary.ru/item.asp?id=9296378>. (in Russian)
- [18] D.A. Tashmukhamedova, and M.B. Yusupjanova, *Journal of Surface Investigation: X-ray, Synchrotron and Neutron Techniques*, **15**(5), 1054 (2021). <https://doi.org/10.1134/S1027451021050402>
- [19] J.B. Biersack, and L.G. Haggmark, *Nucl. Instrum. and Meth.* **174**(1), 257 (1980). [https://doi.org/10.1016/0029-554X\(80\)90440-1](https://doi.org/10.1016/0029-554X(80)90440-1)
- [20] Y. Yamamura, Y. Mirzuno, and H. Kimura, *Nucl. Instr. and Meth. Phys. Res. B*, **13**(1-3), 393-395 (1986). [https://doi.org/10.1016/0168-583X\(86\)90535-5](https://doi.org/10.1016/0168-583X(86)90535-5)
- [21] X. Rissel, and I. Ruge, *Ion implantation*, (Nauka, Moscow, 1982). (in Russian)

## МЕХАНІЗМ ЗМІНИ ЕМІСІЇ ТА ОПТИЧНИХ ВЛАСТИВОСТЕЙ W ТА Mo ПІСЛЯ БОМБАРДУВАННЯ НИЗЬКОЕНЕРГІЙНИМИ ІОНАМИ

Д.А. Ташмухамедова<sup>а</sup>, Б.Е. Умірзаков<sup>а</sup>, Ю.С. Ергашов<sup>б</sup>, Ф.Й. Худайкулов<sup>с</sup>, Х.Є. Абдієв<sup>а</sup>

<sup>а</sup>Ташкентський державний технічний університет імені Іслама Карімова, Ташкент, 100095 Республіка Узбекистан







<sup>б</sup>Національний університет Узбекистану імені Мірзо-Улугбека, Ташкент, 100173 Республіка Узбекистан

<sup>с</sup>Білорусько-Узбецький міжгалузевий інститут прикладної технічної кваліфікації, Ташкент, 100071 Республіка Узбекистан

У статті наведено результати дослідження складу, емісійних і оптичних властивостей полікристалічних зразків W і Mo, імплантованих іонами Ba<sup>+</sup> і покритих субмоношаровими атомами Ba, за допомогою Оже-електронної спектроскопії, методу вторинної емісії  $\sigma$ , а також фотоелектронного квантового виходу  $\Upsilon$ . Експериментальна частина виконувалася апаратно під вакуумом  $P \approx 10^{-6}$  Па. Показано, що під час імплантації іонів Ba у поверхневих шарах тугоплавких металів формується механічна суміш W + Ba та Mo-Ba типу. Встановлено, що значення коефіцієнта вторинної електронної емісії  $\sigma$  та квантового виходу фотоелектронів  $\Upsilon$  при однаковому значенні роботи виходу  $\varphi$  у разі імплантації іонів Ba<sup>+</sup> значно більші, ніж у випадку осадження атомів. Отримані експериментальні результати обґрунтовані теоретичними розрахунками.

**Ключові слова:** механічні зв'язки; іонна імплантація; ефективність викидів; Оже-спектр; квантовий вихід; плазмові коливання; рівень Фермі

## DEFECTIVE STRUCTURE OF SILICON DOPED WITH DYSPROSIUM

 Khodjakbar S. Daliev<sup>a</sup>,  Sharifa B. Utamuradova<sup>b</sup>,  Alisher Khaitbaev<sup>b</sup>,  
 Jonibek J. Khamdamov<sup>b</sup>,  Shahriyor B. Norkulov<sup>b\*</sup>,  Mansur B. Bekmuratov<sup>c</sup>

<sup>a</sup>Branch of the Federal State Budgetary Educational Institution of Higher Education “National Research University MPEI”,  
1 Yogdu st., Tashkent, Uzbekistan

<sup>b</sup>Institute of Semiconductor Physics and Microelectronics at the National University of Uzbekistan,  
20 Yangi Almazar st., Tashkent, 100057, Uzbekistan

<sup>c</sup>Nukus State Pedagogical Institute named after Ajiniyaz, Nukus, Uzbekistan

\*Corresponding Author e-mail: [nshb19990@gmail.com](mailto:nshb19990@gmail.com)

Received March 02, 2024; revised April 6, 2024; accepted April 8, 2024

In this work, the structural and optical characteristics of silicon (n-Si) samples and its compositions with dysprosium (n-Si-Dy) were analyzed using Fourier transform infrared spectroscopy (FTIR) and Raman spectroscopy methods. Characteristic peaks in the FTIR spectra such as  $640\text{ cm}^{-1}$  (Si-H mode) and  $1615\text{ cm}^{-1}$  (perpendicular stretching mode) were identified, indicating the structural features of the material. The appearance of additional peaks in the n-Si-Dy spectra at  $516.71\text{ cm}^{-1}$  and  $805\text{ cm}^{-1}$  indicates the influence of dysprosium on the structure and defectiveness of the material. Examination of the frequency range (1950–2250  $\text{cm}^{-1}$ ) further confirms local vibration modes associated with defects and interactions with dysprosium. Peaks associated with Dy-Dy stretching, as well as interaction with silicon, were found at  $2110\text{ cm}^{-1}$  and  $2124\text{ cm}^{-1}$ . Analysis of Raman spectra indicates the formation of silicon nanocrystals during annealing, which is confirmed by XRD results. The results obtained provide important insight into the effect of dysprosium on the structure and properties of silicon materials, which could potentially find application in optoelectronics and materials science.

**Key words:** Silicon, Dysprosium, Rare earth elements, Raman scattering, Diffusion, Heat treatment, Temperature

**PACS:** 33.20.Ea, 33.20.Fb

### INTRODUCTION

Although crystalline silicon plays a critical role in the microelectronics industry, its use in optoelectronics faces limitations due to its indirect bandgap semiconductor properties, which reduces the efficiency of emitting light in the visible spectrum. The discovery of strong visible photoluminescence in porous silicon at room temperature [1] has stimulated active research into the development of structures, including silicon nanowires and nanoparticles, as well as the study of their structural and optoelectronic characteristics.

Further studies showed pronounced visible light emission from nanocrystalline silicon films [2] and thin  $\text{SiO}_2$  films containing both crystalline [4] and amorphous [5] silicon nanoparticles. This luminescence is often attributed to the radiative recombination of charge carriers within Si nanoparticles, and its color can be controlled by varying the size of the nanoparticles [21]. Later, intense visible photoluminescence was observed in films of nanocrystalline silicon [3], as well as in thin films of  $\text{SiO}_2$  containing both crystalline [4,7,8,22] and amorphous [6] silicon nanoparticles.

Instrumental testing methods such as infrared spectroscopy and Raman scattering provide a rapid and non-destructive way to determine whether silicon particles are amorphous or crystalline [16,23]. In addition, information about the size of nanocrystallites can be obtained from the shape and position of the maximum of the first-order Raman scattering band [9,17]. In crystalline materials, this band usually takes the form of a Lorentzian line with an intrinsic linewidth of about  $3\text{ cm}^{-1}$  at room temperature. “Finite size effects” that break the overall translational symmetry of the material can lead to low-frequency asymmetric broadening and redshift of the Raman band. Thus, the size of nanoparticles can be determined from the details of the Raman line shape [9,11,18-20].

However, when using this approach, it is important to keep in mind that other factors such as structural damage, alloying, etc. can also cause similar changes [12,15]. In addition, the Raman line can be affected by tensile and compressive stresses, causing red and blue shifts, respectively.

### MATERIALS AND METHODS

In this study, n-Si-Dy composite was synthesized by thermal firing at 1373 K. Infrared spectra and Raman studies were carried out on four samples, including n-Si and n-Si-Dy composites, which further confirmed the presence of both amorphous and nanocrystalline structures in films annealed at 1373 K. Photoluminescence in the visible and near-infrared regions was observed in films containing both amorphous and crystalline particles.

To conduct the study, n-Si silicon samples with an initial resistance ranging from 0.3 to  $100\ \Omega \times \text{cm}$  were selected. The process of doping with dysprosium (Dy) impurities was carried out sequentially using the thermal diffusion method. The samples were chemically cleaned and etched with an HF solution to remove oxide layers from the surface.



Subsequently, films of high-purity Dy impurity (purity 99.999%) were deposited onto a clean silicon surface by vacuum deposition in evacuated quartz ampoules at a vacuum level of  $10^{-6}$  to  $10^{-8}$  Torr using an oil-free vacuum pumping system.

Diffusion annealing of the samples was performed at a temperature of 1373 K for 40 hours, followed by fast and slow cooling to uniformly dope the material and maximize the impurity concentration in silicon. Infrared (IR) spectra were obtained using a Bruker Invenio-X system in the wavenumber range from 400 to 4000  $\text{cm}^{-1}$  employing the attenuated total reflectance (ATR) method. Raman spectroscopy was conducted on a Bruker Senterra II Raman microscope using a 532 nm laser in the wavenumber range from 50 to 4265  $\text{cm}^{-1}$  at room temperature.

## RESULTS AND DISCUSSION

Thin films of dysprosium with high silicon content were successfully prepared by thermal calcination, and an n-Si-Dy composite was created by thermal baking at 1373 K. Raman measurements confirmed the formation of both amorphous and nanocrystalline structures in films annealed at 1373 K. Photoluminescence was observed and interpreted as interband recombination in nanoparticles larger than 2.5 nm, as well as carrier recombination through defect states in smaller nanoparticles.

FTIR spectra were carefully studied to identify structural changes in n-Si and the resulting n-Si-Dy compositions. The FTIR spectra of both the original n-Si and the resulting n-Si-Dy composite are presented in Figure 1.

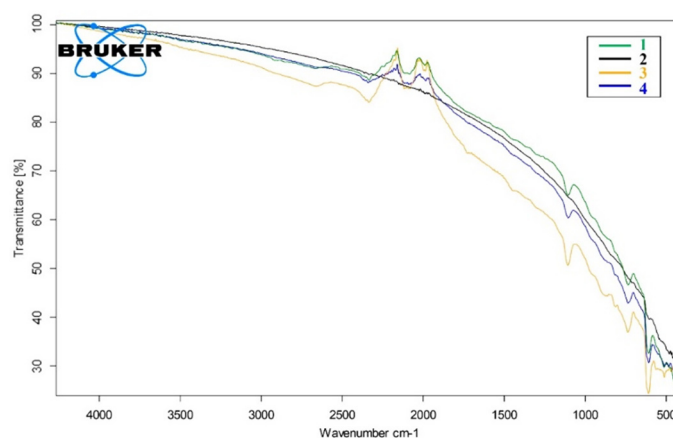


**Figure 1.** FTIR spectra of n-Si and the resulting n-Si<Dy>:

1. n-Si control: thermal firing at 1373 K for 40 hours, subsequent rapid cooling, without polishing;
2. n-Si<Dy> (fast cooling);
3. N-Si (starting material);
4. n-Si-Dy: thermal firing at 1373 K for 40 hours, followed by rapid cooling, with polishing

When analyzing n-Si itself, as well as n-Si-Dy composites obtained on its basis using FTIR spectrometry, in addition to the absorption of light on vibrations of regular atoms of the crystal lattice, in the solid there was also a process of absorption at local x fluctuations associated with defects and impurities. Thus, when analyzing the obtained FTIR spectra, the following patterns were revealed: absorption bands at 1106 and 515  $\text{cm}^{-1}$  of crystalline silicon are associated with the oxygen present in silicon (one must take into account the fact that oxygen in crystalline silicon is lies in the interstices and is an electrically neutral impurity insertion), carbon in crystalline silicon exhibits one antisymmetric stretching ( $\nu_{\text{as}}$ ) vibration, the frequency of which is 605  $\text{cm}^{-1}$ , peaks at 640  $\text{cm}^{-1}$  correspond to Si-H stretching, and peaks at 1615  $\text{cm}^{-1}$  - mode of perpendicular stretching. Dy-doped Si material exhibits additional peaks in its FTIR spectra due to the presence of vacancies and defects in n-Si<Dy> compositions. The peaks at 516.71  $\text{cm}^{-1}$  are due to the Si-Si stretching mode, while the peaks at 805  $\text{cm}^{-1}$  are due to the wagging mode of hydrogen. The frequency range (1950–2250  $\text{cm}^{-1}$ ) was deconvoluted to investigate potential local vibrational modes arising from defects and the formation of new bonds involving Dy.

Peaks located between 2210  $\text{cm}^{-1}$  and 2350  $\text{cm}^{-1}$  are typically attributed to Dy-Dy stretches. The peak at 2070  $\text{cm}^{-1}$  arises from adsorbed hydrogen at defective sites. Peaks at 2110  $\text{cm}^{-1}$  and 2124  $\text{cm}^{-1}$  correspond to Dy-Si and Si-Dy<sub>2</sub>, respectively [10]. Additionally, the peak at 2074  $\text{cm}^{-1}$  corresponds to db-Si-Si-H, where 'db' denotes dangling bonds. The small peak at 2211  $\text{cm}^{-1}$  may be attributed to Dy-induced microcrystallites.

To investigate changes in the FTIR spectra between the original n-Si and the resulting n-Si<Dy> compositions, we conducted a detailed study of the regions from 400 to 800  $\text{cm}^{-1}$  (refer to Figure 2). The resulting spectra clearly demonstrate all the changes occurring during the transition from n-Si to the resulting n-Si<Dy> compositions.

To further investigate the changes during the production of n-Si<Dy> compositions from the original n-Si, Raman spectroscopy was utilized. Raman spectra for four samples, including both n-Si and n-Si-Dy composites, obtained under different conditions and deposited on crystalline Si substrates annealed at 1373 K for 40 hours, are presented in Figure 3. A tail is observed, which does not develop into a distinct peak in any pattern. We assume that this tail is mainly due to scattering from silicon nanocrystals formed during annealing. This is confirmed by a similar low-energy tail observed in other Raman studies of silicon nanocrystals [12]. In these studies, the peak of the Raman band is slightly shifted relative to the Si single crystal band, but its low-energy tail is highly asymmetric and extends out to 450  $\text{cm}^{-1}$ , which is similar to

the tail of our Raman spectra (Figure 3). However, a small part of the scattering in the low-frequency tail of our spectra can be associated with n-Si, for which the Raman peak [10] at  $480\text{ cm}^{-1}$  asymmetrically extends to  $250 - 310\text{ cm}^{-1}$ . We do not observe any scattering below  $400\text{ cm}^{-1}$ , which means that most of the scattering in the low-energy tail of our spectra is due to Si nanocrystals. This conclusion is also confirmed by the results of X-ray diffraction (XRD), which show a fairly high density of Si nanocrystals in films annealed at  $1373\text{ K}$ .

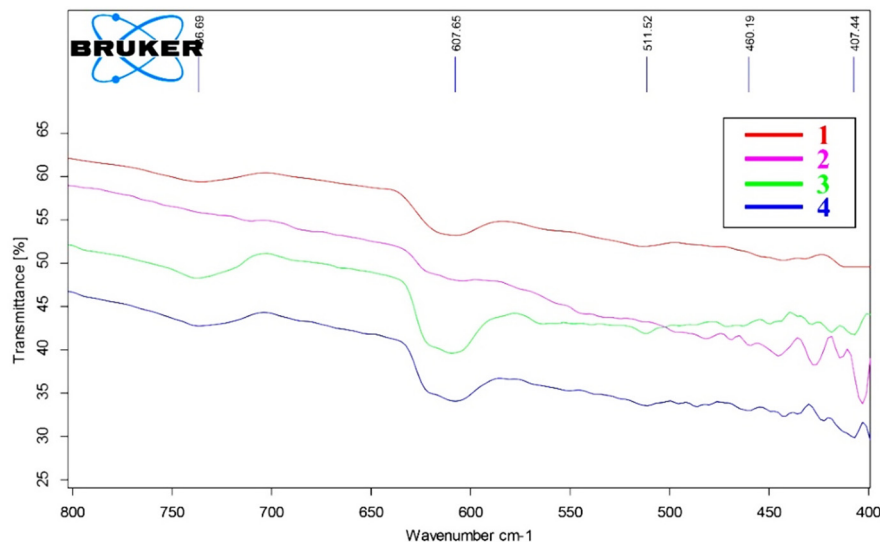


**Figure 2.** FTIR spectra of Si (spectrum region  $400\text{--}800\text{ cm}^{-1}$ ):

1. n-Si control: thermal firing at  $1373\text{ K}$  for 40 hours, subsequent rapid cooling, without polishing;
2. n-Si<Dy> (fast cooling);
3. N-Si (starting material);
4. n-Si-Dy: thermal firing at  $1373\text{ K}$  for 40 hours, followed by rapid cooling, with polishing

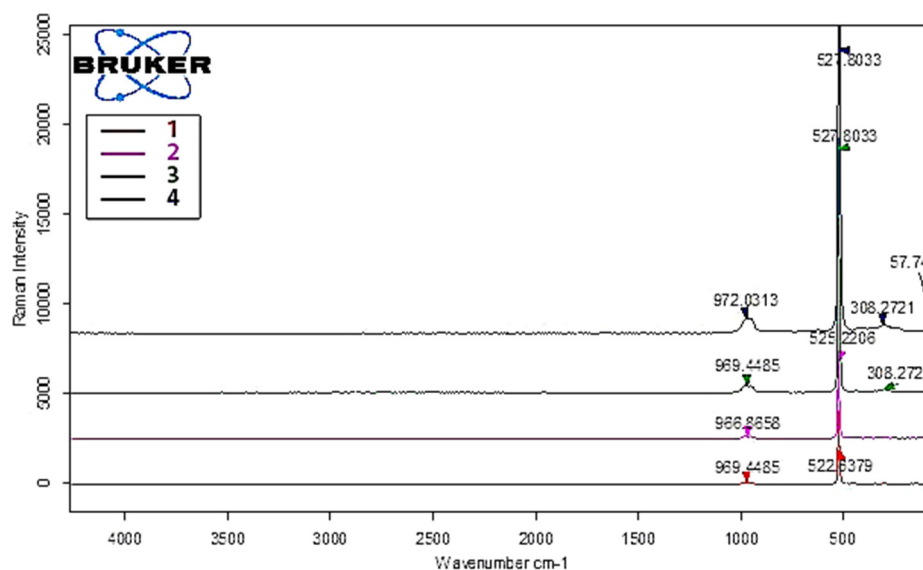


**Figure 3.** Raman spectra for four n-Si and n-Si<Dy> composite samples (range from  $50$  to  $4265\text{ cm}^{-1}$ ):

1. n-Si control: thermal firing at  $1373\text{ K}$  for 40 hours, subsequent rapid cooling, without polishing;
2. n-Si<Dy> (fast cooling);
3. N-Si (starting material);
4. n-Si-Dy: thermal firing at  $1373\text{ K}$  for 40 hours, followed by rapid cooling, with polishing

To analyze changes in the Raman spectrum between the original n-Si and the resulting n-Si<Dy> compositions, we conducted a detailed study of the regions from  $50$  to  $1400\text{ cm}^{-1}$  (refer to Figure 4). The resulting spectra clearly demonstrate all the changes occurring during the transition from n-Si to the resulting n-Si<Dy> compositions.

Based on the data presented in Figure 4, it is evident that the transition from the original n-Si to the resulting composites under different n-Si<Dy> conditions leads to changes in signals around  $307\text{ cm}^{-1}$  and  $960\text{ cm}^{-1}$ . These changes include increased intensity and mixing relative to the signals of the original n-Si. Additionally, the prominent signal in the region around  $522\text{ cm}^{-1}$  during this transition noticeably broadens, indicating a decrease in the crystallinity of the original n-Si.

Previous studies [14] have utilized Raman spectra to estimate the average size of Si and Dy nanocrystals. This can be achieved either by fitting the experimental curve with an expression accounting for finite size effects [14], or by using theoretically predicted dependencies [13] of band position and asymmetry on crystallite size.

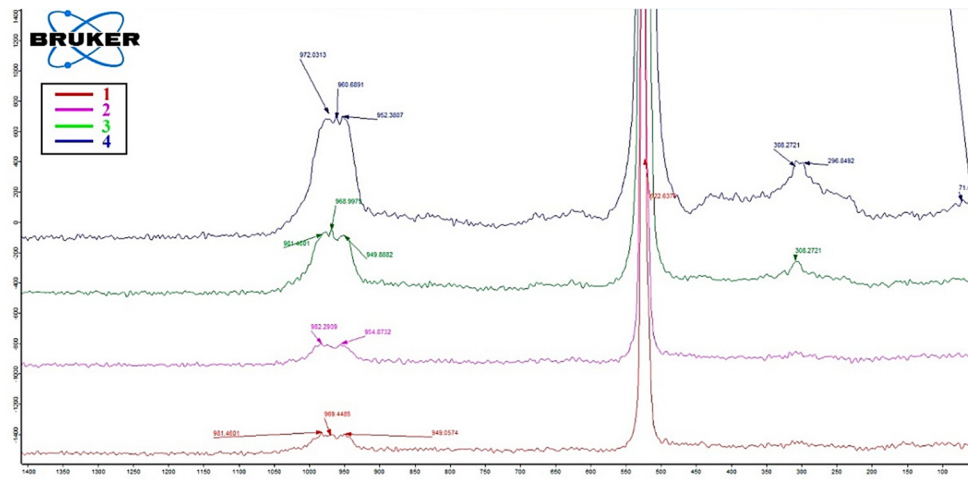


**Figure 4.** Raman spectra for four n-Si and n-Si<Dy> composite samples (range from 50 to 1400  $\text{cm}^{-1}$ ):

1. n-Si control: thermal firing at 1373 K for 40 hours, subsequent rapid cooling, without polishing;
2. n-Si<Dy> (fast cooling);
3. N-Si (starting material);
4. n-Si-Dy: thermal firing at 1373 K for 40 hours, followed by rapid cooling, with polishing

In both approaches, precise determination of the nanocrystal band is crucial, particularly for films grown on n-Si substrates where the  $522 \text{ cm}^{-1}$  band is also present in the Raman spectra. In nanocrystalline silicon films, the intensity of scattered light from the film is relatively high, while scattering from the substrate is significantly reduced due to absorption in the film. This ensures that the shape and position of the band originating from nanocrystals [10] are not distorted when scattered on the substrate. However, in Si-Dy films, the fill factor is relatively small, approximately 10% [7]. The intensity of scattered light from Si nanocrystals is low, whereas the Raman line due to the n-Si substrate remains strong. Figure 3 and 4 illustrate that a distinct band in all spectra peaks at  $522 \text{ cm}^{-1}$  with a width at half maximum of  $4.5 \text{ cm}^{-1}$ . It is evident that scattering from Si nanocrystals is weak and does not significantly impact the shape and position of the substrate signal. In an attempt to isolate the nanocrystal band, we subtracted the baseline, including background luminescence, noise, and the Lorentzian band with the aforementioned peak position and width at half maximum, from the measured spectrum of each film (Figure 3). Initially, the Lorentzian amplitude was set equal to the amplitude of the  $522 \text{ cm}^{-1}$  band in the measured spectra. However, due to the uncertainty in determining the exact intensity level of scattered light from the n-Si substrate, it is challenging to accurately determine the size of Si nanocrystals from the Raman spectra of Si-Dy thin films with a low fill factor.

## CONCLUSIONS

Characteristic peaks were identified in the FTIR spectra, such as the peak at  $640 \text{ cm}^{-1}$  associated with the Si-H mode and the peak at  $1615 \text{ cm}^{-1}$  associated with the perpendicular stretching mode, indicating specific structural features of the material. Additional peaks appeared in the FTIR spectra of n-Si-Dy samples, particularly at  $516.71 \text{ cm}^{-1}$  (Si-Si stretching mode) and  $805 \text{ cm}^{-1}$  (hydrogen wagging mode), suggesting the influence of dysprosium on the structure and properties of the material. These additional peaks indicate potential defects and vacancies in the new Si-Dy compositions, which are crucial for understanding changes in material structure.

Further analysis of the frequency ranges from  $1950$  to  $2250 \text{ cm}^{-1}$  confirmed the presence of local vibration modes associated with defects and the formation of new bonds involving dysprosium. Peaks related to Dy-Dy stretching were detected between  $2210 \text{ cm}^{-1}$  and  $2350 \text{ cm}^{-1}$ , indicating dysprosium interactions in the samples. The peak at  $2070 \text{ cm}^{-1}$  is attributed to adsorbed hydrogen at defect sites, which can influence material properties. Peaks at  $2110 \text{ cm}^{-1}$  (Dy-Si) and  $2124 \text{ cm}^{-1}$  (Si-Dy<sub>2</sub>) suggest the interaction of dysprosium with silicon in the samples. The peak at  $2074 \text{ cm}^{-1}$  corresponds to db-Si-Si-H, where db represents the dangling bond. Additionally, a peak at  $2211 \text{ cm}^{-1}$  may be attributed to dysprosium-induced microcrystals.

Regarding the Raman spectra, a “tail” is observed, which arises from scattering on silicon nanocrystals formed during annealing. This observation is consistent with the low-energy tail observed in other Raman studies of silicon nanocrystals. X-ray diffraction results confirm the high density of Si nanocrystals in films annealed at 1373 K. It's important to note that the observed scattering in the low-energy tail primarily originates from Si nanocrystals and not n-Si.

## ORCID

- ✉ Khodjakbar S. Daliev, <https://orcid.org/0000-0002-2164-6797>; ✉ Sharifa B. Utamuradova, <https://orcid.org/0000-0002-1718-1122>  
✉ Alisher Khaitbaev, <https://orcid.org/0000-0001-9892-8189>; ✉ Jonibek J. Khamdamov, <https://orcid.org/0000-0003-2728-3832>  
✉ Shahriyor B. Norkulov, <https://orcid.org/0000-0002-2171-4884>; ✉ Mansur B. Bekmuratov, <https://orcid.org/0009-0006-3061-1568>

## REFERENCES

- [1] L.T. Canham, “Silicon quantum wire array fabrication by electrochemical and chemical dissolution of wafers,” *Appl. Phys. Lett.* **57**, 1046-1990. <https://doi.org/10.1063/1.103561>
- [2] F. Huisken, H. Hofmeister, B. Kohn, M.A. Laguna, and V. Paillard, “Laser production and deposition of light-emitting silicon nanoparticles,” *Appl. Surf. Sci.* **154–155**, 305 (2000). [https://doi.org/10.1016/s0169-4332\(99\)00476-6](https://doi.org/10.1016/s0169-4332(99)00476-6)

- [3] V. Vinciguerra, G. Franzo, F. Priolo, F. Iacona, and C. Spinella, "Quantum confinement and recombination dynamics in silicon nanocrystals embedded in Si/SiO<sub>2</sub> superlattices," *J. Appl. Phys.* **87**, 8165 (2000). <https://doi.org/10.1063/1.373513>
- [4] F. Koch, and V. Petrova-Koch, "Light from Si-nanoparticle systems - a comprehensive view," *J. Non-Cryst. Solids*, **198–200**, 840 (1996). [https://doi.org/10.1016/0022-3093\(96\)00067-1](https://doi.org/10.1016/0022-3093(96)00067-1)
- [5] Zh. Ma, X. Liao, J. He, W. Cheng, G. Yue, Y. Wang, and G. Kong, "Annealing behaviors of photoluminescence from SiO<sub>x</sub>:H," *J. Appl. Phys.* **83**, 7934 (1998). <https://doi.org/10.1063/1.367973>
- [6] M. Zaharias, H. Freistdt, F. Stolze, T.P. Drusedau, M. Rosenbauer, and M. Stutzmann, "Properties of sputtered a-SiO<sub>x</sub>:H alloys with a visible luminescence," *J. Non-Cryst. Solids*, **164–166**, 1089 (1993). [https://doi.org/10.1016/0022-3093\(93\)91188-9](https://doi.org/10.1016/0022-3093(93)91188-9)
- [7] U. Kahler, and H. Hofmeister, "Silicon nanocrystallites in buried SiO<sub>x</sub> layers via direct wafer bonding," *Appl. Phys. Lett.* **75**, 641 (1999). <https://doi.org/10.1063/1.124467>
- [8] S. Zhang, W. Zhang, and J. Yuan, "The preparation of photoluminescent Si nanocrystal–SiO<sub>x</sub> films by reactive evaporation," *Thin Solid Films*, **326**, 92 (1998). [https://doi.org/10.1016/S0040-6090\(98\)00532-X](https://doi.org/10.1016/S0040-6090(98)00532-X)
- [9] H. Richter, Z.P. Wang, and L. Ley, "The one phonon Raman spectrum in microcrystalline silicon," *Solid State Commun.* **39**, 625 (1981). [https://doi.org/10.1016/0038-1098\(81\)90337-9](https://doi.org/10.1016/0038-1098(81)90337-9)
- [10] Z. Iqbal, and S. Veprek, "Raman scattering from hydrogenated microcrystalline and amorphous silicon," *J. Phys. C*, **15**, 377 (1982). <https://doi.org/10.1088/0022-3719/15/2/019>
- [11] J. Gonzales-Hernandez, G.H. Azarbayejani, R. Tsu, and F.H. Pollak, "Raman, transmission electron microscopy, and conductivity measurements in molecular beam deposited microcrystalline Si and Ge: A comparative study," *Appl. Phys. Lett.* **47**, 1350 (1985). <https://doi.org/10.1063/1.96277>
- [12] I.H. Campbell, and P.M. Fauchet, "The effects of microcrystal size and shape on the one phonon Raman spectra of crystalline semiconductors," *Solid State Commun.* **52**, 739 (1986). [https://doi.org/10.1016/0038-1098\(86\)90513-2](https://doi.org/10.1016/0038-1098(86)90513-2)
- [13] J. Zi, H. Buscher, C. Falter, W. Ludwig, K. Zhang, and X. Xie, "Raman shifts in Si nanocrystals," *Appl. Phys. Lett.* **69**, 200 (1996). <https://doi.org/10.1063/1.117371>
- [14] D.R. dos Santos, and I.L. Torriani, "Crystallite size determination in μc-Ge films by x-ray diffraction and Raman line profile analysis," *Solid State Commun.* **85**, 307 (1993). [https://doi.org/10.1016/0038-1098\(93\)90021-E](https://doi.org/10.1016/0038-1098(93)90021-E)
- [15] Kh.S. Daliev, Z.E. Bahronkulov, and J.J. Hamdamov, "Investigation of the Magnetic Properties of Silicon Doped with Rare-Earth Elements," *East Eur. J. Phys.* **4**, 167 (2023). <https://doi.org/10.26565/2312-4334-2023-4-18>
- [16] Kh.S. Daliev, Sh.B. Utamuradova, Z.E. Bahronkulov, A.Kh. Khaitbaev, and J.J. Hamdamov, "Structure Determination and Defect Analysis n-Si<Lu>, p-Si<Lu> Raman Spectrometer Methods," *East Eur. J. Phys.* **4**, 193 (2023). <https://doi.org/10.26565/2312-4334-2023-4-23>
- [17] P.A. Temple, and C.E. Hathaway, "Multiphonon Raman Spectrum of Silicon," *Physical Review B*, **7(8)**, 3685–3697 (1973). <https://doi.org/10.1103/PhysRevB.7.3685>
- [18] K.J. Kingma, and R.J. Hemley, "Raman spectroscopic study of microcrystalline silica," *American Mineralogist*, **79(3-4)**, 269–273 (1994). [https://pubs.geoscienceworld.org/msa/ammin/article-pdf/79/3-4/269/4209223/am79\\_269.pdf](https://pubs.geoscienceworld.org/msa/ammin/article-pdf/79/3-4/269/4209223/am79_269.pdf)
- [19] G.E. Walrafen, Y.C. Chu, and M.S. Hokmabadi, "Raman spectroscopic investigation of irreversibly compacted vitreous silica," *The Journal of Chemical Physics*, **92(12)**, 6987–7002 (1990). <https://doi.org/10.1063/1.458239>
- [20] B. Champagnon, C. Martinet, M. Boudeulle, D. Vouagner, C. Coussa, T. Deschamps, and L. Grosvalet, "High pressure elastic and plastic deformations of silica: in situ diamond anvil cell Raman experiments," *Journal of Non-Crystalline Solids*, **354(2-9)**, 569–573 (2008). <https://doi.org/10.1016/j.jnoncrysol.2007.07.079>
- [21] A.S. Zakirov, Sh.U. Yuldashev, H.J. Wang, H.D. Cho, T.W. Kang, J.J. Khamdamov, and A.T. Mamadalimov, "Photoluminescence study of the surface modified and MEH-PPV coated cotton fibers," *Journal of Luminescence*, **131(2)**, 301–305 (2011). <https://doi.org/10.1016/j.jlumin.2010.10.019>
- [22] Sh.B. Utamuradova, H.J. Matchonov, Zh.J. Khamdamov, and H.Yu. Utemuratova, "X-ray diffraction study of the phase state of silicon single crystals doped with manganese," *New Materials, Connections Oath Applications*, **7(2)**, 93–99 (2023). [http://jomardpublishing.com/UploadFiles/Files/journals/NMCA/v7n2/Utamuradova\\_et\\_al.pdf](http://jomardpublishing.com/UploadFiles/Files/journals/NMCA/v7n2/Utamuradova_et_al.pdf)
- [23] Kh.S. Daliev, Sh.B. Utamuradova, J.J. Khamdamov, M.B. Bekmuratov, "Structural Properties of Silicon Doped Rare Earth Elements Ytterbium," *East Eur. J. Phys.* **1**, 375–379 (2024). <https://doi.org/10.26565/2312-4334-2024-1-37>

#### ДЕФЕКТНА СТРУКТУРА КРЕМНІЮ, ЛЕГОВАНОГО ДИСПРОЗІЄМ

Ходжакбар С. Далієв<sup>а</sup>, Шаріфа Б. Утамурадова<sup>б</sup>, Алішер Хайтбаєв<sup>б</sup>, Джонібек Дж. Хамдамов<sup>б</sup>,  
Шахрійор Б. Норкулов<sup>б</sup>, Мансур Б. Бекмуратов<sup>с</sup>

<sup>а</sup>Філія Федерального державного бюджетного навчального закладу вищої освіти «Національний дослідницький університет МПЕІ», вул. Йогду, 1, м. Ташкент, Узбекистан

<sup>б</sup>Інститут фізики напівпровідників та мікроелектроніки Національного університету Узбекистану, 100057, Ташкент, Узбекистан, вул. Янги Алмазар, 20

<sup>с</sup>Нукусський державний педагогічний інститут імені Аджиніяза, Нукус, Узбекистан

У цій роботі було проаналізовано структурні та оптичні характеристики зразків кремнію (n-Si) та його композиції з диспрозієм (n-Si-Dy) за допомогою методів інфрачервоної спектроскопії з перетворенням Фур'є (FTIR) та спектроскопії раманівського розсіювання. Були ідентифіковані характерні піки в спектрах FTIR, такі як 640 см<sup>-1</sup> (режим Si-H) і 1615 см<sup>-1</sup> (режим перпендикулярного розтягування), що вказує на структурні особливості матеріалу. Поява додаткових піків у спектрах n-Si-Dy при 516,71 см<sup>-1</sup> та 805 см<sup>-1</sup> свідчить про вплив диспрозію на структуру та дефектність матеріалу. Дослідження частотного діапазону (1950–2250 см<sup>-1</sup>) додатково підтверджує локальні моди вібрації, пов'язані з дефектами та взаємодією з диспрозієм. Піки, пов'язані з розтягуванням Ду-Ду, а також взаємодією з кремнієм, були знайдені при 2110 см<sup>-1</sup> і 2124 см<sup>-1</sup>. Аналіз спектрів комбінаційного розсіювання свідчить про утворення нанокристалів кремнію під час відпалу, що підтверджено результатами XRD. Отримані результати дають важливе уявлення про вплив диспрозію на структуру та властивості кремнієвих матеріалів, які потенційно можуть знайти застосування в оптоелектроніці та матеріалознавстві.

**Ключові слова:** кремній; диспрозій; рідкоземельні елементи; комбінаційне розсіювання; дифузія; термообробка; температура



## DEFECT STRUCTURE OF SILICON DOPED WITH ERBIUM

 Sharifa B. Utamuradova<sup>a</sup>,  Khojakbar S. Daliev<sup>b</sup>,  Alisher I. Khaitbaev<sup>a</sup>,  
 Jonibek J. Khamdamov<sup>a\*</sup>,  Jasur Sh. Zarifbayev<sup>c</sup>, Bekzod Sh. Alikulov<sup>a</sup>

<sup>a</sup>Institute of Semiconductor Physics and Microelectronics at the National University of Uzbekistan, Tashkent, Uzbekistan

<sup>b</sup>Branch of the Federal State Budgetary Educational Institution of Higher Education "National Research University MPEI", Tashkent, Uzbekistan

<sup>c</sup>Uzbek State University of Physical Education and Sport, Uzbekistan

\*Corresponding Author e-mail: [jonibek.uzmu@gmail.com](mailto:jonibek.uzmu@gmail.com)

Received March 1, 2024; revised April 3, 2024; accepted April 5, 2024

The study of thin-film nanocomposites, including crystalline and amorphous silicon nanoparticles embedded in silicon oxide layers, is a key direction in the field of materials for optoelectronics. This study explored the interest in such composites, including erbium silicide ( $\text{ErSi}_{2-x}$ ), in the context of their applications in non-volatile memory and photovoltaic devices. Particular attention was paid to the structure and properties of such materials, including the analysis of defects in erbium-doped silicon. The results of the study, based on Raman spectroscopy and X-ray phase analysis, made it possible to identify the characteristics of the composition and structure of the studied samples. The identified data confirmed the presence of crystalline phases of Si and Er in the p-Si-Er composite, and also showed the substitution of Er in the p-Si/SiO<sub>2</sub> structure. Additionally, X-ray microanalysis data confirmed the presence of Si, O and Er in the expected concentrations in the composite film. Further research showed that the introduction of erbium atoms onto the silicon surface leads to minor changes in some signals and the appearance of new vibrations in the Raman spectra of the samples. The decrease in the intensity of the peaks belonging to silicon is associated with the weakening and breaking of some bonds in the structure of the silicon crystal lattice and due to the formation of new bonds in which erbium atoms participate. Thus, the results of this study represent a significant contribution to the understanding of the properties and potential of thin film nanocomposites for applications in optoelectronics, and also enrich our knowledge of the effect of doping on the structure and properties of silicon materials.

**Keywords:** Silicon; Erbium; Rare Earth Element; Raman Spectroscopy; Diffusion; Heat Treatment; Temperature; Structure; X-Ray Phase Analysis; Film

**PACS:** 71.20. – b, 71.28. + d

## INTRODUCTION

Thin-film nanocomposites, consisting of crystalline and amorphous Si nanoparticles embedded in silicon oxide layers, have been extensively studied over the past two decades as suitable materials for nonvolatile memory devices, third-generation photovoltaic devices, and other applications. Continued interest in such composites (including Er-doped ones) remains due to the possibility of manufacturing Si-based light sources for optoelectronic devices [1, 2].

Interest in erbium silicide ( $\text{ErSi}_{2-x}$ ) has been growing in recent years, since  $\text{ErSi}_{2-x}$  exhibits a very low Schottky barrier height on n-type silicon (0.3-0.4 eV) [1, 2]. This unique property leads to promising applications, such as the utilization of  $\text{ErSi}_{2-x}$  as source and drain contacts in future ultra-scale complementary metal-oxide semiconductor devices, as it can significantly reduce both contact resistance and total series resistance due to its low Schottky contact barrier. Additionally,  $\text{ErSi}_{2-x}$  finds applications in novel source/drain field-effect transistors featuring a Schottky barrier [3,4].

Despite the low resistivity of  $\text{ErSi}_{2-x}$ , erbium itself can oxidize very quickly due to its high reactivity with oxygen [5]. In many studies on Er silicides reported in the literature,  $\text{ErSi}_{2-x}$  thin films were typically formed by evaporating erbium onto silicon substrates under ultra-high vacuum conditions, followed by annealing to mitigate oxidation issues.

Silicon doped with rare earth elements has attracted the attention of researchers due to potential issues such as inhomogeneities in impurity distribution, complex diffusion processes, and alterations in its properties resulting from the introduction of rare earth elements into the silicon structure.

This paper examines the issue of the defect structure of silicon doped with erbium. Pristine p-Si, erbium-doped silicon p-Si<Er>, and p-Si-Er composites were studied using Raman spectroscopy and X-ray diffraction.

## EXPERIMENTAL PART

For the study, p-Si samples with an initial resistivity of 2.5 Ohm·cm were selected. Prior to alloying, the samples underwent thorough acid-peroxide washing, followed by the removal of oxide layers from their surfaces using an HF solution. After the surfaces of the samples were thoroughly cleaned, films of erbium impurities with special purity (99.999%) were deposited onto the clean Si surfaces using vacuum deposition. Vacuum conditions in the working chamber, with a pressure of approximately  $10^{-7}$ – $10^{-8}$  torr, were maintained by an oil-free vacuum pumping system.

Before diffusion annealing, the samples were placed in evacuated quartz ampoules. Doping of the samples with Er impurities was conducted using the diffusion method at a temperature of 1200°C for 25 hours, followed by rapid and

slow cooling. To investigate the interaction of impurity atoms in silicon, achieving not only uniform doping of the material but also maximum concentration is crucial. Therefore, we considered the optimal conditions for doping silicon with these impurity atoms.

Raman spectra were acquired using a SENTERRA II Raman spectrometer (Bruker, Germany). This fully automated instrument offers excellent sensitivity and a high resolution of  $4.0 \text{ cm}^{-1}$ . Senterra calibration was performed automatically and referenced to NIST acetaminophen and silica standards, ensuring a wavelength accuracy of  $0.2 \text{ cm}^{-1}$ .

The experiments were conducted using a laser with a wavelength of  $\lambda_0 = 532 \text{ nm}$ , a maximum power of  $P_{\text{max}} = 25 \text{ mW}$ , and an acquisition time of 100 s, with the addition of two spectra. This device allows for spectra acquisition in the range from 50 to  $4265 \text{ cm}^{-1}$ .

The Raman spectra were processed to facilitate comparison of intensity ratios between samples. Prior to normalizing the spectra to the peak at  $521 \text{ cm}^{-1}$ , corresponding to the most intense peak in the spectral region from  $4265$  to  $50 \text{ cm}^{-1}$ , a baseline subtraction was performed for each spectrum.

Raman spectra of samples (4 in total) were obtained at room temperature. The acquisition time for the Raman spectrum was about 120 s. The same laser beam that was used to measure Raman scattering was used to study structural changes. Measurements with increasing laser power density were carried out in order to determine the threshold above which irreversible changes occur. The sample temperature was increased by  $20^\circ\text{C}$  under the influence of a laser beam. This temperature increase was estimated using the Stokes/anti-Stokes intensity coefficient formula.

X-ray phase analysis was conducted using a MiniFlex II diffractometer (Rigaku, Japan) equipped with  $\text{CuK}\alpha$  radiation. Diffraction patterns of the compounds were captured in the angle range of  $2\theta = 3\text{--}60^\circ$ . The resulting diffraction pattern was analyzed to identify characteristic signals for the resulting p-Si-Er composites, and the presence of elements was determined based on literature data on the phases and the ICDD card database for known compounds. The obtained results enabled us to draw conclusions about the qualitative composition of the samples. X-ray diffraction spectra were recorded at intervals of  $0.02^\circ$  in two-theta, with an exposure time of 2 s at each point.

## RESULTS AND DISCUSSION

Figure 1 shows the Raman spectra of both the p-Si type silicon itself and the resulting p-Si-Er composites. The Raman spectrum of the initial sample exhibits peaks at  $304$  and  $521 \text{ cm}^{-1}$ , characteristic of cubic silicon, along with a broad peak in the range of  $920\text{--}1005 \text{ cm}^{-1}$  [8–12].

The cubic structure of silicon allows the presence of one first-order Raman-active phonon corresponding to a wave number of  $520 \pm 1 \text{ cm}^{-1}$ , as well as additional peaks with lower intensity [6–11]. According to [13, 14], the vibration at  $304 \text{ cm}^{-1}$  detected in the Raman spectra of silicon is attributed to the longitudinal acoustic mode. The broad peak in the range of  $900\text{--}1100 \text{ cm}^{-1}$  arises from the scattering of several transverse optical phonons and their overtone state [8,9,10]. Upon studying the broad peak in the range of  $920\text{--}1005 \text{ cm}^{-1}$  as presented in Fig. 1, three vibrations were detected at  $944$ ,  $948$ , and  $976 \text{ cm}^{-1}$ , consistent with theoretical calculations [10].

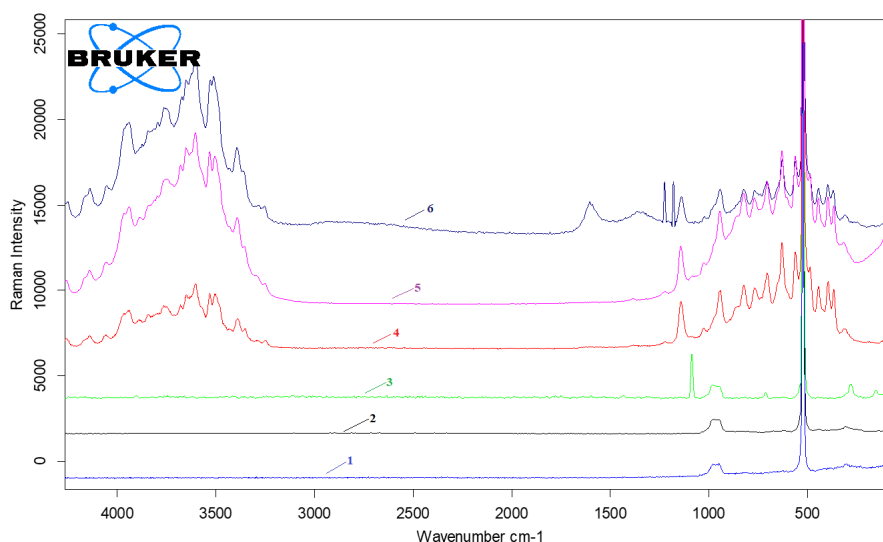


**Figure 1.** Raman spectra of the obtained composites: silicon (p-Si) with erbium (Er)

Sample 1 represents the original p-Si; Sample 2 denotes doped p-Si<Er> (slow cooling); Sample 3 corresponds to doped p-Si<Er, Cr> (fast cooling); Sample 4 represents the resulting composite p-Si-Er-Cr (slow cooling); Samples 5 and 6 denote p-Si-Er (slow cooling) and p-Si-Er (fast cooling) respectively

Further doping of p-Si silicon wafers with erbium results in minor changes and the emergence of new vibrations in the Raman spectra. The intensity of the main silicon peak at  $521 \text{ cm}^{-1}$  decreases by a factor of 1.5, while its width at half maximum remains virtually unchanged at approximately  $4.0 \text{ cm}^{-1}$ . This decrease in peak intensity is likely attributed to the weakening and breaking of bonds in the silicon crystal lattice due to the introduction of erbium atoms.

The vibration intensity at a frequency of  $304\text{ cm}^{-1}$  generally increases, and its width at half maximum decreases from  $8.2$  to  $6.1\text{ cm}^{-1}$ . As a result of studying the broad peak appearing in the region of  $900\text{--}1100\text{ cm}^{-1}$ , three vibrations were also recorded at  $946$ ,  $952$  and  $979\text{ cm}^{-1}$  (Fig. 1). The shift of these vibrations towards the lowest wave numbers compared to the original silicon reaches  $4\text{ cm}^{-1}$ , with the largest shift observed at  $948\text{ cm}^{-1}$ . Also, other signals appear in the Raman spectra of the obtained composites. For example, the wavenumber of  $478\text{ cm}^{-1}$  indicates out-of-plane deformation of Si-O, and the peak of  $842\text{ cm}^{-1}$  indicates Si-O bending. The wavenumber of  $1053\text{ cm}^{-1}$  indicates Si-O-Si stretching. The wavenumber of  $614\text{ cm}^{-1}$  indicates Si-Si bonds [19-21]. In Figure 1, four peaks can also be identified at  $422\text{ cm}^{-1}$ ,  $491\text{ cm}^{-1}$ ,  $875\text{ cm}^{-1}$  and  $1046\text{ cm}^{-1}$ . The peak with a wavenumber of  $422\text{ cm}^{-1}$  corresponds to the impurity vibrational Er-O bond, the signals for the Si-O bond are at  $491\text{ cm}^{-1}$ . The wavenumber at  $1046\text{ cm}^{-1}$  indicates asymmetric stretching of Si-O-Si [19-21]. It is assumed that the two signals corresponding to silicon cannot be detected using the Raman spectrum due to the largest Er weight, since it is completely covered by new Er signals.

The change in the Raman spectrum of p-Si-Er in the range of  $60\text{--}280\text{ cm}^{-1}$  (Fig. 1) is due to the presence of elemental Er and the formation of new bonds between Er-Si [15-17, 22]. In [15], multichannel Raman spectroscopy was used to quantitatively characterize the formation of Pt-Si at the Pt-Si (100) interface, where spectra were obtained from Pt-Si layers up to  $10\text{ \AA}$  thick and from  $<40\text{ \AA}$  Pt-Si at  $140\text{ \AA}$ . According to this work, characteristic vibrations for Pt-Si appear at  $82\text{--}85$  and  $140\text{ cm}^{-1}$ . These works also report Raman modes near  $90$  and  $140\text{ cm}^{-1}$  from Pt-Si, the latter mode being due to the formation of a disordered mixed phase of Pt and Si.

### X-ray phase analysis

X-ray diffraction patterns of erbium films deposited under various conditions are presented in Fig. 2. The lattice constants calculated from the X-ray diffraction patterns of p-Si-Er are Si =  $0.5426\text{ nm}$ , Er =  $0.3572\text{ nm}$  and Er =  $0.5626\text{ nm}$ , respectively. The arrangement of Si and Er atoms along crystalline orientations is triangular. The side lengths of the triangles are  $0.3841\text{ nm}$  for p-Si and  $0.3568\text{ nm}$  for Er, so there is a lattice mismatch [25]. It can be assumed that a certain proportion of defects and deformations will be formed during initial deposition due to lattice mismatch.

The obtained X-ray phase analysis data, presented in Figure 2, indicate the presence of both Si and Er in the composition of the studied samples.

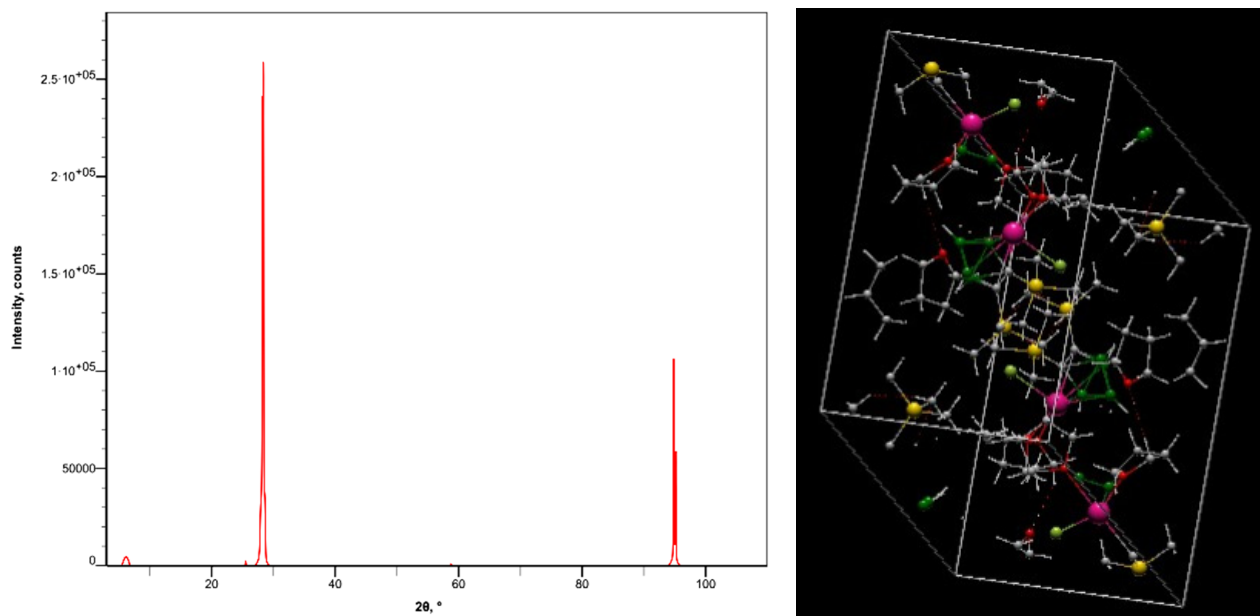


**Figure 2.** X-ray microanalysis of the resulting p-Si-Er composite

As can be seen from the given X-ray phase analysis data (Fig. 2) of the resulting p-Si-Er composite, the elements Si, O and Er are present in the film in the expected concentrations. This result confirms the substitution of Er in the p-Si/SiO<sub>2</sub> structure. The peak at  $28.40$  corresponds to Si originating from the glass substrate [23,24]. The present peak at  $94.80$  is attributed to Er.

Lau et al. [26] studied the effect of the oxide layer impregnated between the metal layer and the Si substrate on the surface morphology of the composite, it is obvious that interfacial contamination is the cause of the formation of surface pores in the silicide layer. These works provide data that the pores consist of ErSi<sub>2x</sub>, therefore the non-planar nature of the ErSi<sub>2x</sub>/Si(111) interfaces in the region of pinholes additionally leads to the formation of polycrystalline ErSi<sub>2x</sub> on the Si surface [26,27]. Consequently, a large number of Si atoms from the substrate diffuse through the depressions, which contain much faster atomic diffusion paths. Lau et al. [26] and Shen et al. [27] found that the shape of the surface holes is rectangular for Er on Si and triangular for Dy on Si.



## CONCLUSIONS

Analysis of the results obtained using Raman spectroscopy shows that the introduction of Er atoms onto the p-Si surface leads to both minor changes in some signals and the appearance of new vibrations in the Raman spectra of the samples. The decrease in the intensity of the peaks belonging to silicon is probably associated with the weakening and breaking of bonds in the structure of the silicon crystal lattice due to Er atoms. The appearance of new vibrations in the range of 60–280  $\text{cm}^{-1}$  in the p-Si-Er spectra is associated with the presence of elemental Er and the formation of new Er-Si bonds. The presence of erbium on the p-Si surface is confirmed by X-ray microanalysis data.

## ORCID

- Khodjakbar S. Daliev, <https://orcid.org/0000-0002-2164-6797>
- Sharifa B. Utamuradova, <https://orcid.org/0000-0002-1718-1122>
- Alisher Khaitbaev, <https://orcid.org/0000-0001-9892-8189>
- Jonibek J. Khamdamov, <https://orcid.org/0000-0003-2728-3832>
- Jasur Sh. Zarifbayev, <https://orcid.org/0009-0002-4097-4996>

## REFERENCES

- [1] I.P. Lisovskiy, A.V. Sarikov, and M.I. Sypko, *Thin film structures with silicon nanoinclusions*, (Knigi-XXI, Kyiv-Chernivci, 2014). (in Ukrainian)
- [2] M. Sopinsky, and V. Khomchenko, “Electroluminescence in SiO<sub>x</sub> films and SiO<sub>x</sub>-film-based systems,” *Current opinion in solid state & materials science*, **7**(2), 97-109 (2003). [https://doi.org/10.1016/S1359-0286\(03\)00048-2](https://doi.org/10.1016/S1359-0286(03)00048-2)
- [3] J. Kedzierski, P. Xuan, E. Anderson, J. Boker, T. King, and C. Hu, “Complementary silicide source/drain thin-body MOSFETs for the 20-nm gate-length regime,” in: *International Electron Devices Meeting 2000. Technical Digest. IEDM*, (2000), pp. 57-60. <https://doi.org/10.1109/IEDM.2000.904258>
- [4] M. Jang, J. Oh, S. Maeng, W. Cho, S. Lee, K. Kang, and K. Park, “Characteristics of erbium-silicided n-type Schottky barrier tunnel transistors,” *Appl. Phys. Lett.* **83**, 2611 (2003). <https://doi.org/10.1063/1.1614441>
- [5] S. Kennou, S. Ladas, M.G. Gimaldi, T.A.N. Tan, and J.Y. Veillen, “Oxidation of thin erbium and erbium silicide overlayers in contact with silicon oxide films thermally grown on silicon,” *Appl. Surf. Sci.* **102**, 142-146 (1996). [https://doi.org/10.1016/0169-4332\(96\)00034-7](https://doi.org/10.1016/0169-4332(96)00034-7)
- [6] Kh.S. Daliev, Sh.B. Utamuradova, J.J. Khamdamov, and Z.E. Bahronkulov, “Electrophysical properties of silicon doped with lutetium,” *Advanced Physical Research*, **6**(1), 42-49 (2024). <https://doi.org/10.62476/apr61.49>
- [7] K.S. Daliev, S.B. Utamuradova, J.J. Khamdamov, and M. B. Bekmuratov, “Structural Properties of Silicon Doped Rare Earth Elements Ytterbium,” *East European Journal of Physics*, (1), 375-379 (2024). <https://doi.org/10.26565/2312-4334-2024-1-37>
- [8] P.A. Temple, and C.E. Hathaway, “Multiphonon Raman Spectrum of Silicon,” *Physical Review B*, **7**(8), 3685 (1973). <https://doi.org/10.1103/physrevb.7.3685>
- [9] K. Uchinokura, T. Sekine, and E. Matsuura, “Critical-point analysis of the two-phonon Raman spectrum of silicon,” *Journal of Physics and Chemistry of Solids*, **35**(2), 171–180 (1974). [https://doi.org/10.1016/0022-3697\(74\)90031-6](https://doi.org/10.1016/0022-3697(74)90031-6)
- [10] I. Iatsunskiy, G. Nowaczyk, S. Jurga, V. Fedorenko, M. Pavlenko, and V. Smyntyna, “Optik- International Journal for Light and Electron Optics,” **126**(18), 1650-1655 (2015). <https://doi.org/doi:10.1016/j.ijleo.2015.05.088>
- [11] A. Wellner, V. Paillard, H. Coffin, N. Cherkashin, and C. Bonafos, “Resonant Raman scattering of a single layer of Si nanocrystals on a silicon substrate,” *Journal of Applied Physics*, **96**(4), 2403-2405 (2004). <https://doi.org/10.1063/1.1765853>
- [12] Sh.B. Utamuradova, A.V. Stanchik, K.M. Fayzullaev, B.A. Bakirov, *Applied Physics*, **2**, 33–38 (2022). (in Russian)
- [13] C. Smit, R.A.C.M.M. van Swaaij, H. Donker, A.M.H.N. Petit, W.M.M. Kessels, M.C.M. van de Sanden, “Determining the material structure of microcrystalline silicon from Raman spectra,” *Journal of Applied Physics*, **94**(5), 3582 (2003). <https://doi.org/doi:10.1063/1.1596364>
- [14] B. Graczykowski, A. El Sachat, J.S. Reparaz, M. Sledzinska, M.R. Wagner, E. Chavez-Angel, and C.M.S. Torres, “Thermal conductivity and air-mediated losses in periodic porous silicon membranes at high temperatures,” *Nature Communications*, **8**(1), 415 (2017). <https://doi.org/10.1038/s41467-017-00115-4>
- [15] J.C. Tsang, Y. Yokota, R. Matz, and G. Rubloff, “Raman spectroscopy of PtSi formation at the Pt/Si(100) interface,” *Applied Physics Letters*, **44**(4), 430 (1984). <https://doi.org/10.1063/1.94755>
- [16] R.J. Nemanich, C.C. Tsai, B.L. Stafford, J.R. Abelson, and T.W. Sigmon, “Initial Phase Formation at the Interface of Ni, Pd, or Pt and Si,” *MRS Proceedings*, **25**, 9 (1984). <https://doi.org/10.1557/proc-25-9>
- [17] J.E. Smith, M.H. Brodsky, B.L. Crowder, M.I. Nathan, and A. Pinczuk, “Raman Spectra of Amorphous Si and Related Tetrahedrally Bonded Semiconductors,” *Phys. Rev. Lett.* **26**, 642 (1971). <https://doi.org/10.1103/PhysRevLett.26.642>
- [18] Kh.S. Daliev, Sh.B. Utamuradova, Z.E. Bahronkulov, A.Kh. Khaitbaev, and J.J. Hamdamov, “Structure Determination and Defect Analysis n-Si<Lu>, p-Si<Lu> Raman Spectrometer Methods,” *East Eur. J. Phys.* **4**, 193 (2023). <https://doi.org/10.26565/2312-4334-2023-4-23>
- [19] M.A. Va’squez, G.A. Rodriguez, G.P. Garcia-Saldago, G. Romeo-Paredes, and R. Pena-Sierra, “FTIR and photoluminescence studies of porous silicon layers oxidized in controlled water vapor conditions,” *Revista Mexicana De Fisica*, **6**, 431 (2007). <https://www.redalyc.org/pdf/570/57053601.pdf>
- [20] M. Bosca, L. Pop, G. Borodi, P. Pacuta, and E. Culea, “XRD and FTIR structural investigations of erbium-doped bismuth–lead–silver glasses and glass ceramics,” *Journal of Alloys and Compound*, **479**, 579 (2009). <https://doi.org/10.1016/j.jallcom.2009.01.001>
- [21] B. Shokri, and M.A. Firouzjeh, and S.I. Hosseini, “FTIR analysis of silicon dioxide thin film deposited by Metal organic-based PECVD,” in: *Proceedings of 19th International Symposium on Plasma Chemistry Society*. (IPCS, 2009).
- [22] N.B. Singh, and U. Sarkar, “Structure, vibrational, and optical properties of platinum cluster: a density functional theory approach,” *J. Mol. Model.* **20**, 2537 (2014). <https://doi.org/10.1007/s00894-014-2537-5>

- [23] K.D.A. Kumar, S. Valanarasu, A. Kathalingam, and V. Ganesh, "Effect of solvents on sol-gel spin-coated nanostructured Al-doped ZnO thin films: a film for key optoelectronic applications," *Appl. Phys. A*, **123**(12), 801 (2017). <https://doi.org/10.1007/s00339-017-1426-z>
- [24] K.D.A. Kumar, S. Valanarasu, A. Kathalingam, and K. Jeyadheepan, "Nd<sup>3+</sup> Doping effect on the optical and electrical properties of SnO<sub>2</sub> thin films prepared by nebulizer spray pyrolysis for opto-electronic application," *Mater. Res. Bull.* **101**, 264 (2018). <https://doi.org/10.1016/j.materresbull.2018.01.050>
- [25] J.A. Knapp, and S.T. Picraux, "Epitaxial growth of rare-earth silicides on (111) Si," *Appl Phys Lett.* **48**, 466-468 (1986). <https://doi.org/10.1063/1.96532>
- [26] S.S. Lau, C.S. Pai, C.S. Wu, T.F. Kuech, and B.X. Liu, "Surface morphology of erbium silicide," *Appl. Phys. Lett.* **41**, 77-80 (1982). <https://doi.org/10.1063/1.93295>
- [27] G.H. Shen, J.C. Chen, C.H. Lou, S.L. Cheng, and L.J. Chen, "The growth of pinhole-free epitaxial DySi<sub>2-x</sub> films on atomically clean Si(111)," *J. Appl. Phys.* **84**, 3630-3635 (1998). <https://doi.org/10.1063/1.368538>

#### ДЕФЕКТНА СТРУКТУРА КРЕМНІЮ, ЛЕГОВАНОГО ЕРБІЄМ

Шаріфа Б. Утамурадова<sup>а</sup>, Ходжакбар С. Далієв<sup>б</sup>, Алішер І. Хайтбаєв<sup>а</sup>, Джонібек Дж. Хамдамов<sup>а</sup>,  
Джасур Ш. Заріфбаєв<sup>с</sup>, Бекзод Ш. Алікулов<sup>а</sup>

<sup>а</sup>Інститут фізики напівпровідників та мікроелектроніки Національного університету Узбекистану, Ташкент, Узбекистан


<sup>б</sup>Філія Федерального державного бюджетного навчального закладу вищої освіти «Національний дослідницький університет МПЕІ», м. Ташкент, Узбекистан

<sup>с</sup>Узбецький державний університет фізичного виховання і спорту, Узбекистан

Дослідження тонкоплівкових наноконкомпозитів, включаючи кристалічні та аморфні наночастинки кремнію, вбудовані в шари оксиду кремнію, є ключовим напрямком у галузі матеріалів для оптоелектроніки. Це дослідження вивчало інтерес до таких композитів, включаючи силіцид ербію (ErSi<sub>2-x</sub>), у контексті їх застосування в енергонезалежній пам'яті та фотоелектричних пристроях. Особливу увагу було приділено структурі та властивостям таких матеріалів, у тому числі аналізу дефектів кремнію, легovanого ербієм. Результати дослідження, засновані на спектроскопії комбінаційного розсіювання та рентгенофазовому аналізі, дозволили виявити особливості складу та структури досліджуваних зразків. Ідентифіковані дані підтвердили наявність кристалічних фаз Si та Er в композиті p-Si-Er, а також показали заміщення Er у структурі p-Si/SiO<sub>2</sub>. Крім того, дані рентгенівського мікроаналізу підтвердили наявність Si, O та Er в очікуваних концентраціях у композитній плівці. Подальші дослідження показали, що введення атомів ербію на поверхню кремнію призводить до незначних змін деяких сигналів і появи нових коливачь у спектрах КРС зразків. Зменшення інтенсивності піків, що належать кремнію, пов'язане з ослабленням і розривом деяких зв'язків у структурі кристалічної решітки кремнію і внаслідок утворення нових зв'язків, в яких беруть участь атоми ербію. Таким чином, результати цього дослідження є значним внеском у розуміння властивостей і потенціалу тонкоплівкових наноконкомпозитів для застосування в оптоелектроніці, а також збагачують наші знання про вплив легування на структуру та властивості кремнієвих матеріалів.

**Ключові слова:** кремній; ербій; рідкоземельний елемент; раманівська спектроскопія; дифузія; термічна обробка; температура; структура; рентгенівський фазовий аналіз; плівка

## SURFACE PROPERTIES AND COMPOSITION ANALYSIS OF NANO-SIZED THIN FILMS OF CDSE: BY SEM ANALYSIS

L.N. Ibrahimova<sup>a</sup>, N.M. Abdullayev<sup>b</sup>, Sevinj R. Azimova<sup>b\*</sup>,  Y.I. Aliyev<sup>c,d</sup>

<sup>a</sup>Institute of Natural Resources, Nakhchivan, AZ-7000, Azerbaijan

<sup>b</sup>Institute of Physics, Ministry of Science and Education of Azerbaijan, Baku, AZ-1143, Azerbaijan

<sup>c</sup>Azerbaijan State Pedagogical University, Baku, AZ-1000, Azerbaijan

<sup>d</sup>Western Caspian University, Baku, AZ-1001, Azerbaijan

\*Corresponding Author e-mail: [sevinjazimova@bk.ru](mailto:sevinjazimova@bk.ru)

Received March 12, 2024; revised April 6, 2024; accepted April 19, 2024

Thin films of cadmium selenide with a thickness  $h = 200-500$  nm were obtained and their surface properties were studied. The studies were carried out using a Scanning Electron Microscope. It was found that with increasing thickness of thin layers, the surface structure becomes smoother. A compositional analysis of the surface of thin layers was also carried out. Elemental analysis was carried out in layers of various thicknesses, the percentage content of chemical elements and the energy spectrum of chemical elements were determined. It has been established that thin CdSe films obtained by chemical deposition are quite pure. The surface of thin layers with a thickness  $h > 400$  nm turned out to be quite smooth, which is an indicator of the formation of a phase in these layers corresponding to the CdSe compound.

**Keywords:** CdSe; Thin films; Compositional analysis; Surface structure; SEM analysis

**PACS:** 61.46.-w; 68.37.-d.

### INTRODUCTION

Chalcogenide semiconductors occupy a special place among non-oxide functional materials. In these compounds, semiconductor, magnetoelectric, ferromagnetic and other physical properties are observed. Therefore, these materials have wide application possibilities. The study of the crystalline and surface structure of chalcogenide semiconductors plays an important role in the formation of their physical properties. Therefore, extensive research is being carried out in this direction [1-5].

It is known that studying the surface structure of materials allows one to obtain extensive information about their size effects. Since micro-composition analysis can be carried out using SEM, this method is widely used. It has been established that the percentage of elements present on the surface can be determined by analyzing the structure and composition of the surface [6-8]. In the course of studying the surface structure and size effect, it was found that changes in the chemical composition affect the size of crystallites. Crystallites that form polycrystals are formed as a result of the connection of elementary lattices. Therefore, when the atoms in the crystal lattice change, the size of the crystallites also changes [9].

The CdSe compound is one of the most studied compounds among chalcogenide semiconductors. The main reason for its interest is that it has different physical properties. In the course of structural studies, it was established that the crystal structure of this compound has high symmetry. The unit lattice parameters with hexagonal systems and space group  $P6_3mc$  are:  $a = 4.2985$  Å,  $c = 7.0152$  Å,  $V = 112.255$  Å<sup>3</sup> [10]. This compound has semiconductor properties, the band gap  $E_g = 1.74$  eV [11]. Although many of the physicochemical properties of the CdSe compound have been studied, the properties of its thin films have not been sufficiently studied. Recently, thin layers of various substances have been studied [12,13]. It has been established that the properties of materials are maintained even in the case of thin layers. The production of thin layers of the CdSe compound and the study of its physical properties further expand the possibilities of its application. In this work, thin CdSe films were obtained on a glass substrate and their microstructure was studied in a Scanning Electron Microscope (SEM).

### EXPERIMENTAL PART

During the research, thin CdSe films with thicknesses of 200, 300, 400 and 500 nm were obtained and the structure of their surface was studied. Thin films of CdSe were obtained by chemical deposition. The solution used to obtain thin layers consists of a composition prepared in the following order: 0.5 M cadmium chloride ( $CdCl_2 \times 2.5H_2O$ ), 13.4 M (25%) sodium hydroxide ( $NH_3OH$ ), 7.4 M triethanolamine ( $C_6H_{15}NO_3$ ), 0.2 M sodium selenosulfate ( $Na_2SSeO_3$ ). The chemical precipitation process was carried out in a laboratory beaker with a capacity of 60 ml at room temperature and normal conditions using a specially developed technology. The method for obtaining thin layers and the phase formation processes is described in detail in [14].

The surface structure of thin films of cadmium selenide with a thickness  $h = 200-500$  nm was studied in a Scanning Electron Microscope (SEM, ZEISS, SIGMA VP). The results obtained were analyzed and the process of phase formation in the layers, composition analysis and size effects were determined.

## RESULTS AND DISCUSSIONS

The morphology of CdSe thin films obtained by chemical deposition was studied using a scanning electron microscope. In the course of research using an SEM microscope, not only an analysis of the surface structure of the layers was carried out, but also an analysis of the chemical composition, and the percentage of elements was determined. Surface structures obtained under normal conditions and at room temperature are presented in Figure 1.

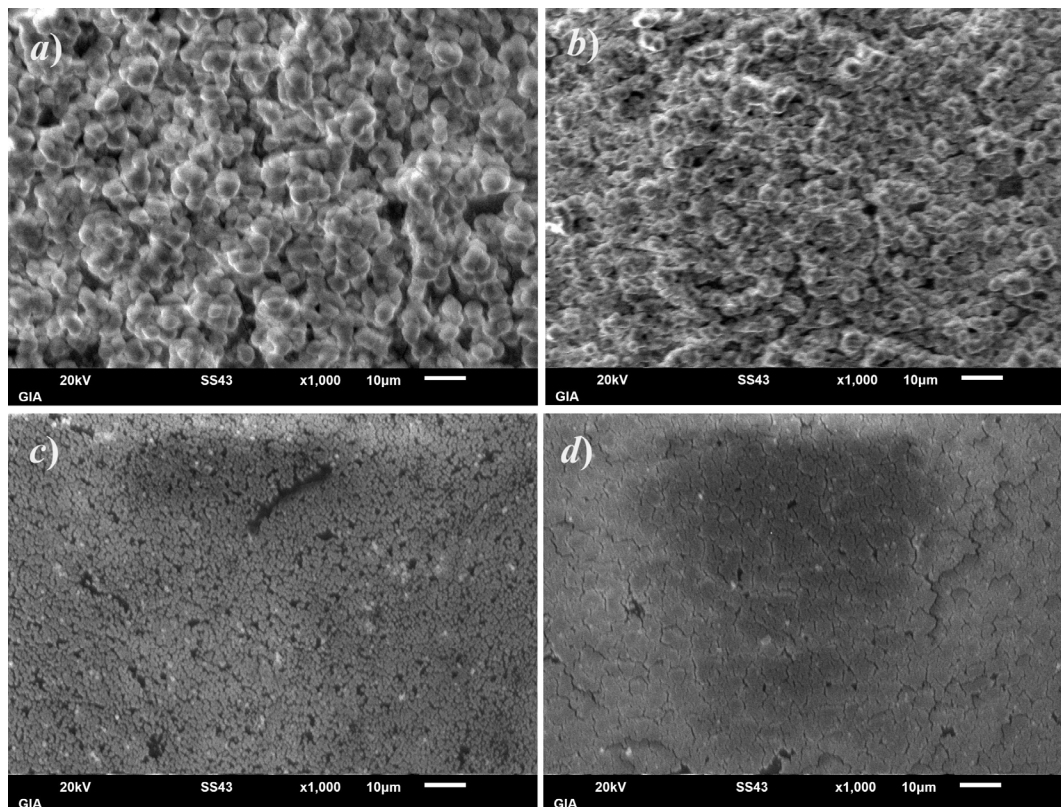


**Figure 1.** Surface structure of thin CdSe films of various thicknesses: *a*)  $h = 200$  nm, *b*)  $h = 300$  nm, *c*)  $h = 400$  nm and *d*)  $h = 500$  nm.

In Fig. 1 shows the morphology obtained at the  $10\ \mu\text{m}$  scale of thin films with thicknesses of  $200$  nm (*a*),  $300$  nm (*b*),  $400$  nm (*c*), and  $500$  nm (*d*). From the structure of the surface of the sample obtained with a thickness of  $h = 200$  nm, it is clear that in these thin layers the structure is not completely formed. An arrangement of crystallites with  $d \sim 4\text{--}5\ \mu\text{m}$  was observed on the surface (Fig. 1*a*). From the surface structure of the resulting sample with a thickness of  $h = 300$  nm, it is clear that in these thin layers the crystallites begin to unite and form a surface structure. Although the structure is not completely formed, the crystallites are more densely packed (Fig. 1*b*). With increasing thickness in thin CdSe films, the process of phase formation becomes more complicated. From the surface structure of the sample obtained with a thickness of  $h = 400$  nm, it is clear that crystallites form a surface structure. Certain defects are observed on the surface, which are small-sized effects that arise during the synthesis of samples (Fig. 1*c*). The process of phase formation was also observed in thin CdSe films as the thickness increased. From the surface structure of the resulting sample with a thickness of  $h = 500$  nm, it is clear that the crystallites form a more closely connected surface structure. Compared to previous layers, the concentration of defects formed on the surface and the size of the defects are also smaller (Fig. 1*d*). As can be seen, during the formation of surface structures of thin layers, the phase formation process continues as the thickness increases.

To perform elemental analysis of CdSe thin films, a chemical elemental spectrum was also obtained. It has been established that elemental analysis of thin layers also identifies elements with a glass substrate. Because some high energy electrons can penetrate into the substrate. Therefore, elemental analysis was carried out on a thin CdSe layer with a thickness of  $h = 500$  nm. The resulting spectrum of chemical elements is shown in Fig. 2. As can be seen from the spectrum, the elements Cd and Se were predominantly found in the thin layer. However, small amounts of the elements Si, S and Ca were also detected, which are also impurities present in the substrate or included in the sample when the layers were produced by chemical deposition.

To determine the amount of chemical elements in thin CdSe films, the percentage of elements in a thin film with a thickness of  $h = 500$  nm is given in Table 1.

From the spectrum shown in Fig. 2 and the values given in Table 1, it is clear that the samples were obtained of sufficiently high purity. When studying the surface structure of thin CdSe layers using scanning electron microscopy, it was found that in these layers obtained by chemical deposition, the properties of the original material are retained. The process of phase formation in thin layers occurred after  $h = 400$  nm.



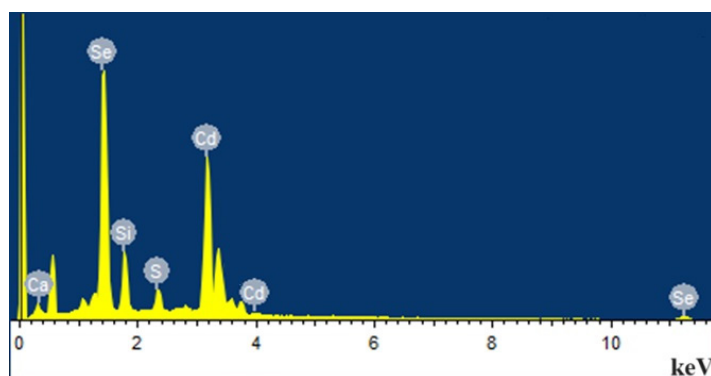


**Figure 2.** Energy spectrum of chemical elements of a thin CdSe film with a thickness of  $h = 500$  nm

**Table 1.** Percentage content of chemical elements in a thin CdSe layer with a thickness of  $h = 500$  nm

Chemical element	Mass (%)	Atom (%)
Si	7.77	20.96
S	2.22	5.24
Ca	1.44	2.71
Se	40.02	38.38
Cd	48.55	32.71
Sum	100	100

## CONCLUSIONS

SEM studies of thin CdSe films obtained by chemical deposition were carried out. During the research, both studies of the formation of the surface structure and analysis of the microcomposition were carried out. As a result of analyzing the spectrum of chemical elements obtained for thin layers, it was found that thin layers obtained on a glass substrate have a fairly high purity. The elements Cd and Se account for 88.57% of the sample mass. It is shown that the remaining elements found in the composition consist of small amounts of impurities that entered the system when purchasing the glass base and sheets. It has been established that the process of phase formation in these layers begins after  $h \sim 400$  nm. Starting from these sizes, CdSe crystallites on a glass substrate combine to form a surface.

## ORCID

Y.I. Aliyev, <https://orcid.org/0000-0001-8896-2180>

## REFERENCES

- [1] T.M. Razikov, S.A. Muzafarova, R.T. Yuldoshov, Z.M. Khusanov, M.K. Khusanova, Z.S. Kenzhaeva, and B.V. Ibragimova, "Growing  $Sb_2Se_3$  films enriched with selenium using chemical molecular beam deposition," *East European Journal of Physics*, **1**, 370-374 (2024). <https://doi.org/10.26565/2312-4334-2024-1-36>
- [2] S.R. Azimova, N.M. Abdullayev, Y.I. Aliyev, M.N. Mirzayev, V.A. Skuratov, A.K. Mutali, and S.H. Jabarov, "Study on the thermodynamic behavior of Sb-Te binary systems with swift heavy-ions irradiation at the high temperatures," *Journal of the Korean Physical Society*, **77**, 240-246 (2020). <https://doi.org/10.3938/jkps.77.240>
- [3] Y.I. Aliyev, N.A. Ismayilova, R.F. Novruzov, A.O. Dashdamirov, H.J. Huseynov, S.H. Jabarov, and A.A. Ayubov, "Electron structure and density of states' calculations of  $Ag_2S$  and  $Ag_2Se$  crystals from first-principle," *Modern Physics Letters B*, **33**(21), 1950242 (2019). <https://doi.org/10.1142/S0217984919502427>
- [4] S.H. Jabarov, N.A. Ismayilova, D.P. Kozlenko, T.G. Mammadov, N.T. Mamedov, H.S. Orudzhev, S.E. Kichanov, et al., "Structural and elastic properties of  $TlInSe_2$  at high pressure," *Solid State Sciences*, **111**, 106343 (2021). <https://doi.org/10.1016/j.solidstatesciences.2020.106343>
- [5] G.M. Agamirzayeva, G.G. Huseynov, Y.I. Aliyev, T.T. Abdullayeva, and R.F. Novruzov, "Crystal structure and magnetic properties of the compound  $Cu_3Fe_{0.5}Se_2$ ," *Advanced Physical Research*, **5**(1), 19-25 (2023). [http://jomardpublishing.com/UploadFiles/Files/journals/APR/V5N1/Agamirzayeva\\_et\\_al.pdf](http://jomardpublishing.com/UploadFiles/Files/journals/APR/V5N1/Agamirzayeva_et_al.pdf)
- [6] A.S. Alekperov, S.H. Jabarov, M.N. Mirzayev, E.B. Asgerov, N.A. Ismayilova, Y.I. Aliyev, T.T. Thabethe, and N.T. Dang, "Effect of gamma irradiation on microstructure of the layered  $Ge_{0.995}Nd_{0.005}S$ ," *Modern Physics Letters B*, **33**(09), 1950104 (2019). <https://doi.org/10.1142/S0217984919501045>
- [7] A.A. Abduvaitov, G.T. Imanova, Kh.Kh. Boltaev, B.E. Umirzakov, D.A. Tashmukhamedova, and G. Abdurakhmanov, "Analysis of the change in the composition of the CdTe surface upon implantation of  $O^{2+}$  ions and subsequent annealing," *Advanced Physical Research*, **6**(1), 36-41 (2024). <https://doi.org/10.62476/apr61.41>
- [8] G.Sh. Ayyubova, S.H. Jabarov, "Crystal structure, surface structure and chemical analysis of  $BaFe_{10.8}In_{1.2}O_{19}$  compound," *UNEC Journal of Engineering and Applied Sciences*, **1**(1), 27-31 (2021). <https://unec-jeas.com/storage/pages/96/gsh-ayyubova-et-al-1.pdf>
- [9] S.H. Jabarov, A.V. Trukhanov, E.A. Kornieva, R.Z. Mehdiyeva, S.E. Kichanov, A.I. Mammadov, E.V. Lukin, and R.E. Huseynov, "Effect of concentration substitution on the size factor in  $Li_{1-x}Na_xNbO_3$  solid solutions," *Journal of Surface Investigation, X-ray, Synchrotron and Neutron Techniques*, **8**, 1198-1200 (2014). <https://doi.org/10.1134/S1027451014060044>

- [10] Y.N. Xu, and W.Y. Ching, "Electronic, optical, and structural properties of some wurtzite crystals," *Physical Review B*, **48**, 4335-4351 (1993). <https://doi.org/10.1103/PhysRevB.48.4335>
- [11] S. Khan, and M.Kh. Hossain, "2-Classification and properties of nanoparticles," *Nanoparticle-Based Polymer Composites*, Woodhead Publishing Series in Composites Science and Engineering, 15-54, (2022). <https://doi.org/10.1016/B978-0-12-824272-8.00009-9>
- [12] N.N. Mursakulov, N.N. Abdulzade, S.H. Jabarov, and Ch.E. Sabzalieva, "Investigation of  $\text{CuIn}_{1-x}\text{Ga}_x\text{Se}_2$  thin films for solar cells obtained by the magnetron sputtering method from two magnetrons shifted to each other," *New Materials, Compounds and Applications*, **6**(2), 140-147 (2022). [http://jomardpublishing.com/UploadFiles/Files/journals/NMCA/v6n2/Mursakulov\\_et\\_al.pdf](http://jomardpublishing.com/UploadFiles/Files/journals/NMCA/v6n2/Mursakulov_et_al.pdf)
- [13] Kh.N. Ahmadova, and S.H. Jabarov, "Obtaining of Al nanosized thin layers and their structural properties," *Arabian Journal for Science and Engineering*, **48**, 8083-8088 (2023). <https://doi.org/10.1007/s13369-022-07449-2>
- [14] L.N. Ibrahimova, N.M. Abdullayev, M.E. Aliyev, G.A. Garashova, and Y.I. Aliyev, "Phase formation process in CdSe thin films," *East European Journal of Physics*, **1**, 493-496 (2024). <https://doi.org/10.26565/2312-4334-2024-1-54>

#### ВЛАСТИВОСТІ ПОВЕРХНІ ТА АНАЛІЗ СКЛАДУ НАНОРОЗМІРНИХ ТОНКИХ ПЛІВОК CDSE: SEM АНАЛІЗ

Л.Н. Ібрагімова<sup>a</sup>, Н.М. Абдуллаєв<sup>b</sup>, Севінж Р. Азімова<sup>b</sup>, Ю.І. Алієв<sup>c,d</sup>

<sup>a</sup>Інститут природних ресурсів, Нахічевань, AZ-7000, Азербайджан

<sup>b</sup>Інститут фізики Міністерства науки і освіти Азербайджану, Баку, AZ-1143, Азербайджан

<sup>c</sup>Азербайджанський державний педагогічний університет, Баку, AZ-1000, Азербайджан

<sup>d</sup>Західнокаспійський університет, Баку, AZ-1001, Азербайджан

Отримано тонкі плівки селеніду кадмію товщиною  $h = 200-500$  нм і досліджено властивості їх поверхні. Дослідження проводили за допомогою скануючого електронного мікроскопа. Встановлено, що зі збільшенням товщини тонких шарів структура поверхні стає більш гладкою. Також проведено аналіз складу поверхні тонких шарів. Проведено елементний аналіз шарів різної товщини, визначено процентний вміст хімічних елементів та енергетичний спектр хімічних елементів. Встановлено, що тонкі плівки CdSe, отримані хімічним осадженням, є досить чистими. Поверхня тонких шарів товщиною  $h > 400$  нм виявилася досить гладкою, що є показником утворення в цих шарах фази, що відповідає сполуці CdSe.

**Ключові слова:** CdSe; тонкі плівки; композиційний аналіз; структура поверхні; SEM аналіз

## STUDY OF CRYSTAL CHARACTERIZATION AND CHEMICAL INTERACTION IN THE TERNARY SYSTEM Ho-Sb-Te

T.M. Ilyasli<sup>a</sup>, N.Sh. Mammadova<sup>a</sup>, F.M. Sadigov<sup>a</sup>,  Ramiz E. Huseynov<sup>b\*</sup>,  Y.I. Aliyev<sup>c,d</sup>

<sup>a</sup>Baku State University, Baku, AZ-1148, Azerbaijan

<sup>b</sup>Institute of Physics, Ministry of Science and Education Republic of Azerbaijan, Baku, AZ-1143, Azerbaijan

<sup>c</sup>Azerbaijan State Pedagogical University, Baku, AZ-1000, Azerbaijan

<sup>d</sup>Western Caspian University, Baku, AZ-1001, Azerbaijan

\*Corresponding Author e-mail: [r.e.huseynov@gmail.com](mailto:r.e.huseynov@gmail.com)

Received March 19, 2024; revised April 5, 2024; accepted April 27, 2024

Complex methods of physical and chemical analysis: differential thermal analysis (DTA), X-ray phase analysis (XRD), microstructural analysis (MSA), as well as density and microhardness measurements, were used to study the nature of chemical interaction in the Ho-Sb-Te ternary system over the entire concentration range along the following sections: 1. Sb<sub>2</sub>Te<sub>3</sub>-Ho<sub>2</sub>Te<sub>3</sub>, 2. Sb<sub>2</sub>Te<sub>3</sub>-HoTe, 3. HoTe-Sb, 4. HoSb-HoTe, 5. Sb<sub>2</sub>Te<sub>3</sub>-Ho, 6. HoSb-Te. The projection of the liquidus surface of the ternary system and the diagrams of the state of internal sections were constructed according to experimental data and literature data on binary systems: Sb-Te, Sb-Ho, Ho-Te. It is established that sections (1), (2), (3), (4) are quasi-binary, and (5), (6) are non-quasi-binary sections of the ternary system. The incongruently melting compound HoSbTe<sub>3</sub> is formed in the Sb<sub>2</sub>Te<sub>3</sub>-Ho<sub>2</sub>Te<sub>3</sub> system and the area of solid solutions based on Sb<sub>2</sub>Te<sub>3</sub> ~ 3-5 mol% at 300K was found.

**Keywords:** System; Cut; Liquidus; Quasi binary; Non-quasi binary

**PACS:** 61.05.C-, 61.66.Fn

### 1. INTRODUCTION

Chalcogenide semiconductors are materials with a wide range of applications. Therefore, these materials' physical and chemical properties have been studied for a long time. The results obtained during the research are also important for the purchase of new semiconductors. In particular, the results obtained during structural studies are important for the explanation of the physical properties of these materials. Therefore, it is important to study the structure and structural phase transitions in chalcogenides [1-5].

Compounds containing  $B_2^V X_3$  ( $B^V$ -Sb, Bi; X-Se, Te) occupy an important place among chalcogenide semiconductors. It was determined that a number of properties of these compounds are resistant to temperature and radiation [6-8]. The ternary phases (solid solutions, compounds) and composite materials based on them have unique properties such as valuable semiconductors, thermoelectrics and topological insulators. Some of them (materials with thermoelectric properties) are used as the positive and negative arms of the thermocouple in the development of energy converters for the conversion of environmentally friendly, economically efficient solar energy into electricity as an alternative energy source, and topological insulators are promising materials in spintronics and quantum computing [9-13].

When obtaining new chalcogenide semiconductors with cation-cation substitutions, conducting structural studies and studying phase analyzes are very important. During the experiments carried out by the X-ray diffraction method, it was determined that a single-phase system does not form during some substitutions. A two-phase and even three-phase system is formed [14,15]. It is important to study the processes of phase formation in these compositions.

Although phase formation processes have been studied in many systems in chalcogenide semiconductors, the Ho-Sb-Te system has not been sufficiently studied. In this study, the Ho-Sb-Te ternary system was studied in a wide temperature and solidity interval, and the process of phase formation in the system, chemical interaction, crystallization areas of the ternary system, and equilibrium processes occurring in the system were studied.

### 2. RESEARCH METHODS

During the study of the ternary system, the synthesis of its alloys was carried out using elements of a special pure brand - Holmium metallicity-Holm-0, antimony-B-4, tellurium-TA-2. When performing the experimental part of the research work, the following methods were used: high-temperature differential-thermal analysis (DTA), X-ray phase analysis, microstructure analysis, determination of microhardness, and density measurement. DTA experiments were carried out in an argon atmosphere in a BTA-987 calorimeter. The DTA method is a unique method for studying the processes occurring due to thermal energy in solid bodies [16,17]. Structural studies were performed using D8 ADVANCE and D2 Phaser devices, microstructure analysis was performed using metallographic microscope MIM-7, and microhardness using PMT-3 brand devices. The X-ray diffraction method is one of the modern research methods for studying the structure of crystals and structural phase transitions. This method allows us to determine lattice parameters, symmetry, and space groups of solids and to determine structural phases [18-20].



The alloys of the studied system were synthesized in a high-temperature furnace at a temperature of 800-1250 K in vacuumed quartz ampoules. To create an equilibrium state in the alloys, they were thermally treated in vacuum ampoules at a temperature of 800 K for 900 hours. The starting component crystallizes in rhombohedral syngonia of  $Sb_2Te_3$  tetradymite type in the  $R\bar{3}m$  space group, lattice parameters:  $a=4.383$ ,  $c=30.487$  Å, and melting temperature: 895 K. The compound  $Ho_2Te_3$  crystallizes in orthorhombic syngonia in space group  $Pbb$  with lattice parameters:  $a=12.17$ ,  $c=8.606$  Å, and melting temperature: 1643 K.

### 3. RESEARCH RESULTS AND DISCUSSION

***HoSb-HoTe system.*** The thermal properties of the HoSb-HoTe system were studied using a W-W/Re thermocouple in an argon atmosphere in a BTA-987 calorimeter in graphite crucibles. 2 endothermic effects were observed in all thermograms. The structure of these compositions was studied by the X-ray diffraction method. The obtained X-ray spectra are given in Figure 1.

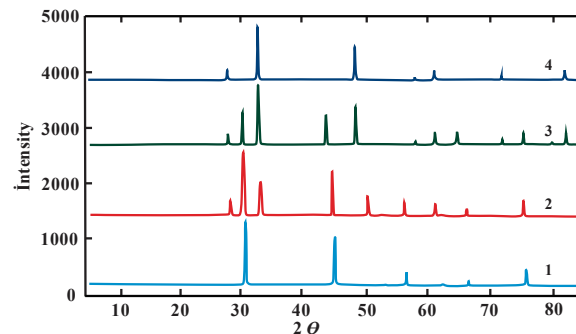


**Figure 1.** X-ray diffraction spectra of the HoSb-HoTe system: 1- HoSb, 2-65 mol%, 3-75 mol%, 4-100 mol% HoTe.

During the analysis of the X-ray diffraction spectra, it was determined that the X-ray spectra of the compositions correspond to the mixture of the starting components. The microstructure analyzes of these compositions were studied under a MIM-7 microscope. The results of the microstructure analysis of HoSb-HoTe alloys are given in Figure 2.

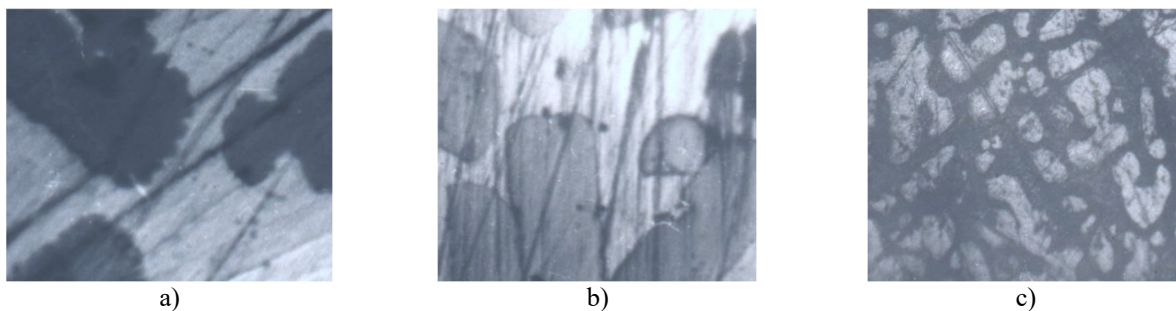


**Figure 2.** Microstructure of alloys of the HoSb-HoTe system: a) 20 mol%, b) 60 mol%, c) 80 mol% HoTe

The microhardness of the obtained compositions was also studied. It was determined that 2615 MPa corresponds to the HoSb phase, and 2575 MPa corresponds to the HoTe phase. Thus, based on the obtained results, a phase diagram of the HoSb-HoTe system was constructed (Figure 3).

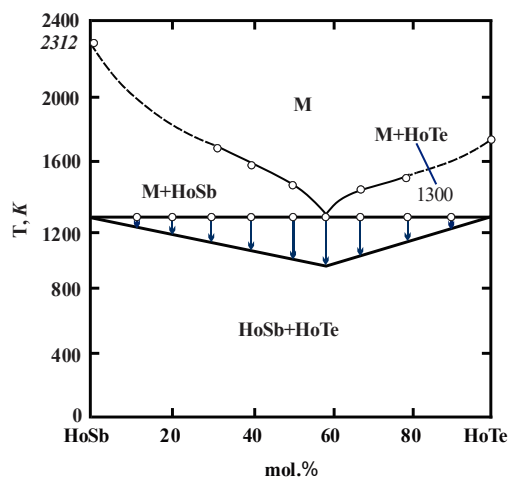


**Figure 3.** Phase diagram of the HoSb - HoTe system.

As can be seen from Figure 3, the HoSb-HoTe system is a quasi-binary part of the Ho-Sb-Te ternary system and is a simple eutectic type. The coordinates of the eutectic are 60 mol% HoTe and 1300 K. The existence of a homogeneous field based on the primary components is practically not determined. A three-phase nonvariant equilibrium process ( $M \leftrightarrow \text{HoSb} + \text{HoTe}$ ) occurred in the eutectic.

**HoTe-Sb system.** Two endothermic effects were revealed during the thermal analysis of the HoTe-Sb system. This indicates that a new phase has not formed in the system. To confirm this process, the structure of the ingredients was studied by the X-ray diffraction method. The obtained spectra are shown in Figure 4. X-ray diffraction spectra show that this composition consists of a mixture of starting materials.

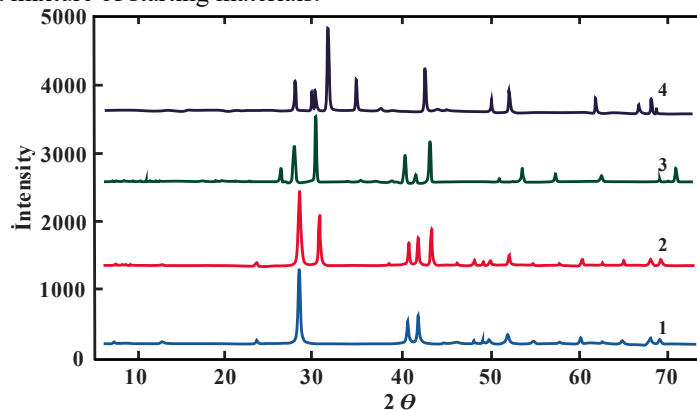


**Figure 4.** X-ray diffraction spectra of the HoTe-Sb system: 1- Sb, 2-40 mol%, 3-75 mol%, 4-100 mol% HoTe.

The microstructure analyses of these compositions were studied under a MIM-7 microscope. The results of the microstructure analysis of HoTe-Sb alloys are given in Figure 5.

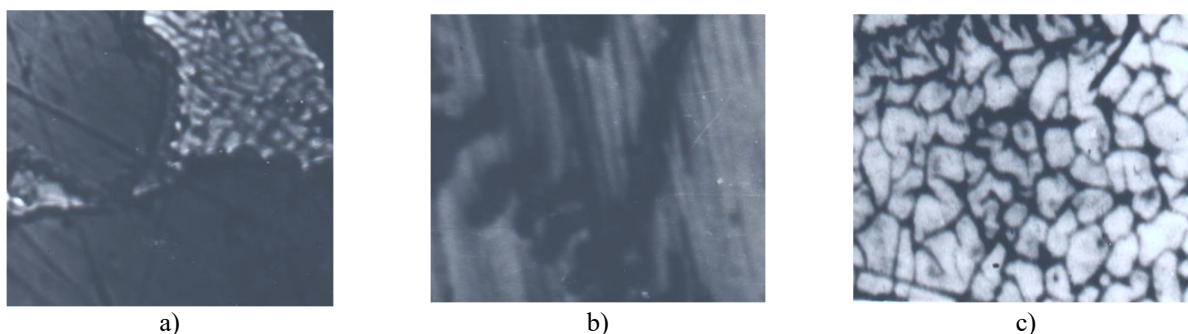


**Figure 5.** Microstructure of alloys of the HoTe-Sb system: a) 20 mol%, b) 50 mol%, c) 90 mol% Sb

The microhardness of the HoTe-Sb system was also investigated. When analyzing the obtained results, it was determined that 750 MPa corresponds to Sb metal, and 2575 MPa corresponds to the HoTe combination.

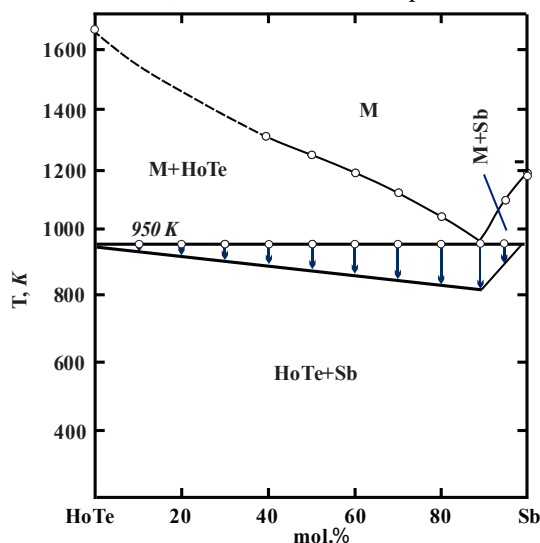


**Figure 6.** Phase diagram of the HoTe - Sb system

Based on the obtained results, a phase diagram of the HoTe-Sb system was constructed (Figure 6). It was determined that the HoTe-Sb system is a quasi-binary section of the Ho-Sb-Te ternary system and is of a simple eutectic type. In the

system, the eutectic is formed by the equilibrium reaction  $M \leftrightarrow \text{HoTe} + \text{Sb}$ . Eutectic coordinates: 90 mol% Sb and 850 K are set. No solubility domain was detected in the system.

**HoSb-Te system.** The thermal properties of the HoSb-Te system were also studied. Based on the obtained DTA spectra, it was determined that three endothermic effects are mainly observed in these compositions. To confirm this process, the structure of the ingredients was studied by the X-ray diffraction method. The obtained spectra are shown in Figure 7. X-ray diffraction spectra show that this composition consists of a mixture of starting materials.

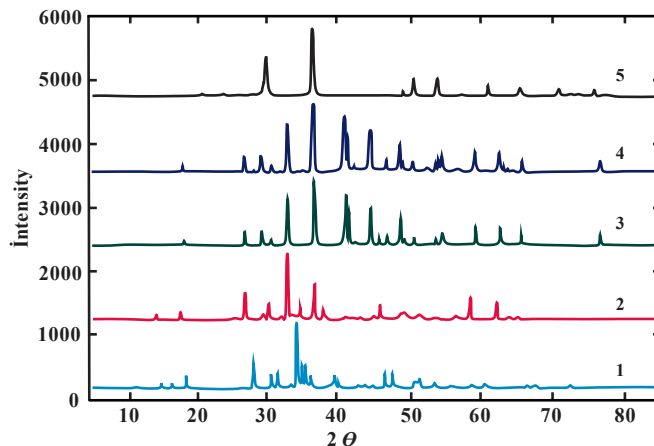


**Figure 7.** X-ray diffraction spectra of the HoSb-Te system: 1- HoSb, 2- 30 mol%, 3- 50 mol%, 4- 80 mol%, 5- 100 mol% Te

To study the surface structure of the HoSb-Te system, microstructure analyzes were carried out under the MIM-7 microscope. The results of microstructure analysis of HoSb-Te alloys are given in Figure 8.

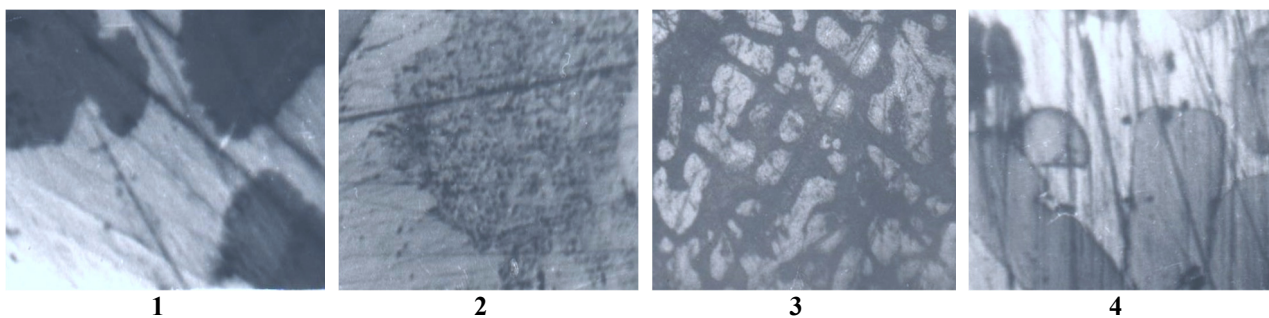


**Figure 8.** Microstructure of alloys of the HoSb-Te system: a) 20 mol%, b) 50 mol%, c) 90 mol% Sb

The microhardness of the HoSb-Te system was also investigated. Analyzing the obtained results, it was determined that the microhardness of 650 MPa corresponds to Te chalcogenide, and the microhardness of 2615 MPa corresponds to the HoSb compound.

Based on the results of the complex analysis, a phase diagram of the HoSb-Te system was constructed (Figure 9).

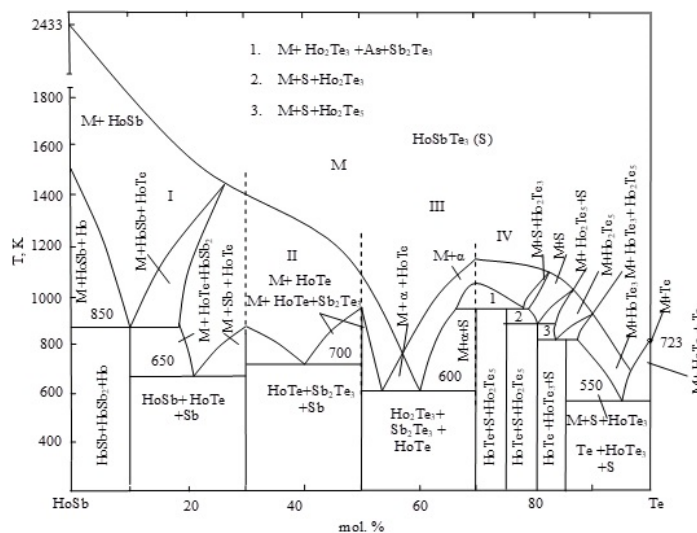
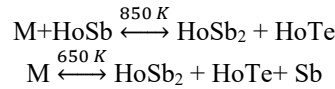


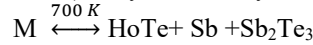
**Figure 9.** Phase diagram of the HoSb - Te system

As can be seen from Figure 9, the chemical interaction occurring in the system has a complex nature, and the system is a non-quasi binary section of the Ho-Sb-Te ternary system and passes through the area of four subordinate triangles.

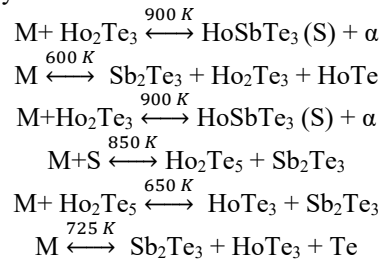
In the first part of the system (0-30 mol% Te) a nonvariant triple peritectic and triple eutectic equilibrium processes were reflected:



In the second part of the system (30-50 mol % Te), only one ternary nonvariant eutectic equilibrium process occurs.



The following 4-phase equilibrium processes take place in the third part (50-70 mol% Te) and the fourth part (75-100 mol% Te) of the system, respectively.



Projection of the liquidus surface of the Ho-Sb-Te ternary system. The tranquility of this triple system was carried out. It was determined that the ternary system is divided into five subordinate systems: 1. HoSb-Ho-HoTe, 2. HoTe-Sb-HoS b, 3. HoTe-Sb-Sb<sub>2</sub>Te<sub>3</sub>, 4. Sb<sub>2</sub>Te<sub>3</sub>-HoTe-Ho<sub>2</sub>Te<sub>3</sub>, 5. Sb<sub>2</sub>Te<sub>3</sub>-Te-Ho<sub>2</sub>Te<sub>3</sub>. The studied internal cross-sections - Sb<sub>2</sub>Te<sub>3</sub>-Ho<sub>2</sub>Te<sub>3</sub>, Sb<sub>2</sub>Te<sub>3</sub>-HoTe, HoTe-Sb, HoSb-HoTe, Sb<sub>2</sub>Te<sub>3</sub>-Ho, HoSb-Te and Sb-Te, Ho-Te, Ho-Sb binary systems with the sides of the triangle, based on literature data and the theory of physico-chemical analysis, the projection of the liquidus surface of the mentioned ternary system in the entire solidity range was established (Figure 10).

The nature of the interaction in the Ln-B<sup>V</sup>-X, B<sup>V</sup>-Sb, Bi, X-Se, and Te ternary systems studied in the order of lanthanoids is of the same type. In all ternary systems, an incongruent melting compound containing LnB<sup>V</sup>X<sup>3</sup> and a B<sup>2</sup>X<sup>3</sup>-based solid solution area of ~5-7 mol % is formed.

The liquidus surface of the system consists of crystallization areas of 13 phases bounded by 26 monovariant curves. The temperature conditions of monovariant and nonvariant equilibrium processes occurring in the system are given in Table 1. 14 nonvariant equilibrium processes occurred in the system, of which five are E<sub>1</sub>-E<sub>5</sub> triple nonvariant equilibrium eutectic points, and nine are nonvariant P<sub>1</sub>-P<sub>9</sub> peritectic equilibrium points.

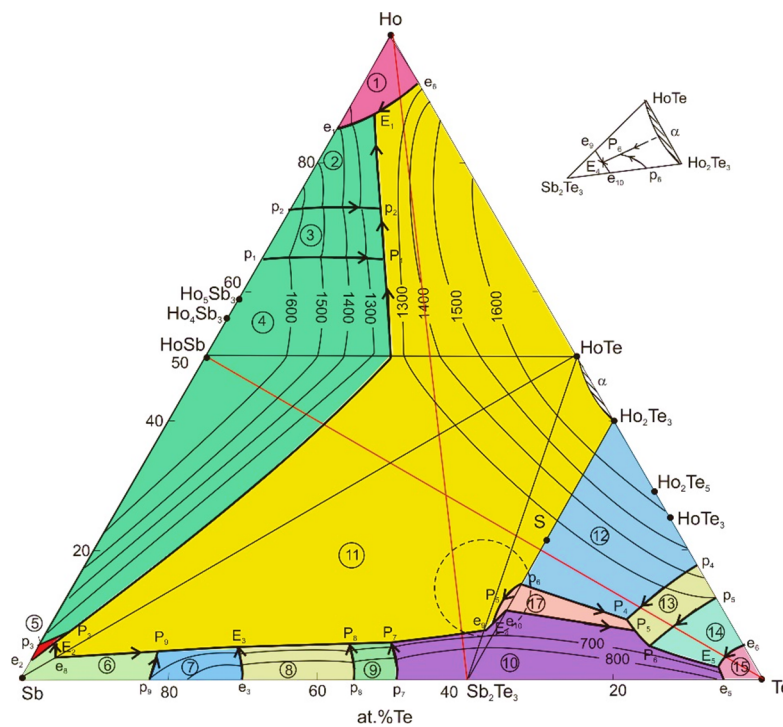


**Figure 10.** Projection of the liquidus surface of the Ho-Sb-Te ternary system  
 1-Ho; 2- Ho<sub>5</sub>Sb<sub>3</sub>; 3- Ho<sub>4</sub>Sb<sub>3</sub> ; 4-HoS b; 5-HoS b<sub>2</sub>; 6-Sb; 7-β; 8-β'; 9-η; 10-Sb<sub>2</sub>Te<sub>3</sub>; 11-HoTe; 12-α(HoTe+Ho<sub>2</sub>Te<sub>3</sub>); 13-Ho<sub>2</sub>Te<sub>3</sub>;  
 14-HoTe<sub>3</sub>; 15-Te; 16-α; 17- HoSbTe<sub>3</sub>(S).

**Table 1.** Temperature conditions of monovariant and nonvariant processes occurring on the liquidus surface of the Ho-Sb-Te ternary system

No	Equilibrium points and curves	Reactions	Temperature, K
1	E1	$M \leftrightarrow Ho + \alpha - Ho_4Sb_3 + HoTe$	650
2	E2	$M \leftrightarrow HoSb_2 + Sb + HoTe$	750
3	E3	$M \leftrightarrow Sb + Sb_2Te_3 + HoTe$	600
4	E4	$M \leftrightarrow S + Sb_2Te_3 + \alpha$	600
5	E5	$M \leftrightarrow Te + HoTe_3 + Sb_2Te_3$	625
6	P1	$M + \alpha - Ho_4Sb_3 \leftrightarrow Ho_5Sb_3 + HoTe$	950
7	P2	$M + \beta - Ho_4Sb_3 \leftrightarrow \alpha - Ho_4Sb_3 + HoTe$	900
8	P3	$M + HoSb \leftrightarrow HoSb_2 + HoTe$	850
9	P4	$M + Ho_2Te_3 \leftrightarrow HoSbTe_3 + \alpha$	900
10	P5	$M + HoSbTe_3 \leftrightarrow Ho_2Te_3 + Sb_2Te_3$	675
11	P6	$M + Ho_2Te_5 \leftrightarrow HoTe_3 + Sb_2Te_3$	725
12	P7	$M + Sb_2Te_3 \leftrightarrow \eta + HoTe$	775
13	P8	$M + \eta \leftrightarrow \beta' + HoTe$	720
14	P9	$M + Sb \leftrightarrow \beta + HoTe$	800

Isothermal lines were drawn every 100 K to monitor the course of monovariant curves in the system. (Figure 11). It was determined that the subsolidus of the Ho-Sb-Te ternary system consists of 24 parts. 12 of them are three-phase, and 12 are two-phase.

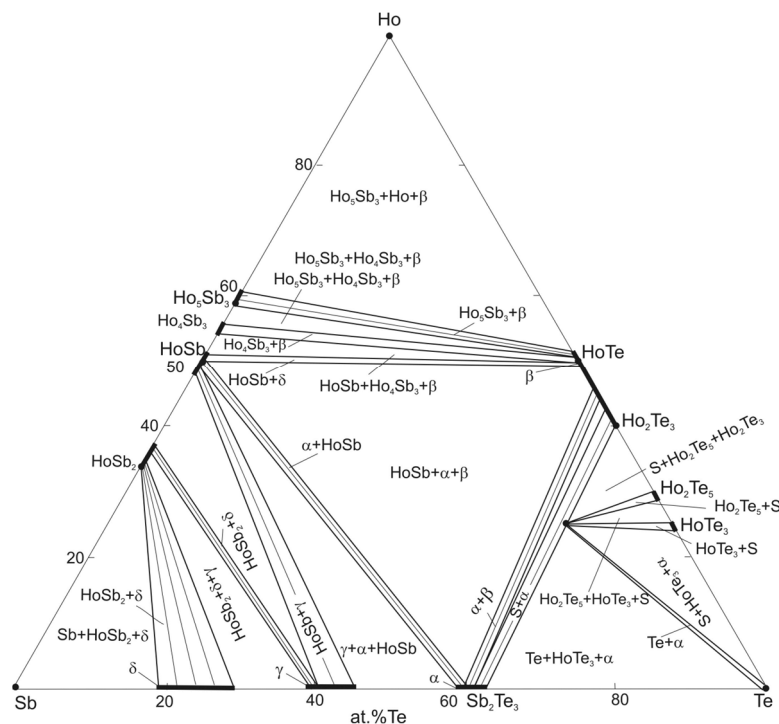


**Figure 11.** Isothermal section of the Ho-Sb-Te system at 300 K

### CONCLUSIONS

1. HoSb-HoTe, HoTe-Sb, and HoSb-Te systems were studied with complex methods of physico-chemical analysis (DTA, RFA, MQA, microhardness and density determination methods) and phase diagrams were constructed.
2. According to the research results, it was determined that the HoSb-HoTe and HoTe-Sb systems are a quasi-binary section of the Ho-Sb-Te ternary system, and the HoSb-Te system is a non-quasibinary section of the Ho-Sb-Te ternary system.
3. The HoSb-Te section passes through the area of four subordinate triangles of the ternary system 1. HoSb-Sb-HoTe, 2. HoTe-Sb-  $Sb_2Te_3$ , 3. HoTe-  $Sb_2Te_3$ -  $Ho_2Te_3$ , 4.  $Sb_2Te_3$ -Te-  $Ho_2Te_3$
4. Based on the research results of HoSb-HoTe, HoTe-Sb, and HoSb-Te sections, the liquidus surface of the Ho-Sb-Te ternary system was established, and the coordinates and temperatures of the nonvariant equilibrium points were determined.
5. A diagram of the isothermal section at 300K was constructed to monitor the processes in the solid phase of the ternary system.

### ORCID

© Ramiz E. Huseynov, <https://orcid.org/0000-0003-0636-3948>; © Y.I. Aliyev, <https://orcid.org/0000-0001-8896-2180>



## REFERENCES

- [1] L.N. Ibrahimova, N.M. Abdullayev, M.E. Aliyev, G.A. Garashova, and Y.I. Aliyevs, East European Journal of Physics, **1**, 493 (2024). <https://doi.org/10.26565/2312-4334-2024-1-54>
- [2] Y.I. Aliyev, Y.G. Asadov, T.M. Ilyasli, F.M. Mammadov, T.G. Naghiyev, Z.A. Ismayilova, M.N. Mirzayev, and S.H. Jabarov, Modern Physics Letters B, **34** (05), 2050066 (2020). <https://doi.org/10.1142/S0217984920500669>
- [3] G.M. Agamirzayeva, G.G. Huseynov, Y.I. Aliyev, T.T. Abdullayeva, and R.F. Novruzov, Advanced Physical Research, **5**(1), 19 (2023). [http://jomardpublishing.com/UploadFiles/Files/journals/APR/V5N1/Agamirzayeva\\_et\\_al.pdf](http://jomardpublishing.com/UploadFiles/Files/journals/APR/V5N1/Agamirzayeva_et_al.pdf)
- [4] Y.I. Aliyev, Y.G. Asadov, A.O. Dashdemirov, R.D. Aliyeva, T.G. Naghiyev, and S.H. Jabarov, International Journal of Modern Physics B, **33** (23), 1950271 (2019). <https://doi.org/10.1142/S021797921950271>
- [5] B.G. Tagiyev, O.B. Tagiyev, A.I. Mammadov, V.X. Quang, T.G. Naghiyev, S.H. Jabarov, M.S. Leonenya, G.P. Yablonskii, and N.T. Dang, Physica B: Condensed Matter, **478**, 58 (2015). <https://doi.org/10.1016/j.physb.2015.08.061>
- [6] S.R. Azimova, N.M. Abdullayev, Y.I. Aliyev, M.N. Mirzayev, V.A. Skuratov, A.K. Mutali, and S.H. Jabarov, Journal of the Korean Physical Society, **77**, 240, (2020). <https://doi.org/10.3938/jkps.77.240>
- [7] S.R. Azimova, Adv. Phys. Res. **3**(1), 46 (2021). <http://jomardpublishing.com/UploadFiles/Files/journals/APR/V3N1/6Azimova.pdf>
- [8] S.R. Azimova, N.M. Abdullayev, Y.I. Aliyev, and M.N. Mirzayev, Modern Physics Letters B, **34** (15), 2050156 (2020). <https://doi.org/10.1142/S0217984920501560>
- [9] I. Liu, and D. Vanderbilt, Physical Review B, **90**, 155316 (2014). <https://doi.org/10.1103/physrevb.90.155316>
- [10] N. Singh, and U. Schwingenschlogl, Physica Status Solidi RRL, **8** (9), 805-808 (2014). <https://doi.org/10.1002/pssr.201409110>
- [11] J.E. Moore, Nature, **464**, 194-198 (2010). <https://doi.org/10.1038/nature08916>
- [12] C.L. Kane, J.E. Moore, Topological Insulators, Physics World, **24**, 32-36 (2011). <https://doi.org/10.1088/2058-7058/24/02/36>
- [13] A.M. Adam, A. Elchataie, A.M.A. Mahamed, P. Petkov, E.M. Ibrahim, Materials Research Express, **5**, 035514 (2018). <https://doi.org/10.1088/2053-1591/aab5e8>
- [14] Y.I. Aliyev, Y.G. Asadov, R.D. Aliyeva, T.G. Naghiyev, S.H. Jabarov, Modern Physics Letters B, **33** (11), 1850128 (2019). <https://doi.org/10.1142/S0217984919501288>
- [15] Yu.I. Aliyev, Yu.G. Asadov, R.D. Aliyeva, S.H. Jabarov, Semiconductors, **51**, 732-739, (2017). <https://doi.org/10.1134/S1063782617060045>
- [16] H.S. Ibrahimova, N.I. Valimatova, Advanced Physical Research, **5** (1), 26-32 (2023).
- [17] S.H. Jabarov, International Journal of Modern Physics B, **32** (27), 1850303 (2018). <https://doi.org/10.1142/S0217979218503034>
- [18] S.F. Samadov, A.S. Abiyev, A.G. Asadov, N.V.M. Trung, A.A. Sidorin, O.A. Samedov, E.P. Popov, E. Demir, T. Vershinina, Y.I. Aliyev, K.M. Hasanov, M.N. Mirzayev, Ceramics International, **50** (2), 3727-3732 (2024). <https://doi.org/10.1016/j.ceramint.2023.11.125>
- [19] N.T. Dang, D.P. Kozlenko, S.E. Kichanov, S.G. Jabarov, A.I. Mammadov, R.Z. Mekhtieva, T.L. Phan, V.G. Smotrakov, V.V. Eremkin, B.N. Savenko, Journal of Electronic Materials, **46** (6), 3373-33801 (2017). <https://doi.org/10.1007/s11664-017-5351-x>
- [20] S.H. Jabarov, S.I. Ibrahimova, F.V. Hajiyeva, E.M. Huseynov, Y.I. Aliyev, Arabian Journal for Science and Engineering, **47** (6), 7817-7823 (2022). <https://doi.org/10.1007/s13369-022-06745-1>

**ДОСЛІДЖЕННЯ ХАРАКТЕРИСТИКИ КРИСТАЛІВ ТА ХІМІЧНОЇ ВЗАЄМОДІЇ  
В ПОТРІЙНІЙ СИСТЕМІ Ho-Sb-Te**

**Т.М. Ільяслі<sup>а</sup>, Н.Ш. Мамедова<sup>а</sup>, Ф.М. Садигов<sup>а</sup>, Раміз Е. Гусейнов<sup>б</sup>, Ю.І. Алієв<sup>с,д</sup>**

<sup>а</sup>Бакинський державний університет, Баку, AZ-1148, Азербайджан

<sup>б</sup>Інститут фізики Міністерства науки і освіти Азербайджанської Республіки, Баку, AZ-1143, Азербайджан

<sup>с</sup>Азербайджанський державний педагогічний університет, Баку, AZ-1000, Азербайджан

<sup>д</sup>Західнокаспійський університет, Баку, AZ-1001, Азербайджан

Для вивчення характеру хімічної взаємодії Ho використовували комплексні методи фізико-хімічного аналізу: диференційний термічний аналіз (ДТА), рентгенофазовий аналіз (РФА), мікроструктурний аналіз (МСА), а також вимірювання густини та мікротвердості. -Sb-Te потрійна система в усьому діапазоні концентрацій по ділянках: 1. Sb<sub>2</sub>Te<sub>3</sub>-Ho<sub>2</sub>Te<sub>3</sub>, 2. Sb<sub>2</sub>Te<sub>3</sub>-HoTe, 3. HoTe-Sb, 4. HoSb-HoTe, 5. Sb<sub>2</sub>Te<sub>3</sub>-Ho, 6. HoSb-Te. Проекцію поверхні ліквідусу потрійної системи та діаграми стану внутрішніх перерізів побудовано за експериментальними та літературними даними для подвійних систем: Sb-Te, Sb-Ho, Ho-Te. Встановлено, що ділянки (1), (2), (3), (4) є квазібінарними, а (5), (6) – неквазібінарними ділянками трійкової системи. У системі Sb<sub>2</sub>Te<sub>3</sub>-Ho<sub>2</sub>Te<sub>3</sub> утворюється інконгруентноплавка сполука HoSbTe<sub>3</sub> і знайдено площу твердих розчинів на основі Sb<sub>2</sub>Te<sub>3</sub> ~ 3-5 мол.% при 300 К.

**Ключові слова:** система; розріз; ліквідус; квазібінарний; неквазібінарний